

Superconducting bolometers for millimeter and submillimeter wave astronomy

Dissertation

zur

Erlangung des Doktorgrades (Dr. rer. nat.) der

Mathematisch-Naturwissenschaftlichen Fakultät

der

Rheinischen Friedrich-Wilhelms-Universität Bonn

vorgelegt von

Nikhil Jethava

aus

Pune, Indien

Bonn, June 2007

Angefertigt mit Genehmigung der Mathematisch-Naturwissenschaftlichen Fakultät der Rheinischen
Friedrich-Wilhelms-Universität Bonn

Referenten: **Prof. Dr. Karl M Menten**^{1,2}
 Prof. Dr. Frank Bertoldi²

¹ Max-Planck-Institut für Radioastronomie

² Universität Bonn

Tag der Promotion: 28. September 2007

Diese Dissertation ist auf dem Hochschulschriftenserver der ULB Bonn
http://hss.ulb.uni-bonn.de/diss_online elektronisch publiziert

Superconducting bolometers for millimeter and submillimeter wave astronomy

Abstract

Bolometers are simple and robust incoherent continuum detectors which nevertheless can reach sensitivities close to the fundamental noise limit. This thesis describes the theory, design, fabrication and testing of the superconducting bolometers, developed in collaboration between the Max Planck Institute for Radio Astronomy (MPIfR), Bonn and the Institute for Photonic Technology (IPHT), Jena, Germany. The voltage biased superconducting bolometer (VSB) offers various advantages over the traditional semiconducting bolometer; it is faster, more sensitive, has a higher dynamic range, allows complete microlithographic fabrication and can be multiplexed with Superconducting Quantum Interference Devices (SQUIDs). The low noise SQUID amplifiers operate at bolometer temperatures and have very low power dissipation. The low impedance characteristics of VSBs and SQUIDs makes them less sensitive to microphonic pickup and it is possible to achieve very low noise equivalent power (NEP) levels. The fabrication of bolometers with integrated SQUIDs and the multiplexing electronics will allow the production of bolometer arrays with several hundred or more pixels.

The superconducting thermistor, deposited on the low stress silicon nitride membrane, is a bilayer of gold-palladium and molybdenum and is designed for a transition temperature of 450 mK. Bolometers for the 1.2 mm atmospheric window were designed, built and tested. Different test arrays with seven bolometers were fabricated to study the properties of the thermistor and the silicon nitride membrane. The thermal conductance (G) of the bolometer is tuned by structuring the silicon nitride membrane into spider-like geometries. The bolometers are divided into three different categories, High-G, Medium-G and Low-G, depending on their thermal conductance. The silicon nitride membrane is continuous for the High-G and it is structured into a spider-like geometry for Medium-G and Low-G bolometers. The thermal conductance of Low-G bolometers is too low for operating with a 300 K background, because under this condition, the bolometer will be driven into the normal conducting state by the radiation alone. The thermal conductance of Medium-G bolometers is appropriate for the operation with a 300 K background and for the experimental purposes the silicon nitride membrane of the Medium-G bolometer is structured into 8-legs, 16-legs and 32-legs spider geometries.

The incident radiation is absorbed by crossed dipoles made from gold-palladium (Au-Pd) alloy with a surface resistance of $10 \Omega/\square$. The base temperature of 300 mK is provided by a liquid ^4He cryostat with integrated ^3He stage. The time constant of the bolometer is derived by measuring the modulated signal of a blackbody using a lock-in amplifier. The noise is measured as a *timeseries* and analyzed using National Instruments' *LabVIEW* package. A bolometer model has been developed to understand the physics of the bolometer. Using the COSMOS finite element analysis (FEA) package, the thermal conductance is obtained for the bolometers of different geometries. The ideal performance of the bolometer is derived from VSB theory and the results from the bolometer model are compared with experimental results.

FEA simulations showed that the deposition of a gold (Au) ring around the absorbing area could increase the sensitivity of the bolometer. Therefore, a new Medium-G layout was fabricated, with a gold ring around the absorbing center patch of the silicon nitride membrane. For the Medium-G bolometer without the gold ring, the measured optical noise equivalent power (NEP) is $1.9 \times 10^{-16} \text{ W}/\sqrt{\text{Hz}}$ and the time constant is in the range between 0.2 and 0.38 ms. For the Medium-G bolometer with gold ring, the measured NEP is $1.7 \times 10^{-16} \text{ W}/\sqrt{\text{Hz}}$ and the time constant is in the range between 1.4 and 2 ms. The gold ring increases the heat capacity, and this is a way to increase the time constant of the bolometer. This will be useful for time domain multiplexed arrays. The performance of Medium-G bolometers is close to the 300 K background limit in the 1.2 mm atmospheric window.

Bonn, 2007
Nikhil Jethava

Key words: VSB, TES, Superconducting bolometer, SQUIDs.

Contents

List of Figures	v
List of Tables	viii
1 Introduction	1
1.1 Receiver Technologies	1
1.1.1 Coherent detectors	2
1.1.2 Incoherent detectors	2
1.2 Scientific background and motivation	3
1.2.1 Star and planet formation	4
1.2.2 Clusters of galaxies and the Sunyaev-Zel'dovich effect	5
1.2.3 Origin and evolution of galaxies	6
1.3 Thesis outline	7
2 Bolometer theory	9
2.1 Basic concept of bolometers	9
2.2 Responsivity of a semiconducting bolometer	9
2.3 Performance parameters of bolometer	11
2.3.1 Photon noise	11
2.4 Superconducting transition edge sensors	14
2.4.1 Strong negative electrothermal feedback	15
2.5 Responsivity of voltage biased superconducting bolometer	16
2.5.1 Noise in Voltage biased Superconducting Bolometers	17
3 Overview of Transition Edge Sensors and SQUIDs	19
3.1 The Silicon nitride membrane	19
3.2 Thermistor layout	20
3.3 The Absorber	23
3.4 Spider geometry	24
3.5 The Superconducting Quantum Interference Device (SQUID)	26
3.5.1 Noise in the SQUID amplifier	27
3.6 Multiplexing of electronics	28
3.6.1 Time division SQUID multiplexing	28
3.6.2 Integrated design	29
3.6.3 Multiplexing scheme and technical trade-offs	31

4	Test arrays and experimental setup	33
4.1	Test array	33
4.2	Electrical circuit diagram	33
4.3	Thermal layout	35
4.3.1	Aluminum horn cavity	38
4.4	Filters	38
4.5	Black coating	39
4.6	SQUID electronics	39
4.7	Experimental setup	41
4.7.1	Temperature readout	43
4.7.2	Martin-Puplett Interferometer	43
5	Modeling of the Bolometer	45
5.1	Introduction	45
5.2	Thermal modeling of the bolometer	46
5.2.1	Finite element analysis	46
5.3	Model of voltage–current characteristics	47
6	Experimental results and modeling	49
6.1	Initial design	50
6.1.1	4SN 1459	50
6.2	4SN 1546	54
6.2.1	Molybdenum wiring scheme	54
6.2.2	Aluminum wiring scheme	54
6.3	4SN 1568–Inverted layout and silicon oxide coating	54
6.4	Basic layout	55
6.5	K0078–5.2 bolometer array – Experiment and Model	56
6.5.1	Model for thermistors of different geometries	58
6.5.2	Estimation of Kapitza resistance	60
6.6	4SN 1601 – Spider geometry	61
6.6.1	4SN 1601 – High-G layout	61
6.6.2	4SN 1601 – Medium-G layout	63
6.6.3	4SN 1601 – Low-G layout	63
6.7	4SN 1610 – Spider geometry	64
6.8	4SN 1610 – High-G – with Ti absorber- Experiment and model	64
6.8.1	$I - V$ and $R - T$ measurements	64
6.8.2	Signal measurements	66
6.8.3	Noise measurements	69
6.8.4	NEP calculations	72
6.8.5	4SN 1610 – High-G – with Au-Pd cross absorbers	72
6.9	4SN 1610 – Low-G layout – Experiment and Model	74
6.9.1	$I - V$ and $R - T$ measurements	75
6.9.2	Time constant measurements	77
6.9.3	Noise measurements	78
6.9.4	NEP calculations	80
6.10	4SN 1762–16-leg Medium-G –without Au ring–Experiment and Model	81
6.10.1	$I - V$ and $R - T$ measurements	81
6.10.2	Modeling of the broken Si_3N_4 membrane	87
6.10.3	Signal measurements	88
6.10.4	Noise measurements	92

6.10.5 NEP calculations	96
6.11 4SN 1762–16-leg Medium-G –with Au ring–Experiment and Model	97
6.11.1 $I - V$ and $R - T$ measurements	98
6.11.2 Signal measurements	100
6.11.3 Noise measurements	106
6.11.4 NEP calculations	108
6.12 Gold ring modeling	108
6.12.1 Incident radiation pattern	108
6.12.2 High-G layout	111
6.12.3 Medium-G layout	111
6.12.4 Different geometries	113
7 Summary and Conclusions	115
A Photographs of experimental setup	121
Bibliography	123
Curriculum Vitae	127
Acknowledgments	129

List of Figures

1.1	An overview of various receiver technologies at different frequency bands	1
1.2	The block diagram of heterodyne receiver assembly.	2
1.3	Scattering of the cosmic microwave background due to the Sunyaev-Zel'dovich effect.	5
1.4	Emission from galaxy $L_{IR} = 10^{12}L_{\odot}$ at different redshifts (Guiderdoni et al. 1998).	7
2.1	The schematic electrical and thermal circuit diagram for a semiconducting bolometer	10
2.2	The schematic diagram for a superconducting TES bolometer.	15
3.1	The schematic diagram of a single pixel bolometer on silicon nitride membrane.	20
3.2	The bilayer structure of Au-Pd/Mo thermistor.	20
3.3	Dependence of critical temperature on the thickness ratio of a bilayer of Mo and Au-Pd	21
3.4	Transition of thermistor film at 100 mK when the Mo/Au-Pd thickness ratio is 0.5 and 0.1.	22
3.5	Distorted transition curve	23
3.6	Schematics of cross absorbers.	24
3.7	The CAD layouts of High-G, Medium-G and Low-G.	25
3.8	Circuit diagram for a dc SQUID.	26
3.9	(a) SQUID $I - V$ curves. (b) Voltage across current-biased SQUID vs applied flux.	26
3.10	Picture of (a) SQUIDS with their magnetic shield and (b) single SQUID current sensor chip.	27
3.11	Current noise of the dc SQUID as a function of frequency.	28
3.12	The time division multiplexing scheme for the SQUIDS.	29
3.13	The layout and produced 288 channels bolometer array	30
4.1	Photograph and schematic diagram of 7-element test array	34
4.2	Photograph of the opened cryostat.	35
4.3	The schematic diagram of cryostat.	36
4.4	ξ plotted as a function of T/T_0	37
4.5	The schematic diagram of radiation pattern inside the aluminum horn cavity.	38
4.6	Photographs of 1.5 K stage filter and 77 K stage filter.	39
4.7	The block diagram for SQUID system.	40
4.8	The functional block diagram of the read-out electronics with SQUID.	41
4.9	Schematic diagram and photograph of the experimental setup	42
4.10	Block diagram of Martin-Puplett interferometer.	44
5.1	$I - V$ and $P - V$ plots of a typical superconducting bolometer.	45
5.2	Steady state distribution from finite element analysis for High-G design	46
6.1	The seven element array from the initial design.	49
6.2	$I - V$ and $R - T$ curve of 4SN 1459 bolometer array with different shunt resistors.	51
6.3	Electrical circuit diagram for seven element bolometer array.	53

6.4	Signal and noise measurements of 4SN 1459 with (a) 33 m Ω , (b) 10 m Ω of shunt resistor.	53
6.5	$R - T$ measurements of 4SN 1546 array with Mo wiring.	54
6.6	$I - V$ and $R - T$ measurements of 4SN 1546 array with Al wiring	55
6.7	CAD diagram of the test array in the basic layout.	56
6.8	$I - V$ and $R - T$ curve of the K0078-5.2 array.	57
6.9	Thermal conductance for High-G layout.	58
6.10	IV model for different geometries of thermistor.	59
6.11	Comparison of G for different thermistors and the estimation of Kapitza resistance.	60
6.12	$I - V$ and $R - T$ curve for 4SN 1601 array in High-G layout.	62
6.13	$I - V$ and $R - T$ measurements of 4SN 1601 in Medium-G layout.	62
6.14	$I - V$ and $R - T$ measurements of 4SN 1601 in Low-G layout.	63
6.15	$I - V$ comparison for 100 μm thermistor in High-G, Medium-G and Low-G layout.	64
6.16	$I - V$ and $R - T$ of 4SN 1610 High-G layout with continuous Ti absorber.	65
6.17	Comparison of $P - V$ and $R - V$ curves for High-G layout with Ti absorber.	65
6.18	Signal and noise measurements of 4SN 1610 in High-G layout with Ti absorber.	66
6.19	Relation between calculated time constant τ as a function of gain L for High-G layout.	67
6.20	Time constant of the bolometer from the 4SN 1610 array with Ti absorber.	67
6.21	Spectral response of the array in High-G layout.	69
6.22	Predicted noise current of the 4SN 1610 array for 100 μm square thermistor with Ti absorber.	70
6.23	Comparison of noise voltage from experiments with that of modeled values for High-G layout with Ti absorber.	70
6.24	NEP plotted as a function of frequency for High-G layout.	71
6.25	$I - V$ and $R - T$ measurements of 4SN 1610 in High-G layout.	72
6.26	τ measurements of the High-G layout with Au-Pd absorbers in 4SN 1610.	73
6.27	Steady state temperature distribution from finite element analysis for Low-G layout.	74
6.28	Calculated conductance for the different Si_3N_4 geometries.	75
6.29	$I - V$ and $R - T$ measurements of 4SN 1610 Low-G spider layout.	76
6.30	Comparison of modeled and experimental $I - V$ for Low-G layout. (b) Relation between τ and loop gain L .	76
6.31	Comparison between measured power, resistance and that of modeled parameters for the Low-G layout.	77
6.32	Relation between τ and loop gain L for the Low-G layout.	77
6.33	(a) Predicted noise current of the Low-G layout. (b) Relation between the measured and calculated noise at different voltage.	79
6.34	Comparison between the measured noise voltage with that of the model for Low-G layout.	79
6.35	NEP plotted as a function of background temperature for Low-G layout.	80
6.36	CAD layout for single pixel Medium-G with 16-legs and 32-legs.	81
6.37	Steady state temperature distribution from FEA for 16-legs Medium-G layout without Au ring.	82
6.38	Experimental results of Medium-G - 16 legs-without Au ring layout 4SN 1762.	83
6.39	$I - V$ and $R - T$ measurements of 4SN 1762.	85
6.40	Comparison of modeled $I - V$ curve with that of experimentally measured $I - V$ for 16-legs Medium-G layout without Au ring.	85
6.41	Comparison between measured and calculated power, resistance for the 16-legs Medium-G layout without Au ring.	86
6.42	(a) Steady state temperature distribution from FEA for 16-legs Medium-G layout without Au ring with broken Si_3N_4 leg. (b) G estimated due to the broken Si_3N_4 leg.	86
6.43	Comparison of different $I - V$ curves for CH1 and CH3.	87
6.44	Signal and noise as a function of modulating frequencies for the 16-legs Medium-G layout without Au ring.	89

6.45	SNR measurements for 16-legs Medium-G layout without gold ring.	90
6.46	τ and signal to noise (SNR) data for 4SN 1762.	90
6.47	NEP plotted as a function of frequency for 16-legs Medium-G layout without Au ring. . .	91
6.48	Spectral relative response of the 16-legs Medium-G layout without Au ring.	92
6.49	Noise measurements for five channels CH2, CH4, CH5, CH6 and CH7 at different voltages.	93
6.50	(a) Relation between the noise measured and calculated at different voltage for 16-legs Medium-G layout without Au ring. (b) Predicted noise current of the 4SN 1762 array. . .	94
6.51	Comparison between noise voltage from experiments and model for 16-legs Medium-G layout without Au ring.	95
6.52	$1/f$ noise characterization for 16-legs Medium-G layout without Au ring.	95
6.53	CAD layout of a single pixel of Medium-G with Au ring with 16-legs and 32-legs design .	96
6.54	Steady state temperature distribution from FEA for 16-legs Medium-G layout with Au ring.	97
6.55	Experimental results of Medium-G - 16 legs.	98
6.56	$I - V$ and $R - T$ measurements of 4SN 1762 at 300 K background.	99
6.57	$I - V$ and $R - T$ measurements of 4SN 1762 at 77 K background.	99
6.58	Comparison of $I - V$ for 16-legs Medium-G layout with Au ring.	100
6.59	Comparison between measured and calculated bolometer parameters, power, resistance for the 16-legs Medium-G layout with Au ring.	101
6.60	Comparison of signal and noise for Medium-G layout with Au ring.	102
6.61	SNR measurements for all the channels at different bias voltages.	103
6.62	τ and Lof 4SN 1762, 16-legs spider Medium-G layout with Au ring.	103
6.63	Noise measurements for six channels at different bias voltages.	104
6.64	Noise measurements for all the channels at different bolometer voltages.	105
6.65	(a) Relation between the measured and calculated noise at different voltages for 16-legs Medium-G layout with Au ring. (b) Predicted noise current of the 4SN 1762 array.	107
6.66	Comparison between measured and calculated noise voltages for 16-legs Medium-G layout with Au ring.	107
6.67	$1/f$ noise characterization for 16-legs Medium-G layout with Au ring.	108
6.68	NEP vs frequency for 16-legs Medium-G layout with Au ring.	109
6.69	Input heat distribution on the center of the silicon nitride membrane.	109
6.70	Thermistor temperature plotted at the input heat radiation location for High-G layout. .	110
6.71	Change in temperature detected by the thermistor as a function of distance for High-G. .	110
6.72	Thermistor temperature plotted at the input heat radiation location for Medium-G. . . .	112
6.73	Change in temperature detected by the thermistor as a function of distance for Medium-G.	112
A.1	Photograph of the feed horn antenna.	121
A.2	Photograph of the seven element array mounted inside the Au coated Cu ring.	121
A.3	Photograph of the Gunn diode.	122
A.4	Photograph of the experimental setup for Martin-Puplett interferometer.	122

List of Tables

4.1	Black coating composition for cavities	39
4.2	Parameters for current sensor SQUID at 4.2 K	40
6.1	Time constant (τ) measurements at different bias voltages for 4SN 1459 array with 33 m Ω and 10 m Ω shunt resistor	50
6.2	Thermal heat capacity budget for High-G layout with Ti film absorber at 450 mK.	68
6.3	Thermal heat capacity budget for High-G layout with Au-Pd cross absorbers at 450 mK.	73
6.4	Thermal heat capacity budget for Low-G layout at 450 mK.	78
6.5	Transition temperature and Transition width (in bracket) for all the channels of 4SN 1762	82
6.6	Thermal heat capacity budget for 16-leg Medium-G layout without Au ring at 450 mK.	88
6.7	Transition temperature and transition width (in bracket) for all working channels of 4SN 1762.	99
6.8	Thermal heat capacity budget for the 16-leg Medium-G layout with Au ring at 450 mK.	106
6.9	<i>Quality factor</i> calculations and the thermal properties of the High-G layout.	111
6.10	<i>Quality factor</i> calculations and the thermal properties of the Medium-G layout	112
6.11	<i>Quality factor</i> calculations for different geometries layouts.	113
7.1	NEFD comparison for different bolometer arrays.	119

Chapter 1

Introduction

The aim of this dissertation is to develop very sensitive detectors for astronomical applications at wavelengths between few hundred μm and few mm.

1.1 Receiver Technologies

Receivers are instruments that convert incoming electromagnetic radiation to an electrical signal. Receivers in radio and (sub)millimeter astronomy are divided into mainly two categories depending on the detection principle, namely coherent heterodyne mixers and incoherent broad band continuum detectors of which bolometers are important examples. In addition, for each category, various detector technologies exist and the choice for the one or the other depends on the frequency range of interest. Fig. 1.1 shows

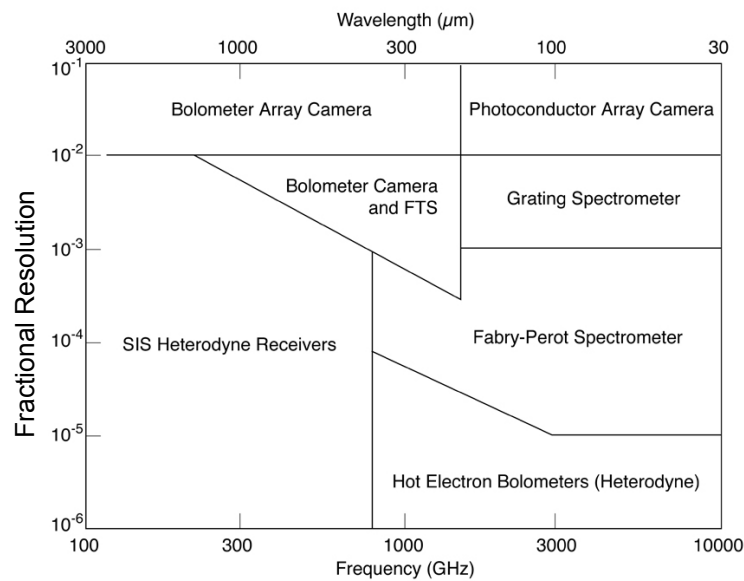


Figure 1.1: An overview of various receiver technologies at different frequency bands.

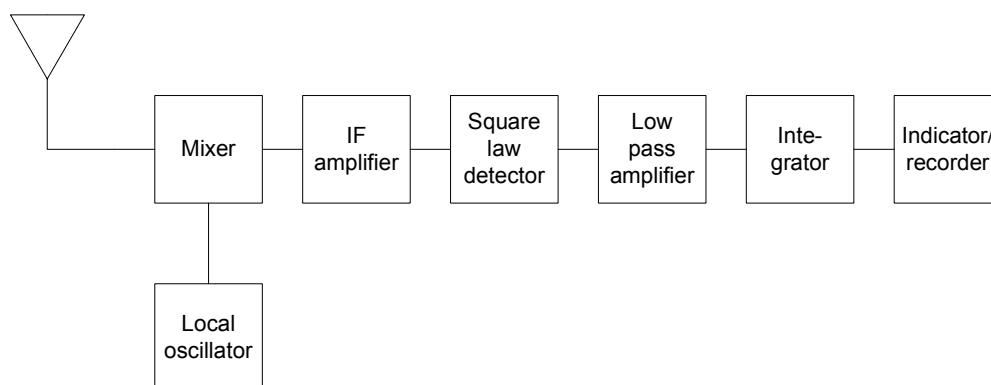


Figure 1.2: The block diagram of heterodyne receiver assembly.

the various receiver technologies used in different frequency bands.

1.1.1 Coherent detectors

Coherent detectors respond to the electric field strength of the incoming radiation and can preserve information about the phase of the signal. Most coherent (sub)millimeter receivers utilize the so-called heterodyne principle. Fig. 1.2 shows the block diagram of typical heterodyne receiver used in radio astronomy. The signal power with center frequency ν_{RF} is coupled to the receiver by an antenna. At (sub)millimeter wavelengths, the antenna signal is coupled directly to the mixer assembly. There, it is superposed (“mixed”) with a signal of a chosen frequency (e.g. that of a spectral line of interest). One of the mixing products, namely the difference frequency (named intermediated frequency, IF), lies in the radio range. This IF signal can be further processed with the well-known, low-noise amplifiers (LNAs) available at the radio frequencies, fed and integrated into a spectrometer. In a heterodyne receiver the largest gain is obtained in the IF amplifier, which also usually determines the pre-detector bandwidth of the receiver. However, the sensitivity of the overall system depends on the gain of the first (mixer) stage, which has to be as sensitive as possible. The most common submillimeter mixers use superconductor-insulator-superconductor (SIS) devices.

Coherent heterodyne receivers are very useful for high resolution spectroscopy in radio and (sub)millimeter astronomy. Since in the heterodyne process the phase of the signal is preserved, it allows their use in the interferometers in which signals from various antennas are combined to “synthesize” high angular resolution.

A drawback of SIS receivers is the relatively small bandwidth (a few GHz). Since a system’s sensitivity changes are proportional to the square root of the bandwidth, this is a drawback for the detection of continuum emission, i.e., emission whose intensity changes slowly with the frequency (in contrast to a “sharp” spectral line).

1.1.2 Incoherent detectors

Incoherent detectors absorb the incoming radiation but they can not preserve the phase information of incoming signal. Development of the incoherent thermal detector called *bolometer*, was started a century ago (Langley 1900). In short, a bolometer system consists of an absorber connected to a heat sink (i.e., area of constant temperature) through an insulating link. The radiation absorbed by the absorber raises its temperature above that of the heat sink. A sensitive thermistor, which is a resistor with a strong

temperature coefficient, senses the temperature change, which is then calibrated to the intensity of the absorbed radiation. Development efforts led to the production of the carbon resistance bolometer (Boyle & Rogers 1959) and, finally, the germanium resistance thermometer (Low 1964). Born & Wolf (1975) explain the absorption of radiation in metal films and Clarke (1971, 1974) applied such films as the radiation absorbers in the bolometers. The semiconducting bolometer operating at ^3He temperature was introduced by Drew & Sievers (1969). Downey et al. (1984) introduced the ion implantation of doped silicon for the thermometers. The principal advantage of the bolometric systems is the high achievable sensitivity because of a large bandwidth. The old generation semiconducting bolometers are now replaced by a new generation of transition edge superconducting voltage biased bolometers that have significant advantages of sensitivity, performance and fabrication technology.

The observations of cosmic microwave background (CMB) radiation, the Sunyaev-Zel'dovich effect, mapping of high z objects as well as of star forming regions require,

- very sensitive bolometer systems
- high mapping speed

Since the 1980s, the latter requirement has led to the development of arrays of bolometers, i.e, nowadays several hundreds of bolometers integrated on one silicon wafer. The new generation of voltage biased superconducting transition edge sensors, the topic of this dissertation, have higher sensitivity and faster response time than the old generation semiconducting bolometers. The response time is defined by the time constant of the bolometer. It is possible to reach the fundamental noise limit and the time constant is of the order of a few milliseconds. The fabrication of superconducting bolometer can be performed completely with micro-lithography processes, hence it is possible to produce large number pixel arrays ($\sim 10^2 - 10^4$).

1.2 Scientific background and motivation

Scientific research in cosmology and astronomy are the main drivers for the development of bolometers at millimeter and submillimeter wavelengths. In this section, the main scientific applications of the bolometers are summarized.

The cosmic microwave background radiation (CMBR) radiation is the remnant from the hot Big Bang. Through its expansion the Universe has cooled to 2.728 K. To a very high degree of accuracy, the CMB radiation is represented by a Planck function with a maximum near 2 mm and covers the sky isotropically. Nevertheless, over the last decade tiny anisotropies (of order 1 part in 100000) have been found and their distribution over angular scales has been determined. These anisotropy measurements have shown that the geometry of the universe is Euclidean and have provided accurate measurements of cosmological parameters.

The spectral energy distribution (i.e. emitted power versus wavelength) of galaxies peaks at optical or near-infrared wavelengths and in the far-infrared range, around 60 – 80 μm . While the shorter wavelength maximum is due to star light the longer wavelength one is due to warm dust heated by the ultraviolet radiation from the massive stars. It falls very steeply with increasing wavelength in the (sub)millimeter portion of the spectrum (see §1.2.3). The millimeter and submillimeter wavelength bands are well suited to study comets and other objects in our solar system, the birth of stars, galaxies and the CMBR and there is an enormous potential for scientific discovery.

Very sensitive bolometer arrays are ideally suited to meet many of the requirements for such discoveries. Using the TES technology it is possible to build focal plane arrays with hundreds of pixels. Additionally, TES arrays will have greater sensitivities than semiconductor bolometers. This combination will make TES bolometer arrays instruments of choice for (sub)millimeter astronomy.

1.2.1 Star and planet formation

Star formation in our and external galaxies occurs in optically invisible regions of molecular clouds that consist of gas and dust. Stars form when dense cloud condensations reach a point where the gravitational forces overcome the thermal pressure, turbulent motion, and the magnetic field that support the cloud. During protostellar collapse, most protostars appear to form a disk since, because of angular momentum conservation, the collapse can only occur along the rotation axis of an initially slowly rotating cloud. Dust emission from molecular clouds is intrinsically weak at (sub)millimeter wavelengths. Because of this, the measured flux density is proportional to the dust column density and, thus, to the total (molecular) column density, meaning the number of hydrogen molecules (the by far most abundant species) per square centimeter. It is also proportional to the temperature and $\lambda^{-2-\beta}$, where λ is the wavelength and the emissivity index, β , has a value between 1 and 2 (Mezger et al. 1982). Pre-stellar cores (“protostars”) in molecular clouds are the sites of ongoing star formation. Therefore, they are the prime laboratories to study pre-conditions of star formation and the earliest stages of the stellar life cycle. Wide-area surveys of these regions with bolometer arrays at (sub)millimeter wavelengths have proved very efficient in finding protostellar condensations and still deeply embedded very young stars. Since the emission is proportional to the total column density, masses of these objects can be directly determined from the observed fluxes. (Motte et al. 1998; Johnstone & Bally 1999).

Many young Pre-Main-Sequence (PMS) stars (T Tauri, FU Ori and Herbig Ae/Be stars) have been detected in thermal dust emission in the submm regime (Weintraub et al. 1989; Beckwith et al. 1990; Mannings 1994). Such stars are still embedded in remnants of the dust clouds in which they formed. In order to find the true properties of the circumstellar dust emission, one needs to separate the disk emission with the emission from the surrounding clouds so it is essential to map the dust emission. This can be done by mapping the region surrounding the stars (Aspin et al. 1994; Sandell & Weintraub 1994; Henning et al. 1998). High resolution mapping with the Submillimeter Common User Bolometers Array (SCUBA) on the James Clerk Maxwell Telescope (JCMT) shows that the many PMS stars have extended dust envelopes or disks (Weintraub et al. 1999). Such studies show that the dust emission from these condensed regions has a surprisingly flat spectral energy distribution suggesting that their dust emission has a lower emissivity index than the general interstellar dust emission (Simon & Guilloteau 1992; Koerner et al. 1993; Hogerheijde et al. 2002). These flat spectral energy distributions could be due to very large dust grains, indicating perhaps the start of planetary system formation. By studying stars of different ages it is possible to find out whether there exists a clear transition period when the dust grains assemble into building blocks of planets (planetesimals) and when the disk is cleared by the newly formed planets.

Observations in the mm/submm regime very sensitive to left-over material from planetary system formation (so-called debris disks). First detected around Vega, such disks, which also have been found around Fomalhaut, β Pictoris and ϵ Eri, are very striking in the submm regime (Holland et al. 1998). Fomalhaut shows a nearly edge-on disk around the central star, really suggesting a planetary system. β Pictoris and Vega show ring-like structures far from the central stars which might be density enhancements in their disks (Greaves et al. 1998). Another typical Vega-like star, ϵ Eri, shows a ring-like structure seen nearly pole-on with a clump in the ring (Greaves et al. 1998). This may be indicative of a region perturbed by the action of a planet.

The discovery of Trans-Neptunian Objects (TNO) has revolutionized the study of the outer solar system in the past decade (Jewitt & Luu 1992). These objects orbit the Sun with orbital semi-major axes of 30 to 50 AU, typically have temperatures of ~ 75 K and are thought to be fossil remnants of the Sun’s accretion disk. More than 800 of such objects have been found (Trujillo et al. 2001; Schulz 2002). TNOs were discovered by optical observations, but observations in the mm/submm regime are essential to understand them physically, e.g., their optical magnitudes constrain the product of the TNO size and albedo; by measuring the thermal emission in the mm regime this degeneracy is broken. Jewitt et al. (2001) used SCUBA (850 μm) and optical observations to measure the albedo and the radius of Kuiper

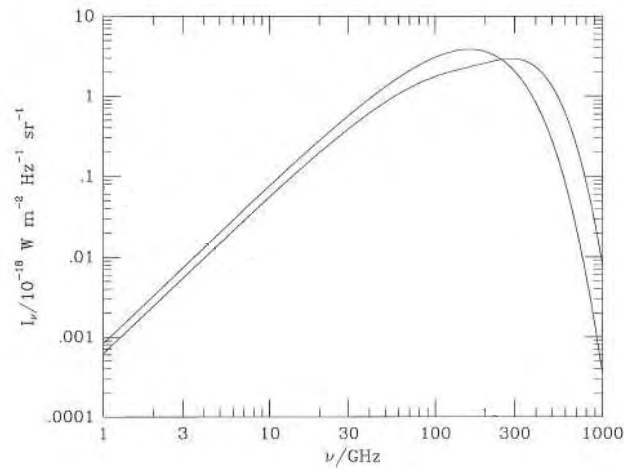


Figure 1.3: The spectrum of cosmic microwave background radiation and the microwave background radiation after passage through a scattering atmosphere due to Sunyaev-Zel'dovich effect. The SZ effect causes a fractional decrease in the low-frequency intensity of the CMBR that is proportional to y .

Belt Objects; they found an $850 \mu\text{m}$ flux density of $\sim 2\text{--}3 \text{ mJy}$ (with RMS of 1 Jy in 5 hours).

1.2.2 Clusters of galaxies and the Sunyaev-Zel'dovich effect

The Sunyaev-Zel'dovich (SZE) effect (Sunyaev & Zel'dovich 1970), arises from the scattering of CMBR photons by electrons gas in the hot plasma filling clusters of galaxies. Photons passing the cluster and collide with electrons gain a tiny amount of energy due to the inverse Compton effect. This causes a distortion in the black body spectrum of the CMBR, namely a depression on the long-wavelength side of it its peak near 2 mm and an enhancement on the short-wavelength side. When imaging a cluster at wavelength longer than 2 mm one will find a depression (negative flux) at the position of the cluster and a positive signal at the short-wavelength side. The intensity of the SZE is independent of the distance to the cluster. Since x-ray emission *is* dependent on the distance, comparison of the SZE mm-signal and the x-ray emission can yield a direct distance measurement. This can be compared with the distance obtained from the Hubble relation, $D = cz/H_0$, where c is the speed of light and z is the cluster's redshift, which can be obtained from optical observations. From this it is clear that SZE observations can be used to determine the Hubble parameter H_0 , the expansion rate of the Universe. The SZ effect provides thus an important cosmological probe.

Other applications in cosmology include measurements of the properties of gas in clusters of galaxies, motions of clusters of galaxies and to study the evolution of the Universe.

Measurements of the Sunyaev-Zel'dovich effect have long been tried (Birkinshaw 1999) and finally successfully accomplished by radio wavelength interferometry (Carlstrom et al. 1996; Reese et al. 2002). High angular resolution data from Chandra have greatly improved our understandings of these objects. They have revealed embedded colder blobs of gas which may be remnants of the past merger activity (Kempner et al. 2002). SZE observations are currently limited to a much lower resolution view of the Intra-Cluster Medium (ICM). When the instrument with sufficient sensitivity will become available, the SZE will provide a valuable independent, detailed vies of these and other processes. For example, it is clear that the dark matter profile in the galaxies is not well understood in detail since the giant radial arcs are too abundant by a factor of 10 under currently accepted cosmological properties (Bartelmann et al. 1998). A high resolution view of the baryons in the clusters of both relaxed and violent, orthogonal to the

view provided by the X-rays, will help to clarify this situation. The high resolution, high sensitivity maps of the SZE in more distant clusters, in combination with X-ray, will allow to estimate the 3D structure and orientation of galaxy clusters (Zaroubi et al. 2001).

The SZE can be used to understand the formation and evolution of structure at high redshift galaxies, because the SZE surface brightness does not dim as the physical system moves further away. Measurements of abundance of clusters of galaxies as a function of redshift also give the strong constraints on the underlying cosmology (Mason et al. 2003; Kuo et al. 2004). The degree of substructure in clusters as a function of mass and redshift is a powerful constraint on cosmology and structure formation scenarios (Evrard et al. 2002; Bond et al. 2005).

1.2.3 Origin and evolution of galaxies

While the Spectral Energy Distribution (SEDs, i.e. emitted power vs. wavelength) of a normal spiral galaxy like the Milky Way has comparable maxima at optical/near-infrared and far infrared (FIR) wavelengths, there are also very luminous, massive galaxies, whose SEDs are dominated by FIR emission. These objects have been named ultraluminous IR-galaxies (ULIRGs). The FIR emission arises from dust that absorbs the copious ultraviolet emission from hot ($T \sim 30000$ K) stars, gets heated and re-emits maximally at FIR wavelengths (between 50 and 100 μm). It is, thus, a direct measure of the rate of star formation. ULIRGs are undergoing massive bursts of star formation with star formation rates of hundreds to \sim a thousand solar masses per year. (The star formation rate in our Milky Way galaxy is a few solar masses per year). Apart from active galactic nuclei (AGN), ULIRGs, with $L_{IR} > 10^{12}L_{\odot}$, are amongst the most luminous objects in the Universe.

In particular in the Early Universe this extreme starburst activity seems to be coeval with AGN activity, at least in the extreme objects that can currently be observed.

Because of the expansion of the Universe, in distant objects this FIR peak in the SED becomes shifted to longer wavelengths (i.e., “redshifted”). For high enough redshifts, this peak wanders into the submillimeter range. This is illustrated by Fig. 1.4, which shows the SED of a typical $L_{IR} = 10^{12}L_{\odot}$ ULIRG calculated for increasing redshifts (top to bottom) for a cosmology with $h=0.5$ and $\Omega_{\text{o}}=1$ (Guiderdoni et al. 1998). It is apparent that the flux in the submm range is nearly insensitive to redshift for $z > 0.5$, because the shift of the 80–100 μm bump counterbalances the dimming with distance. This strong so-called “negative K-correction” effect applies at wavelengths longer than about 250 μm . At these wavelengths the flux density from galaxies at $z > 1$ ceases to decline with the inverse square of distance, but instead remains approximately constant with increasing redshift. A window is thus opened to the detection of all galaxies with similar SEDs at redshifts up to $z \sim 10$ -20. The effect is more pronounced at longer wavelengths: in the millimeter waveband more distant galaxies are expected to produce greater flux densities than their more proximate counterparts.

Observations in the 850 μm and 450 μm bands with SCUBA and in the 1.2 mm band with the Max-Planck Bolometer Array (MAMBO) on the IRAM 30m telescope have resulted in the discovery of numerous high redshift ($z > 2$) *Submillimeter Galaxies* as well as dust emission around high redshift quasars. The star formation rates derived from the observed dust emission are very high (hundreds to thousands of solar masses per year) (Carilli & Yun 1999; Hughes et al. 2002). Many of these submm-selected systems do not have optical counterparts as the dust which emits at submillimeter wavelength absorbs very effectively in the rest frame ultraviolet range.

Many of these highly interesting high-redshift system are found by unbiased mapping of sky regions as large as possible down to extremely low flux density limits. Here is a decisive advantage of array receivers; in fact the whole field opened with the discovery of submillimeter sources in the famous Hubble Deep Field with the 37 element SCUBA array at 850 μm (Hughes et al. 1998).

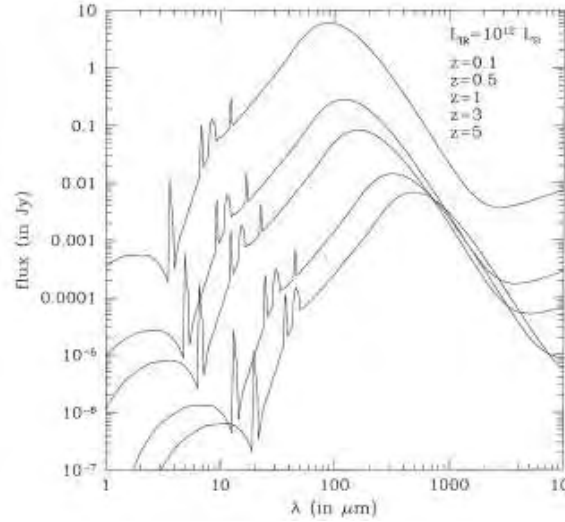


Figure 1.4: Emission from a galaxy with an IR luminosity of $= 10^{12} L_{\odot}$ at different redshifts for a cosmology with $h=0.5$ and $\Omega_{\circ}=1$ (Guiderdoni et al. 1998).

1.3 Thesis outline

This dissertation deals with bolometric direct detectors, which are currently the most sensitive broadband detectors for wavelengths from $200 \mu\text{m}$ to 3 mm . The present generation of bolometer arrays consists of several hundred pixels. The current need of the astronomical community require larger arrays with 10^3-10^4 elements and performance near the fundamental noise limit. The results and model reported in this dissertation are a contribution toward this goal.

At the Max Planck Institute for Radio Astronomy (MPIfR), Bonn, Germany, the development of superconducting bolometer was started in collaboration with the Institute for Photonic Technology (IPHT), Jena, Germany. The fabrication of bolometer and SQUID is performed at IPHT. The testing, experiments and modeling of the bolometer is performed at MPIfR.

Chapter 2 - Bolometer theory

In this chapter, a detailed comparison between the theory of semiconducting and superconducting bolometer, is performed. The responsivity comparison shows the advantages of the new generation TES bolometers over the old semiconducting bolometers. The noise theory for conventional bolometer and superconducting bolometer is explained with inclusion of the photon noise. Signals from superconducting bolometers are detected by Superconducting Quantum Interference Devices (SQUIDs). A brief introduction of SQUID amplifiers and their operating principle is presented.

Chapter 3 - Overview of Transition Edge Sensors and SQUIDs

This chapter introduces the superconducting transition edge sensors and SQUIDs. The incoming radiation is coupled to an absorber and the temperature rise is detected by the superconducting thermistor. The thermistor is deposited on the silicon nitride (Si_3N_4) membrane. The fabrication of thermistor, absorber and the method of structuring the low stress silicon nitride membrane are explained. The output of several TESs can be time division multiplexed (TDM). The TDM scheme and its technical trade-offs are explained.

Chapter 4 - Test array and experimental setup

The layout of the 7-element array that has been fabricated and tested, is presented. The 7-element array is maintained at a base temperature of 300 mK using a ^3He sorption cooler. The filters which define the passband transmission of the bolometers are explained. The detailed explanation of the testing setup is also presented. The temperature measurements are done with a Lakeshore Germanium Resistance Temperature Detector (RTD) using a four wire conductance bridge. The schematics of readout system is explained. The filters and absorbing structure define the spectral response of the system which can be characterized using a Martin-Puplett interferometer. The experimental setup for the measurements of the Martin-Puplett interferometer is shown.

Chapter 5 - Modeling of the bolometer

It is possible to derive the behavior of an ideal bolometer from theory, assuming that the value of the thermal conductance (G) and the resistance-temperature relation are known. In order to understand the bolometer behavior, a model has been developed to compare the experimental results with theory. The values of thermal conductance for all the geometries are obtained from finite element analysis. The thermal model of the bolometer and the procedure for finite element analysis is explained. The derivation of voltage-current ($I - V$) characteristics from the value of the thermal conductance and measured temperature-resistance ($R - T$) dependence is shown.

Chapter 6 - Experimental results and modeling

This chapter presents the experimental results which are important for the conclusions. The initial 7-element array was fabricated into different configurations and the important results are presented. To understand the effects of Au-Pd/Mo thermistor and the low stress silicon nitride membrane, the initial layout was changed to a new layout. In this layout, the seven elements are fabricated with the seven thermistors of different geometrical and physical properties. The comparison between experimental results of different thermistors show that the performance of the $100\ \mu\text{m}$ square thermistor is better than that of the other thermistors, hence the $100\ \mu\text{m}$ square geometry was chosen as standard for next bolometer arrays. In order to increase sensitivity of the bolometer, the silicon nitride membrane is structured in 8-legs, 16-legs or 32-legs. The geometry is divided into three categories, High-G, Medium-G and Low-G, depending on their thermal conductance values. The thermal conductance values decrease from High-G to Low-G layout. The experimental results and the model for High-G, Medium-G and Low-G layouts are discussed in detail. The measurements of time constant (τ) of the bolometer and the calculations of Noise Equivalent Power (NEP) are also presented. The Medium-G layout was found to be suitable to work at 300 K background radiation. The deposition of gold ring on the center absorbing patch of the silicon nitride membrane increases the sensitivity and reduces the time constant of the bolometer. The experimental results and the bolometer model of Medium-G layout with and without addition of a gold ring are shown. The heat capacity (C) budget calculations are performed for all the geometries.

Chapter 2

Bolometer theory

2.1 Basic concept of bolometers

The bolometer is a thermal detector, employing the temperature dependence of the electrical resistance to measure a change in temperature caused by absorbed radiation. The resistivity of different materials has been widely studied and a suitable material can be selected to optimize the bolometer design for various applications. The radiation absorber has high absorptivity over the interested frequency range and has small heat capacity. The supporting substrate (e.g. a Si wafer) has a low heat capacity and large thermal conductivity so that it remains isothermal during the bolometer operation. The thermometer has low heat capacity and low electrical noise and its electrical resistance is a sensitive function of temperature. It is thermally attached to the absorber. A weak thermal link which has both low heat capacity and thermal conductance, appropriate for the application of interest, connects the bolometer to the heat sink. The heat sink is maintained at a stable bath temperature. The mechanical support for the bolometer also has low heat capacity and low thermal conductance.

Bolometers are used for a wide variety of applications at infrared and millimeter wavelengths for laboratory and astronomical measurements. Various applications have different requirements for sensitivity, speed etc. The bolometers are operated at and below ^4He temperatures to increase the sensitivity. The ^3He cooled bolometers (Drew & Sievers 1969) that work at a temperature of 300 mK are widely used in astronomy.

Bolometers belong to the category of square law detectors, giving an output voltage (for the semiconducting bolometers) or output current (for superconducting bolometers), that is proportional to the square of the signal (field) amplitude, equivalent to the signal power. They can have wide bandwidths and large throughputs. The bolometer biasing scheme determines the output of the bolometer. Usually, semiconducting bolometers are current biased, hence the output is a varying voltage. Superconducting bolometers, on the other hand, are voltage biased, hence the output is a varying current.

2.2 Responsivity of a semiconducting bolometer

The incident radiation contains the steady part of power, P , and a time varying part of the amplitude of the power, δP , and the frequency, ω , which is absorbed by the bolometer. Thus, the incident power of $P + \delta P e^{i\omega t}$ [W] causes variations in the bolometer temperature, $T_B = T_o + \delta T e^{i\omega t}$ [K]. The bias current, I , produces time varying heat that can be written as $I^2 R(T) = I^2 [R(T_o) + (dR/dT)\delta T e^{i\omega t}]$ [W]. The bolometer loses power $\overline{G}(T_B - T)$ to the heat sink through the thermal conductance, \overline{G} . The thermal

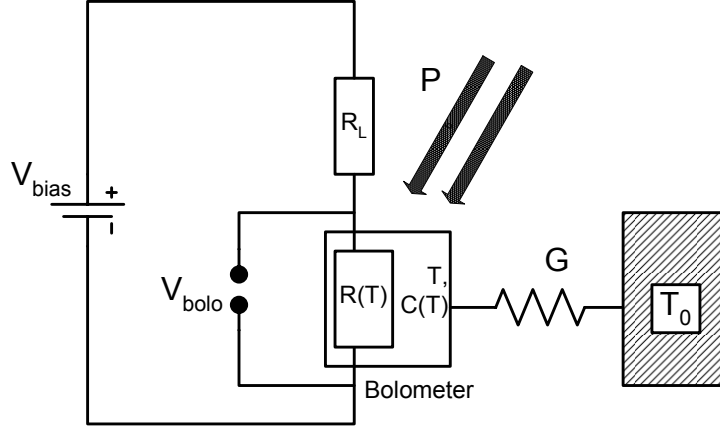


Figure 2.1: A schematic electrical and thermal circuit diagram for a semiconducting bolometer. The bolometer with heat capacity C and resistance R is connected to a thermal bath maintained at constant temperature T_0 through a weak link of thermal conductance G . The incident power absorbed, P , changes the temperature and thus the resistance of the bolometer. The change of the bolometer resistance is detected by measuring the change in the applied bias voltage across the bolometer. In current bias condition, $R_L \gg R(T)$.

conductivity, $\kappa(T)$, depends on temperature, T , and the average thermal conductance as, (Richards 1994),

$$\bar{G} = \frac{A/l}{(T - T_0)} \int_{T_0}^T \kappa(T) dT \quad [\text{W/K}], \quad (2.1)$$

where, l is the path length of the heat flow, T is the heat sink temperature, A is the cross sectional area. Thus, the power flow model is (Richards 1994)

$$P + \delta P e^{i\omega t} + I^2 R + I^2 (dR/dT) \delta T e^{i\omega t} = \bar{G}(T_0 - T) + G \delta T e^{i\omega t} + i\omega C T_1 e^{i\omega t}, \quad (2.2)$$

where G is dynamic thermal conductance at dP/dT at the temperature T_0 and R is the bolometer resistance. Equating the time independent terms gives the steady state heat flow equation that determines the average operating temperature T_0 of the bolometer.

$$P + I^2 R(T_0) = \bar{G}(T_0 - T). \quad (2.3)$$

Equating the time varying terms

$$\delta P / \delta T = G + i\omega C - I^2 (dR/dT). \quad (2.4)$$

The voltage responsivity of a bolometer is (Richards 1994)

$$S_V = \frac{I(dR/dT)}{[G - I^2(dR/dT) + i\omega C]} \quad [\text{V/W}]. \quad (2.5)$$

The effective thermal conductance, G_{Eff} is defined as

$$G_{Eff} = G - I^2(dR/dT). \quad (2.6)$$

The responsivity of a bolometer is influenced by the thermal feedback. To characterize the steepness of transition curve, it is useful to introduce the parameter, α , defined as

$$\alpha = R^{-1}(dR/dT)[K^{-1}]. \quad (2.7)$$

For semiconducting bolometers α is negative ($G_{Eff} > G$) while for superconducting bolometer α is positive ($G_{Eff} < G$). The effective time constant is defined as

$$\tau_{Eff} = C/G_{Eff}. \quad (2.8)$$

Using these definitions, the absorbed power is (Richards 1994),

$$S_V = \frac{IR\alpha}{G_{Eff}(1 + i\omega\tau_{Eff})} [\text{V/W}]. \quad (2.9)$$

The bias current is applied using a voltage source and a load resistor with $R_L \gg R$. In practice, the response of the bolometer can be measured using the changes in electrical power dissipated in the thermometer. The thermal conductance, G , generally increases with temperature so that α decreases, and the responsivity of the bolometer decreases rapidly as it is heated.

2.3 Performance parameters of bolometer

The most important parameters concerning bolometer performance are Noise Equivalent Power (NEP) and time constant (τ). The NEP is a measure of the sensitivity of a bolometer, and is defined as the absorbed power that produces a signal-to-noise ratio of unity at the output. In the presence of a constant background, the NEP can be written as

$$\text{NEP}^2 = \text{NEP}_{detector}^2 + \text{NEP}_{background}^2. \quad (2.10)$$

The noise is measured as a post-detection average, using a filter with a 1 Hz equivalent noise bandwidth so that the unit of NEP is $\text{W}/\sqrt{\text{Hz}}$. The total power detected by the bolometer is the sum of the power supplied by the bias voltage and the background power. Hence, the contribution from the background is considered in the calculations of the total NEP.

For an ideal bolometer the detector noise arises from contributions of photon noise, Johnson noise and phonon noise. Johnson noise is due to the random motion of electrons in the thermometer and is given by (Mather 1982),

$$\text{NEP}_{Johnson}^2 = 4k_B T R / S^2, \quad (2.11)$$

where k_B is the Boltzmann constant and S is the responsivity of the bolometer, i.e. the output voltage per unit power dissipated (V/W).

Phonon noise is due to the quantization of the heat transport (phonons) between the absorber and the heat sink along the thermal conductance G (Mather 1982).

$$\text{NEP}_{Phonon}^2 = 4k_B T^2 G. \quad (2.12)$$

2.3.1 Photon noise

A photon background contribution to the overall NEP arises from the thermal radiation environment. Photon noise arises from the random fluctuations in the rate of absorption from the source quanta.

1. Absorbed power:

Following van Vliet (1967) (Eq. 68), the spectral density in the absorbed power is:

$$SD(P) = 2 \int P_\nu h\nu d\nu + 2 \int P_\nu h\nu \eta(\nu) d\nu, \quad (2.13)$$

where P is the absorbed power, P_ν is the absorbed power per unit optical bandwidth and η is the effective photon mode occupation number. η is given by $\eta = \alpha\epsilon\tau$. α is the bolometer absorptivity, ϵ is the emissivity of the source, τ is the transmissivity of the cold filters and $x = h\nu/k_B T_s$, where T_s is the source temperature. In the case of an optical system, the spectral density is the mean square noise power per unit post-detection bandwidth B referred to the absorber power, $SD(P) = P_N^2/B$, where P_N is the noise power. $\eta_\nu = \alpha\epsilon\tau/(e^x - 1)$.

The power transmitted through a system from a blackbody source with a Planck spectral brightness $P_\nu(\nu, T)$ is (van Vliet 1967),

$$P = \int_0^\infty P_\nu d\nu = \int_0^\infty A\Omega\tau(\nu)B(\nu, T) d\nu \quad [W], \quad (2.14)$$

where, P is the transmitted power, A is the area of radiation source, Ω is a solid angle, $\tau(\nu)$ is the filter transmission, ν is the optical frequency. $A\Omega$ is the throughput of the optical system. For a blackbody source the power per mode is (Richards 1994),

$$P_\nu d\nu = \frac{h\nu d\nu}{e^{(h\nu/k_B T)} - 1}. \quad (2.15)$$

As shown in Kittel & Kroemer (1980), the power $P(\nu, T)d\nu$ in a multi mode source is the number of modes times the power per mode. Thus, the Planck function as the spectral brightness of a blackbody is (Richards 1994),

$$P_\nu d\nu = \frac{2h\nu^3 d\nu}{c^2(e^{h\nu/k_B T} - 1)} \quad [W/m^2 sr]. \quad (2.16)$$

For a system with optical properties of η and a throughput of $A\Omega$, the total absorber power is

$$P_\nu = 2\alpha\epsilon\tau A\Omega \frac{h\nu^3}{c^2} \frac{1}{e^x - 1} = 2\eta_\nu \frac{h\nu^3}{c^2} \frac{1}{e^x - 1} \quad [W]. \quad (2.17)$$

From Poisson statistics, the mean square fluctuations in the number of photons arriving in one second is equal to (Richards 1994),

$$\langle(\Delta n)^2\rangle = P_\nu/h\nu. \quad (2.18)$$

Multiplying by $h^2\nu^2$ to obtain fluctuations in power and by $2B$ to convert a 1 second average to a bandwidth of B Hz gives the first term in Eq. 2.13.

The first term in Eq. 2.13 is the shot noise produced by a Poisson process where the detected photons are not correlated. This term dominates at short wavelengths (optical and near-infrared). The second term in Eq. 2.13 dominates at radio wavelengths and is proportional to the square of P_ν . This means that it is not possible to consider the different sources contributing to P_ν as statistically independent and add the power of the noise sources quadratically. As discussed by Lamarre (1986), the underlying physical phenomenon is that within a given radiation mode, photons come by groups and produce noise that is larger than for a Poisson process (excess noise). If several photons occupy the same mode and have the same volume coherence, they will produce interference phenomena. In this approach the first term in Eq. 2.13 is quantum noise and the second term is due to interference of waves taking into account diffraction phenomena.

Poisson statistics has a discrete probability distribution function. If the fluctuations from enough modes combined are considered, the resulting distribution will be Gaussian. Thus, as shown by Lamarre (1986), the second term in the Eq. 2.13 should have a factor, q , in the denominator. This term is the number of modes of one polarization detected in the frequency band $\Delta\nu$ during the time t , and is given by

$$q = 2A\Omega\Delta\nu t/\lambda^2. \quad (2.19)$$

The most generalized figure of merit is the noise equivalent power (NEP), which is defined as the incident signal power required to obtain the signal equal to the noise in one Hz bandwidth ($\text{Power}_{\text{signal}} = \text{Power}_{\text{noise}}$). The NEP is a measure of the signal to noise ratio (SNR) and not just noise. If the NEP is referred to inside the detector, then the signal power absorbed in the detector is given by Eq. 2.13. It is more useful to refer the NEP at the detector input. The signal power incident on the detector required to produce $\text{SNR}=1$ is

$$(\text{NEP})_{\text{absorbed}}^2 = \frac{P_N^2}{B\alpha^2} = \frac{2}{\alpha^2} \int P_\nu h\nu d\nu + \frac{2}{q\alpha^2} \int P_\nu h\nu \eta(\nu) d\nu. \quad (2.20)$$

From Eq. 2.17, 2.19, and 2.20 the absorbed NEP is

$$(\text{NEP})_{\text{absorbed}}^2 = 4 \frac{A\Omega}{c^2} \frac{(K_B T_s)^5}{h^3} \frac{\epsilon\tau}{\alpha} \left(\int \frac{x^4 dx}{(e^x - 1)} + \frac{\alpha\epsilon\tau}{q} \int \frac{x^4 dx}{(e^x - 1)^2} \right) [\text{W}^2/\text{Hz}]. \quad (2.21)$$

2. Reflected power:

Considering that absorbers are imperfect, it is advisable to consider the power that is reflected by and emitted from them. From van Vliet (1967) (Eq. 71), the spectral density of the reflected power is

$$SD(P_{\text{refl}}) = 2 \int (1 - \eta) P_{\nu\text{-refl}} h\nu d\nu + 2 \int (1 - \eta)^2 P_{\nu\text{-refl}} h\nu d\nu B, \quad (2.22)$$

where P_{refl} is the radiant power absorbed, $P_{\nu\text{-refl}}$ is the absorbed power per unit optical bandwidth and B is the boson factor given by

$$B = 1/(e^{h\nu/k_B T_s} - 1). \quad (2.23)$$

Following the same argument as above, the NEP of the reflected radiation is

$$(\text{NEP})_{\text{reflected}}^2 = \frac{2}{\beta^2} \int (1 - \eta) P_{\nu\text{-refl}} h\nu d\nu + \frac{2}{q\beta^2} \int (1 - \eta)^2 P_{\nu\text{-refl}} h\nu d\nu B, \quad (2.24)$$

where β is the reflection coefficient of the imperfect absorber.

Solving the equation, the NEP is given by

$$(\text{NEP})_{\text{reflected}}^2 = 4 \frac{(1 - \alpha\epsilon\tau)(\alpha\epsilon\tau)}{\beta^2} \frac{A\Omega}{c^2} \frac{(K_B T_s)^5}{h^3} \left(\int \frac{x^4 dx}{(e^x - 1)} + \frac{(1 - \alpha\epsilon\tau)}{q} \int \frac{x^4 dx}{(e^x - 1)^2} \right) [\text{W}^2/\text{Hz}]. \quad (2.25)$$

3. Emitted power:

From van Vliet (1967)(Eq. 72), the spectral density of the emitted power is,

$$SD(P_{\text{emit}}) = 2 \int \eta P_{\nu\text{-emit}} h\nu d\nu + 2 \int (2 - \eta)\eta P_{\nu\text{-emit}} h\nu d\nu B. \quad (2.26)$$

Following the same argument as above the obtained NEP of the emitted radiation is,

$$(\text{NEP})_{emitted}^2 = \frac{2}{\phi^2} \int \eta P_{\nu-emit} h\nu d\nu + \frac{2}{q\phi^2} \int (2-\eta)\eta P_{\nu-emit} h\nu d\nu B, \quad (2.27)$$

where ϕ is the emission coefficient of imperfect absorber.

Solving the equation, the NEP is

$$(\text{NEP})_{emitted}^2 = 4 \frac{(\alpha\epsilon\tau)^2 A\Omega (K_B T_s)^5}{\phi^2 c^2 h^3} \left(\int \frac{x^4 dx}{(e^x - 1)} + \frac{(2 - \alpha\epsilon\tau)}{q} \int \frac{x^4 dx}{(e^x - 1)^2} \right) [\text{W}^2/\text{Hz}]. \quad (2.28)$$

For real systems, it is possible to assume that the bolometer is cold and absorptive enough for fluctuations in emitted power to be neglected. The empirical solutions for reflected and emitted power give very low values, hence they can be neglected. Hence the photon noise in the bolometer is equivalent to the absorbed NEP (Eq. 2.20),

$$(\text{NEP})_{Photon}^2 = (\text{NEP})_{absorbed}^2 [\text{W}^2/\text{Hz}]. \quad (2.29)$$

Each of the terms above is an uncorrelated noise source and can hence be added together in quadrature. Hence the overall NEP of an ideal bolometer is,

$$\text{NEP}_{Total}^2 = \text{NEP}_{Johnson}^2 + \text{NEP}_{Phonon}^2 + \text{NEP}_{Photon}^2. \quad (2.30)$$

From this expression, it follows that the optimum NEP is obtained by minimizing R , T , G and the background power (Q) and maximizing S . Since the NEP is directly proportional to the operating temperature; lowering the operating temperature decreases the NEP, and therefore increasing sensitivity. However, R , T and G are based on the application requirements which limit the total NEP. Bolometers can be saturated due to the power from a high background, hence, the background power is a dominating factor for the selection of G . The resistance of the bolometer is calculated by matching the impedance with that of the pre-amplifier. This, impedance matching determines the selection of an appropriate R . The base temperature of the cryostat is determined by the available technology, and the transition temperature T is fixed.

The thermal time constant, τ , is a measure of the response time of the bolometer to incoming radiation and is given by

$$\tau = C/G. \quad (2.31)$$

Thus, the larger the value of G , the faster the detector response. Hence there is a trade-off to be made between the NEP and τ in the selection of G .

2.4 Superconducting transition edge sensors

Superconducting transition edge sensors (TES) are operated on the very sharp transition from the normal to the superconducting state, hence they are very sensitive thermistors. The superconducting material is chosen according to the application requirements. In our case the optimum transition temperature is at 450 mK and it is achieved using an Au-Pd/Mo thermistor. Advantages of the superconducting bolometers over the conventional semiconducting bolometers are:

- In many cases the bolometer performance is limited by a trade-off between sensitivity and speed. The voltage biased superconducting bolometer (VSB) has a much better combination of speed and sensitivity. The strong negative electrothermal feedback decreases the time constant of the bolometer. In the transition range, the resistance of the TES is a sensitive function of temperature hence a small change in the temperature can be detected by the TES.

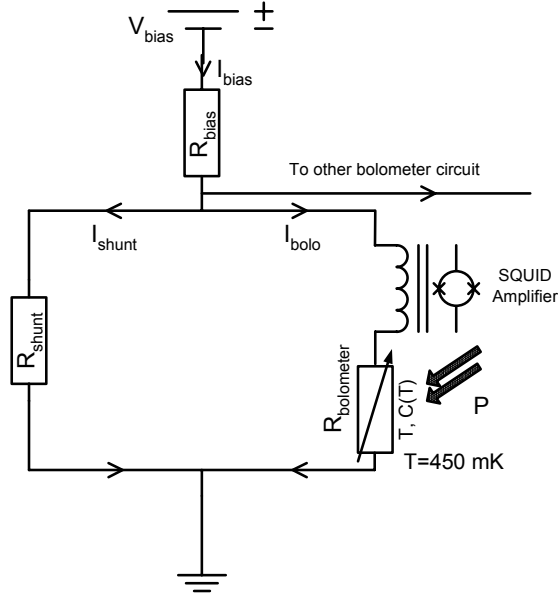


Figure 2.2: The schematic diagram for a superconducting TES bolometer. The TES, maintained at transition temperature T with heat capacity C and resistance $R_{bolometer}$, is connected to a thermal bath maintained at a constant temperature, T_o , through a weak link of thermal conductance G . T_o is 300 mK. The absorbed incident power P changes the temperature and effectively changes the resistance of the bolometer. The bolometer is voltage biased so changes in resistance are measured by applying a constant bias voltage. $V_{bolo} = V_{bias}$. The output current, I_{bolo} is detected by SQUID amplifiers. A shunt resistor with very low resistance is mounted in parallel to the bolometer. In the testing setup, $R_{bolometer}$ is 1 – 5 Ω and R_{shunt} is 10 – 33 m Ω . The bias voltage can be varied in the range between 1 and 6 V. The normal state resistance of the bolometer is 1 to 5 Ω in different experiments. R_{bias} is 1045 Ω . In voltage biased condition, $R_{bias} \gg R_{bolometer} \gg R_{shunt}$.

- For astronomical applications, it is desirable to manufacture large pixel bolometer cameras. Superconducting bolometers are fabricated by a completely micro-lithographic procedure. The Superconducting Quantum Interference Device (SQUID) amplifiers can also be deposited on the silicon nitride membrane during bolometer fabrication which operates the possibility for the fabrication of several hundred pixel bolometer arrays. The size of the array is decided by the application of interest.
- The SQUID amplifiers can be designed to have very low power dissipation. They work at low temperature making it possible to be install them in close proximity to the bolometer array. In addition, both TESs and SQUIDs are low impedance devices, so they are less sensitive to microphonic pickup than semiconductor bolometers.
- The wires connecting the bolometer and SQUID electronics present thermal links between different temperature stages inside the cryostat. Multiplexing of electronics reduces the numbers of wires, hence the thermal load on the ^3He stage is also reduced.

2.4.1 Strong negative electrothermal feedback

Early superconducting TESs were operated with a constant-current bias, which resulted in positive electrothermal feedback (ETF) (Clarke et al. 1977). This resulted in the temperature to increase with

increasing signal leading to instability. This instability can be avoided by negative feedback using a constant voltage bias and measuring the bolometer current (Irwin 1995). The change in the sensor current can be measured by a SQUID. The schematic diagram for a TES is as shown in Fig. 2.2. The power measured by the bolometer is the sum of power due to bias current and input radiation.

$$P_{Total} = P_{Signal} + P_{Bias}, \quad (2.32)$$

where $P_{Bias} = V_{Bias}^2/R$. Thus from Eq. 2.32 it can be concluded that,

$$T \uparrow \Rightarrow R \uparrow \Rightarrow P_{Bias} \downarrow \Rightarrow P_{Total} \downarrow \Rightarrow T \downarrow. \quad (2.33)$$

As will be shown in § 2.5, the temperature T essentially remains constant. This is called *strong negative electrothermal feedback*. It is caused by the sharpness of the transition. The advantages of strong negative ETF are:

- It speeds up the detector. Theory and experiment show that in this mode the detector time constant can be more than two orders of magnitude smaller than the intrinsic thermal time constant (τ).
- The detector is linear over a wide range of incoming signal power.
- No external feedback circuit is necessary since, once the correct bias voltage is applied, the thermometer stays at its transition temperature.

2.5 Responsivity of voltage biased superconducting bolometer

Consider a bolometer with heat capacity C that is connected to a heat sink at temperature T_o with an average thermal conductance \overline{G} . The incoming signal power P and the bias power V_b^2/R heats the bolometer to its transition temperature T , where V_b is the bias voltage and R is the resistance of the bolometer. When the time varying signal $\delta P e^{i\omega t}$ is incident, the temperature changes by $\delta T e^{i\omega t}$. The power flow model for superconducting bolometer is (Lee et al. 1996, 1998),

$$P + \delta P e^{i\omega t} + \frac{V_b^2}{R} - \frac{V_b^2}{R^2} \frac{dR}{dT} e^{i\omega t} = \overline{G} (T - T_o) + G \delta T e^{i\omega t} + i\omega C \delta T e^{i\omega t}, \quad (2.34)$$

where C is the heat capacity, T_o is the bath temperature, T is the operating temperature, \overline{G} is the average thermal conductance, G is the differential thermal conductance of the weak link at temperature T and R is the TES resistance. Eq. 2.34 can be separated into time independent and dependent terms respectively, as

$$P + V_b^2/R = \overline{G}(T - T_o), \quad (2.35)$$

$$\delta P e^{i\omega t} = \left(\frac{P_b}{T} \alpha + G + i\omega C \right) \delta T e^{i\omega t}, \quad (2.36)$$

where α describes the sharpness of the transition. As explained in § 2.4.1, the negative ETF reduces the temperature response δT , since the bias power compensates the change of signal power in the bolometer. Thus the effective thermal conductance of the TES, which controls the VSB temperature response, is (Lee et al. 1996)

$$G_{Eff} = \frac{P_b}{T} \alpha + G + i\omega C. \quad (2.37)$$

The effective thermal feedback is increased by the effect of negative ETF. Here the defined loop gain is defined by $L_\omega(\delta P + \delta P_b) = L_\omega \delta P_{Total} = -\delta P_b$, which is analogous to an electronic feedback circuit. The gain is the frequency-dependent term and is given by

$$L_\omega = \frac{P_b \alpha}{GT(1 + i\omega\tau_o)} = \frac{L}{(1 + i\omega\tau_o)}, \quad (2.38)$$

where L is the DC gain. The gain rolls off at $\omega > 1/\tau_o = G/C$. The VSB output is the change of bias current and its current responsivity is defined as $S_i = \delta I / \delta P$. Hence

$$S_i = \frac{-1}{V_b} \frac{L}{(L + 1)} \frac{1}{(1 + i\omega\tau)}, \quad (2.39)$$

where $\tau = \tau_o/L + 1$ is an effective time constant (Lee et al. 1998). In case of $L \gg 1$ with $\omega \ll 1/\tau$, the responsivity $S_i \sim -1/V_b$ is given by the bias voltage. The frequency response of the VSB rolls off at higher frequency $1/\tau$, rather than $1/\tau_o$.

2.5.1 Noise in Voltage biased Superconducting Bolometers

The overall NEP of the bolometer is governed by Eq. 2.30. In the case of the VSB, the Johnson noise generates a fluctuating current in the closed circuit with a spectral density $i_n^2 = 4kT/R$. The contribution from Johnson noise is reduced by $1/(L + 1)$ for $\omega < 1/\tau_o$ and gradually increases with frequency until it reaches its normal value for $\omega > 1/\tau$. The SQUID amplifier adds a noise term of i_{squid}^2 . The various excess noise sources like fluctuations in T_o , microphonics, contact shot noise, resistivity fluctuations, superconducting flux noise, may cause additional noise contributions in VSBs.

The noise equivalent power of the VSB can be given as (Lee et al. 1998)

$$NEP^2 = NEP_{photon}^2 + \gamma NEP_{phonon}^2 + NEP_{Johnson}^2 \left(\frac{\tau}{\tau_o} \right)^2 \left(\frac{1 + \omega^2 \tau_o^2}{1 + \omega^2 \tau^2} \right) + \frac{i_{SQUID}^2}{|S_i|^2} + NEP_{excess}^2 [W^2/Hz], \quad (2.40)$$

where photon noise, phonon noise and Johnson noise are explained in § 2.3. Phonon noise contains the term γ , which is a factor less than unity representing an adjustment in the thermal fluctuation noise for the gradient in temperature along the thermal link. This factor is approximately $1 - (1 + n/2)t + (2 + n)(2 + 3n)t^2/12$, where $t = 1 - T_o/T$ (Mather 1982) and n is 1, 2 ... n . Like the photon noise, NEP is referred at the bolometer input and is independent of the measurement frequency. In both cases, the voltage noise and the current noise of the bolometer output decrease rapidly after $\omega\tau > 1$ because of the frequency dependence of the responsivity. Excess low frequency noise, called $1/f$ noise is a problematic issue in bolometers. The $1/f$ noise has become less significant due to the improvements in material and electrical contacts, electrical sources and shielding technology in the bolometer.

Low frequency noise due to changes in the temperature of the heat sink can also be important. Slow drifts in the temperature can be reduced by active temperature regulation. Fast fluctuations such as noise due to boiling of cryogenics can be reduced by a passive low pass filter of low heat capacity and a weak thermal link with a speed of response G/C that is small compared with ω_S .

Chapter 3

Overview of Transition Edge Sensors and SQUIDs

The fabrication of TES and SQUID is done by our collaborators at the Institute for Photonic Technology (IPHT), Jena, Germany.

The general philosophy behind the fabrication process is that the thermal conductance of the bolometer is adjusted by structuring the silicon nitride membrane. This can also be achieved by changing the thickness of silicon nitride membrane. All bolometers were designed to operate under a 300 K background, but they can also be used under lower background levels. The former requirement was chosen because working under room temperature makes it much easier to test the bolometers. For very low background and to make the cross-section to cosmic rays negligible, the silicon nitride membrane can be structured in a *spider-web* design and such a fabrication experiment has been successfully performed at IPHT. The fabrication (Chapter 4) of and experiments (Chapter 6) on a bolometer system with a band center wavelength of 1.2 mm is described here. A bolometer system with a band center wavelength of 870 μm was also fabricated and tested simultaneously at the IPHT.

The thermistor is fabricated using a bilayer of molybdenum/gold-palladium (Mo/Au-Pd). The gold-palladium (Au-Pd) alloy allows tuning of the molybdenum's critical temperature over one order of magnitude. Au-Pd can further be used for shunt resistances, absorber patterns and bond pads. The thermistor is deposited on a silicon nitride membrane. The radiation is coupled via a conical feed horn to an absorber. Alternatively, a continuous titanium (Ti) film absorber is used or a grid of dipole-like Au-Pd absorbers. The fabrication of VSBs is compatible with the SQUID manufacture. In the future, the SQUID layers may be merged with the bolometer layers and the fabrication of TESs and SQUIDs on a single silicon wafer might be possible.

3.1 The Silicon nitride membrane

A crucial part of the bolometer is a free-standing silicon nitride (Si_3N_4) membrane. It is deposited on a standard 4 inch $\langle 100 \rangle$ silicon wafer, coated with about 1 micron thick silicon nitride film, using chemical vapor deposition (CVD) or plasma enhanced chemical vapor deposition (PECVD). On the backside of the wafer, windows are etched in the silicon nitride film using reactive ion etching (RIE). Once all patterns on the front side are finished, this side is protected with a low melting wax, and the silicon is etched with sodium hydroxide (NaOH) through the openings in the backside silicon nitride film until the membranes on the front side are released. NaOH is an anisotropic etchant and so the walls, representing the $\langle 111 \rangle$ crystal plane, are inclined by 54.7° . The wax fulfills two tasks: it protects the metal patterns on the front

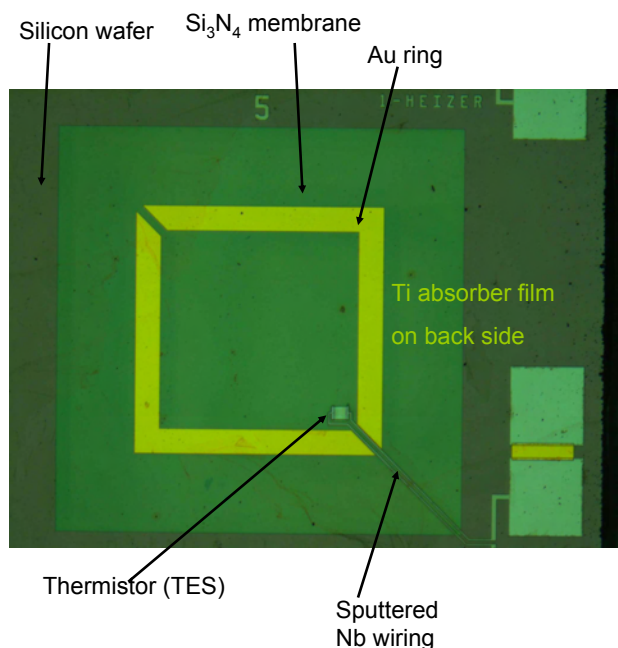


Figure 3.1: Schematic diagram of a single pixel bolometer on a silicon nitride (Si_3N_4) membrane. The thermistor is connected with niobium (Nb) wires.

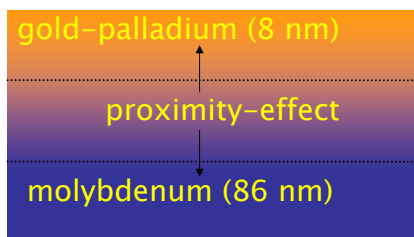


Figure 3.2: The bilayer structure of Au-Pd/Mo thermistor.

side from the alkali etchant and it mechanically supports the released membrane at the end of the process. Then the wax is removed and a final lithography step may be performed on the released membrane. This is challenging because of the fragility of the thin silicon nitride film. Finally the membrane is patterned using RIE to lower its thermal conductance. From transition temperature (T_c) measurements at different bias currents, the derived thermal conductance G of the non-patterned membrane is about 4 nW/K at 400 mK. Theoretically, this results in a photon noise limited performance NEP of $1 \times 10^{-16} \text{ W}/\sqrt{\text{Hz}}$, which was confirmed experimentally (§ 6.8; 6.9; 6.10; 6.11). By structuring the membrane in the shape of an 8-legged spider geometry, the thermal conductance can be decreased, thereby, improving the NEP.

3.2 Thermistor layout

The thermistor is a superconducting thin film with a target transition temperature T_c . A sputtered molybdenum (Mo) thin film was chosen which has a transition temperature of 800 mK. By in situ

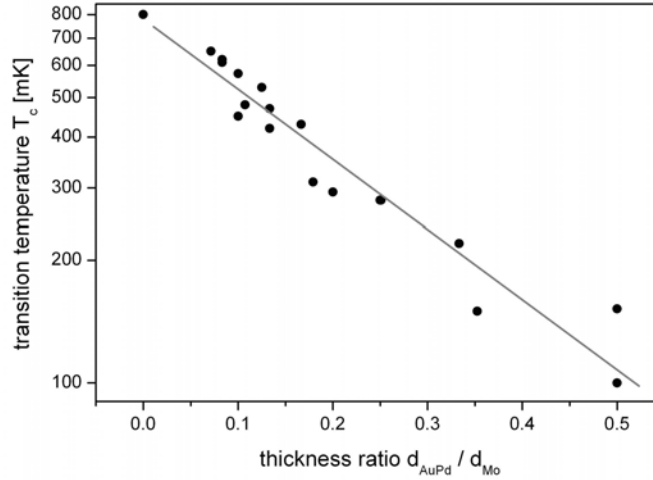
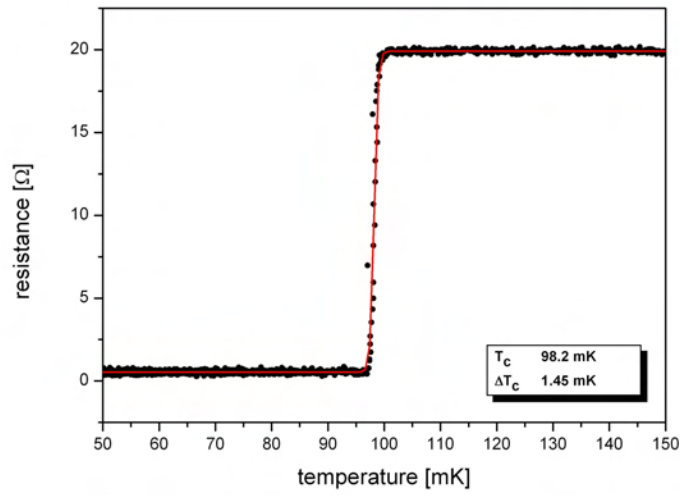


Figure 3.3: Dependence of critical temperature T_c on the thickness ratio of a bilayer of molybdenum and an alloy gold-palladium. These measurements were performed at the IPHT.

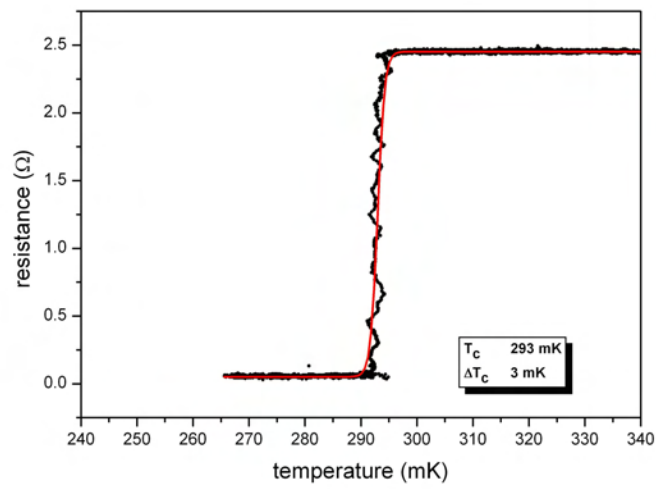
sputtering of a normal metal on top of the molybdenum film it is possible to tune the T_c via the proximity effect. Instead of using a standard material like gold or copper, an alloy of gold and palladium (Au-Pd) is used (Boucher et al. 2006). Palladium is a strong Pauli paramagnetic material so the lowering of T_c is stronger in comparison to a nonmagnetic normal metal. If the film thickness is small in comparison to the coherence length N , the value of T_c depends on the thickness ratio between the normal conductor and that of the superconductor. In this case the T_c can be tuned between 800 mK and 100 mK. The Fig. 3.3 shows the relation between the variation in critical temperature and the thickness ratio of a bilayer of Au-Pd and Mo. Fig. 3.2 shows the bilayer structure of the thermistor.

The target T_c can be reproduced from run to run within a 50 mK error margin, and has been shown to be stable over a period of about one year. Fig. 3.4 shows two different samples with transitions at 100 and 300 mK, respectively. The transition width (ΔT_c) becomes larger with higher temperature, which is expected due to increased thermal fluctuations.

In addition, it was found that a broadening of ΔT_c depends on the polycrystalline structure of the bilayer film, and, thus, on the actual physical conditions of the surface of the substrate. A huge difference was seen when using different substrates like sapphire or silicon oxide, but even for silicon nitride substrates, significant variation in the ΔT_c broadening values was observed from batch to batch. In the case of a combined bolometer and SQUID fabrication process this means that it would be highly preferable to start the manufacturing from a bare wafer with the deposition of the thermistor film. However, the fragile bilayer film can be easily damaged by the subsequent fabrication steps. Therefore, particular care should be taken with the protection of this film. An obvious way for such protection would be a covering layer, ideally made from a dielectric insulator, since other materials would influence the electrical properties of the bilayer. So far a suitable material has not been found, since standard dielectric films like SiO or SiO₂ have been shown to have a dramatic impact on the transition. The shape of the transition curve is distorted probably due to a substantial mechanical stress and sometimes additional steps appear within the original transition, as can be seen in Fig. 3.5. The data presented in this section is obtained from measurements performed at the IPHT.



(a)



(b)

Figure 3.4: (a) Transition of thermistor film at 100 mK when the Mo/Au-Pd thickness ratio is 0.5. Due to the proximity effect, the transition temperature is shifted to 300 mK when the Mo/Au-Pd thickness ratio is 0.1, shown in figure (b). These measurements were performed at the IPHT.

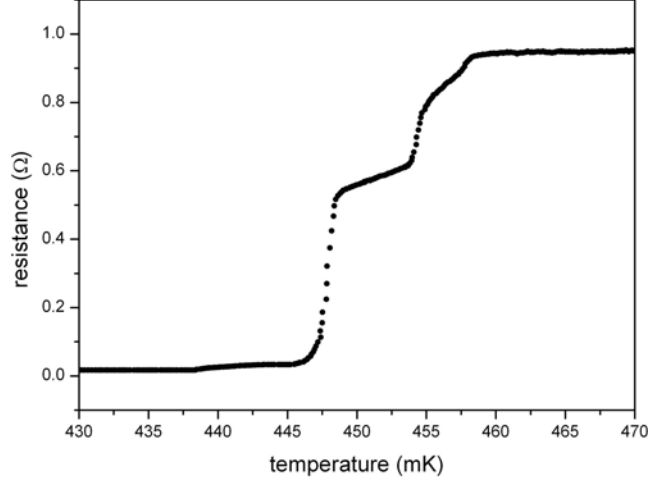


Figure 3.5: Distorted transition curve, possibly due to mechanical stress. In some manufacturing runs, a distorted transition curve of thermistor film was observed. These measurements were performed at the IPHT.

3.3 The Absorber

Separation of the absorption properties from the thermometric sensing properties allows an additional degree of freedom in the design of the bolometers. The common approach is to use a thin metallic film evaporated onto a lossless dielectric substrate. The dielectric material is aimed to have a much lower heat capacity than the sensing element, the Au-Pd/Mo thermistor in our case.

If the dielectric is lossless and if multiple internal reflections are ignored, the absorptance for the radiation incident normally from the dielectric side is (Nishioka et al. 1978)

$$A = \left| \frac{4n}{(1+n)^2} \right| \frac{4Z_o n R}{|R(1+n) + Z_o|^2}, \quad (3.1)$$

where Z_o is the impedance of free space ($377 \Omega/\square$), R is the surface resistance and n is the refractive index of the substrate. For common dielectrics, the surface resistance is in the range of $200 \Omega/\square$ to $400 \Omega/\square$. Continuous high resistance metal films are difficult to deposit and have poor reproducibility. In the initial design (§ 6.1) and the High-G design of the new layout (§ 6.4) a continuous thin titanium (Ti) film was deposited as an absorbing layer. The capacitive grid dipole Au-Pd absorbers are used in spider geometries (§ 6.6).

Au-Pd dipole absorbers

The radiation band of interest for the experiment has a center wavelength of 1.2 millimeter. The radiation is coupled to the silicon nitride membrane in front of a quarter-wavelength back-short via conical feed horns. The energy is absorbed by a small grid of dipole-like antennas whose impedances are designed to match the impedance of free space. The absorber dipoles are made out of a gold-palladium alloy, which is also used in the bilayer film. The sputtered films are patterned using a lift-off technique. Electromagnetic simulations and calculations show that the surface resistance of the absorber should be $10 \Omega/\square$ for the actual dipole geometry. Simulations are performed by Theoretische Elektrotechnik group, University of Wuppertal (Hansen & Wu 2006). In array 4SN 1762, the cross absorbers have a surface impedance of

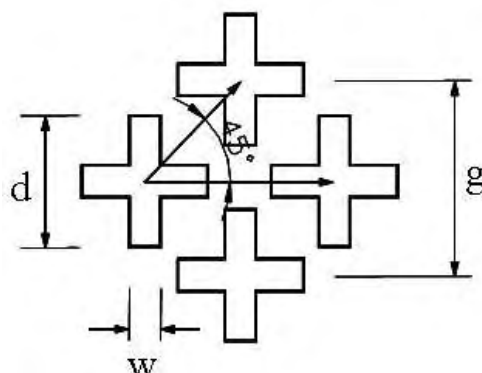


Figure 3.6: Schematics of cross absorbers. The cross absorbers are derived from an area weighted mean conductance of the equivalent continuous thin film absorbing layer. Cross represent the metal.

$10 \Omega/\square$. The efficiency of the cross absorber was found equivalent to that of a continuous Ti film absorber or $377 \Omega/\square$ (§ 6.10, 6.11).

The advantages of cross absorbers are:

1. They are *frequency selective*. The absorption efficiency is highest when the length of the dipole antenna (length 'd' in Fig. 3.6) is half of the wavelength of interest ($\lambda/2$). Thus the absorption works coherently with the filters defining the transmission band. Since the absorption works only for the radiation band of interest, signals at any other frequency are not coupled to the absorber.
2. It is possible to make the absorption polarization sensitive by depositing only a grid of dipole absorbers instead of a cross absorber.

3.4 Spider geometry

Silicon nitride membranes are used for bolometer manufacturing for the following reasons:

1. The responsivity of the bolometer is inversely proportional to the thermal conductance. Since silicon nitride is an amorphous material, the thermal conductivity κ is low and decreases at cryogenic temperatures, thereby increasing the sensitivity of the bolometer.
2. For silicon nitride, it is possible to tune the thermal expansion coefficient. Using non-stoichiometric silicon nitride, the thermal expansion coefficient is matched with that of the silicon to decrease the stress on the bolometer assembly.
3. The durability of a silicon nitride is high because it is a hard material.
4. The technology of a silicon nitride membrane on a Si wafer has been used for similar applications (Kreysa et al. 1996; Mauskopf et al. 1997; Osterman et al. 1997).

As shown in Eq. 2.39, current responsivity and time constant of the bolometer are inversely proportional to the thermal conductance of the membrane. To gain control over these parameters, a 8-leg spider structured membrane with different leg widths was fabricated. The membranes were categorized in Low-G, Medium-G and High-G depending on their thermal conductance. The size of the silicon nitride membrane is $3300 \mu\text{m} \times 3300 \mu\text{m}$ and the membrane is structured into a spider structure to reduce the thermal conductance. The leg width for the Low-G is $100 \mu\text{m}$, the leg width for Medium-G membrane is $300 \mu\text{m}$ and the High-G one is a continuous silicon nitride membrane.

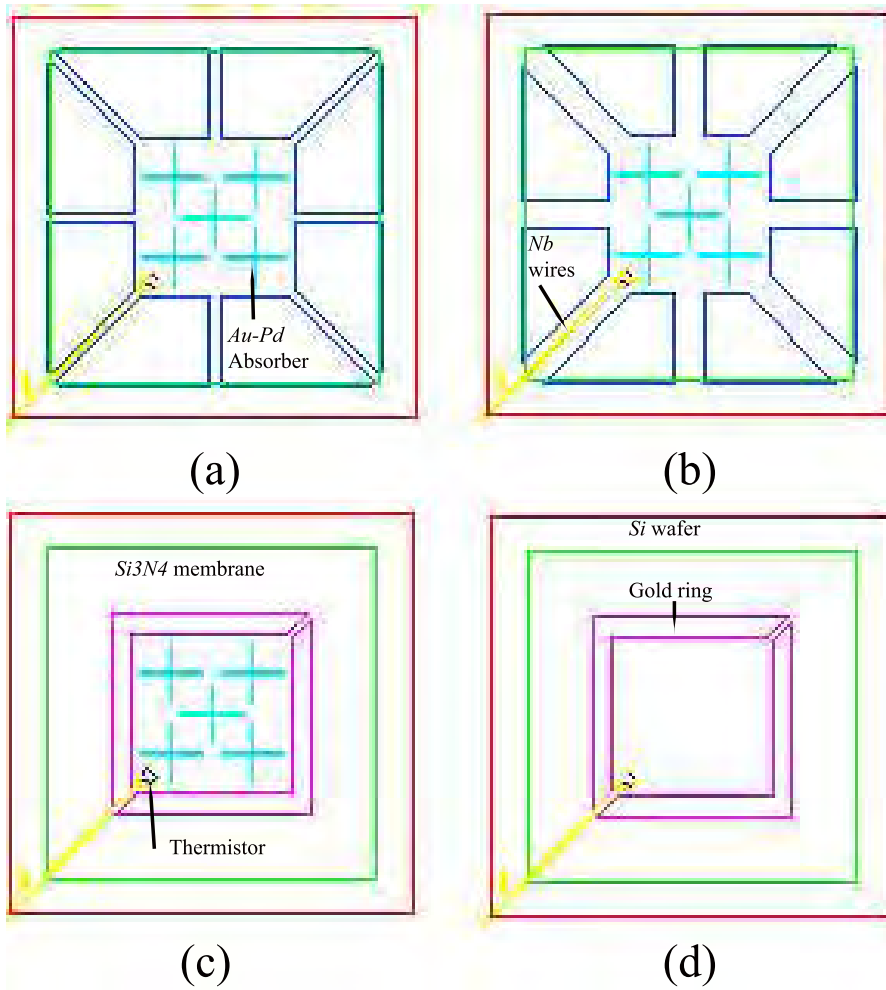


Figure 3.7: CAD layouts of different bolometer geometries. (a) A single pixel of Low-G design which has a leg width of $100 \mu\text{m}$. (b) A single pixel of Medium-G design which has a leg width of $300 \mu\text{m}$. (c) A single pixel of High-G design which has a continuous membrane. (d) A single pixel High-G layout without cross absorber. The crosses are the dipole Au-Pd absorbers. A single silicon nitride membrane is $3.3 \text{ mm} \times 3.3 \text{ mm}$ in dimension and the absorbing center patch is of $1.6 \text{ mm} \times 1.6 \text{ mm}$ in dimension. The thermistors are connected with niobium wires.

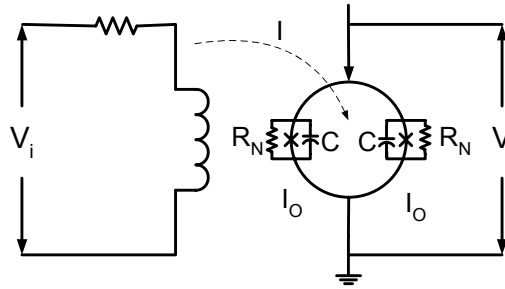


Figure 3.8: Circuit diagram for a dc SQUID equipped with a coupling loop that electrically induces a magnetic flux Φ . The double junction quantum interferometer is formed by two Josephson junctions connected by a superconducting ring.

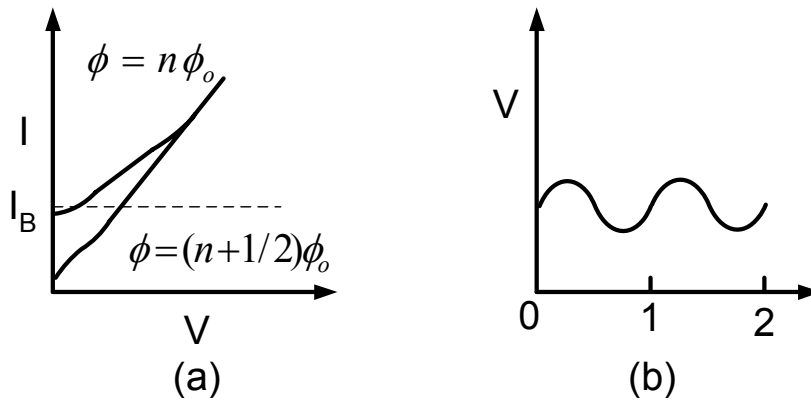


Figure 3.9: (a) SQUID $I - V$ curves for applied flux $\Phi = n\Phi$ and $(n + 1/2)\Phi$, where Φ is time a flux quantum. If the supercurrent is less than the critical current, no voltage develops across the insulating barrier. (b) Voltage across current-biased SQUID as a function of applied flux.

3.5 The Superconducting Quantum Interference Device (SQUID)

Generally SQUID amplifiers are used for low impedance superconducting bolometers. Direct coupled (dc) SQUIDs are preferred over radio frequency (rf) SQUIDS for applications of bolometer readout due to their simplicity. The dc SQUID is based on the properties of a resistively shunted Josephson junction. Josephson devices operate at liquid-helium temperatures (1-4 K) and exploit the macroscopic quantum properties of superconducting junctions.

- Josephson effect: Josephson (1962) proposed that Cooper pairs would be able to tunnel through two superconductors separated by a thin insulating barrier without developing a voltage across the barrier. Such a flow of pairs constitutes a supercurrent. The supercurrent i_s generates a phase difference $\Delta\Phi$ between the phases of the order parameters in the two superconductors according to the relation $i_s = i_1 \sin(\Delta\Phi)$, where i_1 is the critical current (Clarke 1971). The Josephson effect occurs when $i_s \leq i_1$; when $i_s > i_1$ a finite voltage develops across the barrier.

The energy difference between two sides of a junction is known as the coupling energy of the junction and is given by $E_c = -\Phi_0 i_1 / 2\pi$. If i_1 is of the order of one milliamper, E_c is about two electron volts which is less than the binding energy of a single hydrogen atom. For this reason, the Josephson junction may be used for sensitive detection.

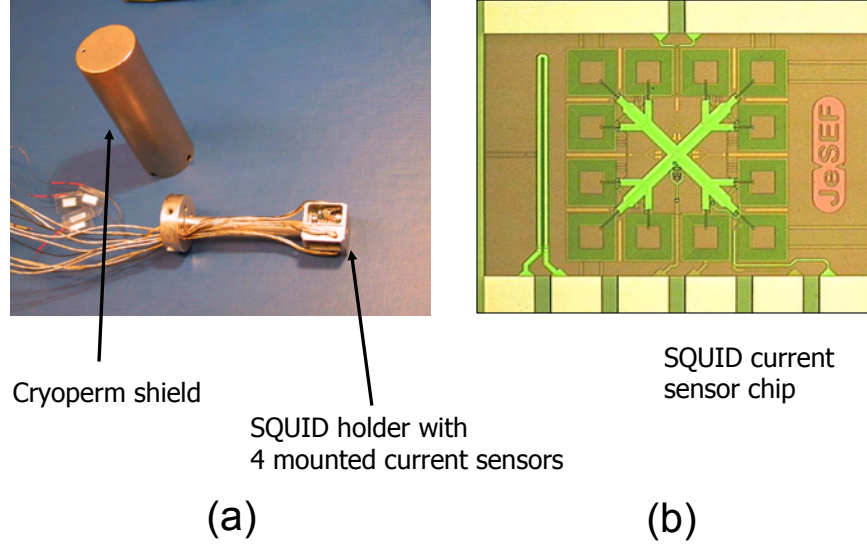


Figure 3.10: (a) Picture of SQUIDS with their magnetic shield. The SQUID amplifiers are mounted at ^4He temperature. (b) Photograph of a single SQUID current sensor chip.

A Josephson junction can carry a lossless supercurrent up to a critical value I_0 , above which it enters into a resistive state. The $I - V$ curve of the junction has $V = 0$ for junction current less than I_0 and develops a finite voltage for the junction current $> I_0$.

Fig. 3.8 shows the superconducting loop of a dc SQUID. It contains two tunnel junctions that are shunted by resistors R_N and capacitors C . When an external current is applied across the SQUID, it divides between the two branches subject to the condition that the total magnetic flux Φ through the loop is quantized in units of the flux quantum Φ_0 . When the applied flux is an integral multiple of Φ_0 , then there is no circulating current. In this case, both junctions carry the same current and the critical current of the SQUID is given by, $I = 2I_0$. When the external flux is not an integral multiple of Φ_0 then to meet the quantization condition, a circulating current has to be present, i.e. one of the junctions will exceed its critical current $I < 2I_0$. Fig. 3.9 (a) shows the $I - V$ curve of the SQUID in the two cases. The dashed line is the load line for a constant current bias. With an increase in the external flux, the SQUID voltage oscillates between the two $I - V$ curves shown in Fig. 3.9 giving the response shown in Fig. 3.9 (b). The SQUID is generally operated in a flux-locked mode with a feedback circuit to keep Φ constant. A detailed explanation of SQUID is given in Clarke (1974). Fig. 3.10 (b) photograph of the SQUID. SQUIDS used as amplifiers must be magnetically shielded to protect them from external magnetic noise.

3.5.1 Noise in the SQUID amplifier

The SQUIDS used during the experiments are of the CCblue (Supracon 2003) low- T_c dc variety, designed as current sensors with low input inductance (350 nH) and low current noise. The SQUID has an integrated input coil and a heater. For mechanical protection and easy handling, the SQUID is bonded to a circuit board and magnetically shielded by a niobium screen. It has three pairs of solder terminals

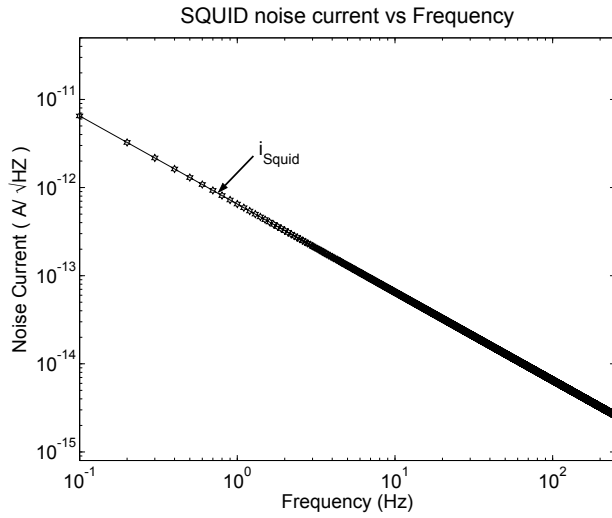


Figure 3.11: Current noise of the dc SQUID as a function of frequency.

with normal metal wire bond connections: one is for the SQUID output, one for the feedback coil and one for the heater resistor. This resistor is integrated on the SQUID chip and allows easy expelling of frozen flux in the SQUID loop. Two terminals with screws are available with superconducting wire bond connections to the input coil of the SQUID. The advanced SQUID package may be used immersed in liquid helium or in the vacuum. The noise current of the SQUID amplifier, i_{squid}^2 is $(6.5 \times 10^{-13})^2/f$ A/ $\sqrt{\text{Hz}}$ at $f > 0.1$ Hz. Fig. 3.11 shows the current noise of the SQUID as a function of frequency.

In the lower frequency range (< 1 Hz), the spectral density of flux noise or of magnetic field noise scales as $1/f$ (Martinis & Clarke 1986). The fluctuations of the critical current, I_c , in the Josephson junctions can create the $1/f$ noise. Such a $1/f$ noise (or ‘flicker noise’) can significantly limit the performance of practical devices at low frequencies. $1/f$ noise has been observed in low T_c SQUIDs, but is generally not a serious issue, while, in high T_c SQUIDs $1/f$ noise is a severe problem. The $1/f$ noise from I_c fluctuations is orders of magnitude higher in high T_c SQUIDs than in low T_c SQUIDs (Martinis & Clarke 1986).

3.6 Multiplexing of electronics

VSBs can be arranged in arrays. The multiplexing of the SQUID electronics reduces the number of electrical wires and SQUID readout sensors, which allows the fabrication of arrays with several hundred pixels.

3.6.1 Time division SQUID multiplexing

A SQUID amplifier can be switched rapidly between an operational state and a non-operational superconducting state by biasing the SQUID with a current of roughly $100 \mu\text{A}$. If n SQUIDs are stacked in series with $n + 1$ electrical address leads the driving current between an adjacent pair of leads will result in only one SQUID being operational. With the other SQUIDs in the superconducting state, the output voltage across the entire array is exactly equal to the voltage across the one active SQUID. In this manner, only one amplifier is necessary for n detectors, although the data rate is n times faster. Adding in the connections for a common TES bias and feedback signal, a total of $n + 7$ wires are needed.

In time division multiplexing (TDM), each TES is instrumented by a separate first-stage SQUID. An M boxcar modulation function is applied sequentially by turning on the first-stage SQUIDs in a column.

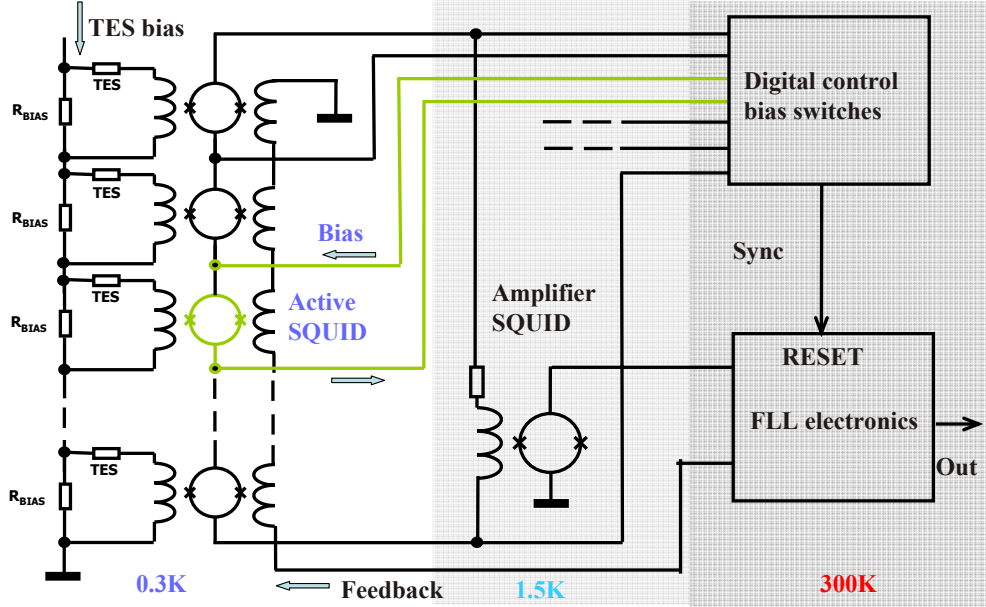


Figure 3.12: The time division multiplexing scheme for the SQUIDs.

The bandwidth of the TES is limited by a one-pole low-pass L/R filter formed by the inductance of the SQUID's input coil and the resistance of the TES (Irwin 2002). The signal is filtered before it is multiplied by the modulation function, since the low-pass filter rolls off at frequencies below the bandwidth of the sinc function. Thus, the TES cannot be used as the modulating element without a degradation of the SNR. Digital bias controls address a row M first-stage SQUIDs sequentially. The current through the address resistor is inductively coupled to a second-stage SQUID shared by all the first-stage SQUIDs in a column. The coupling to the second stage can occur either through a transformer coil that is common to all of the first-stage SQUIDs (Fig. 3.12) or through separately wound input coils from each channel to the second-stage.

A feedback flux is provided to the switched first-stage SQUIDs to linearize them. Since only one SQUID in a column is on at a time, one feedback coil can be common to all SQUIDs in the column. At high switching rates, inductive coupling from the common feedback coil to the input coil can be a source of crosstalk between the 'on' channel and all of the 'off' channels in the column. The inductive coupling is canceled by connecting each TES to the input coils of two SQUIDs with oppositely wound feedback coils. Only one SQUID of the pair is turned on. This 'balanced pair' configuration geometrically nulls the coupling between the feedback coil and the input coil. The feedback is applied by room-temperature electronics that have an analog-to-digital converter (ADC), a field-programmable gate array (FPGA), and a digital-to-analog converter (DAC) for each multiplexed column. When the SQUID associated with a pixel is on, its output is measured by the ADC. The appropriate feedback signal to null the flux of the 'on' SQUID is applied by the DAC to the common feedback coil. When the SQUID is turned off, the value of the DAC voltage required to null the SQUID flux is stored in the FPGA; the next time the pixel is turned on, the feedback algorithm is continued using the previous flux value.

3.6.2 Integrated design

A technology which allows the manufacturing of detector and readout on one chip would substantially simplify the task of integrating multiple pixel bolometer arrays.

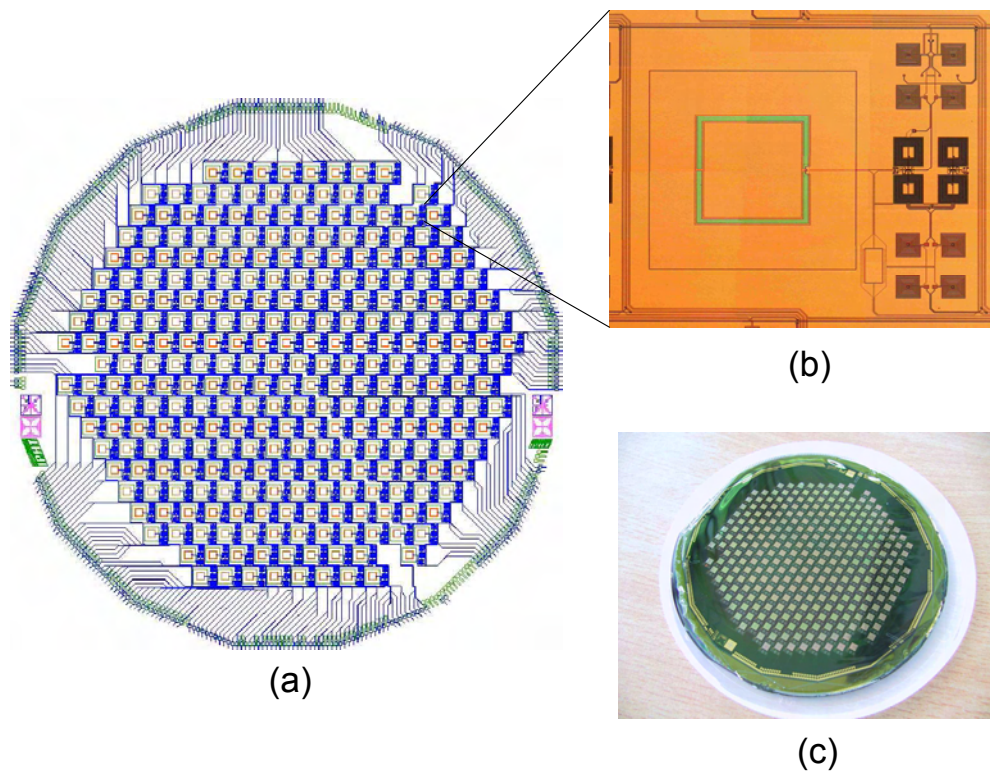


Figure 3.13: (a) The layout of the 288 channels LABOCA camera with superconducting bolometers with integrated electronics. (b) A single pixel element with integrated electronics. (c) The produced 288 channels bolometer wafer. The wafer was manufactured as a fabrication exercise.

The integration of SQUIDs and TESs is based on the two boundary conditions:

- The size and the spacing between bolometer pixels is defined by the aperture of the coupling feed horn. For 1.2 mm wavelength, the pixel size is 3.3 mm and the grid spacing is 4.5 mm. This means that there is a space of 1.2 mm between two pixels, which is sufficient for SQUID switches and corresponding wiring. In the case of 870 micron wavelength, the size of a pixel is 3 mm and the grid spacing is 4 mm resulting in a space between two pixels of 1 mm. In the case of a 350 micron wavelength setup, the pixel size is 1.5 mm and the grid spacing is 2 mm, so the available space is 500 μm , which is sufficient.
- The wiring scheme corresponds to a multiplexed readout in the time domain. The fixed number of bolometers (in this case 10) are fed with a common bias and the associated readout SQUIDs are connected in a superconducting loop with a common feedback, as shown in the Fig 3.12. This simplifies the wiring and reduces the number of required bond pads for electrical connections to the second stage amplifier.

Of particular importance is the consideration of adequate cooling of dissipative elements, such as the biasing, damping and shunt resistances. The entire array is mounted in a vacuum chamber, which means that cooling can only result from thermal transport through the single crystal silicon wafer via the gold bond wires. The thermal boundary resistance (Kapitza resistance : Swartz & Pohl 1989) can affect the heat removal at low temperatures. To minimize this, the area of all resistors was chosen to be as large as possible, and some cooling fins were added in sites with space restrictions.

3.6.3 Multiplexing scheme and technical trade-offs

There are various technical trade-offs like bandwidth usage efficiency, complexity of 300 K electronics, SQUID connections, power dissipation, SQUID noise, and filters to be considered to choose for the ideal multiplexing scheme. Some of the issues are discussed here.

In TDM, the dead time due to switching transients reduces the number of channels that can be multiplexed in the available bandwidth. In TDM, the one-pole L/R filter used to limit the pixel bandwidth must have a knee frequency that is $3 + 2\sqrt{2} \approx 5.8$ times higher than the thermal response bandwidth in order for the detector's operation to be stable. Similarly, in a Frequency Domain Multiplexing (FDM), the passband must be ≈ 5.8 times wider than the thermal response bandwidth.

TDM requires complex electronics due to the switched digital feedback needed to linearize the SQUIDs. Custom electronics are required, although components with sufficient performance are commercially available. FDM requires complex electronics to simultaneously demodulate the signals over the whole passband. A dedicated analog circuit for each pixel could be used for the demodulation, but this approach would be difficult for very large arrays. A column of detectors can also be instrumented with an ADC and a digital-signal processor to digitally demodulate all the signals simultaneously. Demodulation with sinusoids is computationally intensive. It will be challenging both to develop fast room-temperature electronics and to fit them into the power specifications of a satellite mission, especially for higher frequency systems. Considering all these aspects and the available technology at the disposal it was decided to use TDM for our application.

Chapter 4

Test arrays and experimental setup

The important bolometer properties like time constant, responsivity, noise, NEP are highly dependent on the geometrical and physical properties of the thermistor and the silicon nitride membrane. The physical thermistor properties like resistance, shape, transition temperature and transition curve sharpness, have a strong impact on the bolometer performance. To investigate the different geometries of thermistor and bolometer, and to determine the suitable geometry for our application, test arrays with seven bolometers were fabricated. See § 6.4 for a description of thermistors of different geometries and properties. Depending on the layout, a test array serves the purpose of testing different thermistors simultaneously which speeds up the experiments and allows monitoring the uniformity of the fabrication.

4.1 Test array

In a *test array*, seven thermistors are placed on the silicon nitride membrane (Si_3N_4) and one on the silicon (Si) wafer. The thermistor on the wafer is thermally so well connected that it was not possible to measure a load curve. However, thermistors on the silicon wafer are useful to measure the intrinsic critical temperature (T_c), since they are not affected by radiation. Fig. 4.1 shows the test array layout. The SQUID is connected to the thermistor using niobium-titanium wires. A gold (Au) ring is placed around the absorbing center patch of the silicon nitride membrane. The absorbing center patch is defined by the illumination pattern of the horn antenna. Gold has high thermal conductivity hence the deposition of a gold ring increases the thermalization of the absorbing center patch. The incoming radiation increases the temperature of the silicon nitride membrane. Since thermalization of the absorbing center patch is quite uniform, the change in temperature is efficiently sensed by the thermistor. See § 6.12 for the detailed analysis of behavior of the bolometer due to addition of the gold ring. A continuous titanium (Ti) film, which acts as a radiation absorber, is deposited at the back of the silicon nitride membrane. During the fabrication process, the shunt resistor is also deposited on the silicon wafer. Fig. 4.1 (c), shows the connection diagram of the thermistor. Niobium has a critical temperature of 9 K. At 0.3 K, only the lattice contribution to the thermal conductivity is left so the contribution of niobium to thermal conductance and heat capacity is very small.

4.2 Electrical circuit diagram

Fig. 2.2, shows the electrical circuit diagram of the bolometer. The resistor R_{bias} provides the constant current source, I_{bias} , which is divided into two branches, I_{shunt} and I_{bolo} . The shunt resistor (with resistance R_{shunt}) affects the VSB load curve. To understand this effect, a similar experiment is repeated with different R_{shunt} values, 10 and 33 m Ω (§ 6.1.1). The normal state resistance of the bolometer, R_{bolo}

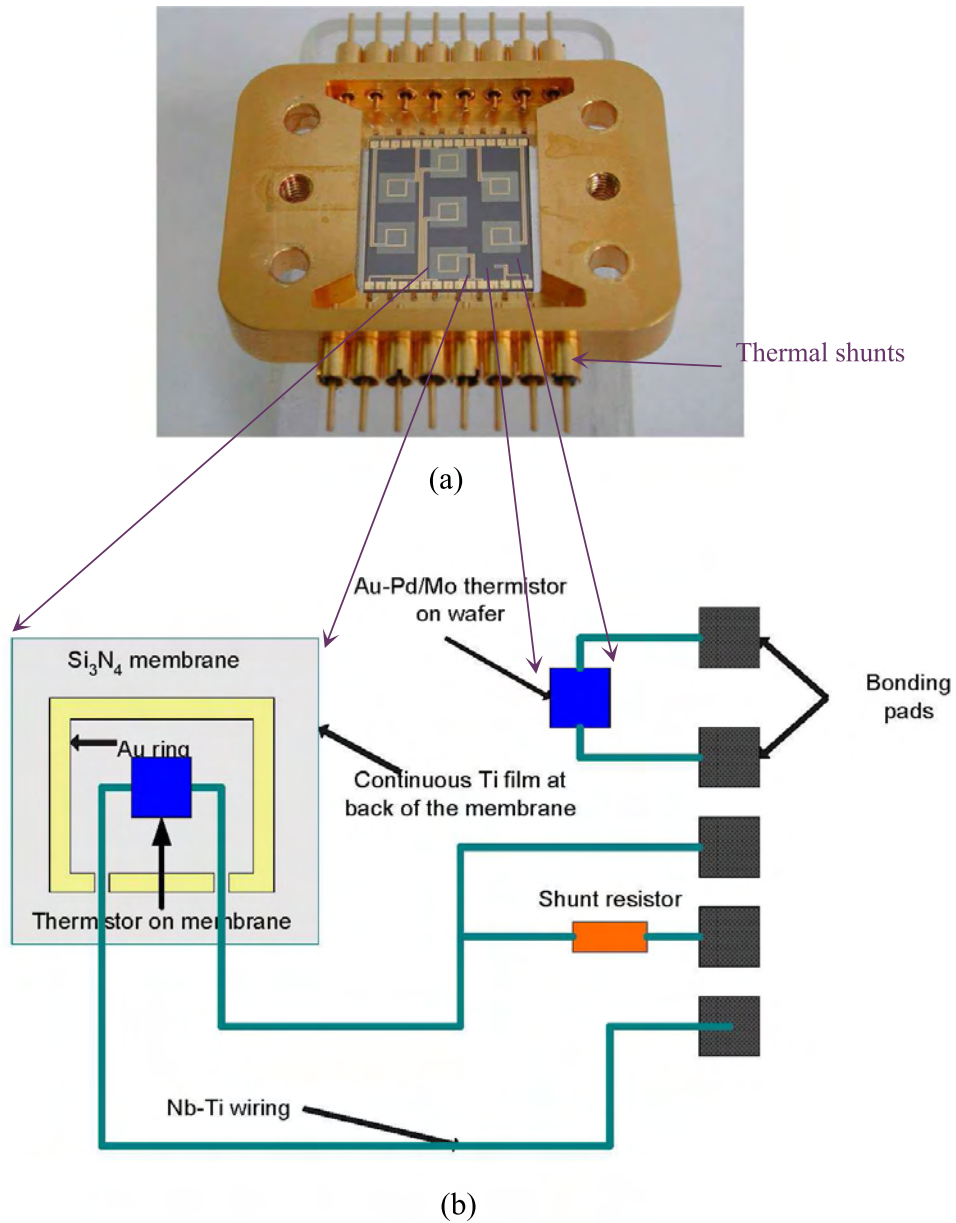


Figure 4.1: (a) Photograph of test array. The heat is dissipated through thermal shunts to the bath temperature. The wafer is connected to the thermal shunt using $50\ \mu\text{m}$ thick gold wires. The bolometers are bonded with aluminum wires. The Nb wires are $250\ \mu\text{m}$ thick and the Au ring is $150\ \text{nm}$ thick. The width of the A ring is $0.2\ \text{mm}$. (b) Schematic diagram of single pixel bolometer and wiring diagram. The silicon wafer is of dimension $16.21\ \text{mm} \times 16.21\ \text{mm}$. Each silicon nitride membrane is $3.3\ \text{mm} \times 3.3\ \text{mm}$ in dimension. Each bolometer has also shunt resistor which can be used optionally. The thermistor is connected to the SQUID using niobium-titanium wires. The whole assembly is mounted on the ^3He stage.

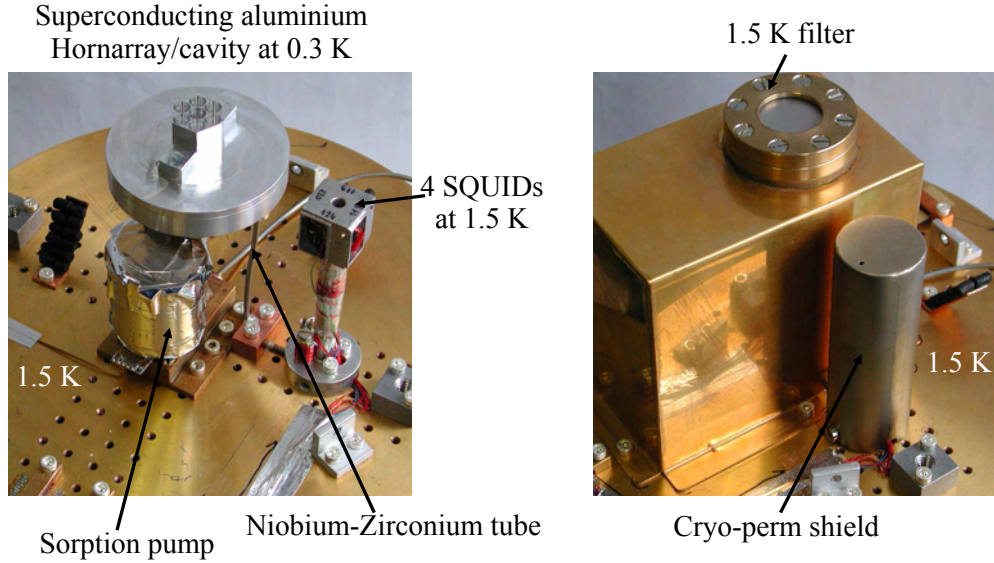


Figure 4.2: The left panel of the figure shows the opened cryostat showing the aluminum horn antenna array, SQUIDs and sorption pump mounted on the ^4He work surface. The ^4He bath is pumped to 1.5 K. The SQUIDs are designed to work at 1.5 K. The photograph shows the early stage with 4 SQUIDs mounted on ^4He surface. As shown in the right panel, the assembly is enclosed by copper radiation shield carrying the 1.5 K filter.

is 1Ω . From Fig. 2.2, it is possible to derive the equation for current (Eq. 4.1) and voltage (Eq. 4.2). The detector current is measured by SQUID amplifiers.

$$I_{bolo} = \frac{I_{shunt} R_{shunt}}{R_{bolo}}. \quad (4.1)$$

$$V_{bolo} = (I_{bias} - I_{bolo}) R_{shunt}. \quad (4.2)$$

I_{bolo} is the output current measured by the SQUID amplifier. It is amplified by SQUID FLL electronics. Two gain settings of the FLL electronics are used during the experiments. The low gain corresponds to the gain of 150000 and high gain corresponds to the gain of 2550000.

4.3 Thermal layout

Figs. 4.2 and 4.3 show a photograph and the schematic diagram of the horn antenna and SQUID assembly. After the cryostat window, the radiation passes through the two filters which provides the high frequency (thermal) radiation rejection and the definition of the pass band. The seven element array is placed behind the aluminum horn antenna. The bolometer is connected to the SQUID using niobium-titanium wires running through the niobium-zirconium (Nb-Zr) tube. The SQUIDs are placed inside the Cryoperm shield. The assembly of superconducting aluminum horn array/cavity, niobium-zirconium tube and Cryoperm shield provides excellent magnetic shielding which is very essential for the SQUID amplifier to operate.

The seven element array is bonded on the gold coated copper ring. The incoming radiation is coupled to the each bolometer via a horn antenna. The whole assembly is placed at a base temperature of 300 mK and the bolometers are maintained at the transition temperature of 450 mK. The zero background gives an intrinsic NEP of the detector which is proportional to the product of temperature and square root of

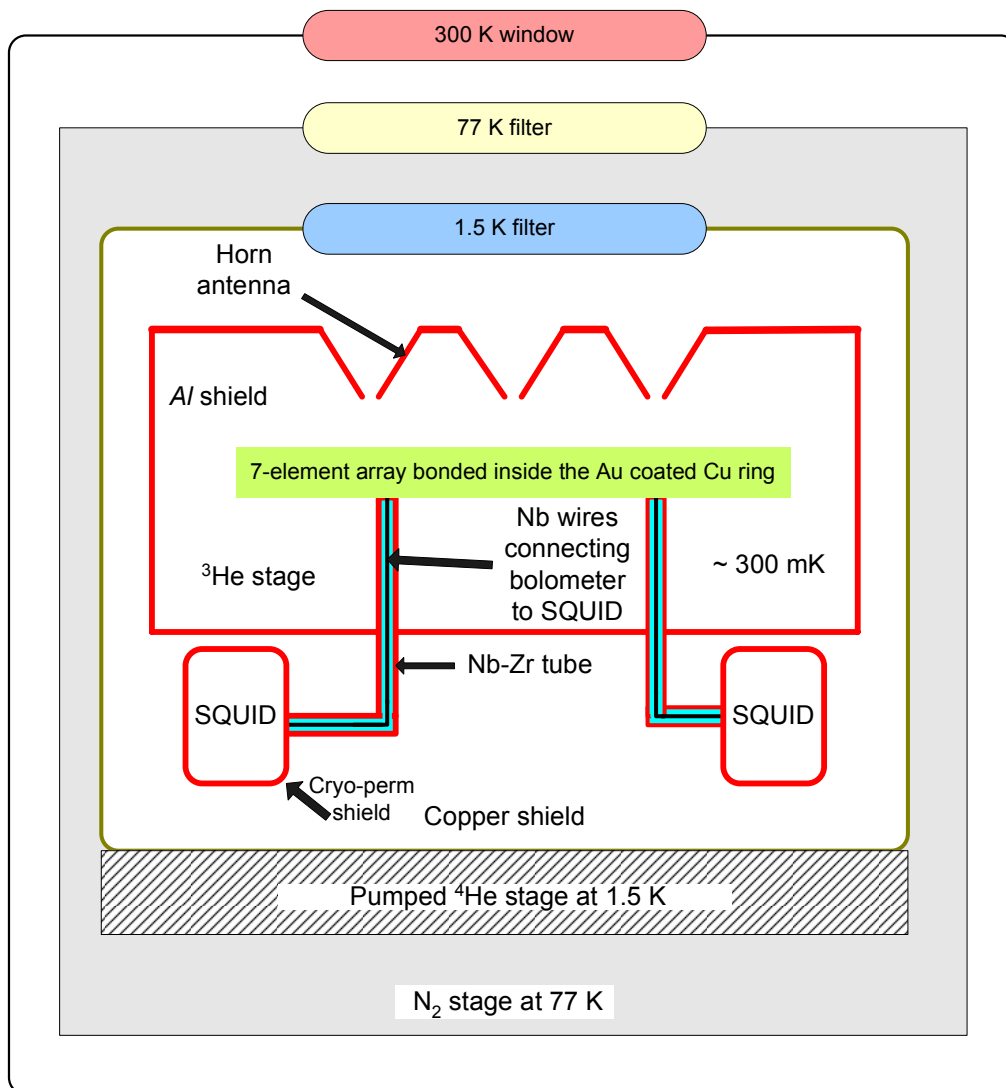


Figure 4.3: Schematic diagram of the cryostat. A Teflon window with inductive mesh is installed at 300 K. A c-cut crystal quartz filter is mounted at 77 K which blocks the high frequency background. A Multi-layer Mesh filter at 1.5 K temperature defines the transmission band. The radiation is coupled to the bolometer absorber via an aluminum horn antenna. The bolometer is connected to the SQUID using niobium-titanium wires.

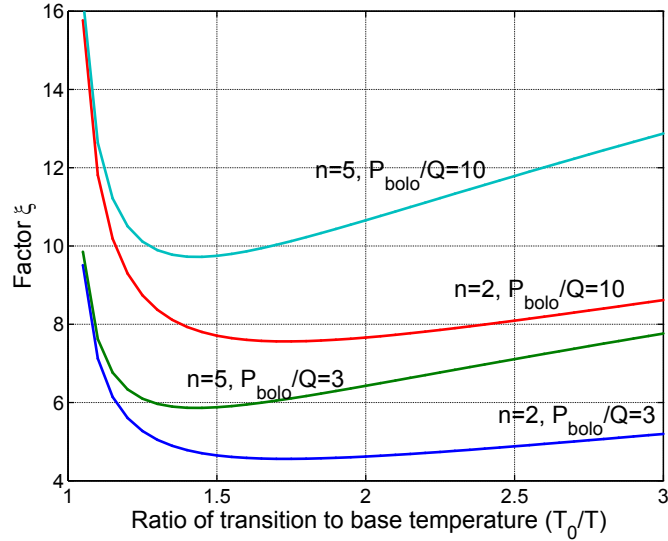


Figure 4.4: ξ plotted as a function of T/T_0 . The factor ξ is used to minimize the NEP as the function of T/T_0 at different conditions. For $n = 2$ and $P_{\text{bolo}}/Q = 3$, a shallow minimum leaves additional freedom in the choice of T/T_0 . For the silicon nitride membrane, n is 2 (Holmes et al. 1999).

heat capacity ($TC^{1/2}$), so for a fixed response time the NEP is proportional to $TC^{1/2}$. The heat capacity C of the bolometer material is proportional to T for metals or T^3 for dielectrics. The intrinsic NEP is therefore $\propto T^{3/2}$ and $T^{5/2}$ for metals and dielectrics, respectively. Hence, minimizing the detector operating temperature will result in the lowest achievable NEP.

An optimization scheme based on the variation of two parameters (Hoevers et al. 2000) is considered to minimize the noise and improve the performance of the VSB. The first is the power law exponent n of the thermal transport between the bolometer and the heat bath, yielding a thermal conductance $G \propto T$ and the ratio of the Joule power dissipated in the bolometer P_{bolo} and the second is the incoming sky power Q . $n = 2$ is the case of heat transport by electrons in a normal metal and $n = 5$ is valid for electron-phonon dominated transport. P_{bolo}/Q should allow for uncertainties in the actual power levels from the sky. The NEP as a function of temperature is

$$\text{NEP} = \xi [4\kappa_B T_0 Q]^{1/2}, \quad (4.3)$$

where, $\xi = [\gamma n (1 + P_{\text{bolo}}/Q) (T/T_0) (1 - T_0/T)^n]^{1/2}$, γ accounts for a temperature gradient in the thermal link to the heat bath temperature and T/T_0 is the ratio of working temperature to the bath temperature (Lee et al. 1996). A minimum NEP is found for $T/T_0 = 1.6$ in case of $n = 2$ (see Fig. 4.4). Thus, the optimum bolometer performance is achieved when the transition temperature T_c is ≈ 1.5 times the base temperature (T_0). The base temperature for the cryostat is 300 mK, so the transition temperature of 450 mK is optimum.

The ^3He stage has an internal Cryopump and a sealed ^3He charge forming a self contained refrigerator to be integrated in the ^4He apparatus. This technique is explained in detail by White (1979). The incoming radiation is coupled to the bolometer absorber via an aluminum horn antenna. Aluminum has a transition temperature of 1.4 K (Matsuo et al. 1973), hence it is in the superconducting stage when in operation which gives perfect magnetic shielding to the array.

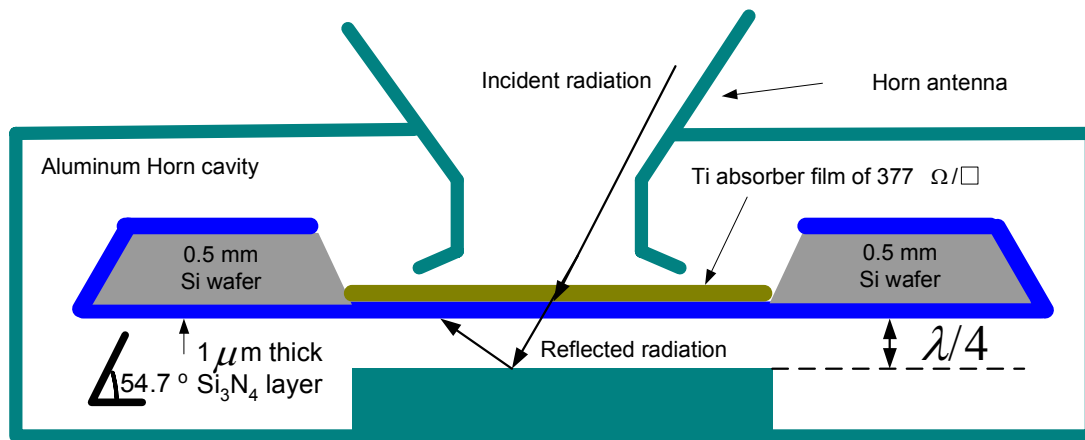


Figure 4.5: The schematic diagram of radiation pattern inside the aluminum horn cavity.

4.3.1 Aluminum horn cavity

Fig. 4.5 shows the schematic diagram of aluminum horn cavity. In a free standing metallic film of $377 \Omega/\square$, 50 % of the radiation gets absorbed, 25 % gets reflected and 25 % gets transmitted. The electromagnetic simulations done by Theoretische Elektrotechnik group, University of Wuppertal (Hansen & Wu 2006), show that 100 % of radiation can be coupled by the same film on a silicon nitride membrane if a reflector is placed at a distance of quarter wavelength. The membrane is placed at a distance of $\lambda/4 = 0.3 \text{ mm}$ from a reflector part of the aluminum cavity.

4.4 Filters

Bolometers are intrinsically wide band incoherent detectors, hence it is very important to have bandpass filters to restrict the response to selected wavelength ranges. The requirements for these filters are high passband transmission and high stopband rejection. Combinations of filters are installed at the different temperature stages. The monolithic multilayer mesh (MMM) (Gemünd et al. 1994) filter is mounted at the 1.5 K temperature stage. The band of interest is approached sequentially by the combination of several optical elements, starting from the lowest wavenumber. Each element is chosen in such a way that a mismatch or negative interference with other elements does not occur and the specific spectral property can be reached. The superposition of spectra of individual elements result in the desired bandpass filter spectrum. Free-standing meshes are made of the metal foils with a periodic pattern of specific apertures. The mesh or its spectrum defines the passband but its high wavenumber properties are poor for blocking because the mesh soon becomes transparent according to its visual transmittance, typically of the order of 10 %. Thus high wavenumber blocking in the neighboring passband is achieved by the MMM filter. The filter has a low-wavenumber passband characteristics and offers a stopband of $T < 10^{-2} \text{ cm}^{-1}$. The MMM filter is sandwiched between two borosilicate glass (Pyrex) plates. This filter has a cut at a wavenumber of $\sim 10 \text{ cm}^{-1}$ at room temperature. The fabrication details are explained in Gemünd et al. (1994). Fig. 4.6 shows a photograph of the filters for 1.5 K and 77 K stage.

The filter in the 77 K temperature stage is a c-cut crystal quartz multilayer interference filter. This crystal offers good blocking in for wavenumber $1500 \text{ cm}^{-1} < \nu < 6000 \text{ cm}^{-1}$ because of absorption. At 300 K there is a Teflon window followed by an inductive mesh as a radio frequency interference (RFI) filter.

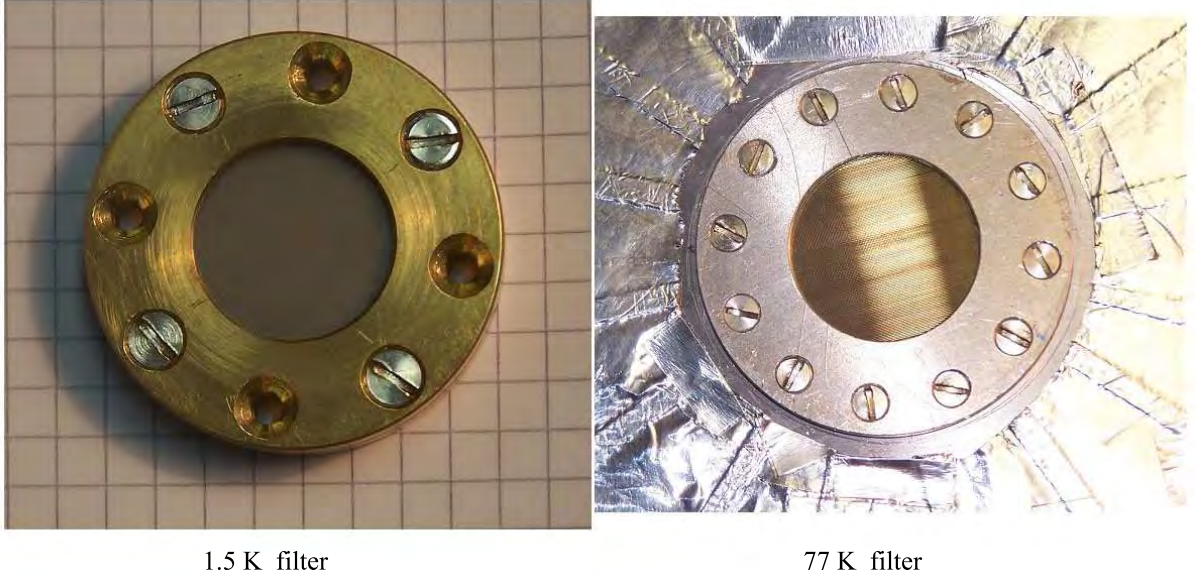


Figure 4.6: Photographs of 1.5 K stage filter and 77 K stage filter. Both filters have structured surfaces acting as a anti-reflection coating.

Table 4.1: Black coating composition for cavities

Ingredient	Mass composition
Stycast 2850 FT	68 %
Catalyst 9	5 %
Carbon Lampblack	7 %
150-250 μm Diameter Glass Beads	20 %

4.5 Black coating

The reflective metal parts inside the copper shield (Fig. 4.3) can cause interference by scattered radiation. In order to avoid such interference, the metallic parts are coated with *Black* coating. It is practically very difficult to produce a perfect shield, but in order to reduce the level of scattered radiation, a black coating is applied on the reflective surfaces like the top surface of aluminum horn antenna, ^4He shield, the top surface of the 1.5 K stage filter and small metallic parts. The ingredients to create the mixture of *Black* coating are shown in Table. 4.1 (Colin 2006). The filters are used to keep unwanted radiation from falling on the receiver but they are also essential to avoid high frequency noise. A small high frequency leak at ^4He or ^3He stage could cause a big noise power to saturate the bolometer. The blackbody has a steep spectrum in the submm regime, which means that the high frequency leakage can cause enormous input power which can heat up the whole array. Hence, the filters are chosen accordingly and superinsulation is applied around the 77 K shield.

4.6 SQUID electronics

A low temperature dc SQUID is designed as a current sensor with low input inductance (350 nH) which provides a very low current noise referred to the input of the SQUID. The SQUIDs made by the IPHT have following features:

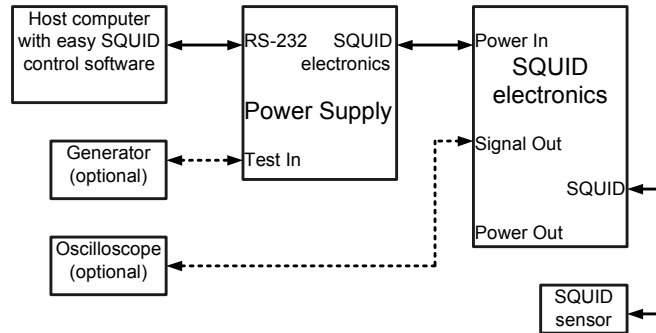


Figure 4.7: Block diagram of the SQUID system. The SQUID electronics is connected to the SQUID sensor. The power supply is connected to RS232 socket of the host computer with cable and to the SQUID electronics. The power supply should provide 220–110 V/50–60 Hz in AC socket or 10–18 V in DC socket.

Table 4.2: Parameters for current sensor SQUID at 4.2 K

SQUID parameters at 4.2 K (open input coil)	Value	Unit
SQUID critical current I_C	33	μ A
SQUID resistance R_N	1.74	Ω
Voltage swing ΔV	43	μ V
Input coil coupling $1/M_{INP}$	0.6	μ A/ ϕ_o
Feedback coil coupling $1/M_{fb}$	15.2	μ A/ ϕ_o
Equivalent flux noise	< 2.5	$\mu\phi_o/\sqrt{\text{Hz}}$

Resistance at room temperature	Value	Unit
Input coil	50.6	k Ω
SQUID	74	Ω
Feedback coil	1.9	k Ω
Heater	133	Ω

- Fabricated using all-refractory Nb/Al-AlO_x/Nb technology.
- Small chip size of 2.5 mm × 2.5 mm.
- Low input inductance of the SQUID of 350 nH.
- Input coil and feedback coil integrated on chip and inductively coupled to the SQUID.
- Low current noise of the SQUID (better than 2.5 pA/ $\sqrt{\text{Hz}}$).
- Integrated on chip heater to expel frozen flux.

Fig. 4.7 shows the block diagram of the SQUID system. The output of the SQUID amplifier is connected to the SQUID electronics. The easy *SQUID* software tool is used to access the SQUID hardware and to tune the SQUID amplifier (Supracon 2003). The functional diagram for the SQUID electronics is shown in Fig. 4.8. The FLL unit is directly coupled to a SQUID via three twisted copper (Cu) wires. The FLL electronics amplifies the SQUID voltage deviations, integrates it and in FLL mode couples the output current to the feedback coil through the feedback resistors $R_{\text{Feedback-1,2}}$, compensating the

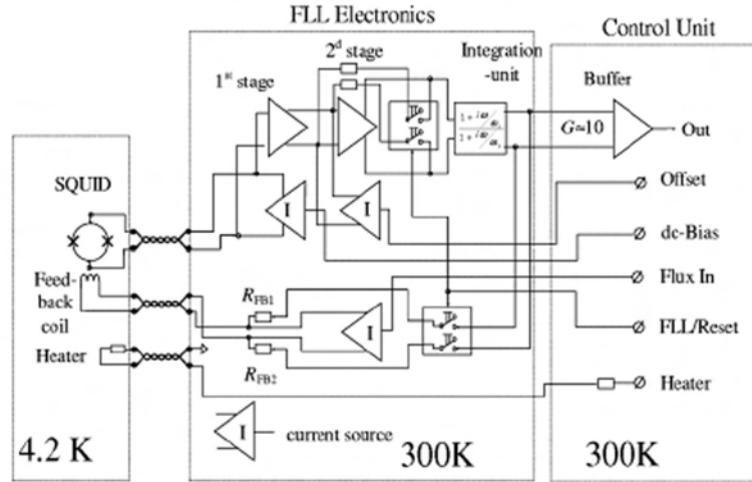


Figure 4.8: The functional block diagram of the read-out electronics with SQUID.

external flux change in the SQUID (Oukhanski et al. 2006). Thus the voltage at the output of the FLL unit is proportional to the magnetic flux in the SQUID. The FLL unit can be connected to a grounded as well as to a ground free SQUID sensor. For this reason all signal sources necessary for the SQUID operations are made as differential current sources. The current noise for each differential current source does not exceed $1.5 \text{ pA}/\sqrt{\text{Hz}}$.

The output from the SQUID is dc coupled to the SQUID read-out electronics. Such electronics have the advantages of high sensitivity due to high slew rate of the system, wide bandwidth and high dynamic range. Drung et al. (1990) has described the working principles of directly coupled read-out electronics in more detail. Low-drift directly coupled read-out electronics, capable to operate over a wide temperature range was developed by IPHT, Jena (Oukhanski et al. 2003). The thermal drift is lower than 30 nV/K in a temperature range from $15 \text{ }^\circ\text{C}$ up to $80 \text{ }^\circ\text{C}$. The electronics is tested with two low-transition temperature SQUID sensors. In the flux-locked-loop (FLL) mode, the SQUID readout electronics allows to work with a maximum small-signal bandwidth of about 6 MHz . It is necessary to ensure stable operation of the SQUID system at large distances between the SQUID sensor and the readout electronics. The electronics has an output white noise level of about $0.33 \text{ nV/Hz}^{-1/2}$ and $6.5 \text{ pA/Hz}^{1/2}$ with a corner frequency for the $1/f$ noise is as low as 0.1 Hz and 10 Hz , respectively.

4.7 Experimental setup

Fig. 4.9 shows the experimental setup. The horn array can be replaced by a metal plate to measure the load curve ($I - V$) at 0.3 K background. The $I - V$ curves are also measured at 77 K and 300 K background (Chapter 6). The noise is acquired by the National Instrument's peripheral component interconnect (PCI) 8-channel dynamic signal data acquisition card and the data is analyzed by the *timeseries* programs developed in *LabVIEW*. The signal is measured by a lock-in amplifier at different chopping frequencies in order to calculate the time constant (τ). The time constant curve is fitted to determine the τ . The signal is created from a blackbody (Electro Optical Inc. 1995) maintained at the temperature of 1273 K . A chopper wheel is installed in front of the blackbody radiation window to create an approximately sinusoidal signal for each frequency. According to VSB theory the time constant of the bolometer is very small (e.g. § 6.10; 6.11) so to characterize the time constant accurately, the frequency range of the signal should be high. Since the mechanical chopper has a maximum frequency of

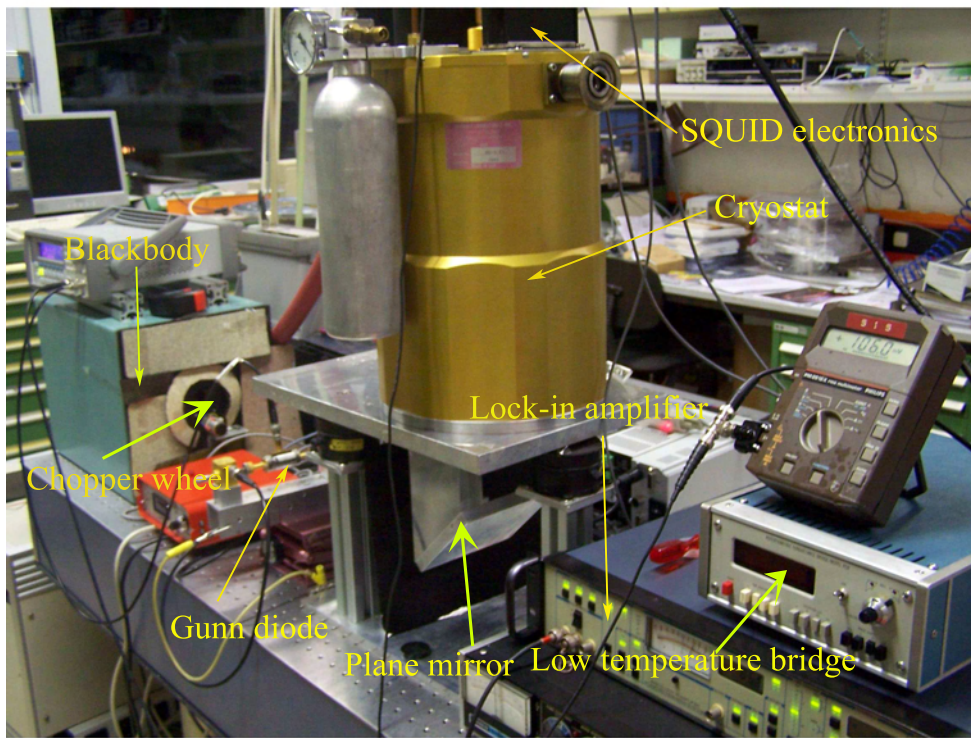
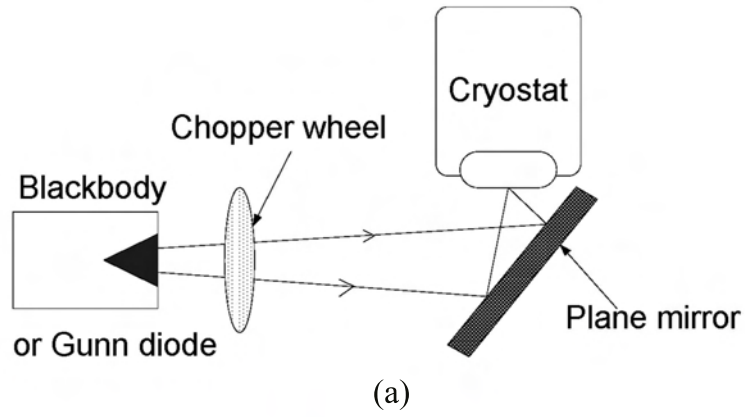


Figure 4.9: (a) Schematic diagram of the experimental setup. The signal comes from the blackbody or the Gunn diode. The cryostat is shown in Fig. 4.3 (b) Photograph of the experimental setup in the laboratory.

350 Hz, a high frequency signal is derived from a Gunn diode. The latter can be modulated electronically up to several KHz. The incoming radiation is reflected by a mirror installed at 45° to fall onto the bottom looking cryostat window and eventually onto the bolometer. The SQUID electronics is mounted on the top of cryostat. After phase sensitive detection, the amplitude and relative phase of the output signal is recorded. The time constant is derived by fitting the amplitude to time constant (τ) equation ($A_o[1 + \omega^2\tau^2]^{-1/2}$), where A_o is the dc amplitude of the signal in the experimental setup.

4.7.1 Temperature readout

A Germanium resistive temperature detector (RTD) sensor is used in the ^3He stage to measure the temperature below 1 K. Germanium RTDs are negative temperature coefficient sensors and have highest accuracy, reproducibility, and sensitivity from 0.05 K to 30 K. They are resistant to ionizing radiation, but are not recommended for use in magnetic fields.

The 4-wire temperature sensor is read via a bridge circuit which returns conductance values. The resistance and the corresponding temperature are taken from the calibration data. The current value measured at the each bolometer channel is converted into resistance in order to define the $R - T$ characteristics for each bolometer, $R_{bolometer} = V_{bolometer}/I_{bolometer}$.

4.7.2 Martin-Puplett Interferometer

A Martin-Puplett interferometer (Martin & Puplett 1969) is a version of the Michelson interferometer which uses a wire grid polarizer as a beam splitter and roof mirrors for reflectors. The beam splitter has high efficiency from below 2 to above 100 cm^{-1} . Such a spectrometer contains two roof mirrors located at right angle to each other and oriented perpendicular to each other. A beamsplitter is placed at the vertex of the right angle and oriented at a 45° angle relative to two mirrors. The radiation is incident on the beam splitter and then divided into two parts, each of which propagates down one of the two arms and is reflected off one of the mirrors. The two beams are then combined and transmitted out of the other port because the plane of polarization has been turned by 90° by the roof mirrors. When the position of one mirror is continuously varied along the axis of the corresponding arm, an interferogram is observed.

The Martin-Puplett interferometer (MPI) is used to measure the optical response of the system (Gromke 1996). Two radiation sources are maintained at 77 K and 300 K. The difference between the 77 K and 300 K blackbody radiation provides the signal to the bolometer. The rotating wire mesh grid is placed in between the 77 K and 300 K source to modulate the polarization of the incoming radiation to bolometer. Fig. 4.10 shows the block diagram of the interferometer used to measure the spectral response.

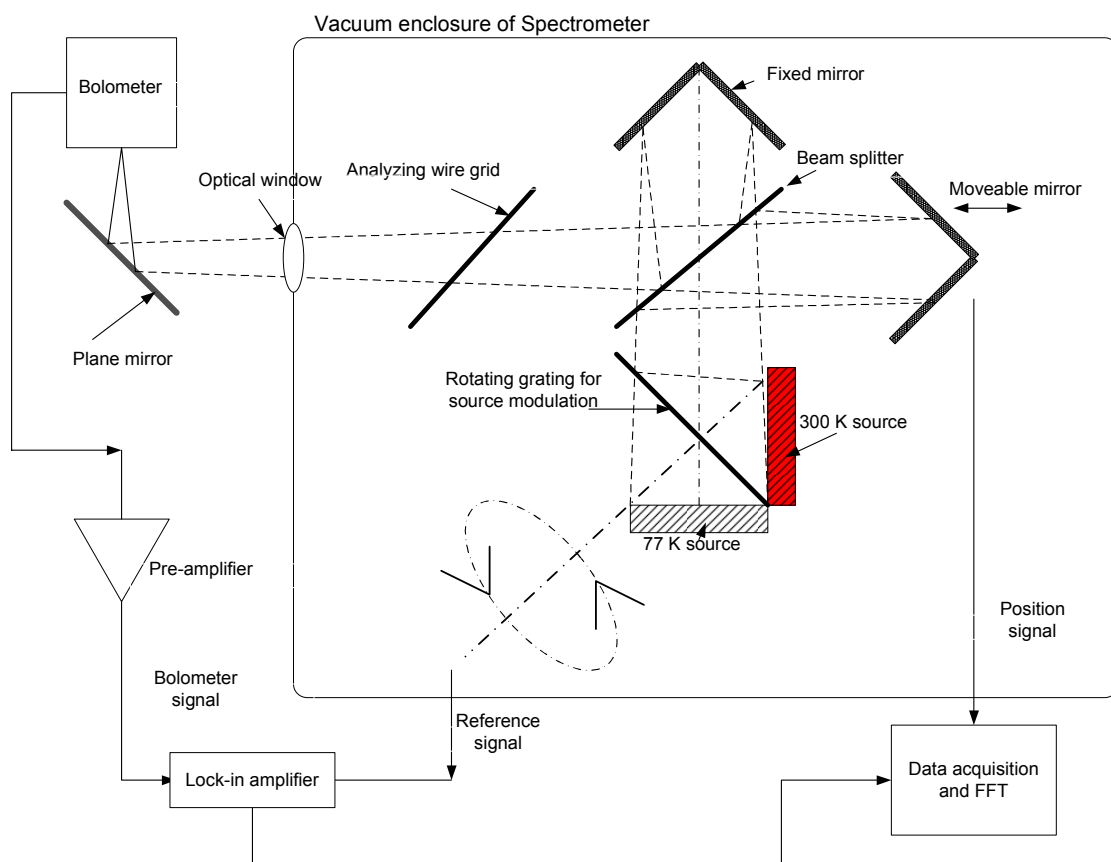


Figure 4.10: Block diagram of Martin-Puplett interferometer.

Chapter 5

Modeling of the Bolometer

5.1 Introduction

Eq. 2.39 gives the responsivity of a TES which is independent of power loading so the detector is linear and the bias power P_b stays constant. The responsivity is inversely proportional to the loop gain (L) and L is dependent on value of G . Hence, in order to calculate the current responsivity, the thermal conductance should be known. Fig. 5.1 shows the $I - V$ curve of a TES (see Chapter 6 for experimental results in detail.).

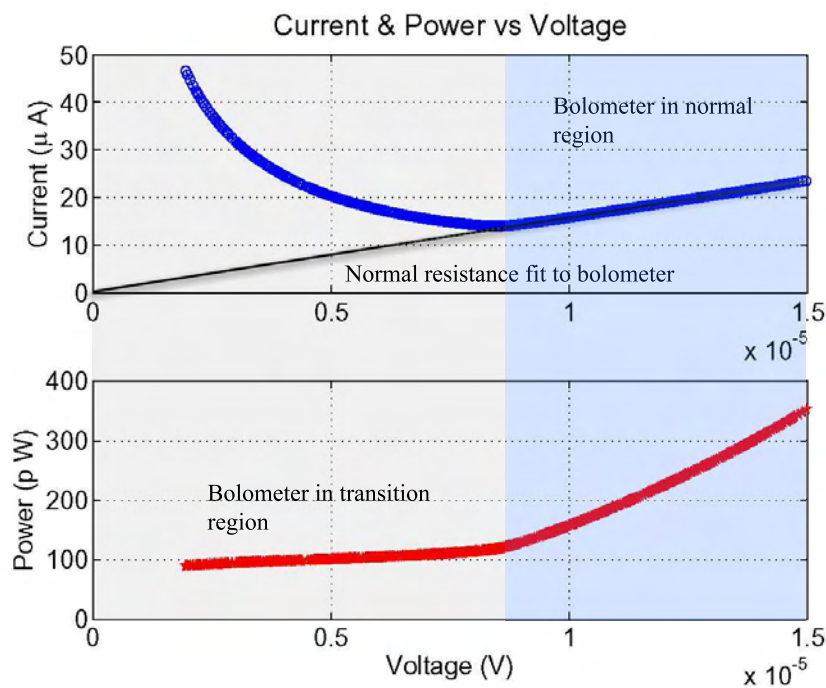


Figure 5.1: The data from one of the experiments (see Chapter 6 for more details). The top panel shows the $I - V$ measurements. The bottom panel shows the power plotted against the bolometer voltage. When the bias voltage is applied the resistance changes so in the transition region $I \propto 1/V_b$, P_b is constant and in the normal state the bolometer acts like a ohmic resistor.

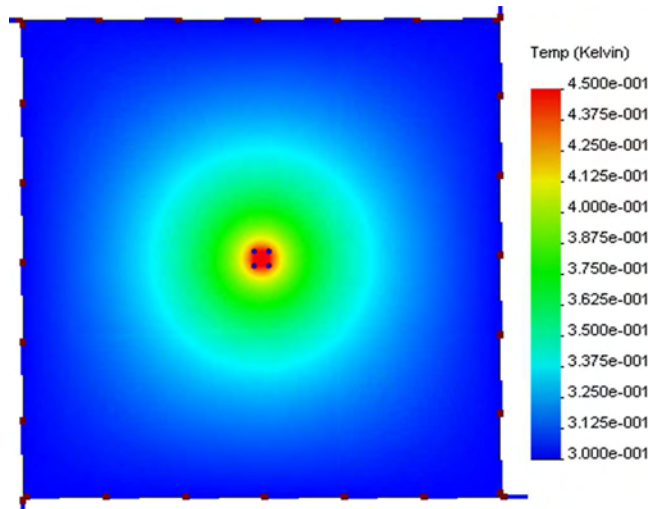


Figure 5.2: Steady state distribution from finite element analysis for the High-G design. The thermistor is placed in the middle and maintained at transition temperature. The edge of the low stress silicon nitride membrane is maintained at 300 mK. The temperature distribution can be read off the scale on the right hand side.

5.2 Thermal modeling of the bolometer

The COSMOS finite element analysis (FEA) package was used to perform the thermal modeling of the TES and determine its thermal conductance.

5.2.1 Finite element analysis

FEA uses a computer model of a physical structure to analyze the behavior of that structure under load or stress. In FEA, the material and the stress parameters are assigned to a grid over the surface (the mesh) defining how the structure will behave under certain loading conditions. FEA can be used for mechanical, thermal, and electromagnetic modeling under boundary conditions set by the user.

In our case of thermal modeling of bolometers, the thermal conductivity of the material is defined over the temperature range 0.1 – 1 K.

The FEA is divided into three steps:

- Pre-processing \Rightarrow During pre-processing material properties required by the thermal analysis and the specified material model are defined. A material model describes the behavior of the material with changing values of its physical parameters. The material properties are obtained from the COSMOS materials library or user-defined material libraries. The thermal conductivity (κ) of silicon nitride is assumed equivalent to the ‘C₁’ geometry determined experimentally Holmes et al. (1999). Fig. 3.1 shows a schematic diagram for the High-G configuration. The silicon nitride membrane has dimensions of 3.3×3.3 mm and a thickness of around $1 \mu\text{m}$. The silicon nitride membrane is thermally connected to the silicon wafer at 0.3 K so in FEA the membrane temperature at the edge is 0.3 K. The expected transition temperature of the Au-Pd/Mo thermistor is 0.45 K. The temperature is changed from 0.1 – 1 K in steps of 0.1 K and the corresponding values of thermal conductivity (Holmes et al. 1999) are used to obtain the thermal conductance in that temperature range.
- Meshing \Rightarrow The process starts with the creation of a geometric model. Then, the program subdivides the model into small pieces of simple shapes called elements connected at common points called

nodes. This is called meshing. FEA programs look at the model as a network of interconnected elements. It is possible to create a mixed mesh of solid and shell elements. The solid mesh is appropriate for bulky or complex 3D models while shell elements are suitable for thin parts. The mesh parameters are element size (e) for the specified entities, element growth ratio (r) and number of layers of elements (n). Assuming a certain e for meshing then the average element size in layers radiating from the entity will be: $e, e \times r, e \times r^2, e \times r^3, \dots, e \times r^n$. The mesh radiates from vertices to edges, from edges to faces, from faces to components, and from a component to connected components. Since the membrane thickness is $1 \mu\text{m}$, parabolic triangular shell elements are used for shell meshing. A parabolic triangular element is defined by three corner nodes, three mid-side nodes, and three parabolic edges. This meshing allows selecting the faces to be meshed and allows assigning the desired thicknesses of materials. It is possible to repeat this process as many times as desired. The adjacent shells are bonded automatically and the mid-surface of a generated shell element coincides with the associated face or surface. It is possible to define the parameters. A parameter is defined by name, type, unit, and a value or expression.

- Post-processing \Rightarrow Post-processing involves understanding the results after running the analysis. The COSMOS thermal analysis gives estimates of the nodal temperature, temperature gradient in the X-, Y- and Z-directions of the selected reference geometry. The resultant heat flux vectors are in units of W/K. In order to obtain the thermal conductance, the resultant heat flux is multiplied by the length of the membrane and divided by its cross-sectional area. The unit for the thermal conductance is W/mK. The temperature gradient of the membrane obtained from simulations is shown in Fig. 5.2 (b).

5.3 Model of voltage–current characteristics

Eq. 2.34 gives the power flow model for VSB. Using steady state energy balance equation for the bolometer,

$$W = G_s(T - T_o). \quad (5.1)$$

Assuming that the variation of the thermal conductance with temperature can be expressed as a power law, $G_s(T, T_o) = G_{so}(T/T_o)$, where G_{so} is the thermal conductance at the temperature $T = T_o$. The temperature variation of the thermal conductivity of the thermal link, (κ), is expressed as a power law (Mather 1982).

$$\kappa(T) = \kappa_0 \left(\frac{T}{T_o} \right)^\beta, \quad (5.2)$$

where $\kappa_0 = \kappa(T_o)$. Taking the variation of thermal conductivity with temperature across the thermal link into account

$$W = \frac{\int_{T_o}^T \kappa(t) dt}{\int_0^L \frac{1}{A(x) dx}}, \quad (5.3)$$

where $A(x)$ is the cross-sectional area of the thermal link at position x but without loss of generality, the cross section is assumed to be the constant. Hence, $A(x) = A$. Integration of Eq. 5.3 yields

$$W = \frac{A}{L} \frac{\kappa_0 T_o}{(\beta + 1)} (\phi^{\beta+1} - 1), \quad (5.4)$$

where $\phi = T/T_o$. Hence from the Eqns. 5.1 and 5.4

$$G_s(\phi) = \frac{A}{L} \frac{\kappa_0}{(\beta+1)} \frac{(\phi^{\beta+1} - 1)}{\phi - 1} = \frac{G_{s_0}}{(\beta+1)} \left(\frac{\phi^{\beta+1} - 1}{\phi - 1} \right), \quad (5.5)$$

where $G_{s_0} = \kappa(A/L)$. A is the cross sectional area of the thermal link at position x , which is assumed to be constant. This leads to following equation

$$P(\phi) = \frac{G_{s_0} T_0}{\beta+1} (\phi^{\beta+1} - 1) - Q = G_s T_0 (\phi - 1) - Q, \quad (5.6)$$

where Q is the incident power, β is a constant, which is 1 for a metallic thermal link and 3 for a crystalline dielectric link (Pobell 1992). β is 1, in our case. The curves with zero background are calculated ($Q = 0$). Eqns. 5.7 and 5.8 allow modeling the $I - V$ characteristics of a bolometer if the variation of resistance (R) as a function of the thermistor temperature, $R - T$ is known. The experimental values of resistance and temperature are obtained at 0 K background, when the bolometer voltage is $1.5 \mu\text{V}$. During the experiments, there is no radiation falling on the membrane and the bias voltage is low so it is assumed that the $R - T$ measurements are not affected by the strong negative electrothermal feedback. The $I - V$ characteristics of an ideal bolometer can be generated by incrementing T from T_0 to T_{max} .

$$V = [PR(T)]^{1/2}. \quad (5.7)$$

$$I = [P/R(T)]^{1/2}. \quad (5.8)$$

In Eq. 5.6, the value of G_s is obtained from thermal analysis using FEA (§ 5.2) and the $I - V$ behavior can be estimated from Eq. 5.7 and Eq. 5.8. The relation between resistance and temperature is obtained from the $R - T$ measurements for each experiments. Using this method, the various geometries of bolometer can be modeled.

Chapter 6

Experimental results and modeling

In this chapter, the experimental results for different bolometer geometries are presented. Only results which are considered to be important and contributing to the understanding of TESs are shown. The detailed models of High-G, Medium-G and Low-G layouts are selected.

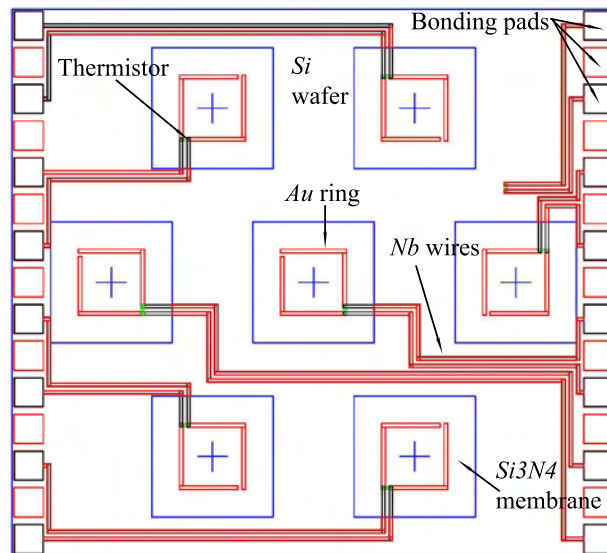


Figure 6.1: The seven element array from the initial design. The low stress silicon nitride membrane is deposited on a silicon wafer of dimension $16.3 \text{ mm} \times 16.3 \text{ mm}$. A single silicon nitride membrane is $3.3 \text{ mm} \times 3.3 \text{ mm}$ in dimension. The Au ring creates the thermalized patch of $1.6 \text{ mm} \times 1.6 \text{ mm}$ around the center of the silicon nitride membrane. The thermistor of size $260 \mu\text{m} \times 70 \mu\text{m}$ is placed on the Au ring. The width of the Au ring is $100 \mu\text{m}$ and the thickness is 150 nm .

Table 6.1: Time constant (τ) measurements at different bias voltages for 4SN 1459 array with 33 m Ω and 10 m Ω shunt resistor

33 m Ω shunt resistor			
Voltage	6.02 μ V	31.1 μ V	56.6 μ V
CH5- τ	5.90 ms	2.64 ms	2.52 ms
10 m Ω shunt resistor			
Voltage	2.18 μ V	5.98 μ V	
CH1- τ	5.7 ms	2.97 ms	
Voltage	3.04 μ V	6.04 μ V	
CH5- τ	3.53 ms	2.81 ms	
Voltage	2.18 μ V		
CH6- τ	3.84 ms		

6.1 Initial design

The development effort started by importing the semiconducting bolometer design. The development of semiconducting bolometers at the MPIfR is explained by Kreysa et al. (1998, 2002). Fig. 3.1 shows the photograph of single bolometer. The CAD drawing for the initial design is shown in Fig. 6.1. The silicon nitride membrane is not structured hence the gold ring is used to define the constant thermalized area. A homogeneous titanium (Ti) layer is applied on the back acting as a radiation absorber. The Au-Pd/Mo thermistor is placed on the gold ring. The thermistor is connected via niobium (Nb) wires. The behavior of the gold ring on the silicon nitride membrane is modeled using finite element software (§ 5.2). The seven channels connected to the bolometer are referred as CH1, CH2, ..., CH7.

6.1.1 4SN 1459

The fabrication of this bolometer array is similar to the standard fabrication; the only difference is the normal state resistance of the thermistor, which is 5.8 Ω . The geometrical structure is identical to the initial layout and the measured voltage-current ($I - V$) and resistance-temperature ($R - T$) curves are smooth. This experiment was repeated with different shunt resistances and with/without background. The series resistor of 1045 Ω is used and the applied bias voltage is in the range 1 and 6 V.

33 m Ω – shunt resistor

In the beginning, a 33 m Ω shunt resistor was used. The results from CH2, CH5, CH6 and CH7 are shown in Fig. 6.2 (a) and (b). The signal to noise ratio (SNR) and τ values for CH5 are measured at different bias voltages. The measured SNR varies from 1200 to 1500 and the τ varies from 2 to 6 ms, depending on the applied bias voltage (Table 6.1). When the bolometers are in the transition region near to the superconducting range, they are more sensitive to radiation. Such behavior is modeled for High-G model (§ 6.8). The measurements are performed on CH6, the results are shown in Table 6.1.

In the experiment with closed input, the $R - T$ values are measured at different bias voltage. It was found that the transition width increases with increase in the bias voltage. The applied bias voltage should be as small as possible to determine the correct $R - T$ characteristics e.g. in the experiments, 1 mV to 3 mV of bias voltage was used which corresponds to ~ 15 nV of voltage across the bolometer. At such a low voltages the negative ETF do not influence the thermistor, hence the intrinsic $R - T$ transition can be measured.

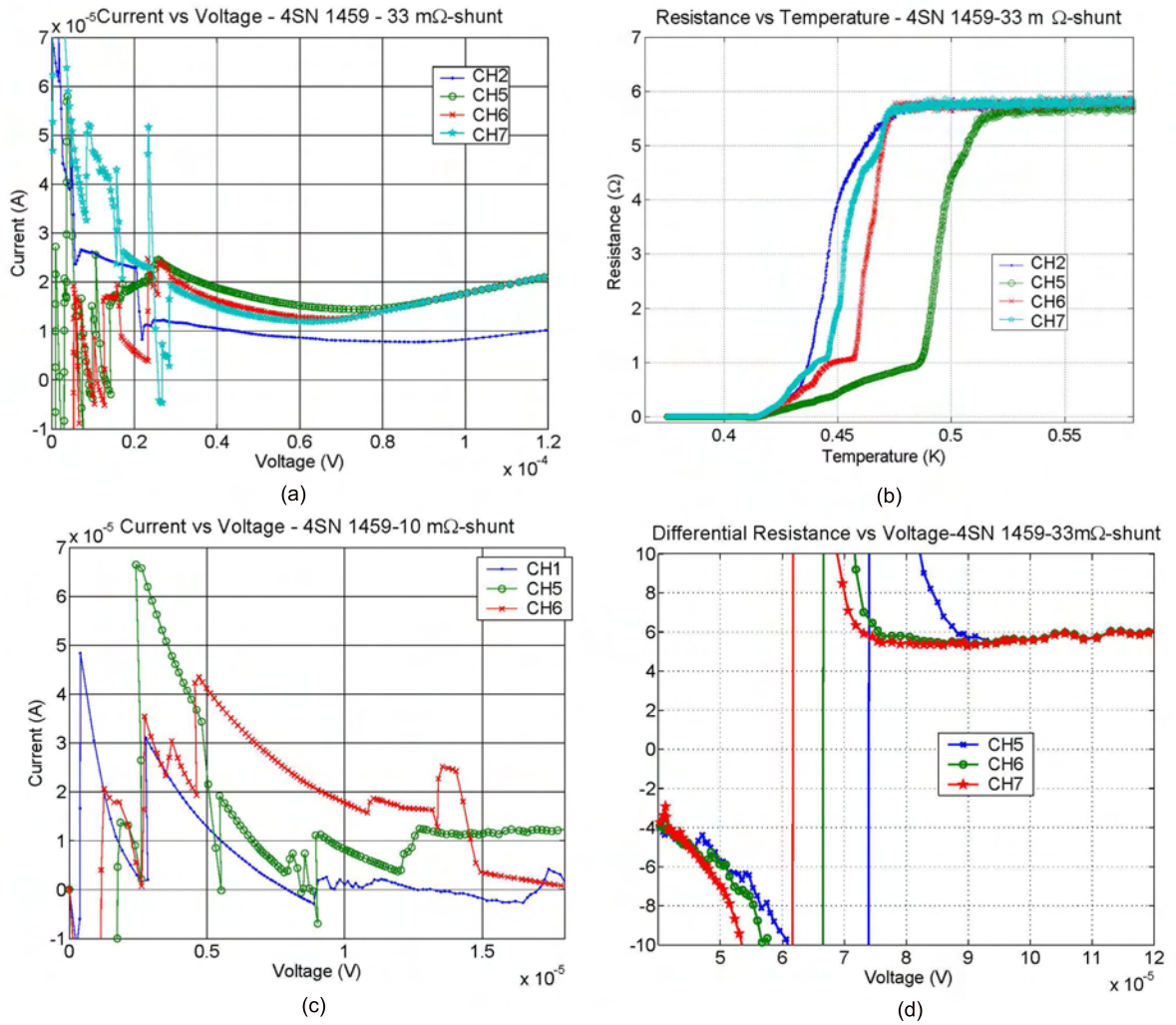


Figure 6.2: (a) $I - V$ curve with 33 mΩ shunt resistor. (b) $R - T$ curve with 33 mΩ shunt resistor. (c) $I - V$ curves from the experiment with 10 mΩ shunt resistor. The $R - T$ curves are similar to those obtained from experiment with 33 mΩ shunt resistor. (d) Differential resistance plotted as a function of bolometer voltage for an experiment with 3 mΩ of shunt resistor. The measurements are performed at 300 K background. Comparison of subplots (a) and (c) reveals that the operating range increases with the decrease in shunt resistor value.

The standard sets of measurements, like $I - V$ and $R - T$ are performed with different background temperatures. There are still jumps in the $I - V$ and $R - T$ curve. The Au-Pd/Mo thermistor is mounted on the gold ring. It was suspected that the thermistor connection to the gold ring may introduce the jumps in the $I - V$ or $R - T$ measurements. The new array was fabricated without Au ring and the experiments are performed to understand the thermistor behavior (§ 6.5).

- *Hysteresis effect*: During the measurement of the $I - V$ curve, a hysteresis effect was observed. When high bias voltage is applied, the current exceeds the critical value so the thermistor goes into the normal range and by reducing the bias voltage the transition range is achieved. Hence all the $I - V$ measurements are performed in reverse direction, i.e., first applying the high bias voltage which overcomes the hysteresis effect and then reducing the bias voltage, which moves the thermistor from normal to superconducting state.

10 m Ω – shunt resistor

The change in the shunt resistor resistance affects the transition width and the steepness of the transition curves. Comparison of Figs. 6.2 (a) and (c) shows that the operating range increases with a decrease in the shunt resistor resistance. During this experimental run, $I - V$ and $R - T$ measurements could only be measured for CH1, CH5 and CH6. The SNR is in the range 1200 and 1500 and τ is in the range 3 and 6 ms.

The measured values of the time constant for CH1, CH5 and CH6 are shown in Table 6.1. It was tried to correlate the measured $R - T$ values with the applied bias voltage, unprocessed current and conductance data. When the bolometers are in the superconducting or the transition state near to the superconducting level, the current flows through the bolometer rather than the low value shunt resistor. In the near-superconducting transition region the current passing through the bolometer and the shunt resistor is not known since it depends on the particular resistance value at that point. Hence, it is difficult to correlate the applied bias voltage and $R - T$ characteristics. The (c) and (d) panels of Fig. 6.2 show the $I - V$ and $R - T$ curve. As explained above, in the transition region, the current flowing through the bolometer is not known so the resistance value have to be fixed to a predefined value to obtained the $R - T$ curves. The normal state resistance value of each bolometer is obtained from the differential resistance in $I - V$ measurements (Fig. 6.2 (d)). The normal state resistance value is fixed to 5.8 Ω .

In Fig. 6.4, the signal and the noise are plotted together. It is seen that both the, noise and the signal decreases with increasing the frequency. The average SNR is from 1000 to 1500 and the estimated optical NEP is $5.1 \times 10^{-16} \text{ W}/\sqrt{\text{Hz}}$.

During the experiments, a run away heating effect was observed. This is the increase in temperature of the bolometer assembly due to a high bias voltage applied across the bolometer. This effect was predominantly seen at lower shunt resistor resistances. The bias current applied to the bolometer flows through thin superconducting wires. These are niobium-titanium wires which become superconducting below 10.8 K and have very high resistance at room temperature (Goldsmid 1966). If there is any weak spot in the wire, the high bias voltage increases the heat dissipation, so the temperature increases and it goes into the normal state. In normal state, the heat dissipation in the wire is high, hence more wire segments get heated which increases the heating effect. To solve the problem of run away heating, the bolometers were rewired and the connections are rechecked but the effect was observed in all the experiments with low resistance shunt resistors. As shown in Fig. 6.3, the two parts of wire carrying the total bias current are replaced with thick tinned copper wires. The run away heating effect was not observed any more after replacement with the tinned copper wires.

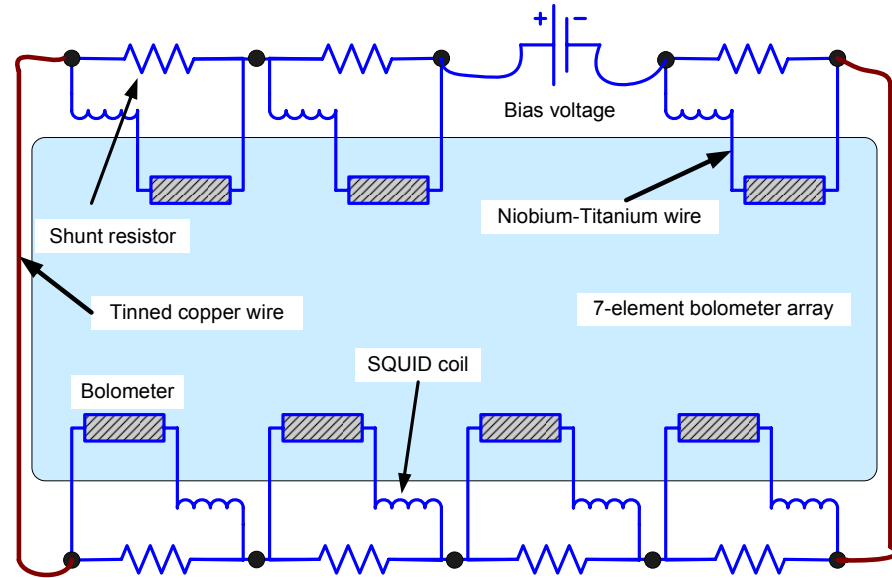


Figure 6.3: Electrical circuit diagram for the seven element bolometer array. The two patches of Niobium-Titanium wires carry the total bias current hence to avoid the *run away* heating effect, they were replaced by Tinned copper wires. Figure is not to scale.

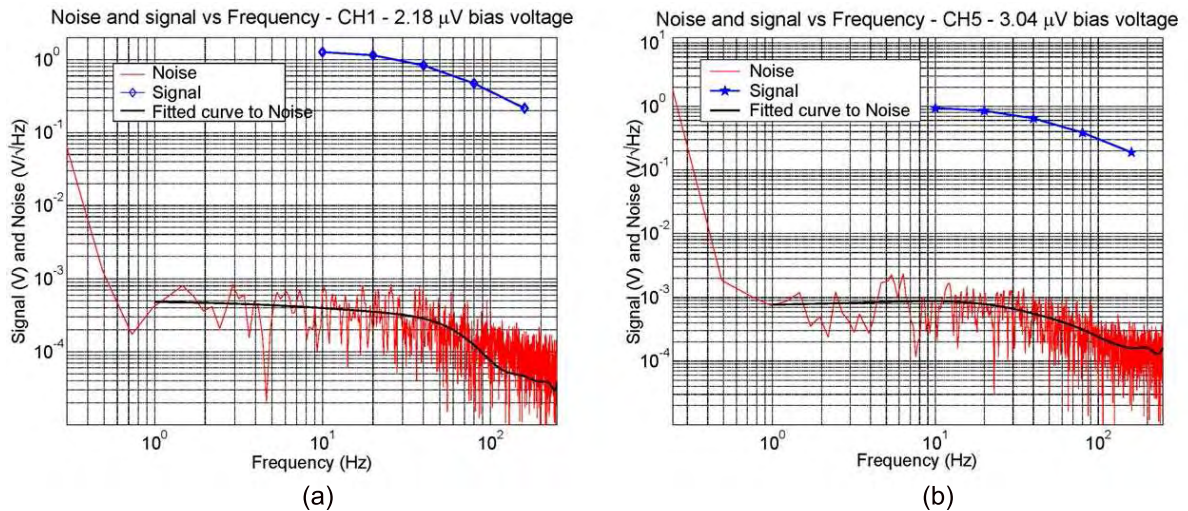


Figure 6.4: (a) Signal and noise measurements of 4SN 1459 with 33 mΩ of shunt resistor. (b) Signal and noise measurements with a 10 mΩ shunt resistor. The measurements are performed for CH1 and CH5. A curve is fitted to the noise using an 88 Hz low pass filter function. An 88 Hz low-pass filter is installed in the data acquisition electronics to avoid anti-aliasing. The noise spectra are not integrated for long enough for frequencies below 0.3 Hz

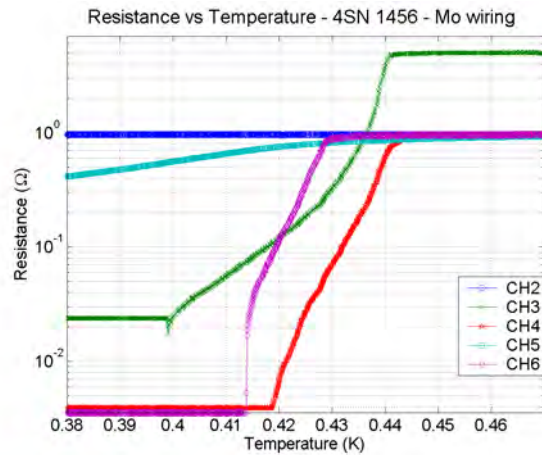


Figure 6.5: $R - T$ measurements of 4SN 1546 array with molybdenum wiring. The transition temperature of the molybdenum is too low to have stable operating conditions, hence the $I - V$ curves were not measured. The measurements are performed at 300 K background.

6.2 4SN 1546

In the experiments with the initial layout there were always some jumps detected in the $I - V$ and $R - T$ curves. The thermistor contact to the gold ring may produce the jumps as might the use niobium used for wiring. In order to test these ideas, in this fabrication run, bolometers with molybdenum and aluminum wires were manufactured.

6.2.1 Molybdenum wiring scheme

The thermistor is a bilayer of Au-Pd/Mo. Molybdenum serves as a base layer. The transition temperatures for niobium and molybdenum are 9 K and 0.6 K, respectively. It is easy to do the wiring with molybdenum which then creates a homogeneous connection. Fig. 6.5 shows the $R - T$ measurement of the array. The transition temperature for molybdenum is too low for stable operation. The high bias voltage applied across the bolometer can be sufficient to break the superconducting state of molybdenum hence no stable $I - V$ curves were measured. The $R - T$ curves were not smooth and jumps were observed during the measurements, hence it was decided against the molybdenum wiring scheme.

6.2.2 Aluminum wiring scheme

Fig. 6.6 shows the experimentally determined $I - V$ and $R - T$ curves. Some channels did not show any output, and jumps were observed in the $I - V$ measurements. The $R - T$ transitions were also not smooth and overall the results were not satisfactory. Hence, it was decided to fabricate all the future bolometers with the niobium wires.

6.3 4SN 1568—Inverted layout and silicon oxide coating

In the manufacturing process, the thermistor is first deposited on the clean wafer and the further processes are performed subsequently, i.e. niobium wiring, adding SQUID and SQUID electronics. Thermistors are very fragile so they have to be protected while these further processes are performed. In the inverted layout all the processes were done initially and then the thermistor layer was deposited on the wafer as

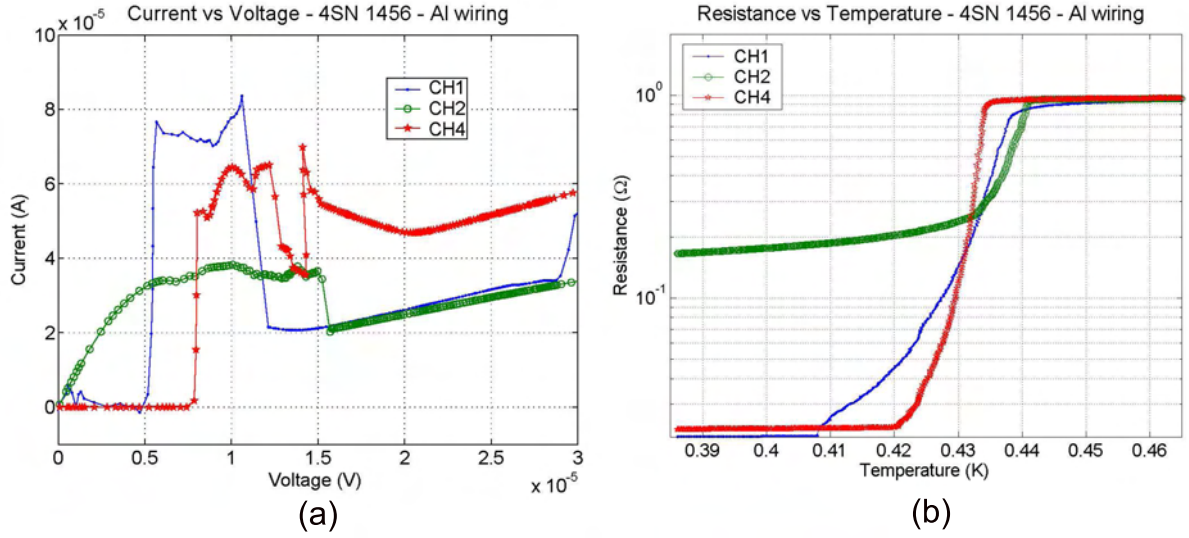


Figure 6.6: $I - V$ and $R - T$ measurements of 4SN 1456 array with Al wiring. The measurements are performed at 300 K background.

a last step. In this experiment, it was not possible to measure any $I - V$ or $R - T$ curves. Hence the conclusion is, the thermistor has to be deposited directly on the silicon nitride first.

Another way to protect the thermistor layer is by depositing the silicon oxide (SiO) on top of the thermistor. This is also explained in § 3.2. But, the SiO coating caused a very broad transition along with occasional jumps within the transition. In addition, since niobium wires are thicker than the Au-Pd/Mo thermistor, the results were often irreproducible; some pixels were not working, some showed high resistances or broadened transitions and some were disconnected completely. Another possible solution is to start with the bilayer in the first place, and coat it during all subsequent fabrication steps with a helping resist mask, which will be removed in the end. That way the properties of the bilayer will be unchanged.

6.4 Basic layout

With the initial bolometer design, different experiments were performed by changing the bolometer properties, e.g., normal state resistance and fabrication process, but with unsatisfactory results. In $I - V$ and $R - T$ measurements some jumps were observed, and in the $I - V$ measurements the transition region was not smooth. The thermistors were connected to the gold ring for all the bolometers with the initial design. It was suspected that the transition from Au-Pd/Mo thermistor to the gold ring could introduce jumps in the measurements. Hence, to understand the thermistor properties, it was decided to mount thermistors with different geometrical and physical properties on the bare silicon nitride membrane and the silicon wafer. An array is fabricated with seven different thermistors, mounted on the silicon nitride (Si_3N_4) membrane and on the silicon (Si) wafer, without any absorber layer. Fig. 6.7 shows the CAD layout of the array.

The thermistors are as follows:

- CH1 / CH8 \Rightarrow Square $20 \mu\text{m} \times 20 \mu\text{m}$ – on Si_3N_4 membrane / Si wafer.
- CH2 / CH9 \Rightarrow Square $20 \mu\text{m} \times 20 \mu\text{m}$ – 1Ω resistance, with gold strips in series between wiring and thermometer – on Si_3N_4 membrane / Si wafer.

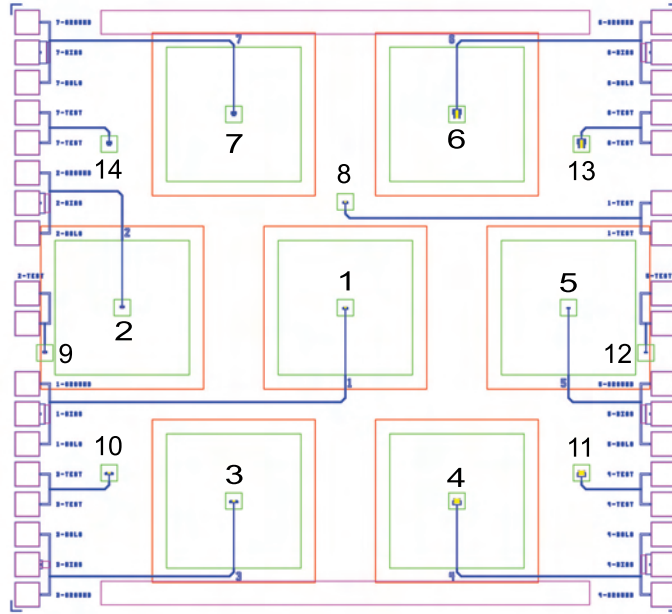


Figure 6.7: The test array in basic layout. Seven different thermistors are placed on the silicon nitride membrane and on the silicon wafer to understand the behavior of the Au-Pd/Mo thermistor. The thermistors are connected with niobium wires. The thermistor geometries and properties are explained in § 6.4.

- CH3 / CH10 \Rightarrow Strip $20 \mu\text{m} \times 100 \mu\text{m}$ – 5Ω resistance – on Si_3N_4 membrane / Si wafer.
- CH4 / CH11 \Rightarrow Square $100 \mu\text{m} \times 100 \mu\text{m}$ – on Si_3N_4 membrane / Si wafer.
- CH5 / CH12 \Rightarrow Square $4 \mu\text{m} \times 4 \mu\text{m}$ – on Si_3N_4 membrane / Si wafer.
- CH6 / CH13 \Rightarrow 5 paralleled Strips $20 \mu\text{m} \times 100 \mu\text{m}$ – on Si_3N_4 membrane / Si wafer.
- CH7 / CH14 \Rightarrow Rectangle $60 \mu\text{m} \times 20 \mu\text{m}$ with gold banks on the sides – on Si_3N_4 membrane / Si wafer.

6.5 K0078-5.2 bolometer array – Experiment and Model

The seven channels connected are CH1, CH2, CH4, CH5, CH9, CH11 and CH12.

As shown in Fig. 6.8 (b), the $R - T$ curves for all the thermistors are measured but the $I - V$ curves are measured only for the thermistors mounted on the silicon nitride membrane. This was an experiment with a $33 \text{ m}\Omega$ shunt resistor without radiation, i.e., with 0.3 K background. Given that there is no background radiation, the intrinsic $R - T$ transition of the bolometer can be measured. Also, in the *Basic layout*, there is no provision of radiation coupling, hence an experiment at 300 K background would not reveal additional information.

Analysis of loadcurve

- CH1 \Rightarrow is the central pixel of the 7-element array with $20 \mu\text{m}$ square thermistor. This channel showed a smooth transition curve.

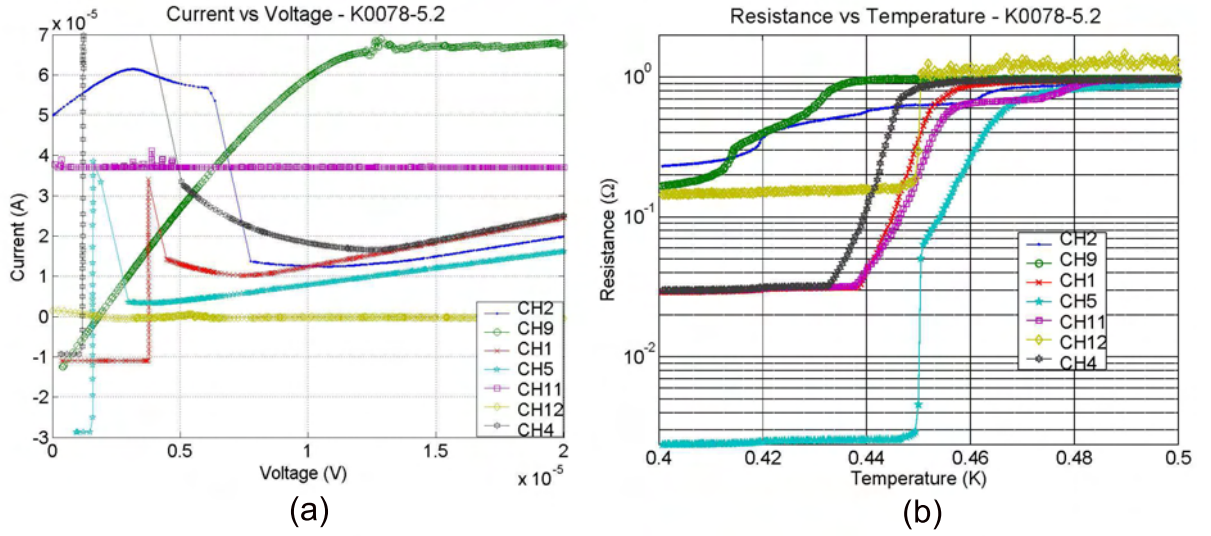


Figure 6.8: $I - V$ and $R - T$ measurement of the K0078-5.2 array. The normal state resistance is 1Ω . The $I - V$ and $R - T$ plots are shown in (a) and (b) respectively. Measurements are performed at 0.3 K background.

- CH2 \Rightarrow is a $20 \mu\text{m}$ square thermistor with gold strips. In the $R - T$ measurements, an extra series resistance of $100 \text{ m}\Omega$ was measured, which is due to the gold strips on the thermistors.
- CH3 \Rightarrow is a $20 \mu\text{m} \times 100 \mu\text{m}$ size thermistor with normal state resistance on 5Ω . Since the normal state resistance is higher, the slope of the $I - V$ curve is different for this channel (Fig. 6.12 (a)).
- CH4 \Rightarrow is the biggest thermistor of $100 \mu\text{m}$ square. This showed smooth $I - V$ and $R - T$ curves. It is observed that the operating region is wider than that of the thermistor of different geometries. The transition curve is steeper near to superconducting range so the τ of the bolometer should be small.
- CH5 \Rightarrow is a $4 \mu\text{m}$ square thermistor. Since the thermistor is small, it is not thermally well connected to the silicon nitride membrane. Thus, small bias voltage is sufficient for the transition from a superconducting to a normal state. This was observed during $I - V$ measurements so the transition region is smaller compared to different thermistor geometries.
- CH6 \Rightarrow has parallel strips of $20 \mu\text{m} \times 100 \mu\text{m}$ in order to create the total area of $100 \mu\text{m} \times 100 \mu\text{m}$. In the integrated fabrication of TES and SQUID, it is important to protect the thermistor before further processing. A striped thermistor would provide better adhesion for a SiO or SiO₂ layer. The $I - V$ and $R - T$ curves are as shown in Fig. 6.12.
- CH7 \Rightarrow is the $60 \mu\text{m} \times 20 \mu\text{m}$ size thermistor with gold banks on the side. The $I - V$ curve for this channel was not measurable because of fabrication defects.
- The thermistors mounted on the silicon wafer did not show any $I - V$ curve. These thermistors are thermally well connected to the silicon wafer and the applied bias voltage is not sufficient enough to drive them out of the superconducting state. During the $R - T$ measurements, the whole array is heated using an external bias voltage, hence it is possible to measure $R - T$ for thermistors placed on the silicon wafer.

Several experiments are performed with the same array in order to characterize the thermistors of other geometry. Only thermistors on the silicon nitride membranes showed both $I - V$ and $R - T$ curves.

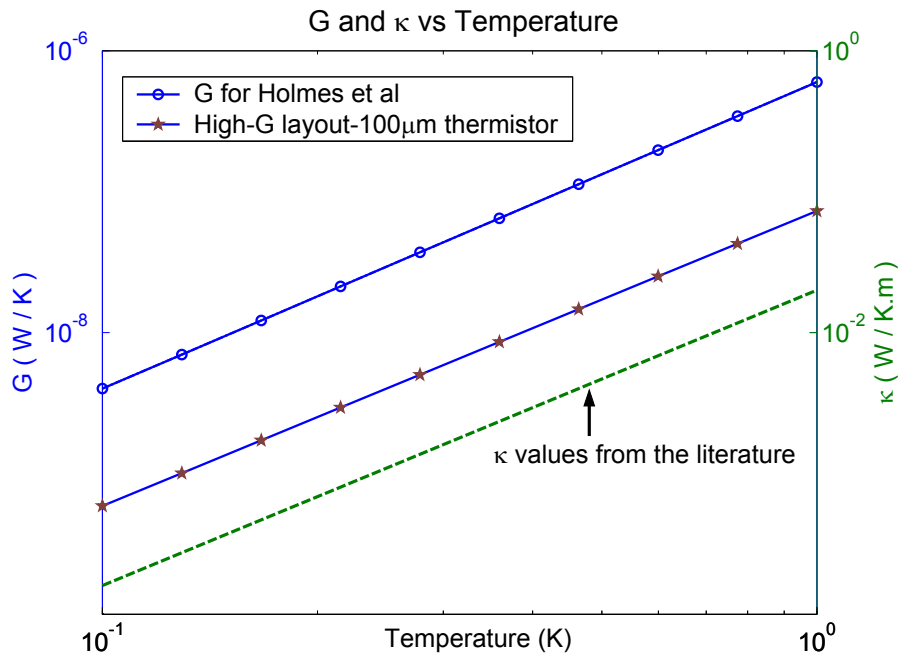


Figure 6.9: Thermal conductance for High-G layout. The plotted value of κ is obtained from Holmes et al. (1999). Using the FEA model, G of sample ‘C1’ from Holmes et al. (1999) is calculated and plotted.

Hence in all the future experiments, only the thermistor deposited on the silicon nitride membranes (CH1, CH2, ..., CH7) are connected to seven channels.

The comparison between thermistor of various geometries shows that the thermistor with bigger geometry e.g. $100\mu\text{m} \times 100\mu\text{m}$ has higher dynamic range and has steeper transition curve (§ 6.4) close to the superconducting regime. The thermistors with smaller geometries like $4\mu\text{m}$ square have less contact area with the membrane so they are not thermally well connected to the membrane. While the thermistors with bigger geometry like $100\mu\text{m}$ square have more contact area so they are thermally well connected to the membrane. For the small thermistors, the bias voltage required to go into transition range is smaller than that of the big thermistors e.g. the thermistor of $100\mu\text{m} \times 100\mu\text{m}$ goes into transition at $120\mu\text{V}$ and thermistor of $4\mu\text{m} \times 4\mu\text{m}$ goes into transition at $60\mu\text{V}$.

Thermistors with larger area than $100\mu\text{m} \times 100\mu\text{m}$ would occupy a significant fraction of absorbing area so there is a need to compromise between the thermistor size and the absorbing area. Since the thermistor with area of $100\mu\text{m}$ square showed better performance than other thermistors, it was decided to use $100\mu\text{m}$ square as the standard geometry for the thermistor. The seven element array with $100\mu\text{m}$ square thermistor in spider geometries was fabricated (§ 6.7).

6.5.1 Model for thermistors of different geometries

In this section, the simulations of thermistors of different geometries are presented for *basic layout* array (§ 6.4). Fig. 6.9 shows the calculated thermal conductance for High-G layout. The thermal conductance for the Holmes et al. (1999) experiment is simulated to verify the model. The values of κ are obtained from the literature (Holmes et al. 1999) which are plotted as the second Y-axis in Fig. 6.9. From the estimation of the thermal conductance, as explained in § 5.3, the $I - V$ behavior for different geometries of thermistor are simulated; the required resistance–temperature dependence is obtained from the $R - T$ measurements. Fig. 6.10 shows the comparison between measured and simulated $I - V$ curves. The

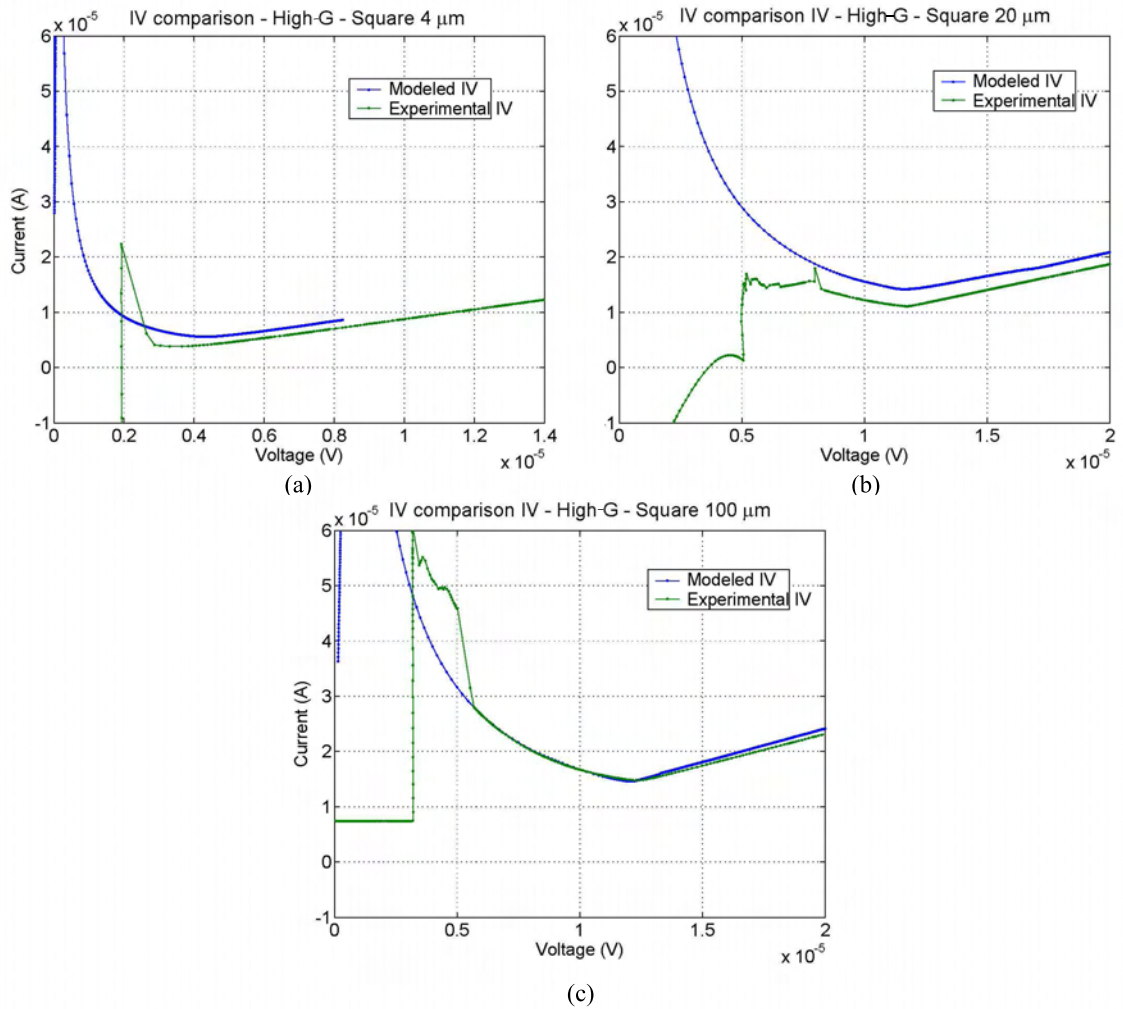


Figure 6.10: $I-V$ model for different geometries of thermistor. The comparison of modeled $I-V$ and measured experimental $I-V$ for $4 \mu\text{m}$ square thermistor Fig. (a), $20 \mu\text{m}$ square thermistor Fig. (b), and $100 \mu\text{m}$ square thermistor Fig. (c).

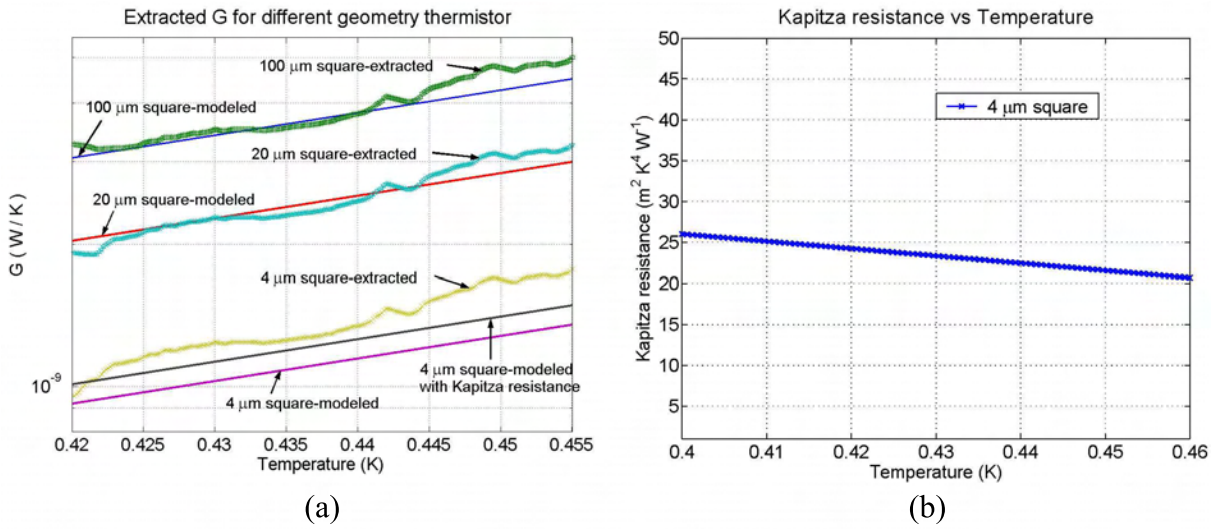


Figure 6.11: (a) Modeled G and extracted values of G from experiments for thermistor of different geometries. The curve for extracted value of G is not smooth because of unevenness and jumps in $R - T$ measurements. (b) Estimated Kapitza resistance for 4 μm square thermistors.

variations in the $R - T$ measurements can cause discrepancies in the measured and modeled $I - V$. Such discrepancies may also arise from the Kapitza (thermal boundary) resistance (Swartz & Pohl 1989). The 100 $\mu\text{m} \times 100 \mu\text{m}$ thermistor has larger contact area with the silicon nitride membrane so it is thermally better connected to the membrane. It was found that the Kapitza resistance is not a major contributor (see § 6.5.2 for estimation of Kapitza resistance). The operating point on the $R - T$ transition moves to higher resistance with increase in the bias power. In the transition region the bolometer current decreases with increase in the bias voltage (V_b) and the curve is proportional to $-1/V_b$. As explained in § 6.4, for several experiments it was observed that the 100 μm square thermistor shows better performance over other thermistor geometries. Hence it was decided to fabricate the seven element in spider geometry with 100 μm square thermistors. The experimental and modeled results for 100 μm square thermistor is explained in § 6.8.1.

6.5.2 Estimation of Kapitza resistance

Using $I - V$ and $R - T$ measurements, the relation between voltage across the bolometer and the temperature of the bolometer can be determined. Thus, the power across the bolometer in transition range is determined. Using Eq. 2.37, the value of the thermal conductance in the transition range is extracted. Fig. 6.11 compares the thermal conductance obtained from the finite element analysis and the extracted from the experiments for High-G layout. The $R - T$ curves are measured only during the transition range hence the thermal conductance is estimated only for the transition region. Even as all the thermistors are placed in the High-G layout, the thermal conductance is different for thermistors. This is because the thermal conductance varies as logarithmic ratio of thermistor area to the silicon nitride membrane area. Hypothetically, if a circular silicon nitride membrane and geometry of thermistor is assumed, then the thermal conductance is proportional to the logarithm of the ratio of thermistor diameter to the silicon nitride membrane diameter. Same principle can be applied for the square size thermistor and silicon nitride membrane.

The thermistor size affects the heat capacity of the bolometer. Since the contribution of thermistor to heat capacity is very small, the change in geometry of the thermistor does not affect the total heat

capacity significantly. Fig. 6.11 (a) compares the thermal conductance obtained from FEA and extracted from the experiments. It was observed that, the extracted thermal conductance follows closely to the modeled thermal conductance for 100 μm square and 20 μm square thermistors. The discrepancy between extracted and modeled thermal conductance for 4 μm square thermistor is higher. Due to discrepancy in the thermal conductance of 4 μm square thermistor, the modeled $I - V$ do not have good fit to the measured $I - V$ (Fig. 6.10 (a)).

The larger thermistor, e.g. 100 μm square, 20 μm square, has larger contact area with the silicon nitride membrane hence the Kapitza (thermal boundary) resistance between thermistor and the silicon nitride membrane is not significant. The smaller size thermistor, e.g. 4 μm square, has less contact area with the silicon nitride membrane hence a possible boundary resistance between the surfaces can affect the bolometer performance. The discrepancies between measured and modeled thermal conductance for 4 μm square thermistor could be due to the thermal boundary resistance. Here, an estimate of the Kapitza resistance obtained from the comparison between modeled and experimental thermal conductance is presented.

The Kapitza conductance, H_K , for bolometer is (Baker & Wyatt 1987; Swartz & Pohl 1989)

$$H_K = (i_{bolo}^2 R_n) / (A \times [T_{bolo}^n - T_{bath}^n]), \quad (6.1)$$

where i_{bolo}^2 is the bolometer current, A is the contact area, T_{bolo}^n is bolometer temperature and T_{bath}^n is the bath temperature. The value of n is 4. For 4 μm square thermistor, the Kapitza conductance is calculated in the transition range. The values for Kapitza resistance estimated from the model calculations are plotted in Fig. 6.11 (b). The value of Kapitza resistance is fed into the bolometer model and the thermal conductance of 4 μm thermistor is calculated. An estimation of the thermal conductance for 4 μm thermistor with Kapitza resistance is shown in Fig. 6.11 (a). The comparison between the modeled thermal conductance with Kapitza resistance and the extracted thermal conductance shows discrepancies. 4 μm area, is near to the limit of the lithography, hence there can be difference in the deposited surface area. The niobium bonding pads of the thermistor have bigger surface area than the 4 μm square thermistor, which can thermally affect the bolometer properties.

6.6 4SN 1601 – Spider geometry

Reduction of the thermal conductance increases the sensitivity of the bolometer. Efforts were made to structure the silicon nitride membrane so it is possible to tune the thermal conductance (G) according to the requirements. As explained in § 3.4, the membrane is structured into Low-G, Medium-G and High-G configurations. Fig. 3.7 shows the spider geometry of Low-G, Medium-G and High-G.

6.6.1 4SN 1601 – High-G layout

For this experiment, the seven channels are connected to all the thermistors on the silicon nitride membranes. The properties of each thermistors are explained in § 6.5. Fig. 6.12 shows the $I - V$ and $R - T$ measurements of array when the experiment was performed at 300 K background. Due to fabrication defects, it was not possible to measure the $I - V$ and $R - T$ curves for 60 $\mu\text{m} \times 20 \mu\text{m}$ size with gold banks on the side of the thermistor. The transition width of the bolometer in the $R - T$ measurements is directly proportional to the applied bias voltage. It was observed that the transition range of a TES is directly proportional to the thermistor size. The transition range of the 100 μm square thermistor is the biggest, and the transition range of 4 the μm thermistor is the smallest. CH2, a 20 μm square thermistor with gold strips, showed an extra 200 m Ω of resistance in series. This resistance is due to the deposition of the gold strips on the thermistor. The normal state resistance of CH3 is 5 Ω . CH6 has parallel strips of 20 $\mu\text{m} \times 100 \mu\text{m}$ so the total area is 100 $\mu\text{m} \times 100 \mu\text{m}$. During several experiments, it was not possible to obtain the stable operating conditions for CH6. Sometimes, the applied bias voltage was insufficient to

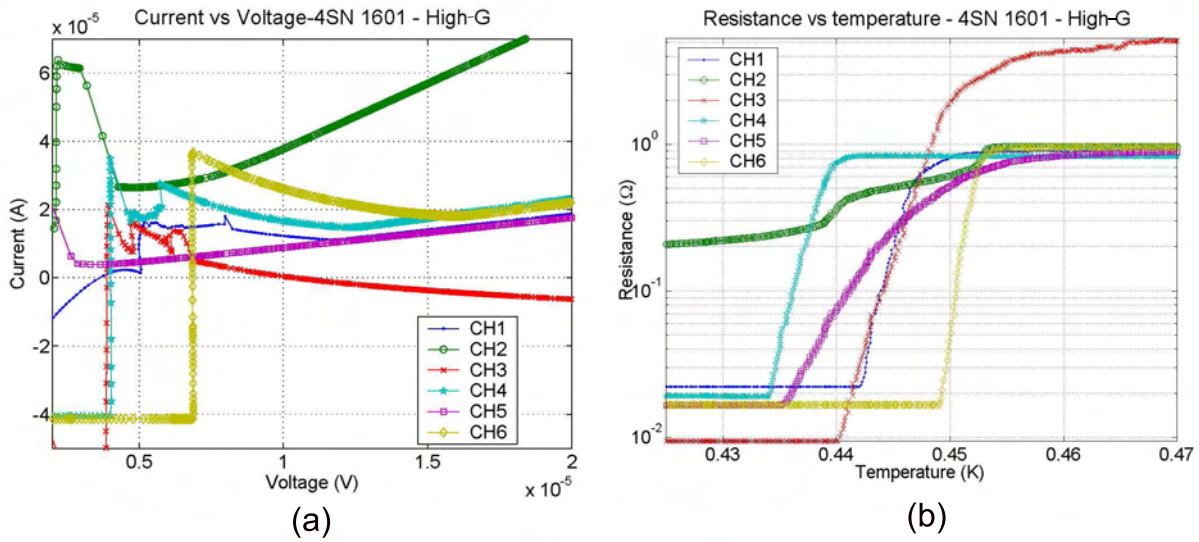


Figure 6.12: $I - V$ and $R - T$ curve for 4SN 1601 array in High-G layout. The normal state resistance is 1Ω . $33 \text{ m}\Omega$ of resistor is used as a standard shunt resistor. The $I - V$ and $R - T$ plots are shown in (a) and (b) respectively. The measurements are performed at 300 K background.

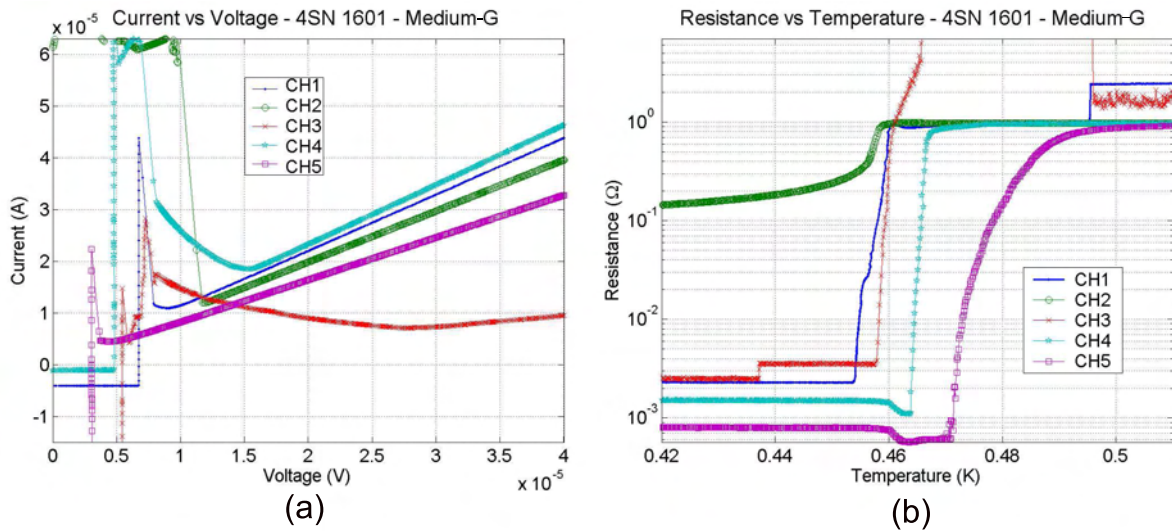


Figure 6.13: $I - V$ and $R - T$ measurements of 4SN 1601; spider Medium-G layout. The design has 8 legs of $300 \mu\text{m}$ width. The measurements are performed at 300 K background.

overcome the *Hysteresis effect*, so an extra heat input was required to break the superconducting state. An extra heat input increases the base temperature of the cryostat, so the sensitivity of the bolometer is affected. The $100 \mu\text{m}$ square thermistor showed better performance in comparison with thermistors of other geometries. The bottom panel of Fig. 6.10 shows a comparison of $I - V$ curves of the $100 \mu\text{m}$ square thermistor. The $R - T$ measurements are inputs to bolometer modeling.

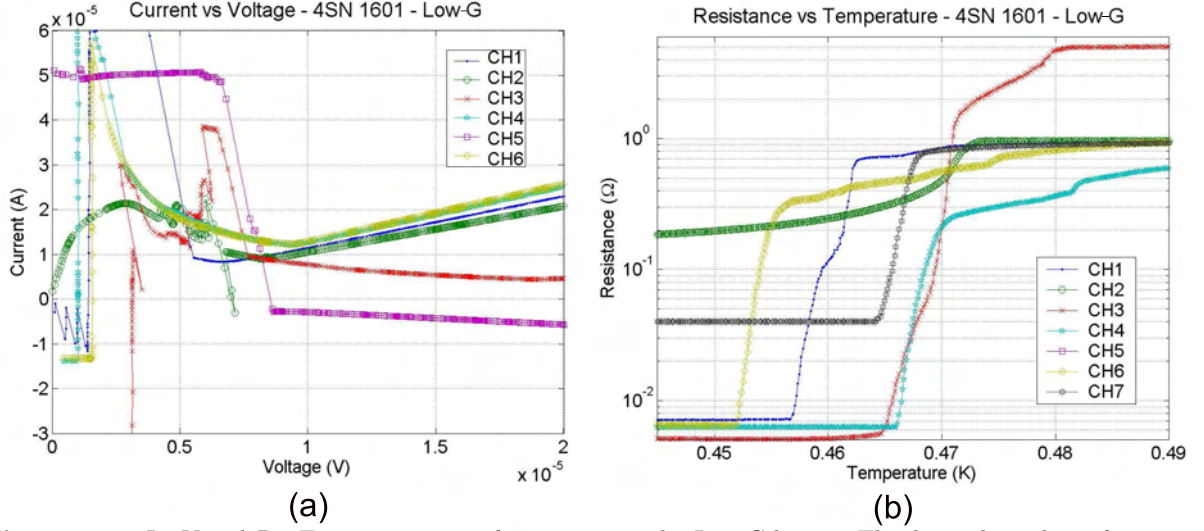


Figure 6.14: $I-V$ and $R-T$ measurements of 4SN 1601; spider Low-G layout. The design has 8 legs of $100\ \mu\text{m}$ width. The measurements are performed at 0.3 K background.

6.6.2 4SN 1601 – Medium-G layout

The $I-V$ and $R-T$ measurements of the Medium-G layout are shown in Fig. 6.13. All the thermistors on the silicon nitride membrane are connected to bolometer channels. During the experiment, some jumps were seen in the $R-T$ curves. In the $I-V$ measurements, some jumps are seen near the superconducting stage which correlate with jumps from $R-T$ curves. Although $R-T$ transitions were observed for all the channels, the $I-V$ curves for CH6 and CH7 were not measurable. Upon investigation it was learned that the wires carrying bias voltage to CH6 and CH7 were open. This fault was repaired in all the subsequent experiments. The thermistor properties are similar and $100\ \mu\text{m}$ square thermistor showed better performance in terms of steepness of $I-V$ curve and transition region. The detailed experimental results and modeling for different Medium-G layouts are presented in § 6.10 and § 6.11.

The silicon nitride membrane was structured (4SN 1601) to tune the thermal conductance of the bolometer. There were jumps in $I-V$ and $R-T$ measurements but the overall behavior of the array was as expected. The thermal conductance decreases from High-G to Low-G configuration. Hence the bias voltage required to go from the superconducting state to normal state also decrease from High-G to Low-G design. This was confirmed from the experiments.

6.6.3 4SN 1601 – Low-G layout

The $I-V$ and $R-T$ curves from the experiment with no background radiation are shown in Fig. 6.14. All the seven thermistors on silicon nitride membranes are connected to the SQUID channels. The temperature transitions for different thermistors are in the range $\pm 20\ \text{mK}$. All the channels show similar characteristics. Since the thermal conductance is smaller than other layouts, less bias voltage is required to go into transition region. Similar to previous experiments, the $100\ \mu\text{m}$ square thermistor showed better performance. Here, the transition range was higher and $I-V$ curves were steeper near to the superconducting stage. Fig. 6.15 shows a comparison of $I-V$ data for High-G, Medium-G and Low-G layouts.

Similar experiment was performed at 300 K background radiation but the $I-V$ or $R-T$ curves could not be measured. This is because the thermal conductance of the Low-G layout is too low to work with 300 K background. The incident power from 300 K background heats the bolometer above its transition temperature and the bolometers stay in the normal range.

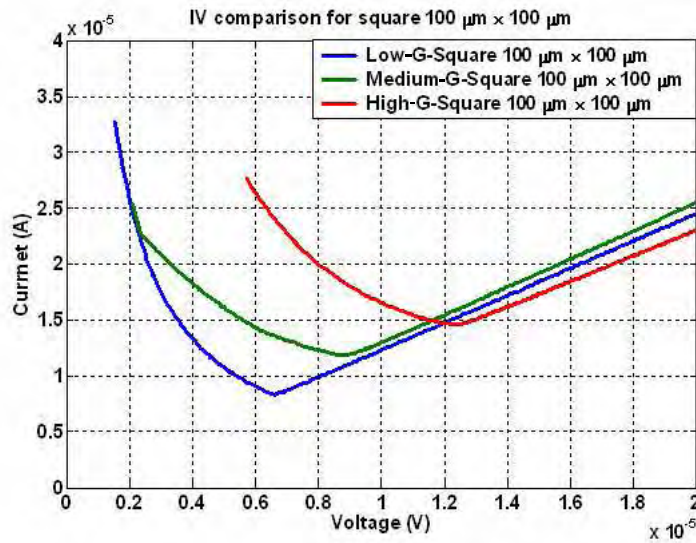


Figure 6.15: $I - V$ comparison for $100 \mu\text{m} \times 100 \mu\text{m}$ thermistor measured in High-G, Medium-G and Low-G configuration of 1601 design. For High-G and Medium-G layouts the measurement is performed at 300 K background and the measurements of Low-G layout are performed at 0.3 K background.

6.7 4SN 1610 – Spider geometry

In the previous experiments, the performance of the $100 \mu\text{m} \times 100 \mu\text{m}$ thermistor was better in that the $I - V$ curves were steeper and there was a bigger operating range. In the next fabrication run, the silicon nitride membranes were structured into High-G, Medium-G and Low-G configuration and all the thermistors were of $100 \mu\text{m}$ square geometry. In this layout cross absorbers were used for the first time (§ 3.3).

In array 4SN 1610, due to fabrication problems, a large fraction of the legs in the 8-leg Medium-G layout were broken so no stable experimental results could be obtained. Too high stress during the deposition of the silicon nitride on the silicon wafer could be the cause. In order to solve this problem for Medium-G layout, in the next array design, the leg width is decreased and the number of legs are increased, resulting into same value of the thermal conductance. The new Medium-G with 16 legs and 32 legs, 4SN 1762 is fabricated, (§ 6.10, 6.11).

6.8 4SN 1610 – High-G – with Ti absorber- Experiment and model

The High-G layout was fabricated with, both, continuous titanium absorbers and gold-palladium cross absorbers. Thus, it is possible to compare the efficiency of the new cross absorbers with the old continuous titanium film absorbers.

6.8.1 $I - V$ and $R - T$ measurements

Both, modeled $I - V$ and experimental $I - V$ curves are similar to those shown in Fig. 6.10 (c). Fig. 6.17 (a) and (b), respectively, compares the experimental behavior of power-voltage ($P - V$) and resistance-voltage ($R - V$) curves with a bolometer model. In the transition region any change in V_b leads to a change in the the bolometer resistance, R , so that $I \propto 1/V_b$ with P_b constant. In the transition region,

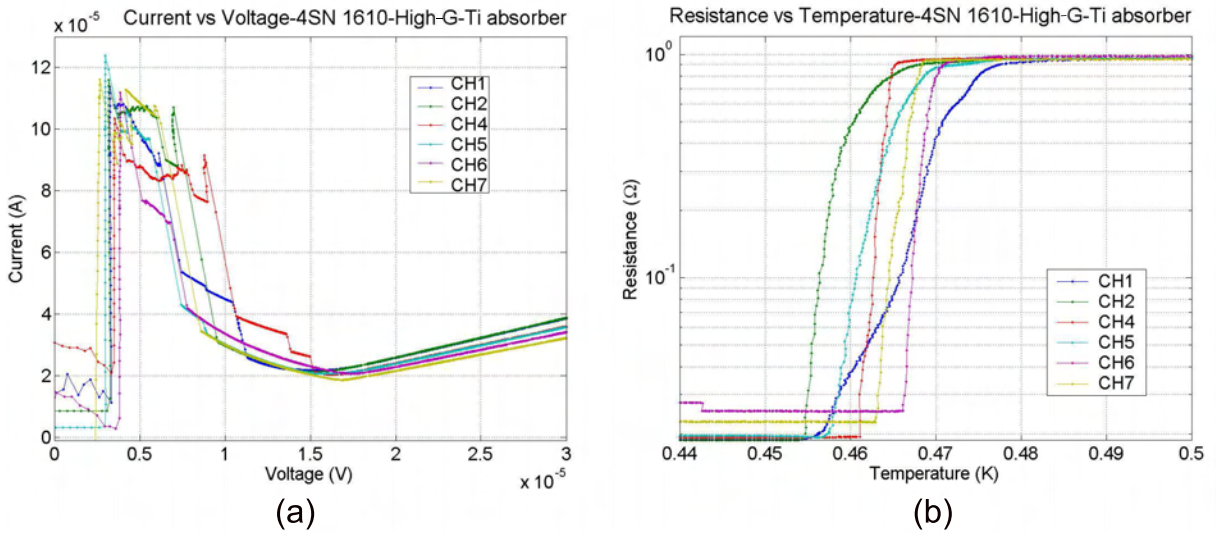


Figure 6.16: $I - V$ and $R - T$ measurements of 4SN 1610 High-G layout with continuous titanium absorbers. All the thermistors are $100 \mu\text{m}$ square size and mounted on the continuous silicon nitride membrane. The measurements are performed under 300 K background.

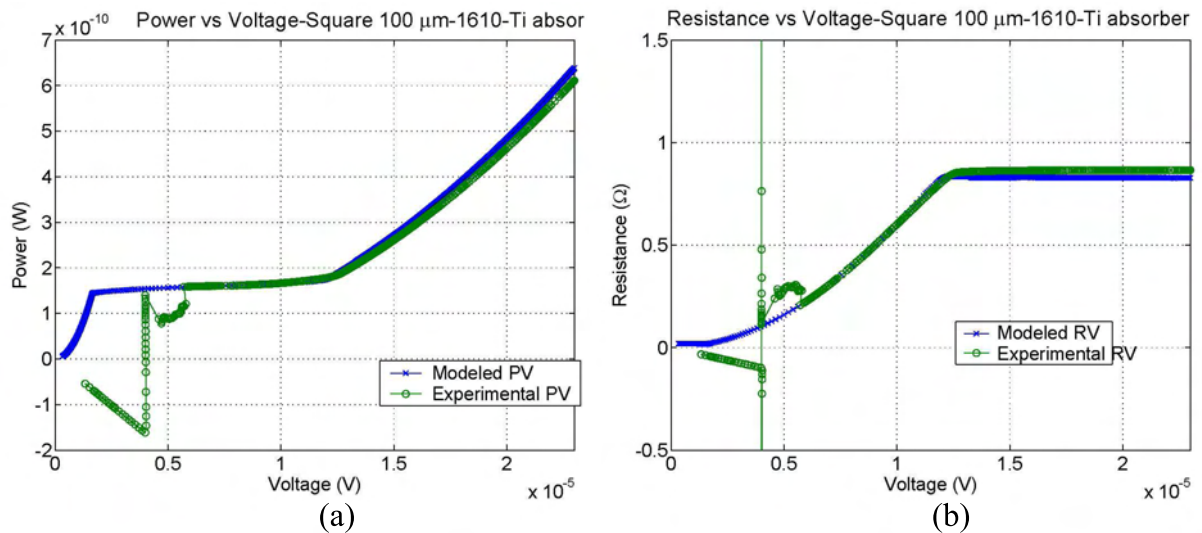


Figure 6.17: Measured power (P) and resistance (R) for bolometer with $100 \mu\text{m}$ square thermistor, compared with modeled parameters. The Y axis is power and resistance of bolometer plotted against voltage across the bolometer, respectively in (a) and (b).

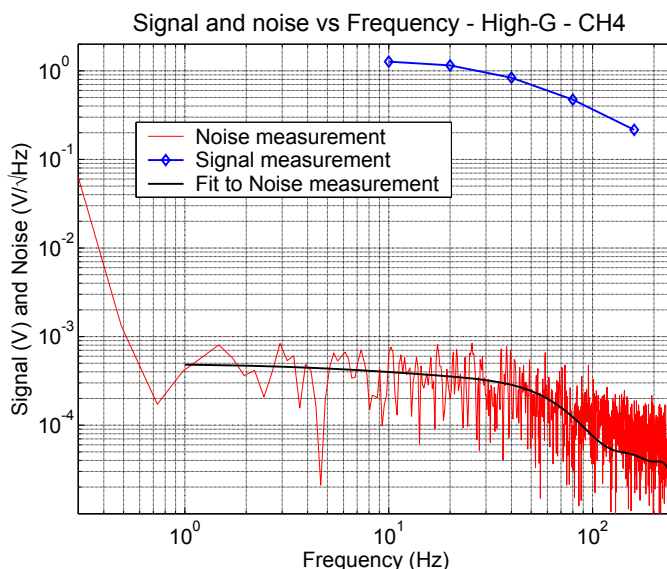


Figure 6.18: The signal and noise for 100 μm square thermistor of 4SN 1610 array in High-G layout with Ti absorber. The noise curve is fitted with a low pass filter function.

when the optical load is negligible, the bias power (P_b) is at its maximum value. As P is increased, P_b decreases ($P + P_b$ is held constant in feedback circuit) and the responsivity is kept constant. When the applied bias voltage crosses the threshold value, due to the heat generated by bias power the bolometer goes into normal range (Fig. 6.17 (b)). The bolometer is in the transition range from 5 μV to 16 μV of bolometer voltage. These measurements were performed with 300 K background hence the background contributes to the total power. The TES is operated at high background so that P_{bias} is significantly less than P_{total} , effectively suppressing some of the ETF effect and reducing the overall loop gain.

6.8.2 Signal measurements

A thin titanium absorber film is deposited on the back of the silicon nitride membrane. Fig. 6.18 shows the signal measured for a 100 μm square thermistor with a lock-in amplifier. The signal and noise is plotted against the frequency of incoming radiation in the same plot. The frequency of incoming blackbody radiation is varied by a chopper wheel.

Time constant measurements

Experiments were performed on the same array with 300 K background. The measured values of the time constant are shown in Fig. 6.20. When the bolometers are near to the normal range, their intrinsic time constants are not affected by the strong negative electrothermal feedback, hence, they have high values. In the middle of the transition range ($\sim 8 \mu\text{V}$ bolometer voltage) the transition curves are steepest, hence the time constant of the bolometer is at minimum.

The heat capacity calculations for the High-G layout bolometer with a 100 μm square thermistor are shown in Table 6.2. The gold ring is a main contributor to the heat capacity. The strong negative ETF decreases the time constant of the bolometer significantly but in our case the addition of gold ring decreases this effect. The incident beam has a gaussian pattern and causes heating of the membrane. Due to high thermal conductivity of the gold, the area inside the gold ring acts as constant thermalized patch so all the heat generated due to the incoming radiation is coupled to the thermistor. Simulations were performed to verify the effects of gold ring (§ 6.12).

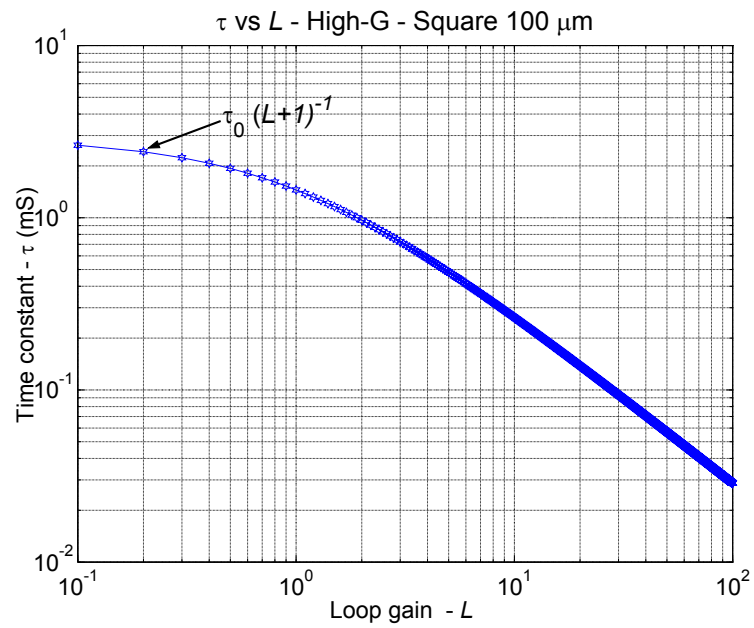


Figure 6.19: Relation between calculated time constant τ as a function of gain L for High-G layout.

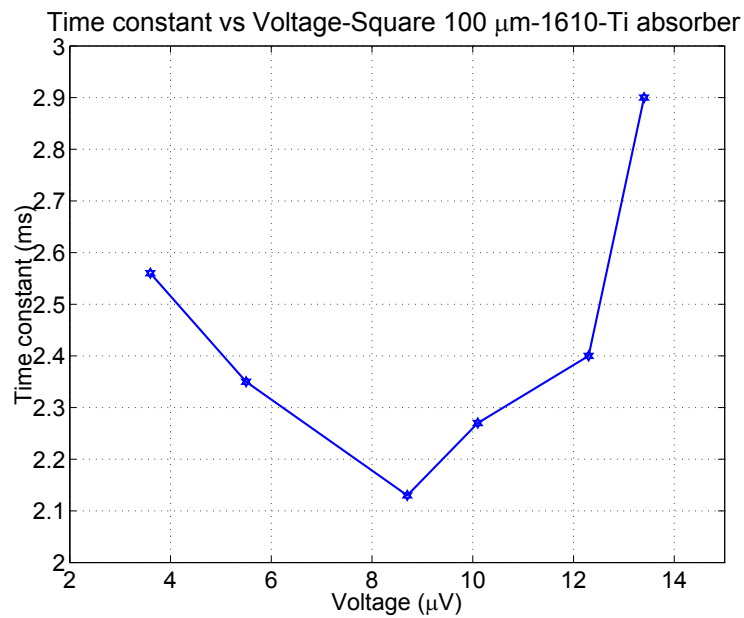


Figure 6.20: Time constant of the bolometer from the 4SN 1610 array with Ti absorber. Near to the normal range, the steepness of the transition curve decreases, hence τ increases. The transition curve is steepest in the middle of the transition range, hence τ is at a minimum.

Table 6.2: Thermal heat capacity budget for High-G layout with Ti film absorber at 450 mK.

Material	C_ν Electron (J/cm ³ K ²)	C_ν Lattice (J/cm ³ K ⁴)	Volume (cm ³)	C (J/K)
Thermistor:				
Au-Pd	2.5×10^{-4}	4.2×10^{-4}	8.6×10^{-11}	1.3×10^{-14}
Mo	1.1×10^{-3}	9.3×10^{-4}	8.6×10^{-10}	5.0×10^{-13}
Electrical Leads:				
Nb		8.6×10^{-6}	3.8×10^{-9}	2.9×10^{-15}
Au ring	6.8×10^{-5}	4.5×10^{-5}	2.1×10^{-7}	6.3×10^{-12}
Absorber:				
Ti	3.2×10^{-4}	2.5×10^{-5}	1.4×10^{-8}	2.1×10^{-12}
Si ₃ N ₄		8.2×10^{-8}	8.2×10^{-6}	6.1×10^{-14}
Total				8.9×10^{-12} J/K

The total heat capacity of the bolometer for High-G layout is calculated to be 8.9×10^{-12} J/K. The modeled thermal conductance near to the normal range is 4.5×10^{-9} W/K. Therefore, the calculated intrinsic time constant (τ_0) is 2 ms. This time constant is attained when the bolometers are near to the normal range so there is no strong negative ETF. The measured τ is 2.9 ms when the bolometers are near to the normal range. Using the experimental time constant and the modeled thermal conductance, the calculated heat capacity of the bolometer is 1.3×10^{-11} J/K. The measured heat capacity is higher than the calculated one (Table 6.2). For the calculations, pure materials were considered but impurities can increase the heat capacity. The discrepancy can also be explained, if the thermal conductance of the bolometer is lower than calculated from the FEA model. For the heat capacity calculations, the thickness of titanium film absorber is assumed to be 5 nm but there can be uncertainties in thickness measurements. During the fabrication, the titanium film is deposited such that the surface resistance is $377 \Omega/\square$. Thus, the surface resistance is a determining factor for the process of film deposition.

Power dissipated in the thermistor causes a temperature rise, $\Delta T_{\text{thermistor}} = \Delta P/G_{\text{thermistor}}$. The base temperature will be higher than in the case in which the same power would be dissipated uniformly throughout the absorber, $\Delta T_{\text{opt}} = \Delta P/G_{\text{opt}}$. Thus, the thermal efficiency will be degraded only when the thermal conductance of the absorber becomes comparable to the thermal conductance of the supports. As shown in Table 6.2, the thermal conductance of the niobium wires is smaller than the thermal conductance of an absorber. Therefore, the thermal inefficiencies due to the niobium wires can be neglected. The C of the thin film scales as T hence the thermalization time is temperature independent.

Fig. 6.19 shows the comparison between calculated time constant and loop gain. The curves show the predicted time constant dependence of $\tau = \tau_0/L + 1$, where τ_0 is 2.9 ms. In the transition range the L is ≈ 68 . It is difficult to determine L precisely for each measured τ since dR/dT is current dependent, especially at the lower end of the transition and it is not correct to derive L from the values of α determined from $R-T$ measurements. Also, since the change of total power is very insensitive to the operation point in the strong ETF regime, errors in determining L are as large as factor of 2 (Lee et al. 1998).

Spectral response of the system

The spectral response of the different channels was measured using a Martin-Puplett Spectrometer (§ 4.7.2). Fig. 6.21 shows the spectral response of CH6. It is very important to understand the spectral behavior of the system. The transmission band is defined by filter characteristics but in practice it is altered by standing waves between filters, reflections from the metallic parts inside the cryostat and in-

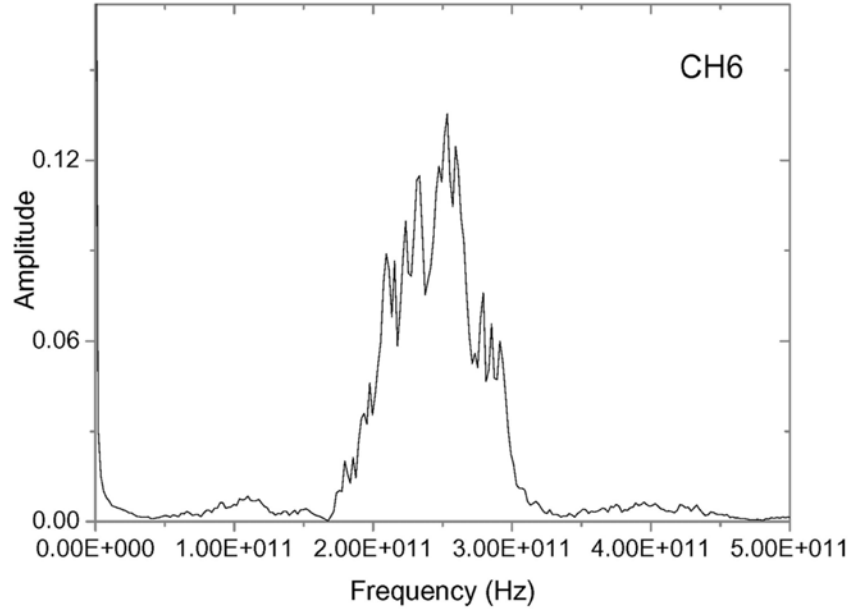


Figure 6.21: Typical spectral response. The measurements were performed with a Martin-Puplett Interferometer.

terference. The spectral response of the system contains all such interfering factors which determine the overall spectral characteristics. The ripples in the spectrum are due to the lack of anti-reflection coatings on the filters.

6.8.3 Noise measurements

The noise is measured as a *timeseries* and analyzed using the *LabVIEW* program. The different noise current contributions obtained from the model are plotted in Fig. 6.22. The parameters are calculated at $10 \mu\text{V}$ bolometer voltage. The total noise current is obtained by adding Johnson, phonon (thermal fluctuation) noise and SQUID noise quadratically. It is possible to derive the noise voltage from the noise current. The measured noise voltage is $2.6 \times 10^{-5} \text{ V}/\sqrt{\text{Hz}}$ and the noise calculated from the model is $1.9 \times 10^{-5} \text{ V}/\sqrt{\text{Hz}}$. The noise measurements with a lock-in amplifier are consistent with those obtained using a time-series analyzer. The measured noise is compared with the signal in Fig. 6.18.

A fundamental limit for the noise in a bolometer is set by thermal fluctuations in a simple thermal circuit consisting of a single heat capacity and a single thermal link to a temperature reservoir. When referred to the bolometer the thermal fluctuation noise power spectrum is at low frequencies and rolls off at the maximum response frequency of the bolometer. Fig. 6.23 compares the noise from the experiments with that obtained from the model. In subplot Fig. 6.23 (a), the measured noise seems to show the $1/f$ noise below 2 Hz, but the length of measured time series was not long enough to measure the noise at low frequencies with high accuracy. The contribution from photon noise, as in § 2.3.1, is also considered. The noise is measured with and without 300 K background in order to study the effect of photon noise. As shown in Fig. 6.23 (b), the estimated value of the noise voltage from various noise current contributions closely follows the measured noise voltage. Bolometers are often operated at switching frequencies of a few Hz so the behavior of the bolometer should be characterized in the low frequency regime. The experimental measured noise is slightly higher than noise predicted from the model. This excess noise

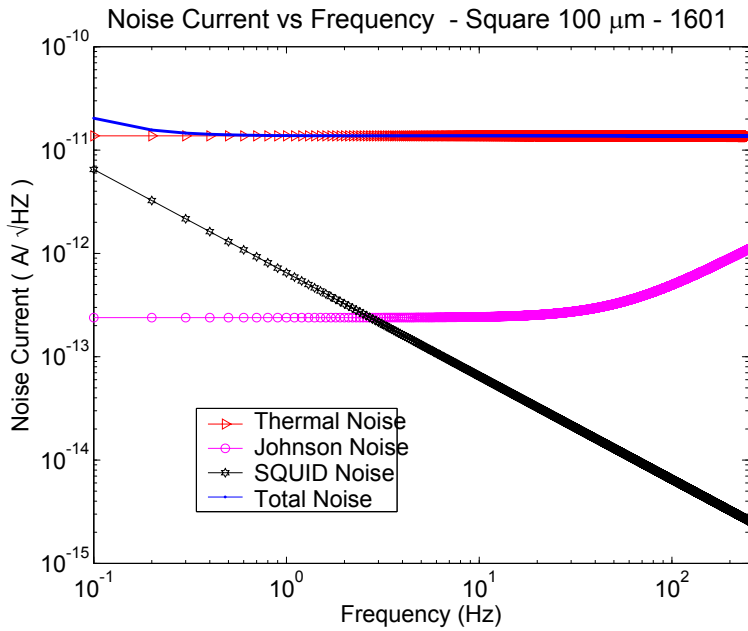


Figure 6.22: Predicted noise current of the 4SN 1610 High-G array for a 100 μm square thermistor with a Ti absorber film. The values are obtained from the bolometer model. The Thermal fluctuation noise (phonon noise) is the main source of noise so the total noise follows it. A bolometer voltage of 10 μV is considered for the calculations.

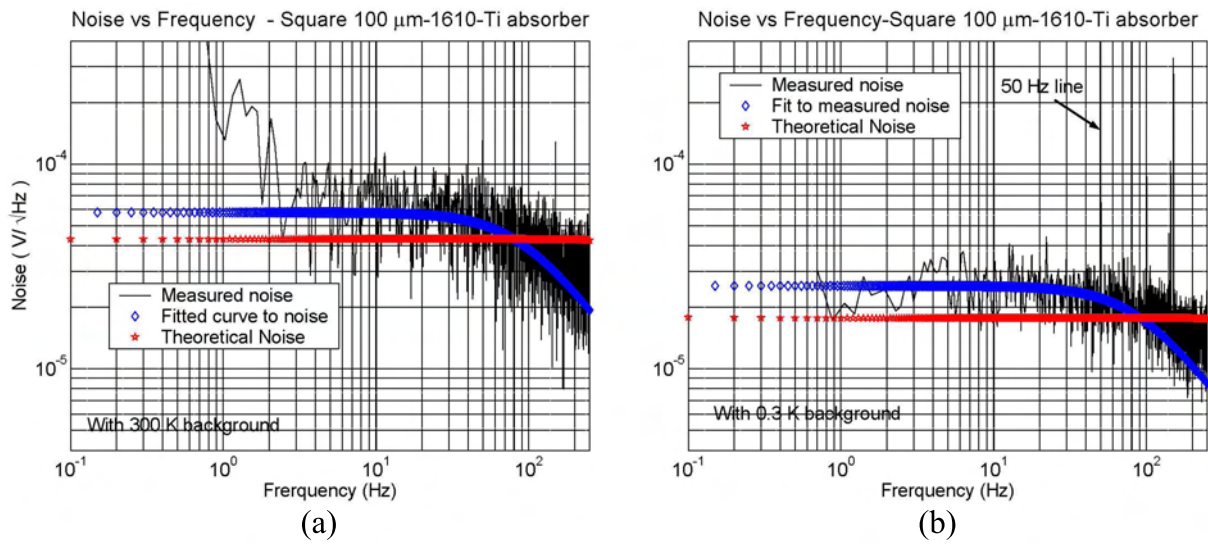


Figure 6.23: Comparison of noise voltage from experiments with modeled values for the High-G layout with Ti absorber. Measured Noise in plot (a) refers to noise measured during experiment with 300 K background and in plot (b), it refers to the noise measured during the experiment with 0.3 K background. The modeled value of noise is also compared with experimentally measured values. The measured noise was fitted to a low pass filter function.

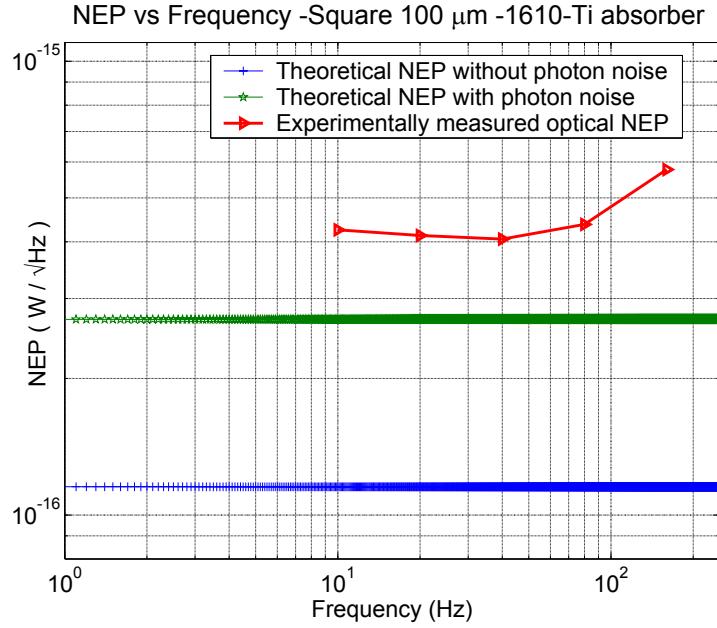


Figure 6.24: NEP plotted as a function of frequency. The NEP obtained from the bolometer model, with and without photon noise contribution is compared with the measured optical NEP.

may arise from microphonics from the suspension and electrical wiring, the resistive fluctuations of superconducting film, superconducting flux motions; the reason for the observed excess noise is not known.

The difference between the measured and the calculated total noise voltage without photon noise is $1.1 \times 10^{-5} \text{ V}/\sqrt{\text{Hz}}$. The noise voltage obtained from the model with photon noise is $4.3 \times 10^{-5} \text{ V}/\sqrt{\text{Hz}}$ and the measured value of the total noise voltage is $5.6 \times 10^{-5} \text{ V}/\sqrt{\text{Hz}}$. The excess noise measured during an experiment with 300 K background is $1.3 \times 10^{-5} \text{ V}/\sqrt{\text{Hz}}$. Thus, the excess noise level for experiment with 300 K background is similar to that of the experiment without 300 K background. The noise due to base temperature fluctuations is defined by *Hooge parameter* (γ_H) which is a function of operating temperature. Since the transition temperature is 0.45 K, the contributions from $\gamma_H(T)$ can be neglected (de Korte et al. 1995; de Nivelles et al. 1997). According to the discussions of de Nivelles et al. (1997), the Hooge parameter is directly proportional to the total heat capacity and the operating temperature of the bolometer. The total heat capacity decreases significantly at the operating temperature of 450 mK. Estimates of the *Hooge parameter* for bolometers mounted on silicon nitride membranes were performed by de Korte et al. (1995). The base temperature of the cryostat in 0.3 K and the extra noise due to the temperature fluctuations at sub-kelvin temperatures is negligible. Maul et al. (1969) have tried to calculate the excess noise due to the boiling of cryogenic liquids, e.g, ^3He , ^4He and N_2 , but no correlation was found.

The responsivity of the VSB does not depend on the small variations in the base temperature and power loading hence the calibration of the receiver is more accurate. When the thermal conductance of the bolometer is limited by the background power, the VSB should yield ideal NEP without constraints of C but in the applications where the speed requirements defines the thermal conductance, a reduction of the NEP is possible from the ideal value.

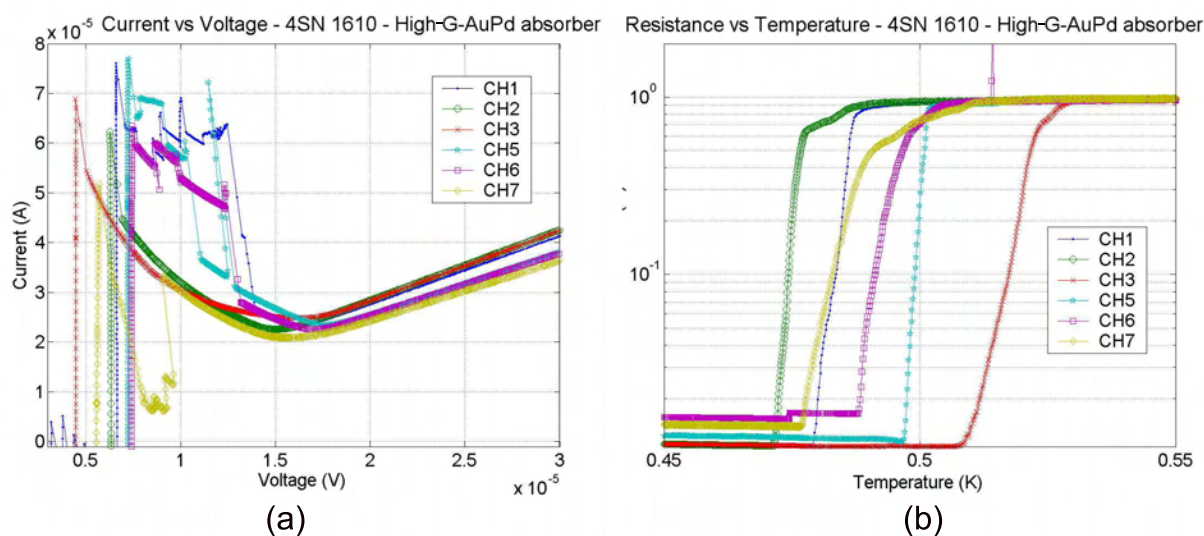


Figure 6.25: $I - V$ and $R - T$ measurements of 4SN 1610; High-G layout with gold-palladium cross absorbers. All the thermistors are $100 \mu\text{m}$ square. The measurements are performed under 300 K background.

6.8.4 NEP calculations

The NEP of TES (§ 2.3) and overall noise in TES (§ 2.5.1) is explained in Chapter 2. Using TES theory (Eq. 2.30), considering the contribution from different noise sources, it is possible to deduce the electrical NEP of the bolometer. Fig. 6.24 shows the comparison between the calculated electrical NEP from model and optical NEP obtained from the experiments. The electrical NEP is calculated from the model with and without contribution of photon noise from 300 K background radiation. The estimated value of NEP without photon noise is $1.1 \times 10^{-16} \text{ W}/\sqrt{\text{Hz}}$ and with photon noise from the 300 K background is $2.7 \times 10^{-16} \text{ W}/\sqrt{\text{Hz}}$.

The optical NEP is the absorber power divided by the signal to noise ratio. From signal and noise measurements the optical NEP is derived at different signal frequency. The optical NEP obtained is $4.5 \times 10^{-16} \text{ W}/\sqrt{\text{Hz}}$ at 20 Hz chopper frequency. The noise measured in the experiment is higher than calculated noise hence the optical NEP is higher than the calculated NEP.

The theoretical NEP is calculated by dividing the measured noise current referred to the SQUID input by the value of the responsivity. The contribution from Johnson noise is suppressed by a factor of τ_o/τ (Mather 1982) because of sharp transition (large α) and strong negative ETF. The NEP calculated from Johnson noise alone can be low in any sensor with high α and $P_b \gg GT/\alpha$ with or without ETF. However, stable low noise operation of a high α sensor with $P_b \gg GT/\alpha$ requires strong ETF. The degree to which the detectors achieve background-limited performance can be described by the ratio of the measured sensitivity under optical load $\text{NEP}_{\text{optical}}$ to the estimated photon noise level $\text{NEP}_{\text{photon}}$. The estimated $\text{NEP}_{\text{optical}}/\text{NEP}_{\text{photon}}$ is 1.36 ± 0.06 ; the $\text{NEP}_{\text{optical}}$ is obtained from the experiments at 300 K background and the $\text{NEP}_{\text{photon}}$ is obtained from the bolometer model. The dynamic range of the bolometer is approximately $\delta TG/\text{NEP}$, where δT is the half-width of the transition and NEP/G is the fluctuation per $\sqrt{\text{Hz}}$ (Clarke et al. 1977). Considering $\delta T \sim 2 \text{ mK}$ and $\text{NEP}/G \sim 10^{-7} \text{ KHz}^{-1}$, the dynamic range is about 10^4 in a 1 Hz bandwidth.

6.8.5 4SN 1610 – High-G – with Au-Pd cross absorbers

In order to test the efficiency of new cross absorbers, an experiment with the 4SN 1610 design in the High-G configuration was performed. Fig. 6.25 shows the $I - V$ and $R - T$ data for this array. Fig. 6.26

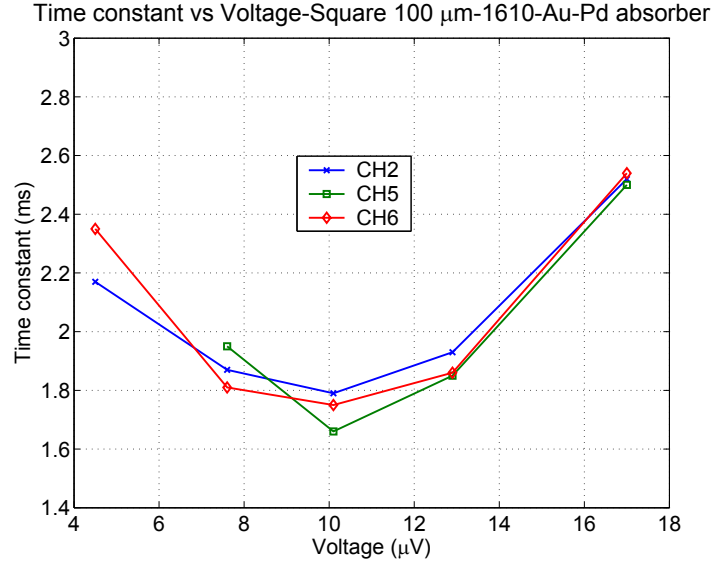


Figure 6.26: Time constant measurements of the High-G layout with Au-Pd absorbers in 4SN 1610.

Table 6.3: Thermal heat capacity budget for High-G layout with Au-Pd cross absorbers at 450 mK.

Material	C_v Electron (J/cm ³ K ²)	C_v Lattice (J/cm ³ K ⁴)	Volume (cm ³)	C (J/K)
Thermistor:				
Au-Pd	2.5×10^{-4}	4.2×10^{-4}	8.6×10^{-11}	1.3×10^{-14}
Mo	1.1×10^{-3}	9.3×10^{-4}	8.6×10^{-10}	5.0×10^{-13}
Electrical Leads:				
Nb		8.6×10^{-6}	3.8×10^{-9}	2.9×10^{-15}
Au ring	6.8×10^{-5}	4.5×10^{-5}	2.1×10^{-7}	6.3×10^{-12}
Absorber:				
Au-Pd	2.5×10^{-4}	4.2×10^{-4}	1.1×10^{-9}	1.6×10^{-13}
Si ₃ N ₄		8.2×10^{-8}	8.2×10^{-6}	6.1×10^{-14}
Total				7.3×10^{-12} J/K

shows the τ values from this experiment. The $I - V$ curves of CH1, CH5 and CH6 (Fig. 6.25 (a)) show jumps. It may be suspected that these jumps are not related to the bolometers but to the SQUID amplifiers. The seven SQUIDS are placed in two magnetically shielded mounts next to the aluminum horn antenna. CH2, CH3, CH7 are connected in one mount and CH1, CH5, CH7 in the other mount.

The total heat capacity of the High-G layout with gold-palladium cross absorbers is 7.3×10^{-12} J/K. Considering its thermal conductance of 4.5×10^{-9} W/K, the intrinsic time constant of the bolometer is 1.7 ms. The optically measured time constant near to the normal range is 2.5 ms which corresponds to a heat capacity of 1.3×10^{-11} J/K. The estimated heat capacity is less than the measured heat capacity. In case of the High-G layout with titanium absorber film, the measured heat capacity was ~ 1.5 times more than the estimated heat capacity. For the High-G layout with gold-palladium absorber, the measured heat capacity is ~ 1.7 times more than the estimated heat capacity. Thus, the difference between the measured and the estimated heat capacity is approximately similar for both the High-G layouts.

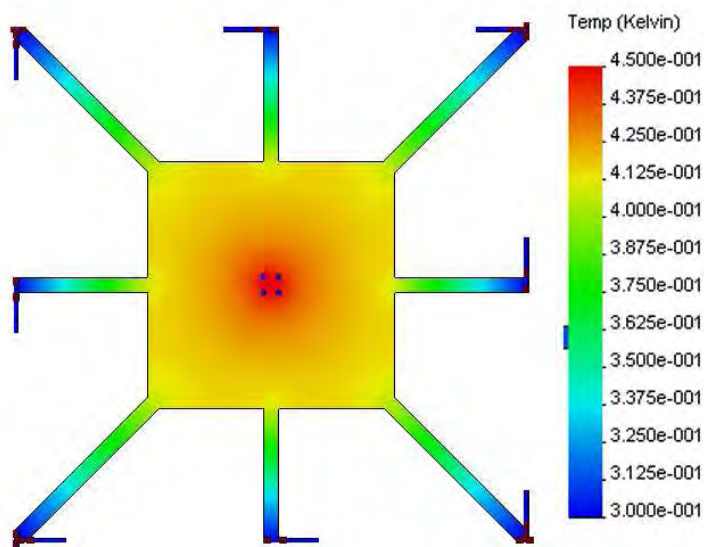


Figure 6.27: Steady state temperature distribution from finite element analysis for Low-G layout. The thermistor is maintained at a transition temperature of 450 mK while the silicon nitride membrane legs are maintained at the bath temperature of 300 mK.

For the High-G layout with titanium film absorber, the SNR is in the range 1000 and 1500 and the τ is ~ 3 ms. Comparison between Figs. 6.20 and 6.26 shows that the bolometers with cross absorber are faster than the bolometers with titanium film absorber. The gold-palladium cross absorbers have less heat capacity than the continuous titanium film absorber hence the total heat capacity of the High-G layout is reduced. Hence, the time constant of the High-G layout is reduced. The SNR is in range of 400 to 750 depending on applied bias voltage. The SNR ratio of the cross absorber bolometer is smaller than that of the titanium film absorber bolometer. In this array, the cross absorbers were fabricated with a surface resistance of $20 \Omega/\square$. Since the coupling to radiation was not perfect, the effective SNR was lower than expected. The NEP of High-G layout with the cross absorbers is $6.5 \times 10^{-16} \text{ W}/\sqrt{\text{Hz}}$.

6.9 4SN 1610 – Low-G layout – Experiment and Model

In order to understand the behavior of the bolometers with spider geometries e.g. Medium-G and Low-G design, a finite element analysis was performed to estimate the value of the thermal conductance. Fig. 6.28 shows the calculated thermal conductance for different silicon nitride membranes. In Fig. 6.27, the results from finite element analysis are plotted. The meshing of the silicon nitride membrane and thermistor is structured as explained in § 5.2. For the FEA modeling, the heat input was applied to the thermistor and the thermal conductance is calculated from the heat flow rate. In the model it was assumed that the thermistor is placed in the middle of the silicon nitride membrane but in practice, the thermistor was mounted at one corner of the absorbing center patch. When the modeling is performed with the thermistor mounted on this spot the derived thermal conductance turned out to be equivalent to that derived from FEA modeling with the thermistor in the center of the silicon nitride membrane.

For the experiment with 300 K background, the incident radiation on the absorbing area generates heat over the absorber surface. If one wants to simulate the situation in which this heat is uniformly distributed then the boundary conditions in FEA should be modified. With these boundary conditions,

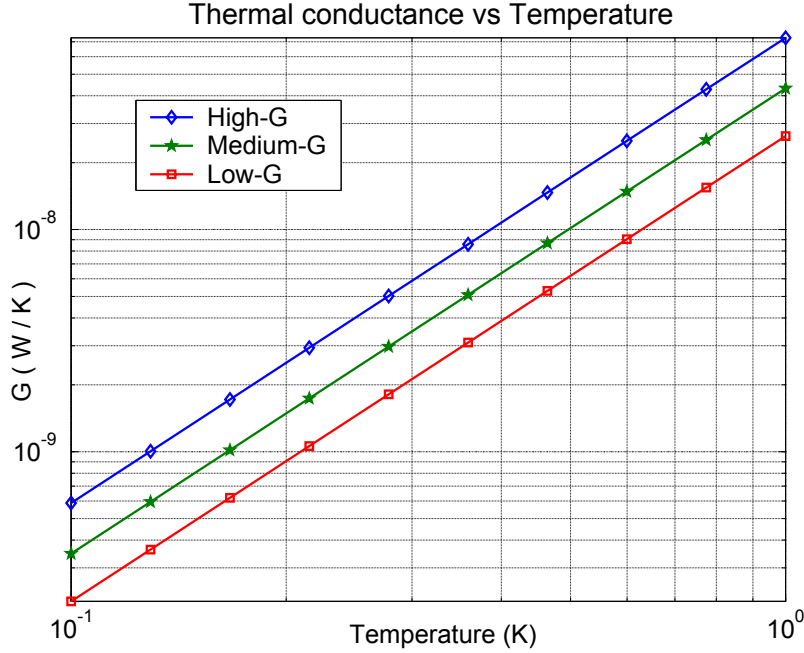


Figure 6.28: Calculated conductance for the different Si_3N_4 geometries. The simulations are performed as explained in § 5.2.

the thermal conductance increases by $\sim 10\%$. The NEP and noise can depend on the radiation load, hence it is correct to use the changed thermal conductance for calculating these values.

6.9.1 $I - V$ and $R - T$ measurements

The Low-G model shown here is compared with experimental results obtained from the 4SN 1610 array. Fig. 6.30 compares the $I - V$ curve obtained from the model with the $I - V$ curve measured during the experiment. The bolometer goes into the transition range at voltages of $6 \mu\text{V}$ and $12 \mu\text{V}$ for the Low-G and High-G layouts, respectively. The shunt resistor's resistance is $33 \text{ m}\Omega$ and the bias resistor's is 1045Ω . Comparisons of $P - V$ and $R - V$ curves are plotted in Fig. 6.31. The expected normal state resistance is 1Ω but the measured resistance during the experiment is 0.8Ω . In transition range the power dissipated in the thermistor is 50 to 60 pW , while for High-G layout, it is 150 to 200 pW . This is expected from the difference in the thermal conductance.

Fig. 6.29 shows the $I - V$ and $R - T$ measurements of the Low-G array in 4SN 1610 design. All the thermistors are of $100 \mu\text{m}$ square. As shown in Fig. 6.29 (a), all the thermistors show similar $I - V$ properties. In the $R - T$ (Fig. 6.29 (b)) measurements, small variations in the critical temperature are observed. In an experiment with 300 K background, it was not possible to obtain the $I - V$ or $R - T$ measurements. The bolometers stayed in the normal range because the 300 K background was sufficient to drive them into it. This was even true for a 77 K background. In the $R - T$ measurements, during several experiments a second transition near to the superconducting stage was observed. The shunt resistor used for this and all the later experiment has $33 \text{ m}\Omega$ and the second transition was observed at approximately the same resistance. When the bolometer resistance is less than the shunt resistance, the system is no longer voltage biased and the second transition is an artifact.

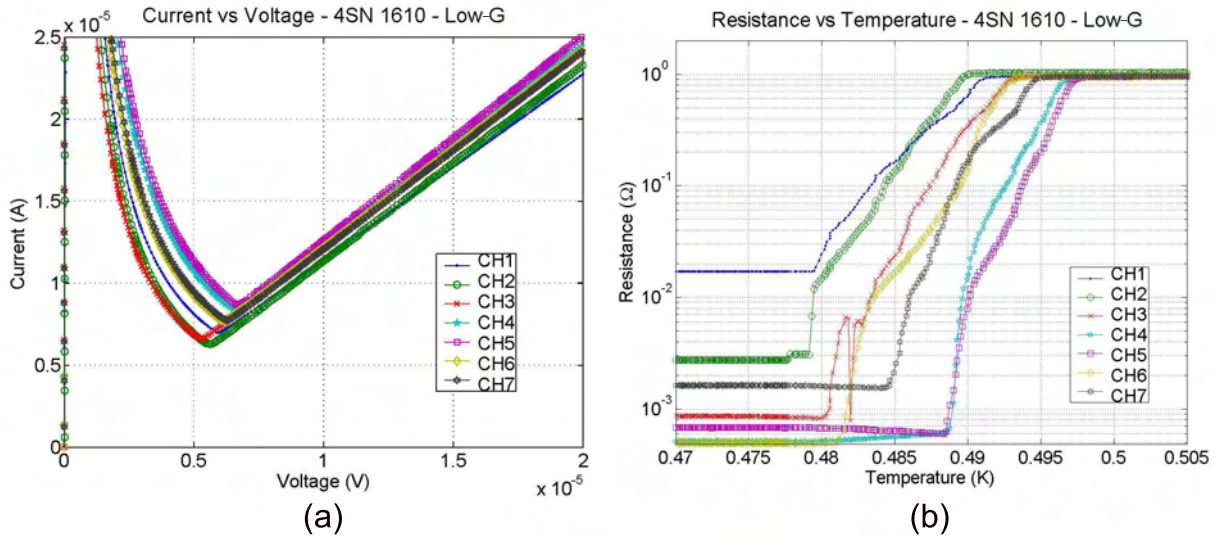


Figure 6.29: $I - V$ and $R - T$ measurements of 4SN 1610 Low-G spider layout. The design has 8 legs of $100 \mu\text{m}$ width. All the thermistors are $100 \mu\text{m}$ square size. The measurements are performed under 0.3 K background.

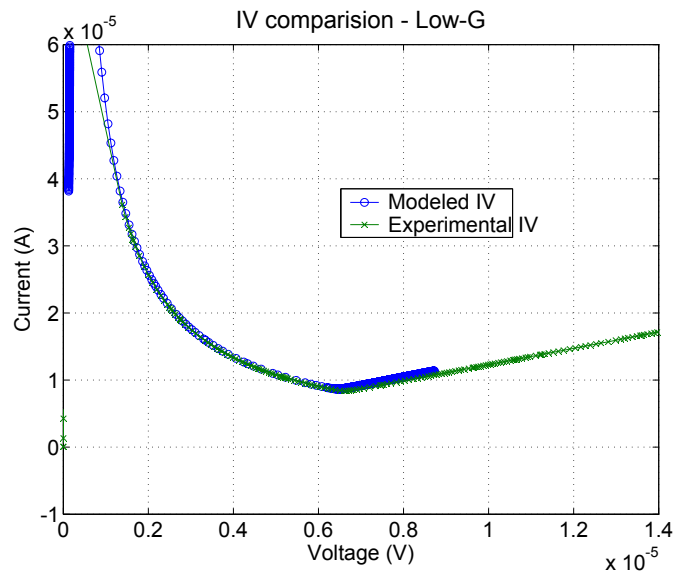


Figure 6.30: Comparison of modeled $I - V$ with that of experimentally measured $I - V$ using $33 \text{ m}\Omega$ of shunt resistor. (b) Relation between τ and loop gain, L for the Low-G layout.

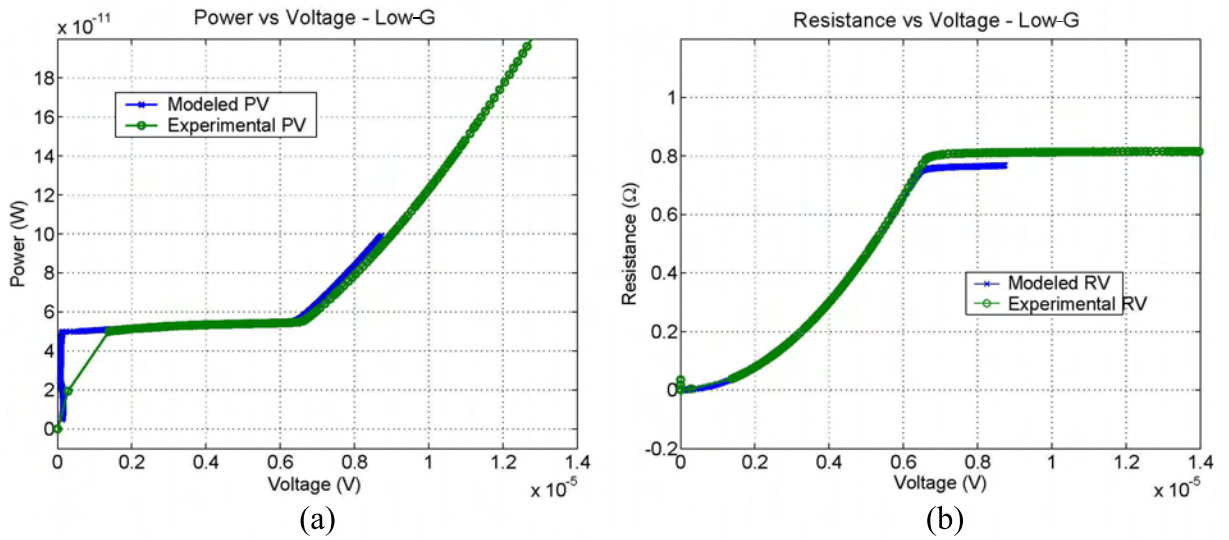


Figure 6.31: Comparison between measured power, resistance and that of modeled parameters for the Low-G layout.

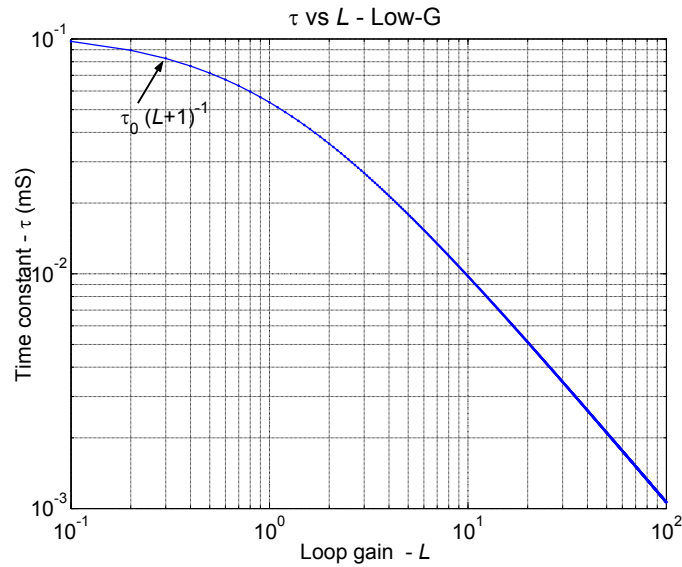


Figure 6.32: Relation between τ and loop gain L for the Low-G layout.

6.9.2 Time constant measurements

The heat capacity calculations for Low-G layout are shown in Table 6.4. The overall heat capacity is considerably lower than for the High-G layout because:

- The silicon nitride membrane is structured so that the deposition of a continuous titanium film is difficult. Hence, instead of a continuous titanium film absorber, Au-Pd cross absorbers are used. The overall heat capacity of an Au-Pd absorber is $\sim 25\%$ lower than that of continuous titanium film absorber (Tables 6.2 and 6.4).

Table 6.4: Thermal heat capacity budget for Low-G layout at 450 mK.

Material	C_ν Electron (J/cm ³ K ²)	C_ν Lattice (J/cm ³ K ⁴)	Volume (cm ³)	C (J/K)
Thermistor:				
Au-Pd	2.5×10^{-4}	4.2×10^{-4}	8.6×10^{-11}	1.3×10^{-14}
Mo	1.1×10^{-3}	9.3×10^{-4}	8.6×10^{-10}	5.0×10^{-13}
Electrical Leads:				
Nb		8.6×10^{-6}	3.8×10^{-9}	2.9×10^{-15}
Absorber:				
Au-Pd	2.5×10^{-4}	4.2×10^{-4}	1.1×10^{-9}	1.6×10^{-13}
Si ₃ N ₄		8.2×10^{-8}	2.5×10^{-6}	1.9×10^{-14}
Total				6.9×10^{-13} J/K

- The Si₃N₄ membrane is structured so there is no need of a gold (Au) ring around the absorbing center patch. The gold ring is the main contributor of the heat capacity hence removing the gold ring will reduce the time constant significantly (Tables 6.2 and 6.4).
- The area of the silicon nitride membrane in the Low-G layout is reduced by ~ 70 % compared to that of the High-G layout.

Gold has higher thermal conductivity than the silicon nitride membrane, hence the deposition a gold ring around the absorbing center patch on the silicon nitride membrane creates an uniform thermalized area. The High-G layout does not have a structured membrane hence the gold ring is required to define the heat flow. Thus, the temperature change caused by radiation is detected by the Au-Pd/Mo thermistor with little loss. The Low-G layout has a structured membrane hence heat flow is well defined, making the gold ring superfluous. The modeling of a gold ring for a structured silicon nitride membrane is shown in § 6.12.

The estimated heat capacity of the bolometer for Low-G layout is 6.9×10^{-13} J/K. Using FEA, the thermal conductance estimated in the transition range near to the normal range is 3.1×10^{-9} W/K. The intrinsic time constant of the bolometer near to the normal resistance range (τ_o) is 0.22 ms. In the transition region, when the bolometer is near to the normal range the negative ETF is lowest hence it is possible to determine the intrinsic time constant accurately. It was not possible to measure the optical time constant so it is not compared with modeled τ values. As shown in the Fig. 6.25, the $I - V$ curves are steeper near to the superconducting range hence the loop gain is higher. The calculated loop gain is ~ 61 which reduces the time constant to $3.6 \mu\text{s}$. Fig. 6.32 compares τ and L . These calculations are valid for $5 \mu\text{V}$ bolometer voltage.

6.9.3 Noise measurements

Since the thermal conductance for the Low-G layout is inadequate to work at a 300 K background, the measurements are not performed. An analysis similar to that explained in § 6.8.4 is performed. Fig. 6.33 (a) shows the noise current distribution from different sources of noise. The total noise is calculated by adding all the sources of noise quadratically. These noise contributions are calculated at $5 \mu\text{V}$ bolometer voltage. The experimentally measured noise at 0.3 K background is 1.6 times higher than the modeled noise. The noise voltage is simulated considering the contribution from photon noise at different background temperature. The simulated noise voltage is 1.5×10^{-5} V/ $\sqrt{\text{Hz}}$ at 0.3 K and

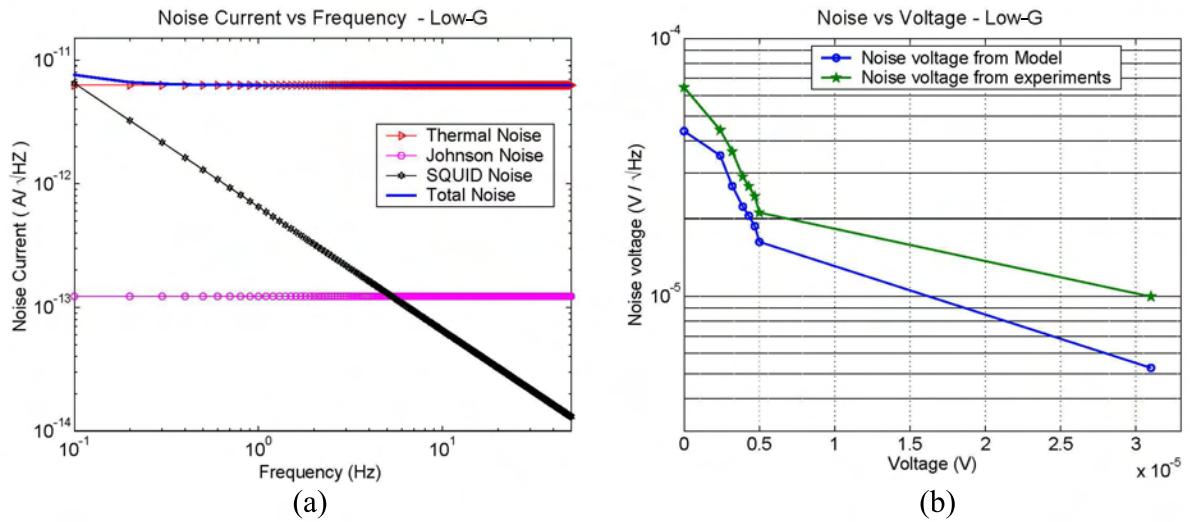


Figure 6.33: (a) Predicted noise current of the Low-G layout. The values are obtained from the bolometer model. Thermal noise (phonon noise) is the main source of noise so it follows the total noise. (b) Relation between the measured and calculated noise at different voltages.

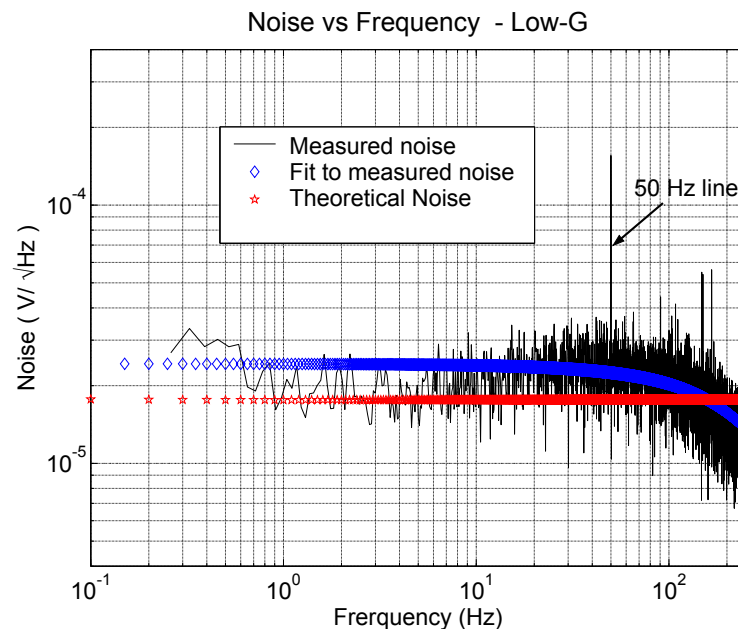


Figure 6.34: Comparison between the measured noise voltage with that of the model for Low-G layout. The measured noise is fitted with a low pass filter function. An 88 Hz low pass filter function is fitted to the measured noise.

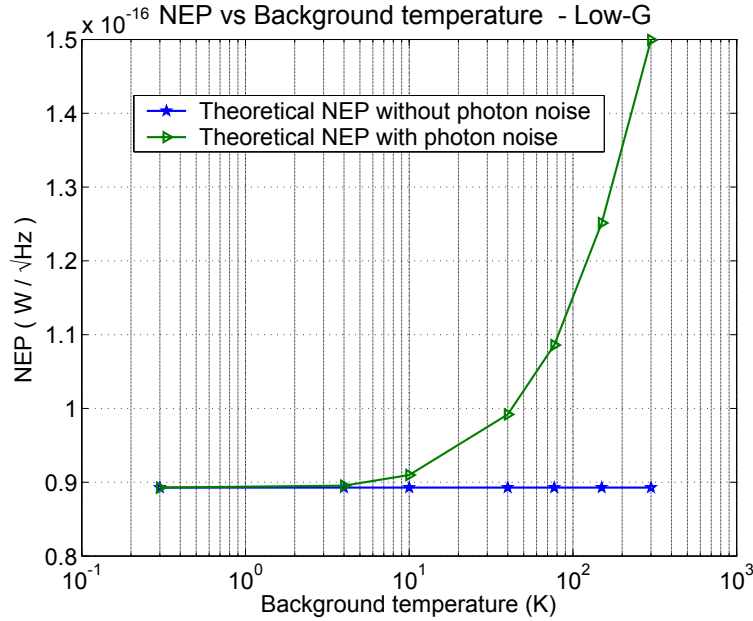


Figure 6.35: NEP plotted as a function of background temperature. The photon noise is calculated at different background temperatures from the bolometer model. Due to inadequate thermal conductance it was not possible to experimentally measure the optical NEP.

$3.6 \times 10^{-5} \text{ V}/\sqrt{\text{Hz}}$ at 300 K. The experimentally measured spectra are obtained by integrating over ~ 200 seconds.

The noise dependence on the bolometer bias was measured. As shown in Fig. 6.33 (b), the noise voltage increases with decreasing bolometer voltage. According to the VSB theory, the detector responsivity (S_i) is proportional to the bias voltage and to the loop gain (L). L is dependent on the steepness of the transition curve (α) hence when the bias voltage decreases the steepness of the curve increases. The calculated noise voltage from the model at different bolometer voltages is compared with the experimentally measured noise. Fig. 6.33 (b) compares the measured and simulated noise voltage at different bolometer voltages. The slope of the noise voltage curve changes at lower bolometer voltages because of strong negative ETF. The $I - V$ curves are steeper near to the superconducting range hence α and S_i increase, which causes the increase in noise voltage. The low pass filter, is obtained by the R-C circuit. The resistor of $18 \text{ K}\Omega$ and the capacitor of $0.1 \mu\text{F}$ was used in shunt circuit to create an 88 Hz anti-aliasing filter. The measured noise values are fitted with a low pass filter function.

6.9.4 NEP calculations

Since it was not possible to measure the the optical NEP, theoretical values of electrical NEP were estimated for different background temperatures. The calculated NEP value without photon noise (0 K background) is $8.9 \times 10^{-17} \text{ W}/\sqrt{\text{Hz}}$.

The NEP of the High-G layout is higher than that of the Low-G by a factor of ~ 5 . The reduced value of the thermal conductance decreases the contribution from the thermal fluctuation (phonon) noise, hence the overall noise voltage decreases. Since the responsivity is inversely proportional to the thermal conductance, the optical NEP of Low-G should be lower by a factor of ~ 3 or more. Since the thermal conductance for the Low-G configuration is too low for 300 K operation, experiments and simulations were performed on a design with higher thermal conductance, i.e. the Medium-G layout. It is possible to design bolometers for lower background, which will reduce the NEP significantly.

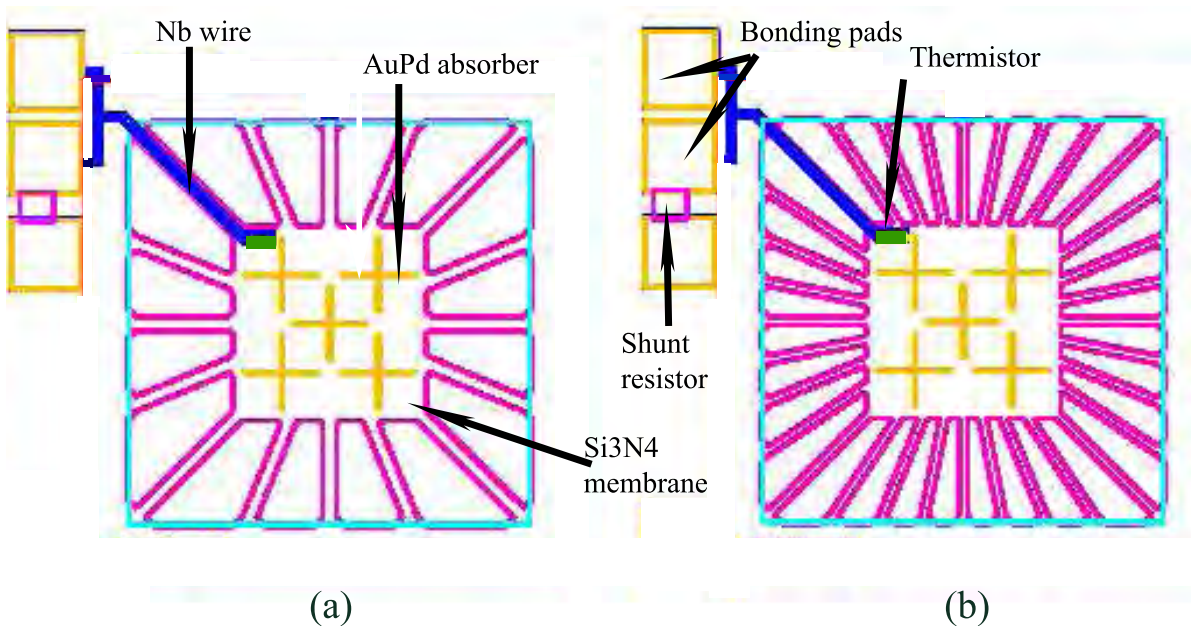


Figure 6.36: CAD layout for single pixel Medium-G layout with 16 legs and 32 legs.

6.10 4SN 1762–16-leg Medium-G –without Au ring–Experiment and Model

Due to fabrication problems, a large fraction of the legs in the 8-leg Medium-G layout were broken whereas the thinner legs of the Low-G layout on the same wafer survived. It was suspected that the stress on the thick legs of the silicon nitride membrane for the Medium-G layout is high. New Medium-G bolometers with 16 and 32 legs were fabricated (4SN 1762). This experiment is performed with 16-leg Medium-G layout without the gold ring. The silicon nitride membrane is $3.3 \text{ mm} \times 3.3 \text{ mm}$ square and the absorbing center patch is $1.6 \text{ mm} \times 1.6 \text{ mm}$. The legs are $850 \mu\text{m}$ long. Fig. 6.36 shows the CAD layout for Medium-G with 16 and 32 legs. The leg width for the 16-leg design is $114 \mu\text{m}$ and for 32-leg design, it is $68 \mu\text{m}$. Radiation is coupled to the dipole cross absorbers, placed on the center patch. The thermistor is placed in one corner of the absorbing center patch in order not to disturb coupling of radiation to the absorber. Since the silicon nitride membrane is structured there is no necessity of gold ring.

Fig. 6.37 shows the steady state temperature distribution from the finite element analysis of the 16-leg Medium-G layout without gold ring. The total thermal conductance of the silicon nitride legs is designed to be same as that of the 8-leg Medium-G design. The meshing and finite element analysis is performed in the standard way.

6.10.1 $I - V$ and $R - T$ measurements

Experiments with 16-leg Medium-G layout were done under $\sim 0 \text{ K}$ and 300 K background. Fig. 6.38 shows the measured $I - V$, $R - T$, $P - V$ and $R - V$ curves at $\sim 0 \text{ K}$ background. As shown in the plots all the $I - V$ and $R - T$ curves are smooth and there are no jumps in the data. It was possible to measure data for all the channels. The spread in transition temperature for all the channels is in the range $\pm 15 \text{ mK}$. In the normal range, the slope of the $I - V$ curves corresponds to the $\sim 3 \Omega$ normal resistance. The $R - T$ measurements are performed at the very low bolometer voltage of $0.3 \mu\text{V}$.

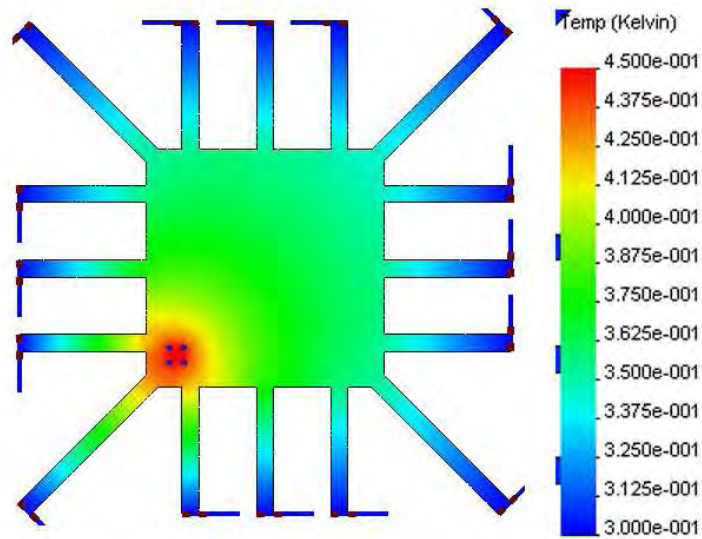


Figure 6.37: Steady state temperature distribution from finite element analysis for a 16-leg Medium-G layout without Au ring. The thermistor is maintained at transition temperature of 450 mK while the silicon wafer is maintained at the bath temperature of 300 mK.

Table 6.5: Transition temperature and Transition width (in bracket) for all the channels of 4SN 1762

CH1 (mK)	CH2 (mK)	CH3 (mK)	CH4 (mK)	CH5 (mK)	CH6 (mK)	CH7 (mK)
471 (2.47)	478 (2.61)	481 (2.37)	477 (2.38)	475 (2.39)	467 (3.06)	469 (2.41)

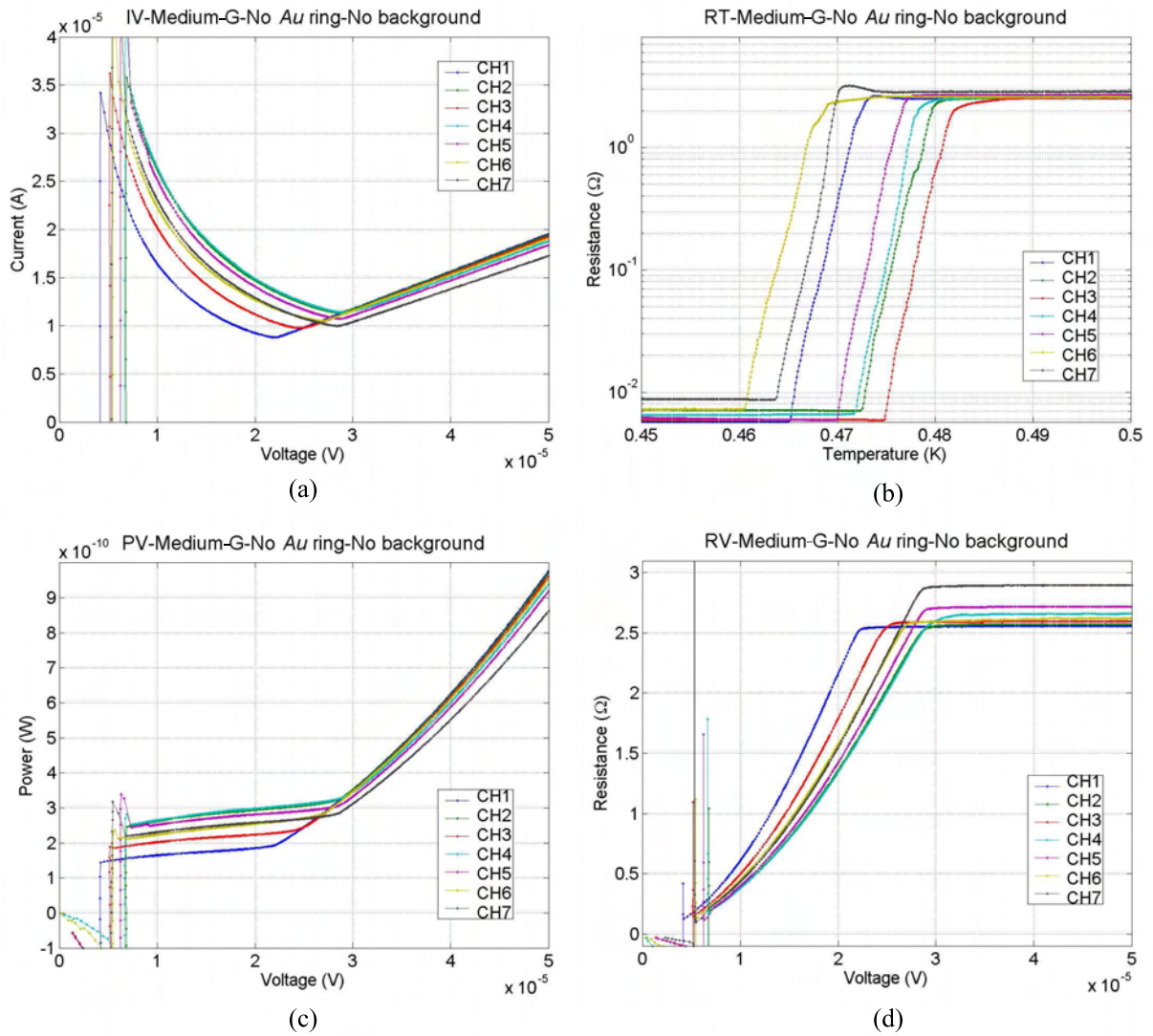


Figure 6.38: Experimental results of Medium-G - 16 leg-without Au ring layout 4SN 1762. This experiment was performed at 0 K background. In panel (a), the $I - V$ measurements for all the channels are plotted. Panel (b) shows the $R - T$ measurements. Panel (c) and (d) show the dependence of the bolometer power and resistance on the bolometer voltage.

In the previous designs the normal state resistance was 1Ω but a value of 3Ω was found to be more suitable. This value was chosen by considering the following issues:

1. The thermistor resistance should be selected to match the SQUID readout. The ideal thermistor resistance value is calculated from the the SQUID inductance and the resistance of the input coil. The contribution from SQUID noise should be lower than $1 \times 10^{-17} \text{ W}/\sqrt{\text{Hz}}$ which corresponds to $1 \text{ pA}/\sqrt{\text{Hz}}$. Ideally the SQUID noise should be negligible i.e. $\text{NEP}_{\text{Squid}} = 0.1 \text{ NEP}_{\text{Total}}$. From the current noise of $1 \text{ pA}/\sqrt{\text{Hz}}$ and using Eq. 2.40, the ideal $V_{\text{bias}} = 10 \mu\text{V}$ and $R = 0.35 \Omega$ is calculated. Thus, in order to obtain the proper bias voltage $R_{\text{Bias}} < R/7 = 70 \text{ m}\Omega$. The shunt resistance used to obtain the bias voltage across the bolometer is $33 \text{ m}\Omega$. In order to obtain sufficient dynamic range the thermistor resistance $R_{\text{thermistor}} > 7R = 2.5 \Omega$. It was therefore, decided to change the normal state resistance of the thermistor from 1Ω to 3Ω .
2. From the previous experiments, it appeared that when the normal state resistance of the bolometer decreased the steepness also decreased. Hence in order to obtain higher steepness (higher α) and to reduce the time constant, the normal state resistance of the thermistor should increase. This has the disadvantage that the operating range of the bolometer is reduced since the transition curve is steeper.
3. Care should be taken to keep the normal state resistance of the TES thermistor low so the bolometer impedance remains at low values in the transition. The value should be selected by optimizing α and the thermistor impedance.
4. The existing technology and equipment at our disposal.

The transition widths for all the channels are calculated from the $R - T$ measurements. It is defined as the difference between the transition temperature when the thermistor resistance is 0.85 the normal state resistance and when it is 0.15 times that value. Table 6.5 shows the transition temperature and the transition widths for all the seven channels calculated at $0.3 \mu\text{V}$ of bias voltage. The transition widths for all the channels is small hence α is high and the τ of the bolometer decreases significantly in the operating range.

Further experiments with the same array were done at 300 K. Fig. 6.39 shows the $I - V$ and $R - T$ curves. As compared to the experiment without background, the bolometers goes into the transition range at lower bias voltage and the transition range is also shifted to the lower temperature values. This is mainly due to the contribution from the background power. During the experiment without background only the bias power heats the bolometers. Hence, a smaller bias voltage is sufficient to drive the bolometer from superconducting to normal state. The background power also affects the $R - T$ measurements in a similar way, hence the transition temperature is different during the experiment at 300 K.

As shown in the Fig. 6.39, CH3 did not produce usable $R - T$ and $I - V$ curves while CH1 showed a very low temperature. The similar experiment without background (§ 6.10.1) showed similar superconducting transitions for all the channels. This could mean that there is an extra signal on the two channels. This might be due to the inhomogeneities in the filter at the 1.5 K stage or inhomogeneities in the horn antennas. The experiments were repeated by rotating the filter or the horn array in steps of 90° , one at a time. The $I - V$ and $R - T$ curves did not change. It is concluded that there are no effects from the filter or the horn antenna. Possible explanations include differences in the thermal conductance, the thermal boundary resistance or the mechanical stress. In § 6.10.2, the silicon nitride membrane is modeled in an attempt to understand the non-working channels.

Modeling of the $I - V$ curve

All the seven thermistors are $100 \mu\text{m}$ square. Figs. 6.40 and 6.41 compare the modeled $I - V$, $R - T$, $P - V$ and $R - V$ curves with experimentally determined ones. Fig. 6.38 (b) shows the $R - T$ measurements

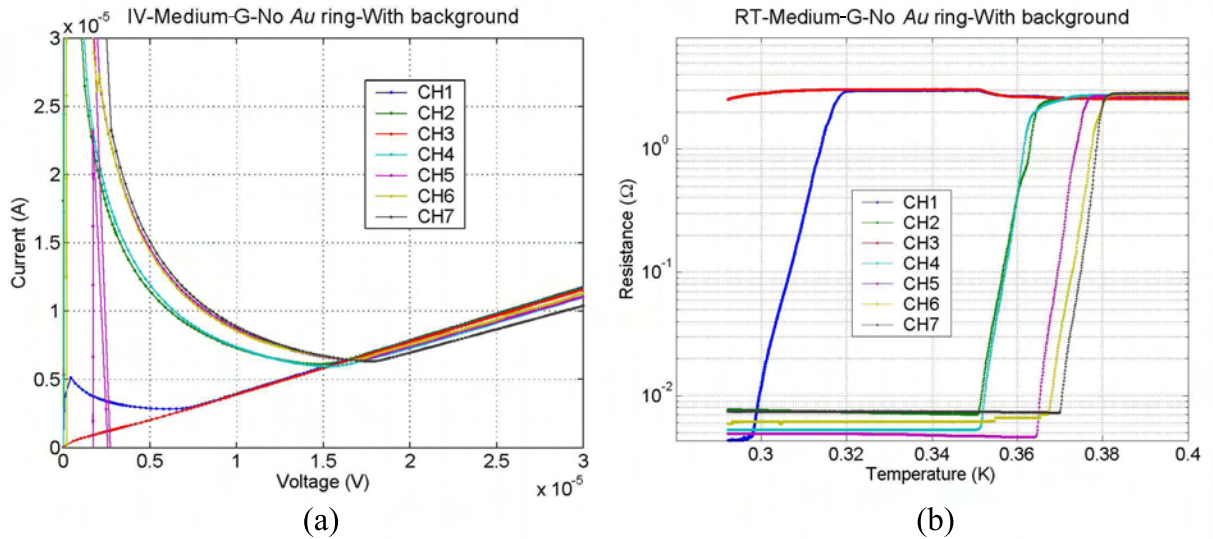


Figure 6.39: $I - V$ and $R - T$ measurements of 4SN 1762, 16-leg spider Medium-G layout without Au ring. The measurements are from the experiment at 300 K background.

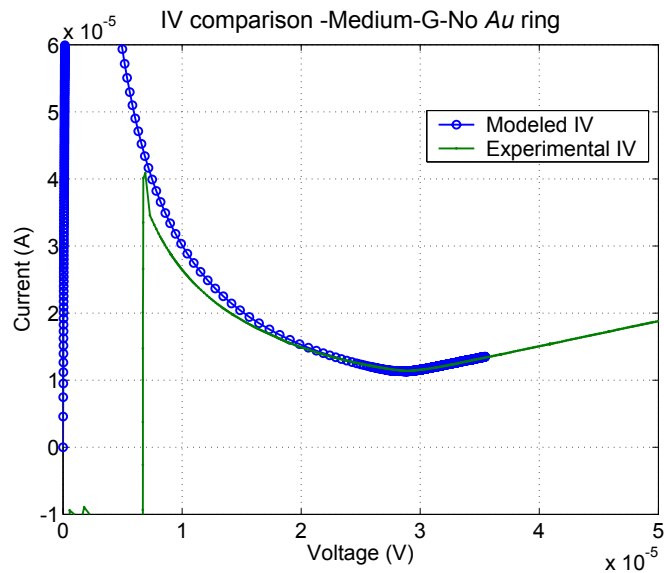


Figure 6.40: Comparison of modeled $I - V$ curve with the experimentally measured one (using a $33 \text{ m}\Omega$ shunt resistor for 16-leg Medium-G layout without Au ring). $I - V$ curves are compared for CH4. The measurements were performed without background.

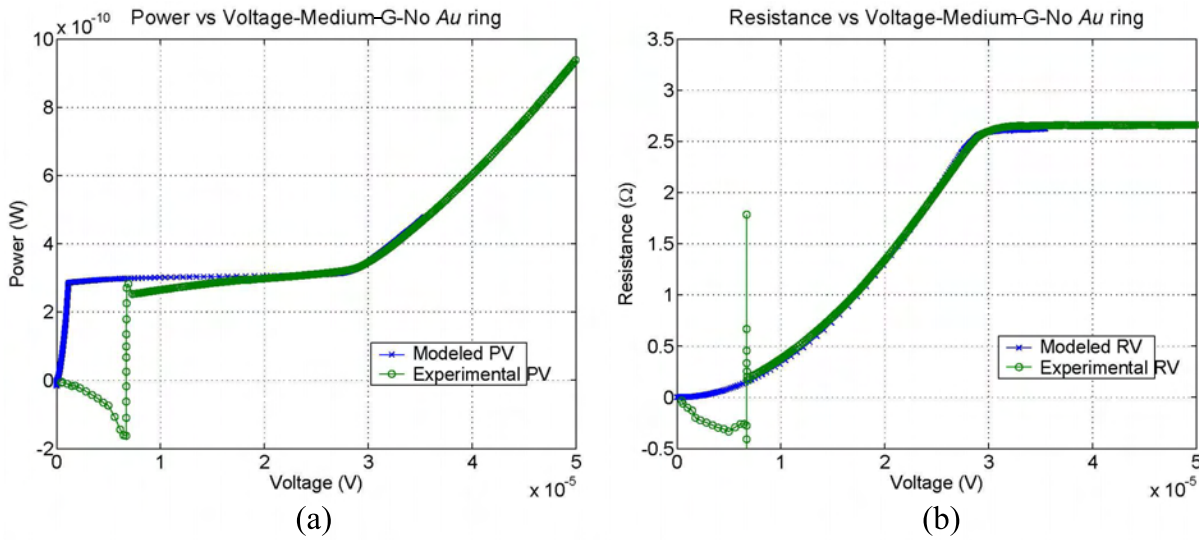


Figure 6.41: Comparison between measured power, (a) and resistance (b) vs. voltage and modeled parameters for the 16-leg Medium-G layout without Au ring. The comparison is shown for CH4.

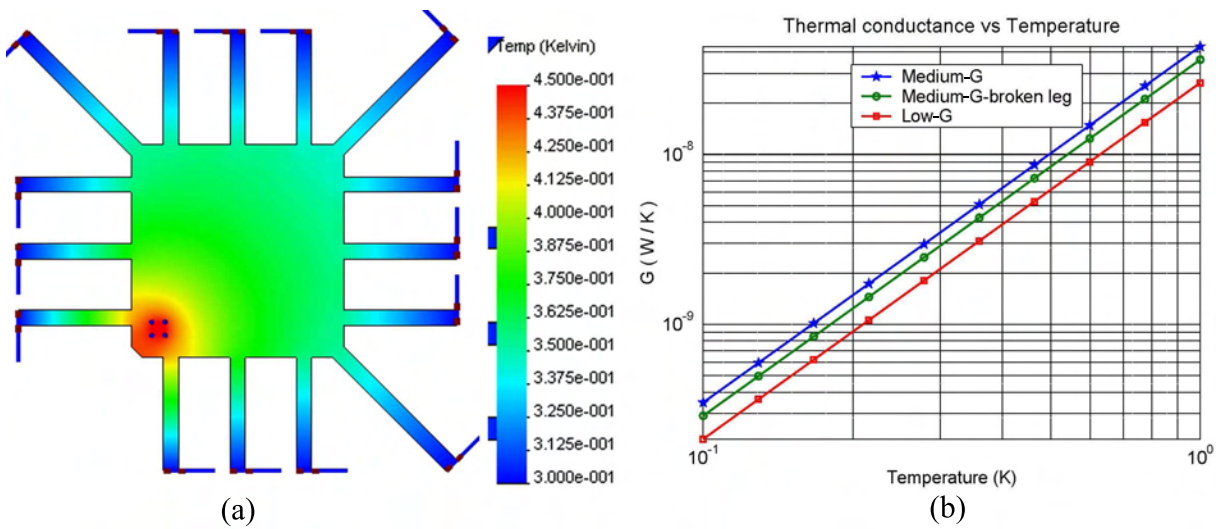


Figure 6.42: (a) Steady state temperature distribution from finite element analysis with broken Si₃N₄ leg. The leg adjacent to the thermistor is assumed to be broken. (b) Thermal conductance calculated for this case.

for all the channels. The transition temperature for all the channels is within a temperature range of ± 15 mK hence the simulation should be valid for all the channels.

The bolometer goes into transition range at a bias voltage of $28 \mu\text{V}$ without background and at $11 \mu\text{V}$ with 300 K background. The power dissipated in the bolometer during the transition is between 275 and 325 pW and the normal state resistance is 2.6Ω . The modeling assumes a shunt resistance of $33 \text{ m}\Omega$ and bias series resistance of 1045Ω .

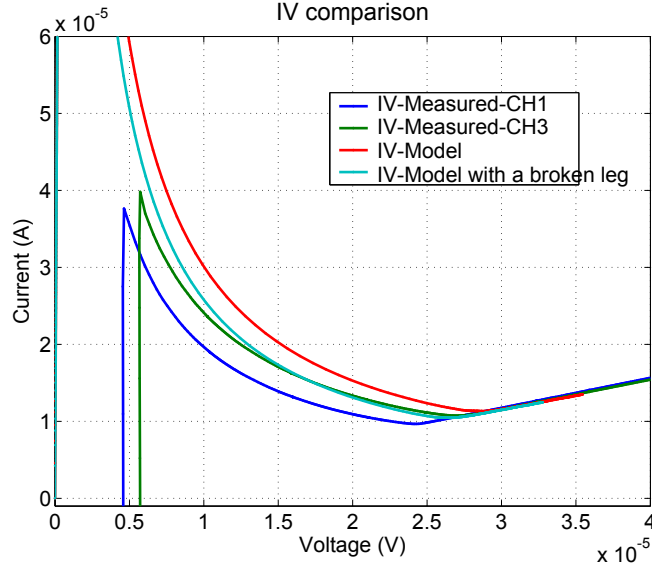


Figure 6.43: Comparison of different $I - V$ curves for CH1 and CH3. Simulated $I - V$ curves are obtained by considering a transition temperature of 450 mK and a thermal conductance equivalent to that of the Medium-G case and the Medium-G case with broken Si_3N_4 leg.

6.10.2 Modeling of the broken Si_3N_4 membrane

To understand the behavior of CH1 and CH3, a hypothetical case is considered, where a Si_3N_4 leg adjacent to the Au-Pd/Mo thermistor is broken. The finite element analysis model is shown in Fig. 6.42 (a). It is assumed that the heat is applied to the thermistor which causes an increase in temperature of the thermistor. Due to the broken Si_3N_4 leg, the direction of heat flow from the thermistor to the wafer changes. Thus, in the silicon nitride membrane, the structure of the heat dissipation to the wafer changes. Fig. 6.42 (b) shows the calculated thermal conductance for the Medium-G layout with broken Si_3N_4 leg. It is compared with the Medium-G and Low-G layout. The change in the thermal conductance is significant because the leg adjacent to thermistor is broken. If the Si_3N_4 leg, farther from the thermistor were broken, the change in the thermal conductance would be less drastic.

For the $R - T$ measurements, the whole array is heated using the external bias power so it will not be affected by the broken Si_3N_4 legs. The $I - V$ measurements are performed by applying the bias power to the thermistor and measuring the output current. A broken Si_3N_4 leg adjacent to thermistor can affect the $I - V$ measurements. This discussion can be applied to CH1 and CH3. For the experiment with 0.3 K background, the $R - T$ curve shows the expected transition temperature but the $I - V$ curve does not correspond to the respective $R - T$ values. If the thermal conductance of CH1 and CH3 is different from that of the other channels, such behavior can be explained. The thermal conductance for these channels can be different, if the Si_3N_4 legs adjacent to the thermistor have a crack which is difficult to see by the naked eye or microscope. Thus, the different $I - V$ curves of CH1 and CH3 can be explained by these simulations. The $I - V$ curves are simulated considering a transition temperature of 450 mK and the thermal conductance of Medium-G with broken leg layout. Fig. 6.43 shows a comparison of the simulated $I - V$ curves and the measured $I - V$ curves for CH1 and CH3. For CH3, the simulated $I - V$ curve of the broken leg case is close to the measured $I - V$ curve, hence, the thermal conductance of CH3 is equivalent to that obtained from the FEA of broken silicon nitride leg (Fig. 6.42). The thermal conductance of CH1 is less than that of a broken silicon nitride membrane.

Table 6.6: Thermal heat capacity budget for 16-leg Medium-G layout without Au ring at 450 mK.

Material	C_ν Electron (J/cm ³ K ²)	C_ν Lattice (J/cm ³ K ⁴)	Volume (cm ³)	C (J/K)
Thermistor:				
Au-Pd	2.5×10^{-4}	4.2×10^{-4}	8.6×10^{-11}	1.3×10^{-14}
Mo	1.1×10^{-3}	9.3×10^{-4}	8.6×10^{-10}	5.0×10^{-13}
Electrical Leads:				
Nb		8.6×10^{-6}	3.8×10^{-9}	2.9×10^{-15}
Absorber:				
Au-Pd	2.5×10^{-4}	4.2×10^{-4}	1.1×10^{-9}	1.6×10^{-13}
Si ₃ N ₄		8.2×10^{-8}	3.2×10^{-6}	2.4×10^{-14}
Total				7.1×10^{-13} J/K

6.10.3 Signal measurements

The Au-Pd cross absorbers are deposited on the silicon nitride membrane to provide optical coupling. Fig. 6.44 shows the signal measured with a lock-in amplifier and the noise observed from the *timeseries* measurement. Fig. 6.45 shows the signal to noise behavior at different bias voltages.

Time constant measurements

It is possible to measure the time constant for the remaining five channels which showed proper $I - V$ and $R - T$ curves. Its variation as a function of bolometer voltage is shown in Fig. 6.46. The time constant in the TES is reduced by the loop gain which depends on the steepness of the transition curve (α). When the bolometers are near to the normal range, their time constant is higher since the transition curve is not so steep there. At this point $\tau_{normal} \approx \tau_o$, where τ_o is the intrinsic time constant of the bolometer. In the middle of the transition curve, where it is steeper, the time constant is reduced. The transition curves are also less steep near the superconducting range hence, as shown in Fig. 6.46, the time constant increases at low bias voltages. Variations are observed in the time constant for different channels but the overall pattern is similar. The time constant is ~ 6 times smaller than that of High-G layout (Fig. 6.20). The absence of the gold ring reduces the total heat capacity significantly, hence the time constant is reduced. The frequency limit of the mechanical chopper of the blackbody is 320 Hz. At this frequency the signal had dropped by only $\sim 20\%$, which makes a meaningful fit to the data unreliable. In order to characterize the time constant more accurately, an electronically modulated Gunn diode in combination with a frequency doubler was used. The signal from the Gunn diode can be modulated from 1 Hz to 1280 Hz, where the bolometer signal amplitude drops by more than 50%. However, the time constant measurements obtained from the Gunn diode were similar to those obtained from the blackbody measurements.

The SNR is highest at a bolometer voltage of $\sim 8.8 \mu V$ where the time constant of the bolometer is smallest (Fig. 6.45). This can be explained by VSB theory:

- As shown in Eq. 2.40, the noise of a VSB depends on its current responsivity (S_i). S_i is a frequency dependent term which is correlated with the loop gain L and the time constant (Eq. 2.39). In the transition range when the curves are steeper, τ decreases and L increases which eventually increases S_i and decreases the contribution from noise current sources. Hence the SNR increases when the time constant decreases.

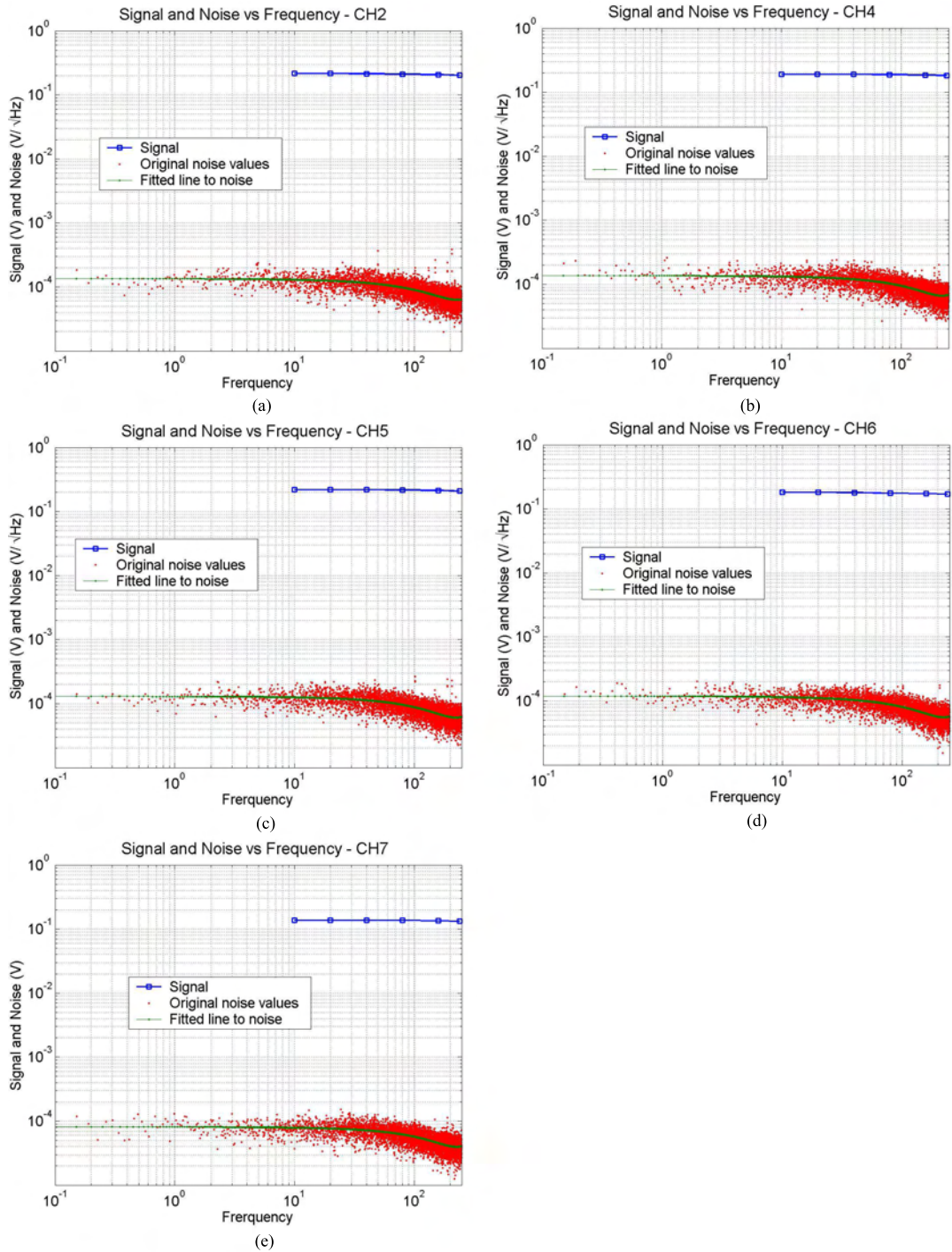


Figure 6.44: Signal and noise as a function of modulating frequencies for the 16-leg Medium-G layout without Au ring. The bolometer voltage is $8.8 \mu\text{V}$. The data acquisition of the noise is performed with *timeseries* measurements. The signal is measured with a lock-in amplifier hence it does not drop off at high frequencies. Measurements are done at 300 K.

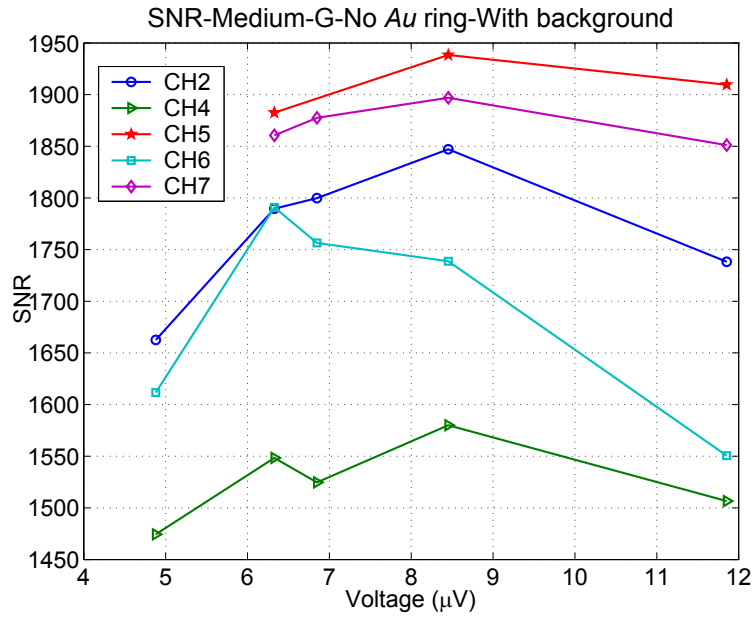


Figure 6.45: Signal to noise measurements for all the channels at different bias voltages for 16-leg Medium-G layout without gold ring.

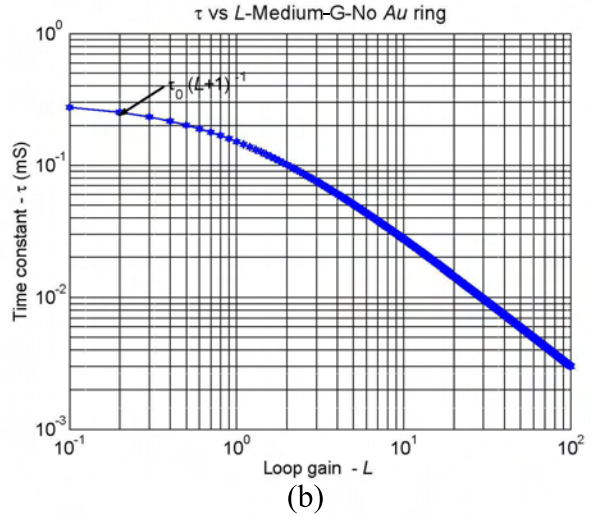
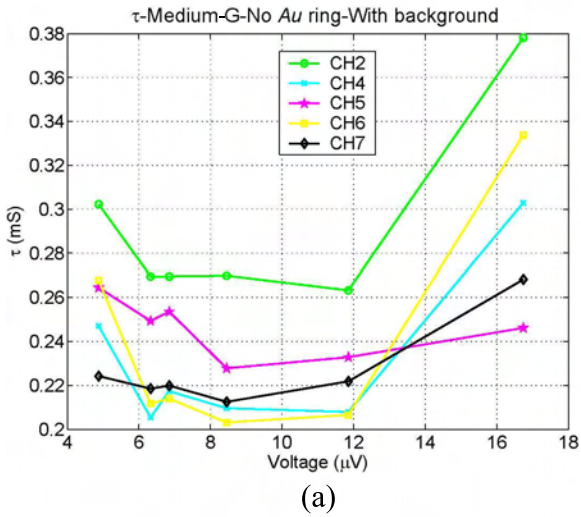


Figure 6.46: τ and signal to noise data for 4SN 1762, 16-leg spider Medium-G layout without Au ring. The measurements are from the experiment at 300 K. (a) The τ plotted at different bias voltages for all the channels. (b) The relation between τ and loop gain L for the same layout.

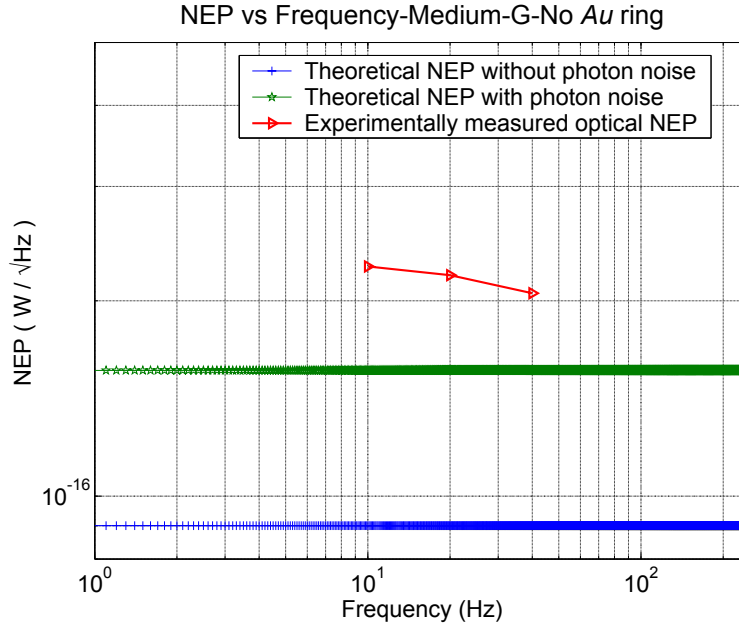


Figure 6.47: NEP plotted as a function of frequency. For comparison, plots of the theoretical NEP, with and without contribution from photon noise of 300 K background are included

The heat capacity (C) calculations for the 16-leg Medium-G layout without the gold ring are shown in Table 6.6. The calculated total heat capacity, C is 7.1×10^{-13} J/K and the thermal conductance from FEA analysis is 3.6×10^{-9} W/K. Using these values, we derive an intrinsic time constant of the bolometer (τ_o) of 0.2 ms. This is the time constant obtained when the bolometer is near the normal range hence it is not affected by the loop gain (L). Here, the thermal conductance is highest and obtained from the finite element analysis model. The heat capacity is less than for the High-G layout because of the reduction of the silicon nitride membrane area and the absence of the gold ring. The experiment reveals a time constant of 0.3 ms near to the normal range which corresponds to a heat capacity of 1.1×10^{-12} J/K. This is the heat capacity near to the normal resistance state. The experimentally measured C is ~ 1.5 times higher than theoretically calculated heat capacity. The measured C can be excessive for the following reasons:

1. For calculations of heat capacity, pure material properties are assumed and small impurities in the material can increase the heat capacity.
2. Heat capacity is obtained from the optical τ_o , which is measured at high bias voltage. Although at these bias voltage levels, the negative ETF effect is small, this can affect the τ_o measurements by a small amount.

Fig. 6.46 (b) shows the relation between τ and L . As shown in the experimental results, due to the strong negative ETF the time constant reduces to 0.21 ms. From the model the calculated time constant is 0.16 ms in the transition range.

Spectral response of the system

The spectral response of the system is measured (Fig. 6.48) with a Martin-Puplett interferometer (MPI: see § 4.7.2). The spectral response has ≈ 110 GHz bandwidth and is centered at a frequency of 250 GHz.

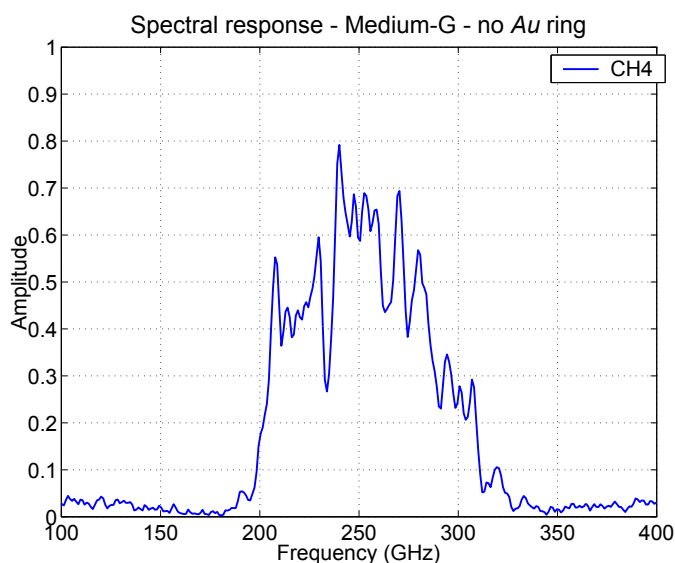


Figure 6.48: Spectral relative response of the 16-leg Medium-G layout without Au ring.

The internal reflections between the cryostat window and the interferometer window can create standing waves between the two surfaces. In order to test this, interferograms were repeatedly measured by changing the distance between the two surfaces and by successively changing the angle by 1° . The spectral response measured in all these attempts was identical. It can thus be concluded that the spectral response is not affected by the standing waves between cryostat and interferometer. Internal reflection between the filters inside the cryostat or within the interferometer could also cause the standing waves. In order to reduce the standing waves within the cryostat, the 1.5 K and 77 K stage filters have anti-reflection coatings. This suggests that the ripples in the transmission band are *Fabry-Perot* interferences mainly produced in the Martin-Puplett interferometer.

6.10.4 Noise measurements

Fig. 6.49 shows the noise measurements for five channels at different bias voltages. The noise spectra are obtained by integrating for ~ 240 seconds. The noise curves are scaled in order to distinguish between noise at different bias voltages. The scale factor is shown at the right corner of each noise spectrum. $1/f$ noise is observed at frequencies below 0.4 Hz at higher bias voltages. These measurements were done without background. Since there is no photon noise contribution, the thermal fluctuation (phonon) noise is the main source of noise.

The noise voltage was measured at different bias voltages. Fig. 6.50 compares the experimentally measured noise with the modeled noise at different bias voltages. The noise for a particular bias voltage is obtained by averaging the noise from 1 to 88 Hz. The bolometer responsivity (S_i) is inversely proportional to bias voltage and the loop gain, L . In the transition region, the steepness of the $I - V$ curve increases and with it L and S_i increases. The noise sources are dependent on the bolometer responsivity, hence the total noise current changes according to the applied bias voltage. Hence, the overall noise voltage of the bolometer also changes in relation with applied bias voltage. The slope of the noise voltage curve is directly proportional to the slope of transition curve. The model noise in Fig. 6.50 refers to the white noise calculated from the bolometer model. With increasing bolometer voltage, the responsivity of the bolometer decreases, and hence the noise voltage also decreases. As shown in the Fig. 6.50, the slope changes because the α is different at intermediate stages of transition curve.

The thermal fluctuation noise is the main source of noise without radiation background. The sources

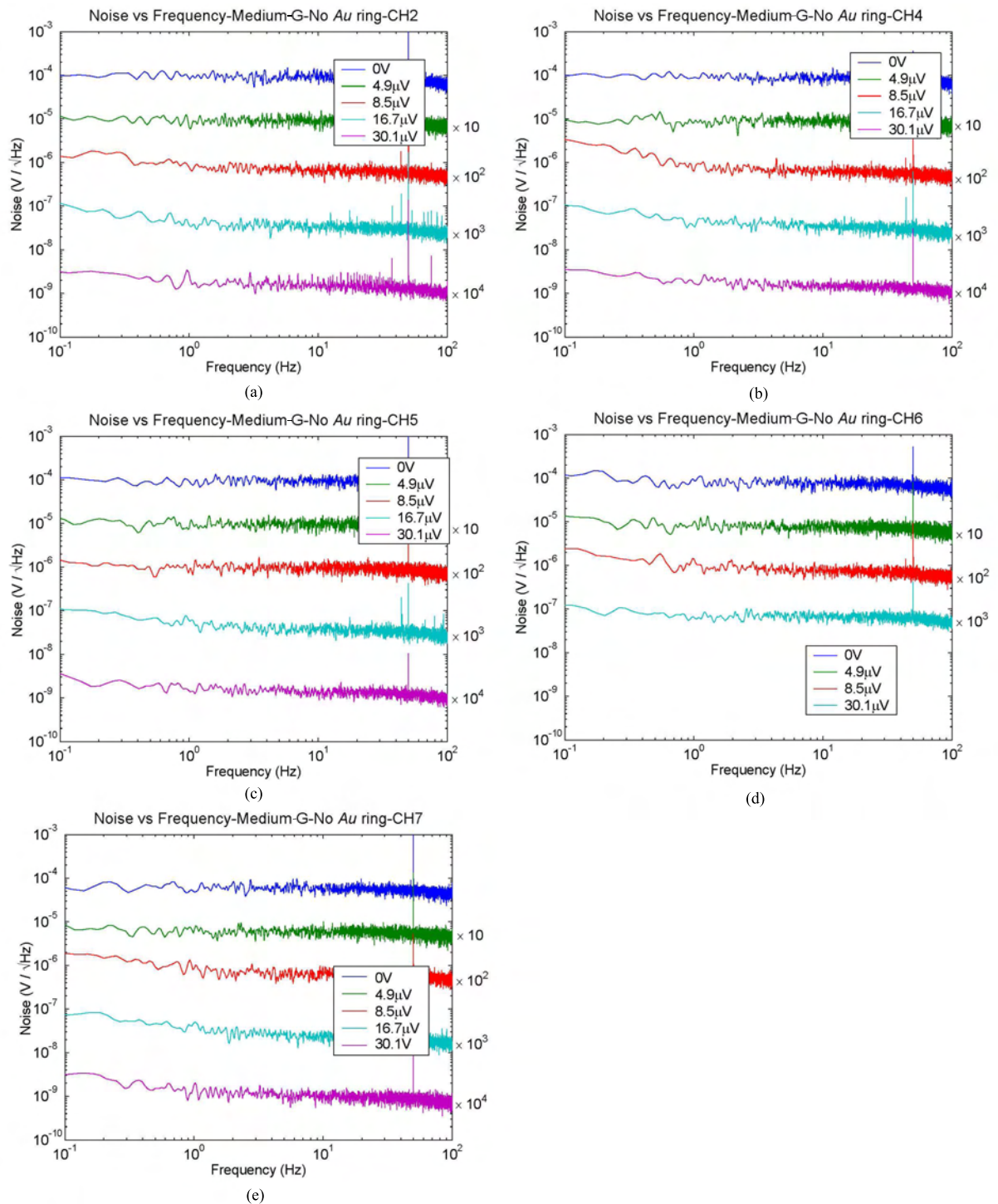


Figure 6.49: Noise measurements for the five channels CH2, CH4, CH5, CH6 and CH7 at different voltages. The Y-axis is scaled by a multiplication factor shown next on the right side of each noise curve.

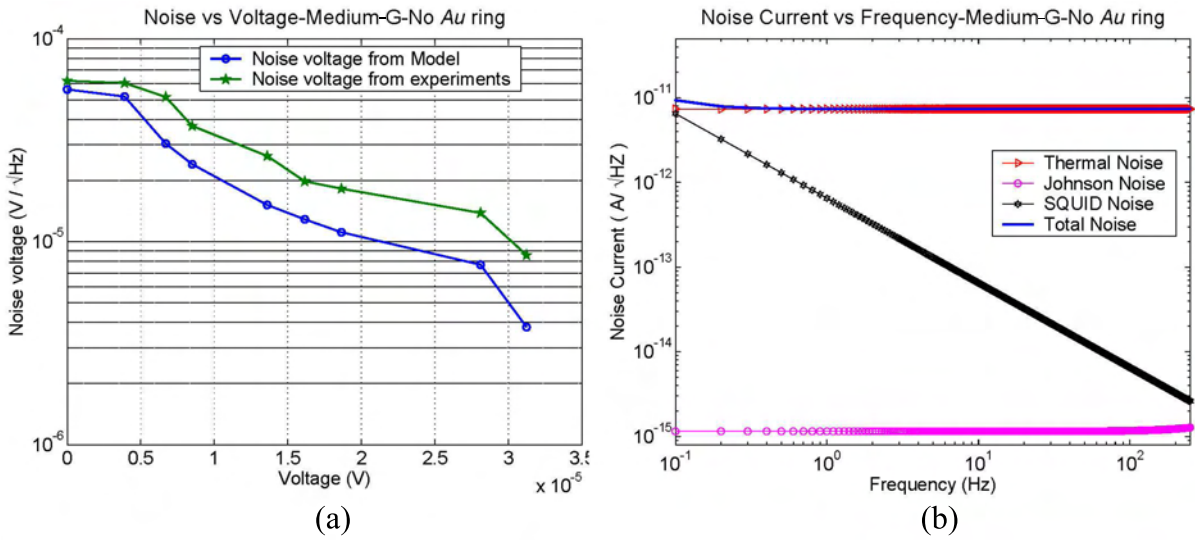


Figure 6.50: (a) Relation between the noise measured and calculated at different voltages for the 16-leg Medium-G layout without Au ring. (b) Predicted noise current of the 4SN 1762 array. The values are obtained from the bolometer model. The thermal noise (phonon noise) is the main source of noise so the total noise follows it. The noise currents are calculated at $8.8 \mu\text{V}$ of the bolometer voltage.

of noise current are plotted in Fig. 6.50 (b). This calculations are done for $8.8 \mu\text{V}$ bolometer voltage without background radiation. The total noise current is obtained by adding all the sources of noise current in quadrature. The noise voltage can be derived from the total noise current assuming that the gain of the SQUID electronics and the bias resistor values are known. The noise measurements are done in a high gain setting, i.e., FLL electronics gain of 2550000, and the 1045Ω of bias resistor is used. The noise voltage obtained from these calculations can be compared to the noise measured from the experiment.

Fig. 6.51 compares the noise voltage from experiments with that of obtained from the model. Subplot (a) is plotted with consideration of the photon noise of a 300 K background and subplot (b) is plotted without contribution from photon noise. The modeled noise voltage is $2.7 \times 10^{-5} \text{ V}/\sqrt{\text{Hz}}$ without background and $7.6 \times 10^{-5} \text{ V}/\sqrt{\text{Hz}}$ with photon noise of a 300 K background. As in High-G (§ 6.8.4) and Low-G (§ 6.9.4) layout, the experimentally measured noise voltage is higher than modeled noise voltage. During some experiments (Fig. 6.49) $1/f$ noise was observed below 0.4 Hz frequency. The modeling for $1/f$ is done in § 6.10.4.

$1/f$ noise characterization

The different sources of noise current plotted in Fig. 6.50 are calculated at $8.8 \mu\text{V}$ of bolometer voltage. The calculations shown in the Fig. 6.52 are performed by assuming that there is no contribution from the photon noise of the 300 K background. As shown in Fig. 6.49, $1/f$ noise is observed in some measurements. Fig. 6.52 shows the noise voltage, measured at different bias voltages. White noise, as predicted at different bias voltages, is also plotted along with measured noise. As already observed in the experiments with the High-G and Low-G layout, the noise measured from the experiments is higher than theoretically predicted. Since the $1/f$ noise contributes at very low frequencies ($< 0.4 \text{ Hz}$), it is difficult to measure its value precisely. $1/f$ noise is less significant at lower and higher bias voltages but its contribution also increases in the transition range (Fig. 6.52). Similar behavior was observed for all the channels. When the bolometers are in the transition range, the sensitivity of the bolometer is higher, hence they are sensitive to interference pickup. When the bolometers are in the normal range or

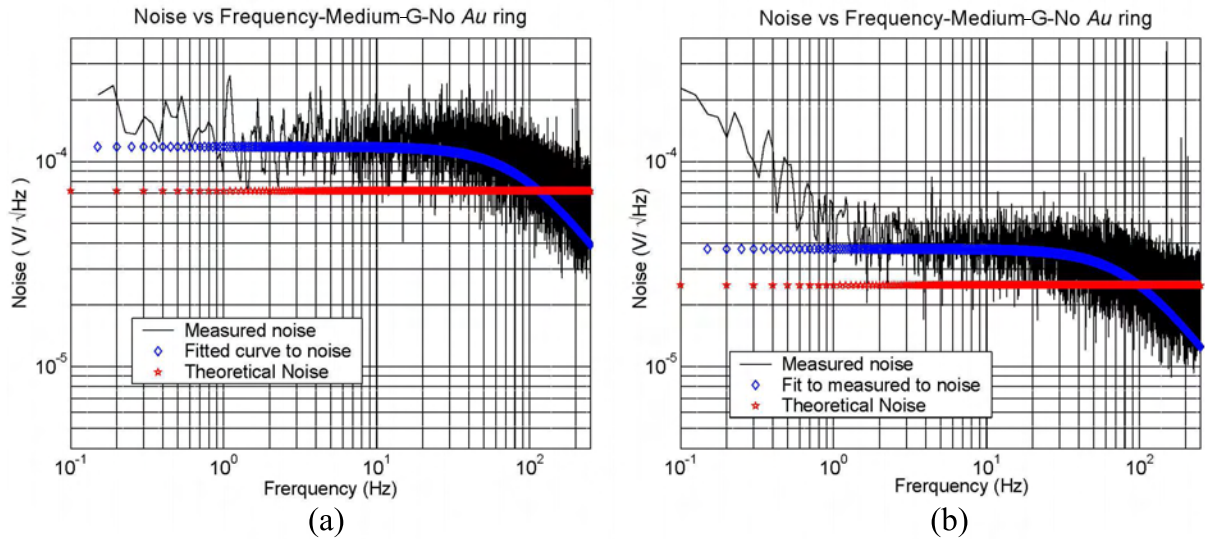


Figure 6.51: Comparison between noise voltage from experiments and the noise voltage from the model for 16-legs Medium-G layout without Au ring. The Measured Noise in the plot refers to the noise measured at (a) 300 K background and (b) 0.3 K background. An 88 Hz low pass filter function is fitted to the measured noise.

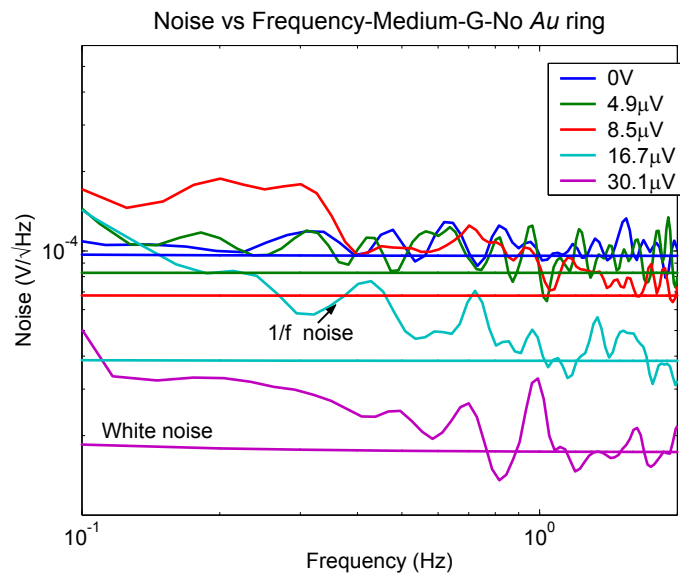


Figure 6.52: Plot is identical to Fig. 6.49 (a) at low frequencies, and plotted together with the white noise calculated from the bolometer noise model.

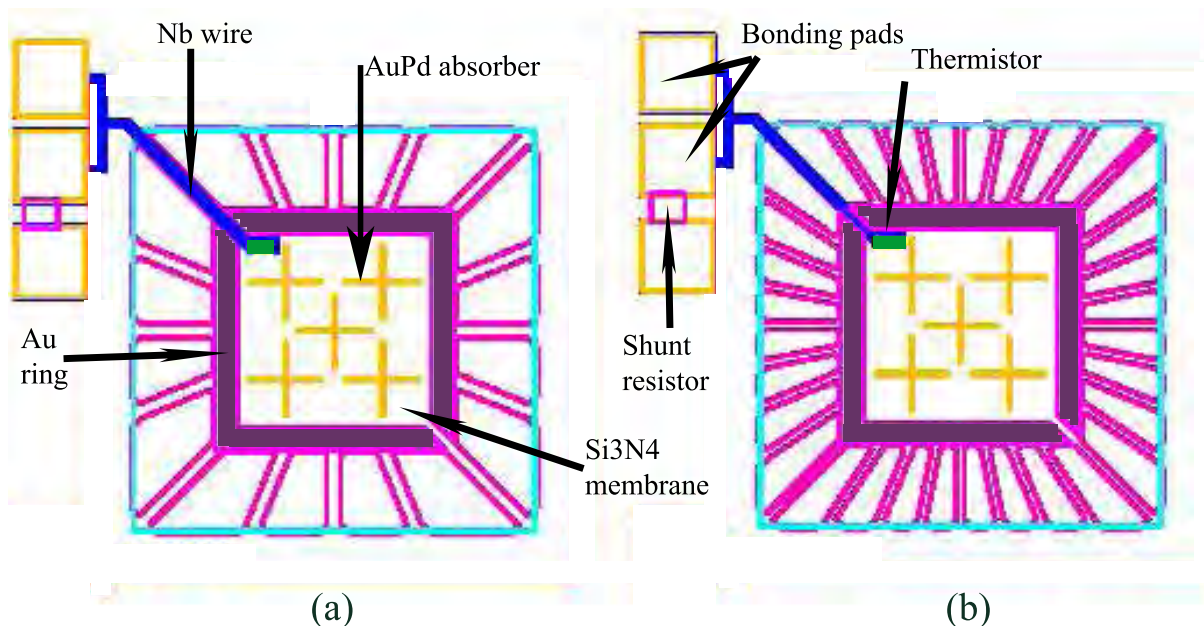


Figure 6.53: CAD layout of a single pixel of Medium-G layout with Au ring with 16-leg and 32-leg design. The value of the thermal conductance is maintained at Medium-G level. The Au ring adds extra heat capacity.

in the superconducting range, the white noise from the bolometer is the dominating noise. It was tried to determine the source of $1/f$ noise but a clear identification was not possible. Bad contacts in TESs can also cause the $1/f$ noise. Fig. 6.49 shows the $1/f$ noise contribution for all the channels. Since it is difficult to measure the $1/f$ noise precisely, it was not possible to systematically correlate it with the bias voltage.

6.10.5 NEP calculations

The signal and noise in Fig. 6.44 were measured at $8.8 \mu\text{V}$ bolometer voltage. The SNR is in the range between 1700 and 1950. The total noise is obtained by adding all the noise sources in quadrature. These measurements are performed at different bias voltages and the average values of the SNR at $8.8 \mu\text{V}$ bolometer voltage, is 1760. The estimated value of the NEP from the model is $9.7 \times 10^{-17} \text{ W}/\sqrt{\text{Hz}}$ without photon noise and $1.7 \times 10^{-16} \text{ W}/\sqrt{\text{Hz}}$ with a photon noise contribution from a 300 K background. Using this SNR value the measured optical NEP is $1.9 \times 10^{-16} \text{ W}/\sqrt{\text{Hz}}$. The best SNR obtained is 1941 which corresponds to the optical NEP of $1.6 \times 10^{-16} \text{ W}/\sqrt{\text{Hz}}$ but for the comparison with other bolometers, the NEP obtained from the average SNR is considered ($1.9 \times 10^{-16} \text{ W}/\sqrt{\text{Hz}}$). The measured NEP is ~ 3 times lower than that of High-G layout. Thus the sensitivity is increased by structuring the silicon nitride membrane. The theoretical NEP is calculated by dividing the estimated total noise current at the SQUID input by the responsivity. As explained in § 6.8.4, the $\text{NEP}_{\text{optical}}/\text{NEP}_{\text{photon}}$ ratio determines the background limited performance. From the model, the $\text{NEP}_{\text{optical}}/\text{NEP}_{\text{photon}}$ is 1.12 ± 0.03 and from the experiments the ratio is 1.28 ± 0.07 .

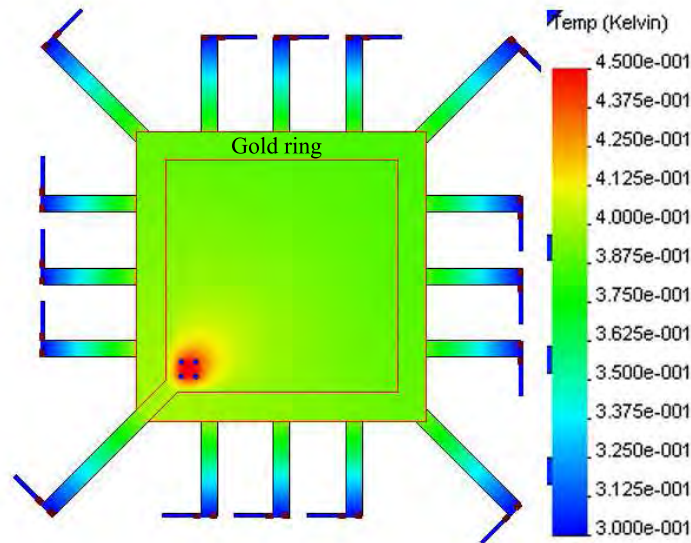


Figure 6.54: Steady state temperature distribution from finite element analysis for the 16-leg Medium-G layout with Au ring. The thermistor is maintained at transition temperature of 450 mK while the silicon wafer is maintained at 300 mK.

6.11 4SN 1762—16-leg Medium-G –with Au ring—Experiment and Model

Since the silicon nitride membrane in Medium-G layout is structured there is no necessity for a gold ring. The area within gold ring in High-G layout acts like a thermalized patch hence any temperature change due to the incoming radiation is coupled to the Au-Pd/Mo thermistor. In array 4SN 1762, a 150 nm thick gold ring was deposited on the silicon nitride membrane to study its effects. § 6.12 compares these specific results with those obtained from finite element analysis.

Fig. 6.53 shows the CAD layout of the 4SN 1762 array with gold ring. As explained in the previous section, due to technological reasons, instead of the 8-leg design, the Medium-G layout was fabricated in 16-leg and 32-leg designs. The silicon nitride membrane is of dimensions of 3.3 mm \times 3.3 mm and the absorbing center patch is of the dimensions of 1.6 mm \times 1.6 mm. The gold ring around the absorbing center patch has the width of 0.2 mm, hence the effective area of the absorbing center patch becomes 2 mm \times 2 mm. The legs of the silicon nitride membrane are 650 μ m long. The thermal conductance is directly proportional to the ratio of cross sectional area of heat flow and heat path length. The addition of the gold ring reduces the heat path length by 76 % so in order to maintain the thermal conductance at Medium-G level, the leg width is reduced by the same amount. The leg width for the 16-leg design is 87 μ m and for the 32-leg design it is 52 μ m. The thickness of the silicon nitride membrane is \sim 1 μ m.

Fig. 6.54 shows the finite element analysis (FEA) for the Medium-G layout with Au ring. The uniformity of meshing improves the FEA analysis hence the parameters could be kept constant for the gold ring meshing and silicon nitride membrane meshing. The gold ring is thinner (150 nm) than the silicon nitride membrane (1 μ m), hence all the parameters of the gold ring, like thermal conductivity, specific heat are scaled proportionally. The heat capacity and thermal conductivity values of the gold at low temperatures are obtained from Du Chatenier & De Nobel (1961).

Both the 16-leg Medium-G layouts with and without gold ring were produced in the same production run. The thermal conductance is kept the same by scaling the silicon nitride leg geometry. An extensive analysis with respect to the gold ring is presented in § 6.12.

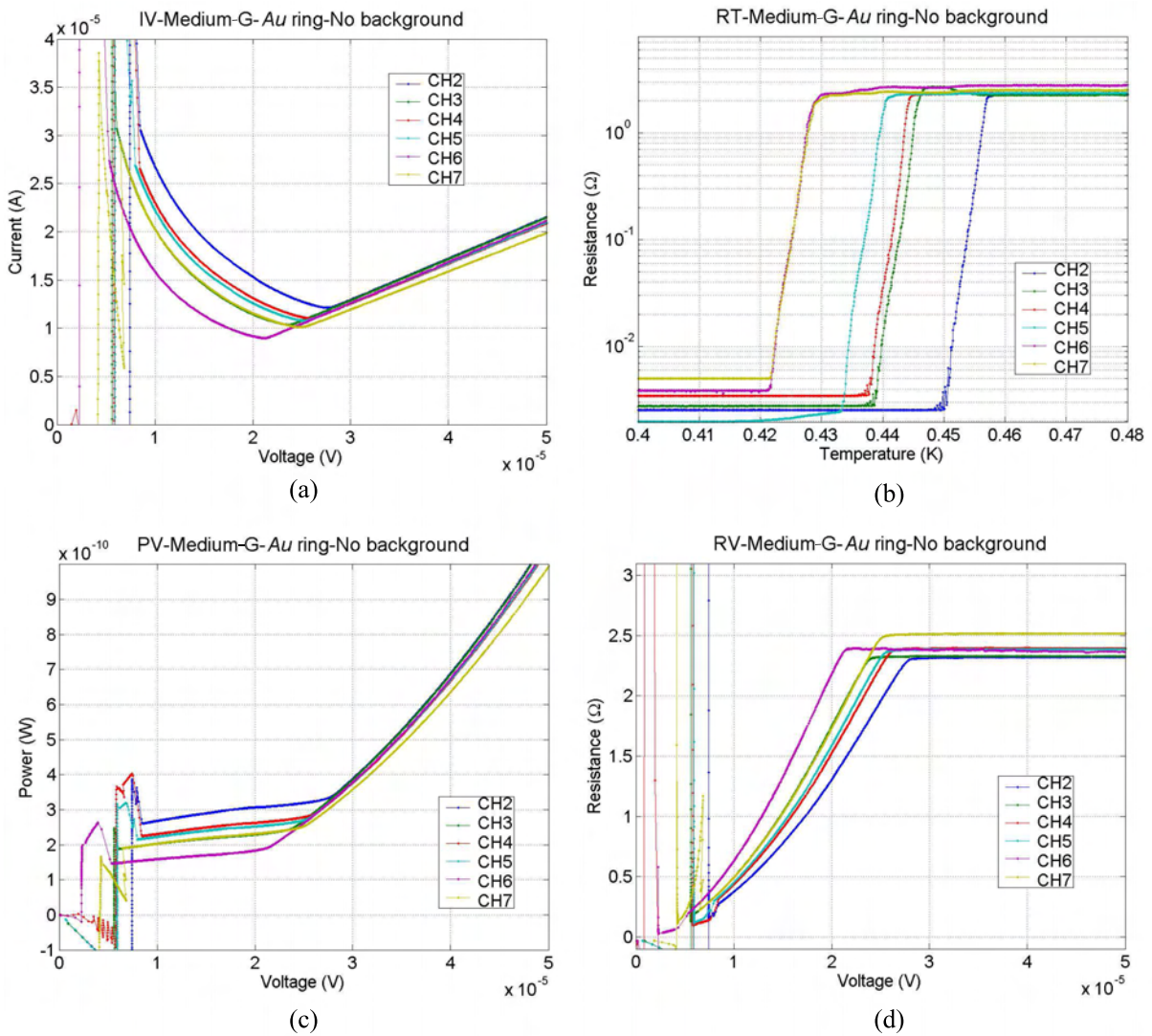


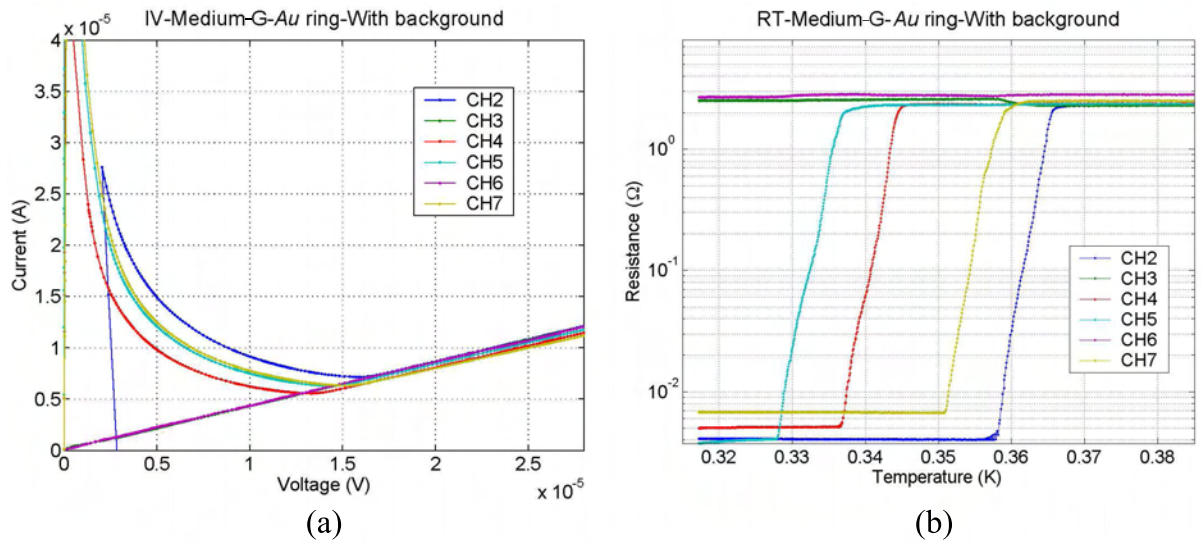
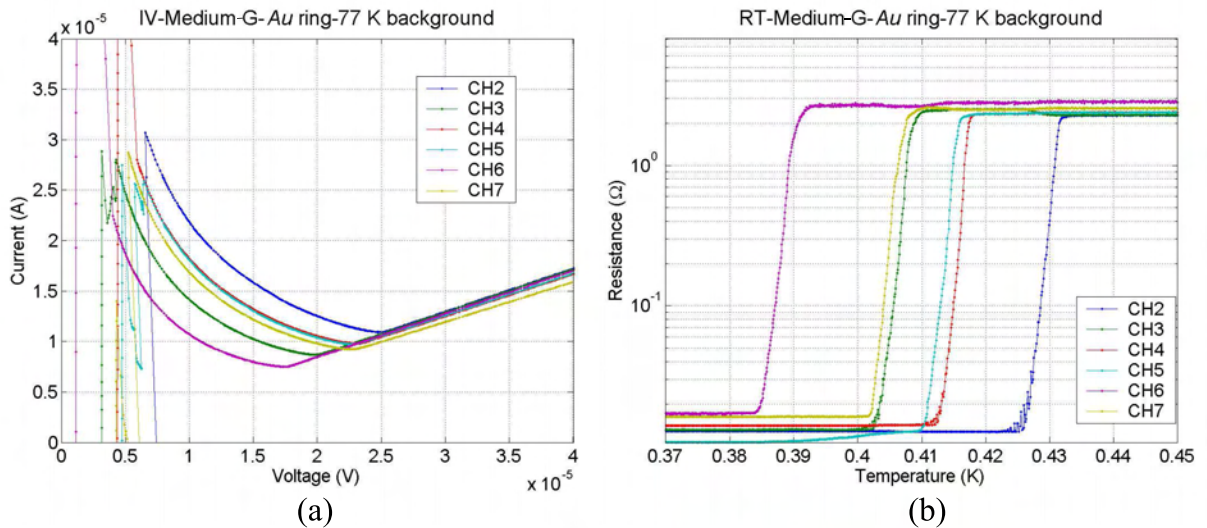
Figure 6.55: Experimental results of Medium-G - 16 leg with Au ring layout 4SN 1762. These experiments are performed without background radiation. (a) $I - V$ measurements for all the working channels. (b) $R - T$ measurements at 1 mV of bias voltage. (c) and (d) The bolometer power and resistance as a function of the bolometer voltage, respectively.

6.11.1 $I - V$ and $R - T$ measurements

Fig. 6.55, shows measurements obtained from the 16-leg Medium-G layout with Au ring without background radiation. Only six channels were working in all the experiments with this array. Fig. 6.55 (b), shows the measured $R - T$ curves. The spread in the transition temperature is ± 15 mK. Subplots (c) and (d), show $P - V$ and $R - V$ curves respectively. The normal state resistance of the TES is $\sim 2.5 \Omega$. Table 6.7 shows the transition temperature and transition width for all the channels. The values of the transition widths are in a similar range as those obtained with the 16-leg Medium-G without Au design. Fig. 6.56 shows the $I - V$ and $R - T$ measurements with 300 K background radiation. Due to the background power, the bolometer goes into transition at lower bias voltages and the transition temperature is reduced.

Table 6.7: Transition temperature and transition width (in bracket) for all working channels of 4SN 1762.

CH2 (mK)	CH3 (mK)	CH4 (mK)	CH5 (mK)	CH6 (mK)	CH7 (mK)
456 (2.62)	445 (2.57)	443 (2.30)	439 (3.01)	430 (2.13)	428 (3.42)

**Figure 6.56:** $I - V$ and $R - T$ measurements of 4SN 1762, 16-leg spider Medium-G layout with Au ring. The measurements were done at 300 K.**Figure 6.57:** $I - V$ and $R - T$ measurements of 4SN 1762, 16-leg spider Medium-G layout with Au ring. The measurements were done at 77 K.

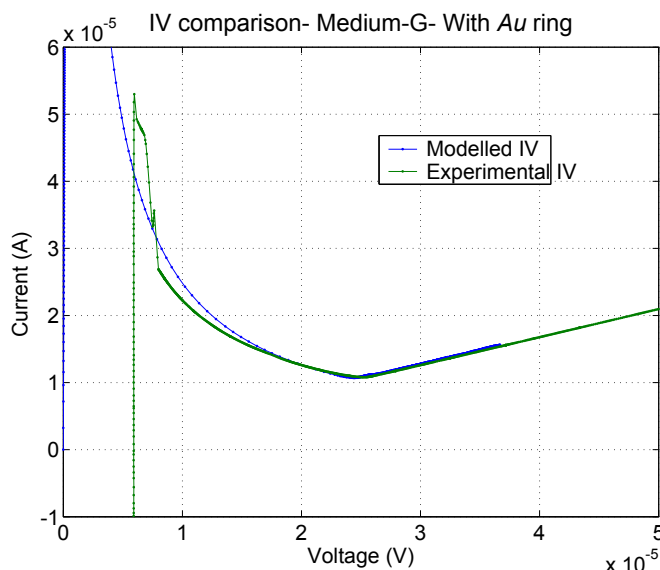


Figure 6.58: Comparison between the experimentally measured $I - V$ and the modeled $I - V$ curve for CH5 of the 16-leg Medium-G layout with gold ring.

CH1 was open and the channels CH3 and CH6 did not show a superconducting transition (Fig. 6.56). Similarly to the previous experiment, the measurements were performed by rotating the 1.5 K filter and the horn antenna by 90° to see any effect due to them. No such effect was observed. Fig. 6.57 shows the $I - V$ and $R - T$ measurements at 77 K. With the background radiation at 77 K, it was possible to measure the $I - V$ and $R - T$ curve for all the channels except CH1, including for CH3 and CH6. Hence we conclude that for CH3 and CH6, thermal conductance is different from that of the other channels. Such behavior can be understood, if the Si_3N_4 leg adjacent to the thermistor is broken or has a undetected crack. § 6.10.2 shows the FEA simulations for such a case. Fig. 6.62 (a), shows the time constant measurements for four channels at different bias voltages.

Modeling of the $I - V$ curve

Figs. 6.58 and 6.59 shows the comparison of $I - V$, $P - V$ and $R - V$ curves obtained experimentally with model curves. The bolometer goes from the transition range to the normal resistance state at $24 \mu\text{V}$ of bias voltage without 300 K background and at $11 \mu\text{V}$ bias voltage with 300 K background. The power dissipated in the bolometer is about 250 pW in the transition range.

6.11.2 Signal measurements

The signal measured with lock-in amplifier is plotted in Fig. 6.60. Since the time constant of the bolometer is larger, at higher frequencies, the signal drops more than in the previous experiment. The signal is measured with a lock-in amplifier so it is not affected by the anti-aliasing filter installed in the data acquisition electronics.

Time constant measurements

The measured value of τ_o is ~ 2 ms at bolometer voltages of $\sim 30 \mu\text{V}$ when the bolometers are near to the normal range. The minimum time constant is measured at of $\sim 6.4 \mu\text{V}$ bolometer voltage. The transition curves are steepest at a bolometer voltage of $\sim 6.4 \mu\text{V}$ so the steepness factor α is highest and hence the

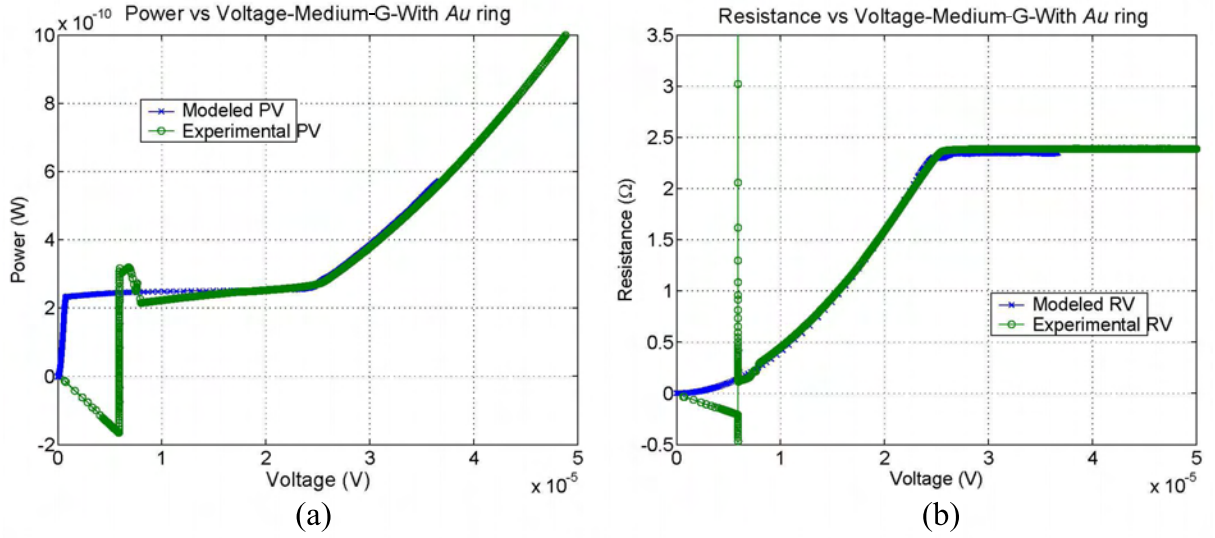


Figure 6.59: Comparison between measured and modeled power and resistance for CH5 of 16-leg Medium-G layout with Au ring.

time constant is lowest. The average value of the measured time constant is 1.5 ms. The measured time constant is higher by a factor of ~ 2 , in comparison to the previous experiment (§ 6.10). The previous experiment was performed with same layout but without the gold ring hence the heat capacity was much smaller. Gold has high heat capacity hence the addition of gold ring increases the total heat capacity significantly and hence the time constant increases. The time constant also depends on the transition width. Tables 6.5 and 6.7 show that the transition widths for these experiments are similar. It can be concluded that the increase in the time constant is mainly due to the extra heat capacity of the gold ring.

Fig. 6.61, shows the SNRs for Channels 2, 4, 5 and 6 at different voltages. The SNR is highest at the voltage where the transition curve is steepest. The time constant is lowest and the SNR is highest at a bolometer voltage of $\sim 6.4 \mu\text{V}$. Fig. 6.60 shows the measured value of signal and noise for all the channels at $6.4 \mu\text{V}$ of bolometer voltage. As shown in the plot, the signal drops more rapidly with frequency than in the previous experiment (Fig. 6.44). Therefore, the time constant of these TESs is higher than of those with Medium-G layout without an Au ring. The time constant and SNR measurements are performed at different bias voltages for all the channels. The SNR values vary in the range 1600 and 2040.

Table 6.8 shows the heat capacity budget calculations for Medium-G layout with Au ring. The calculated total C is 7.0×10^{-12} J/K. The value of the thermal conductance obtained from the model is 3.6×10^{-9} W/K. The calculated intrinsic time constant of the bolometer is 1.9 ms. The measurements with 300 K background give a τ_o of 2 ms. From the measured optical time constant, the total heat capacity from the experiment is 7.2×10^{-12} J/K. The addition of Au ring increases the total C significantly, so the time constant is high.

Fig. 6.62 (b) shows the relation between τ and L for the 16-leg Medium-G layout with Au ring. The bolometer voltage of $6.4 \mu\text{V}$ corresponds to an external bias voltage of 200 mV applied to the bolometer circuit. At this voltage value, the α is highest and the time constant reduces to minimum value of 1.58 ms. This is the experimentally measured optical time constant and from the model the calculated time constant is 1.41 ms.

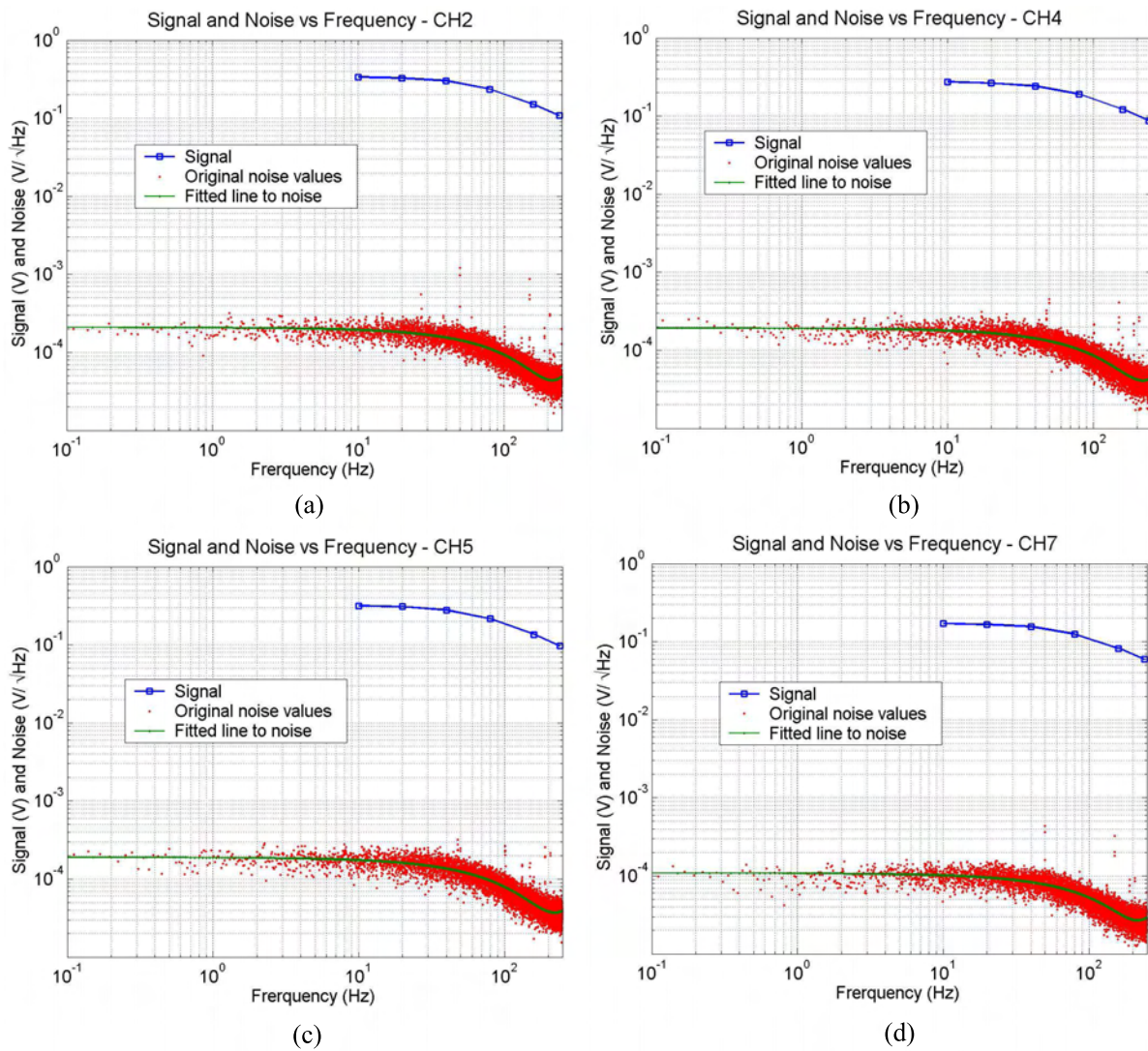


Figure 6.60: Comparison of signal and noise at a bolometer voltage of $6.4 \mu\text{V}$ for Medium-G layout with Au ring. The time constant of this bolometer is large so the signal drops at higher modulation frequencies. An 88 Hz low pass filter function is fitted to the measured noise.

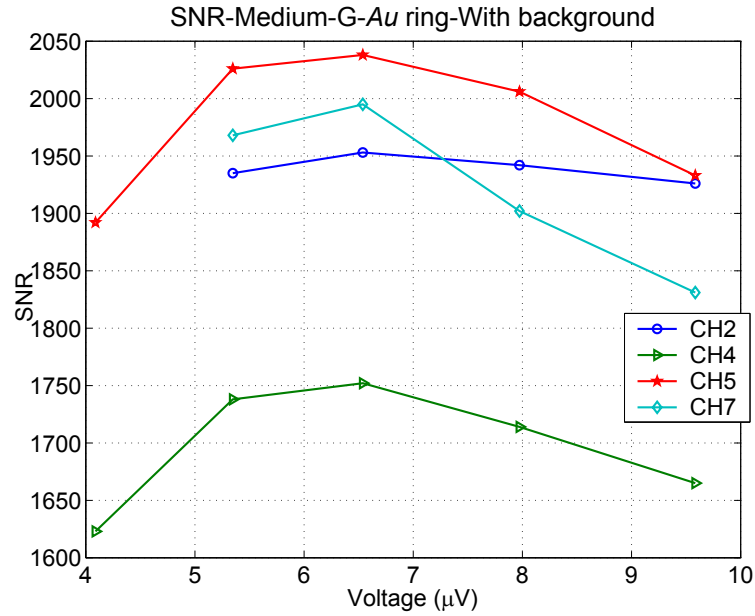


Figure 6.61: SNR measurements for all channels at different bias voltages.

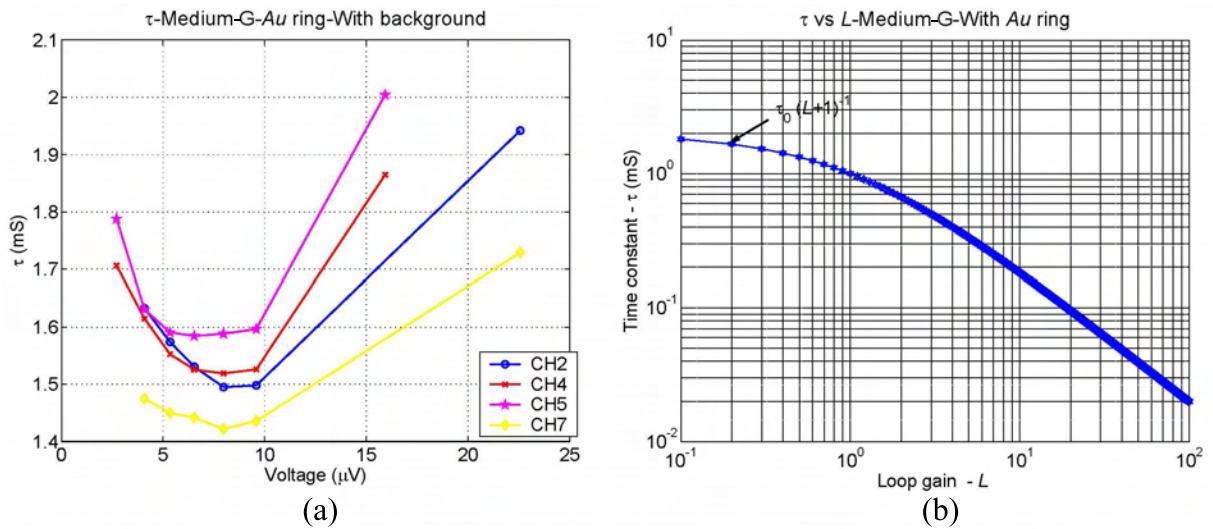


Figure 6.62: τ and loop gain (L) of 4SN 1762, 16-leg spider Medium-G layout with Au ring. The measurements are from the experiment with 300 K background. (a) τ plotted at different bias voltages for all the channels. (b) Relation between τ and loop gain L for the same array.

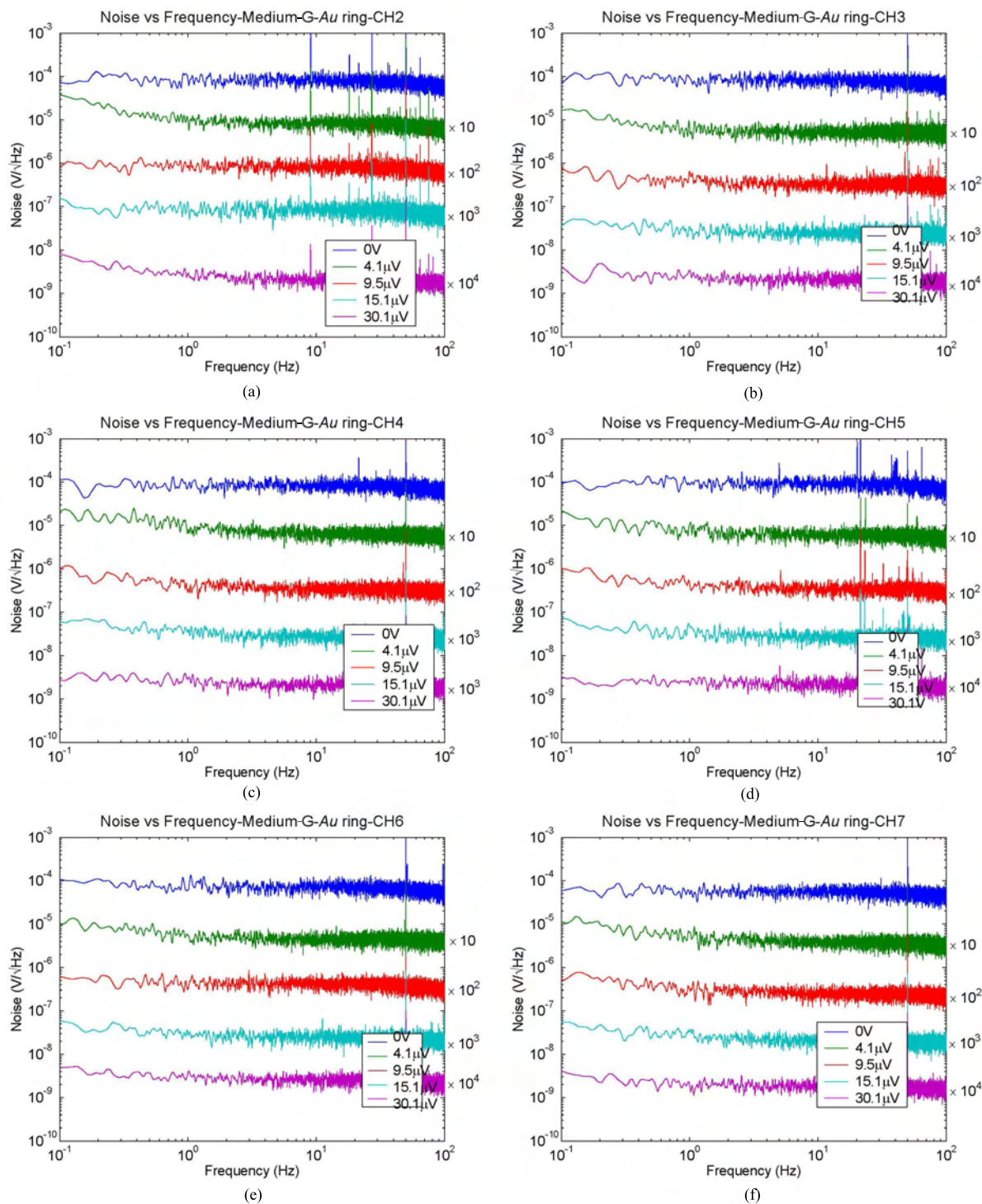


Figure 6.63: Noise measurements for six channels (CH2, CH3, CH4, CH5, CH6, and CH7) at different bias voltages. The Y-axis is scaled by the multiplication factor shown next to each noise curve. Measurements were done without background.

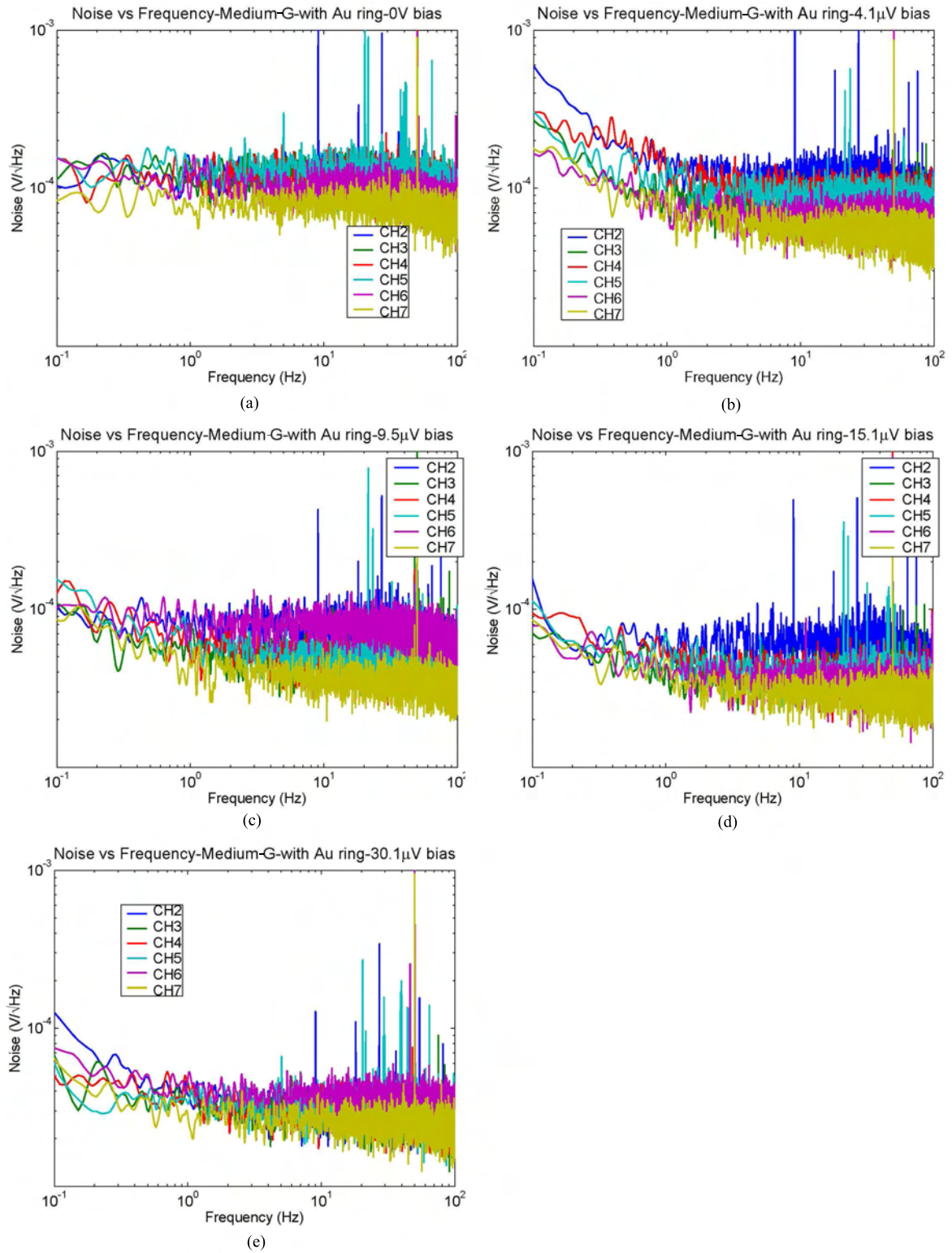


Figure 6.64: Noise measurements for all the channels at different bolometer voltages. The experiment was performed without background.

Table 6.8: Thermal heat capacity budget for the 16-leg Medium-G layout with Au ring at 450 mK.

Material	C_ν Electron (J/cm ³ K ²)	C_ν Lattice (J/cm ³ K ⁴)	Volume (cm ³)	C (J/K)
Thermistor:				
Au-Pd	2.5×10^{-4}	4.2×10^{-4}	8.6×10^{-11}	1.3×10^{-14}
Mo	1.1×10^{-3}	9.3×10^{-4}	8.6×10^{-10}	5.0×10^{-13}
Electrical Leads:				
Nb		8.6×10^{-6}	3.8×10^{-9}	2.9×10^{-15}
Absorber:				
Au-Pd	2.5×10^{-4}	4.2×10^{-4}	1.1×10^{-9}	1.6×10^{-13}
Si ₃ N ₄		8.2×10^{-8}	3.2×10^{-6}	2.4×10^{-14}
Au ring	6.8×10^{-5}	4.5×10^{-5}	1.8×10^{-7}	6.3×10^{-12}
Total				7.0×10^{-12} J/K

6.11.3 Noise measurements

The noise measurements for all the channels are shown in Fig. 6.63. The noise spectra were obtained by integrating for ~ 250 seconds. In order to present the noise at different bias voltages, the noise amplitude is multiplied by a multiplication factor, mentioned at the right end of each spectra. In a few channels, e.g., CH2 and CH5, the 50 Hz noise from the power supply and its corresponding harmonic frequencies are detected. All these measurement are performed without background hence there is no contribution from photon noise. In some cases, $1/f$ noise is observed at frequencies below 0.6 Hz.

Fig. 6.64 shows the noise for all the channels plotted at different bolometer voltages. As shown in Figs. 6.63 and 6.64, CH2 and CH5 show line interference in the noise measurements but no such interference is observed in other channels. During the noise measurements, the data acquisition for all the channels is simultaneous so that correlation analysis can be used to determine whether there is interference between the channels. As shown in Fig. 6.64, the noise level for all the channels is similar at a given bias voltage. The $1/f$ noise pattern at a given voltage (e.g. 4.1 μ V, 30.1 μ V) is similar for all the bolometer channels. This suggests that the $1/f$ noise is not related to a particular channel and is arising from the external source.

The white noise level for each channel can be correlated to the superconducting transition temperature. Bolometers with higher transition temperature shows larger white noise level (e.g. CH2) and bolometers with lower transition temperature (e.g. CH7) shows smaller white noise levels. The noise of CH2 at 0 V bolometer voltage is 6.3×10^{-5} V/ $\sqrt{\text{Hz}}$ and that of CH7 at 0 V bolometer voltage is 3.4×10^{-5} V/ $\sqrt{\text{Hz}}$. These measurements are performed without background so the photon noise is negligible and the main source of noise is phonon noise (Eq. 2.12). Phonon noise is dependent on the transition temperature of the bolometer.

As in the previous section (Fig. 6.50), noise is computed at different bias voltages. Fig. 6.65 (a) shows a comparison of the measured noise bandwidth with that of noise calculated at different bias voltage. The modeled noise refers to the white noise obtained from the bolometer model. Fig. 6.66 compares the experimentally measured noise with the modeled noise for Channel 5. From the model, the calculated noise voltage is 3.1×10^{-5} V/ $\sqrt{\text{Hz}}$ without photon noise and 8.8×10^{-5} V/ $\sqrt{\text{Hz}}$ with the contribution from the photon noise of a 300 K background. The experimentally measured noise spectra were obtained by integrating for ≈ 240 seconds. Similar to previous modeling sections excess noise was observed. As shown in Fig. 6.63, $1/f$ noise is observed at frequencies less than 0.4 Hz.

As in § 6.10.4, it was tried to understand the $1/f$ noise in 16-leg Medium-G layout with Au ring.

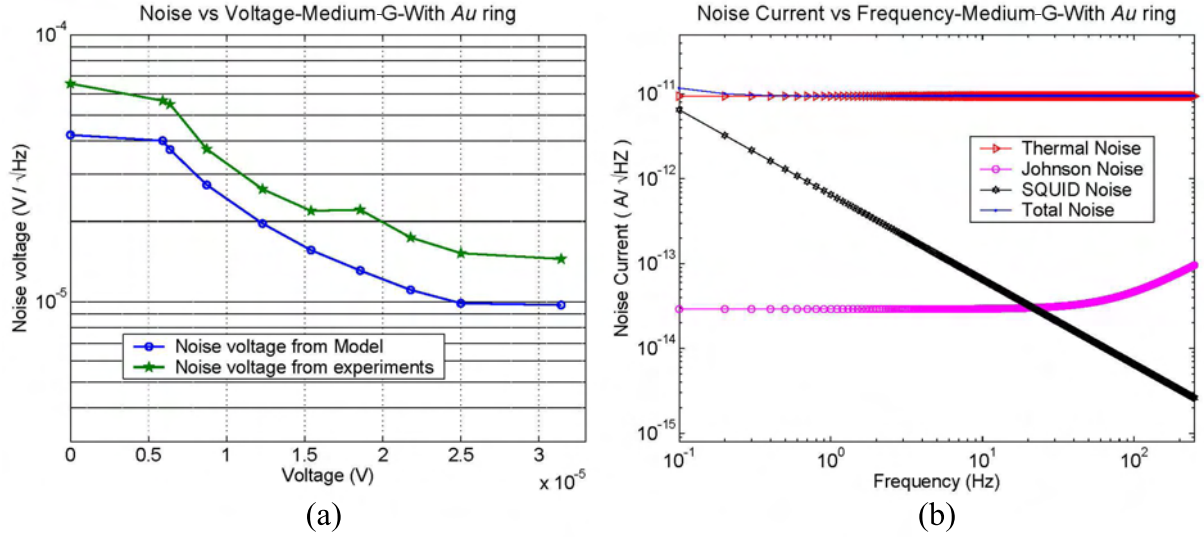


Figure 6.65: (a) Relation between the measured and calculated noise at different voltages for the 16-leg Medium-G layout with Au ring. (b) Predicted noise current of the 4SN 1762 array. The values are obtained from the bolometer model. The Thermal noise (phonon noise) is the main source of noise. The measured noise was fitted to a low pass filter function. The measurements and calculations are shown for CH5.

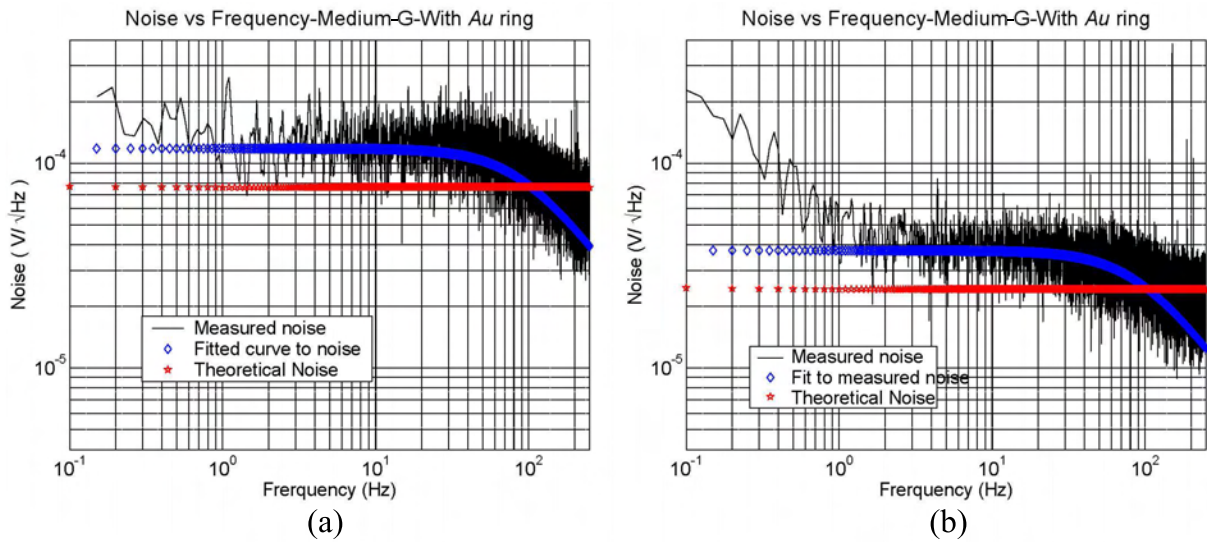


Figure 6.66: Comparison between noise voltage from the experiments and noise voltage from the model for the 16-leg Medium-G layout with Au ring. The measured noise in the plot refers in (a) to the measured noise with 300 K background and in (b) to the measured noise without background. The modeled value of the noise is also compared with that of obtained from the measurements. Data are shown for CH5 at $6.4 \mu\text{V}$ of bolometer voltage. An 88 Hz low pass filter function is fitted to the measured noise.

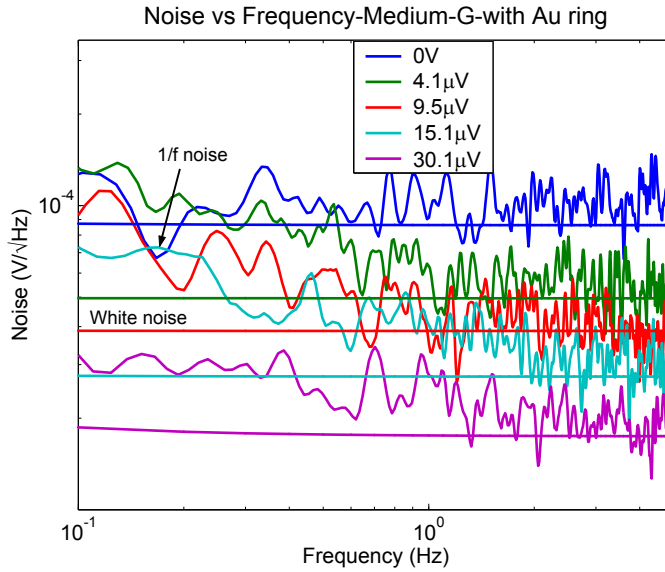


Figure 6.67: The plot is identical to Fig. 6.63 (d) at low frequencies with addition of white noise calculated from the bolometer noise model.

As shown in Fig. 6.63, an additional $1/f$ noise was observed in some measurements. Fig. 6.67 shows the noise voltage for CH5, calculated at different bias voltages. Using the noise model the white noise is predicted at different bias voltages which is also plotted along with the measured noise. As seen from the plot, the total noise level is very close to the theoretically predicted white noise level but an additional $1/f$ noise is seen at lower frequencies (< 0.3 Hz) it is difficult to measure the value precisely. $1/f$ noise is less significant at the lower and higher bias voltages but the contribution increases in the transition range (Fig. 6.64). As explained in §6.10.4, the bolometers are more sensitive to interference pickup in the transition range which can contribute to $1/f$ noise.

6.11.4 NEP calculations

Fig. 6.68 compares the NEP obtained from the model with the experimentally measured optical NEP. The mean SNR is 1896, which corresponds to an optical NEP of 1.7×10^{-16} W/ $\sqrt{\text{Hz}}$. From the model, the NEP estimated without a background, is 9.2×10^{-17} W/ $\sqrt{\text{Hz}}$ and it is 1.6×10^{-16} W/ $\sqrt{\text{Hz}}$ with the photon noise of a 300 K background. From the model the derived $\text{NEP}_{\text{optical}}/\text{NEP}_{\text{photon}}$ is 1.11 ± 0.03 and from the experiment, the measured $\text{NEP}_{\text{optical}}/\text{NEP}_{\text{photon}}$ is 1.29 ± 0.09 . Thus, the performance of Medium-G layout with Au ring is very close to the 300 K background limit.

6.12 Gold ring modeling

6.12.1 Incident radiation pattern

The gold ring is used to produce the uniformly thermalized patch around the center area on the silicon nitride membrane. In order to understand the effects of the gold ring, finite element analysis for the High-G, Medium-G and Low-G layouts were performed. The center patch where the input radiation is absorbed has a size of 2×2 mm. This size is determined by an illumination pattern of the horn antenna. By dividing the absorbing center patch in 25 equal parts, one can study its thermalization (Fig. 6.69).

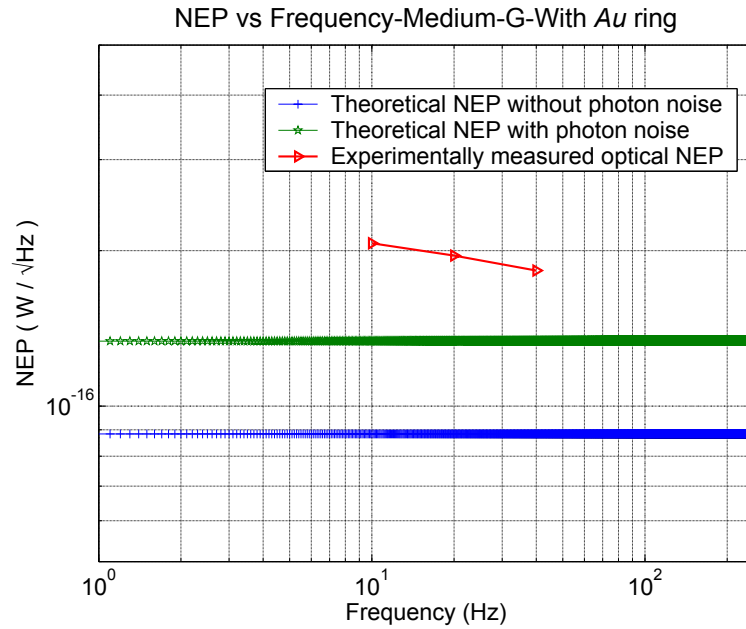


Figure 6.68: NEP plotted as a function of frequency for the 16-leg Medium-G layout with Au ring. NEP obtained from bolometer model is compared with experimentally measured optical NEP.

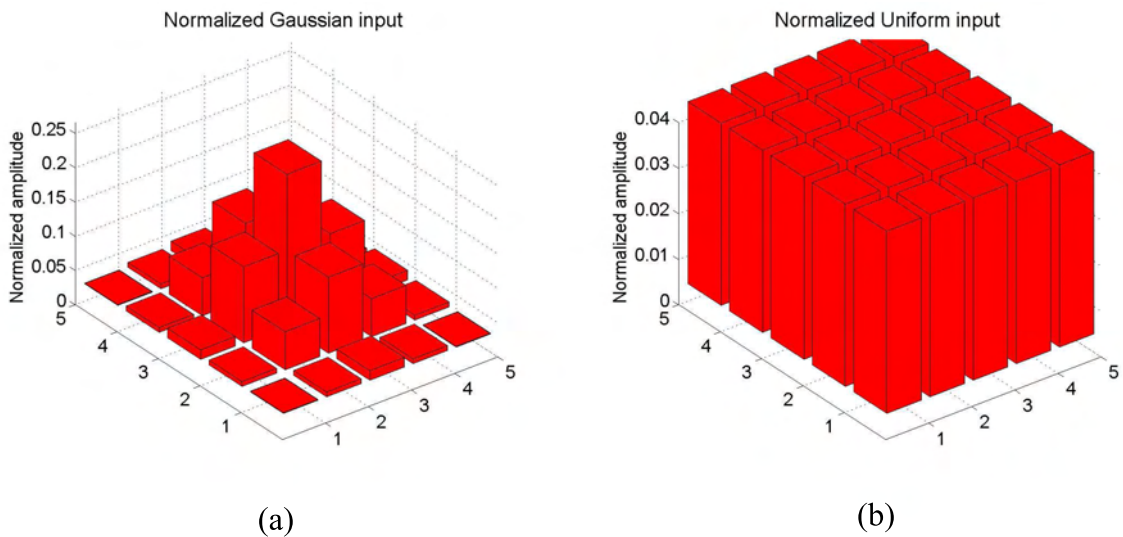


Figure 6.69: Input heat distribution on the center of the silicon nitride membrane. (a) The gaussian input heat distribution. (b) The uniform input heat distribution on the absorbing center patch.

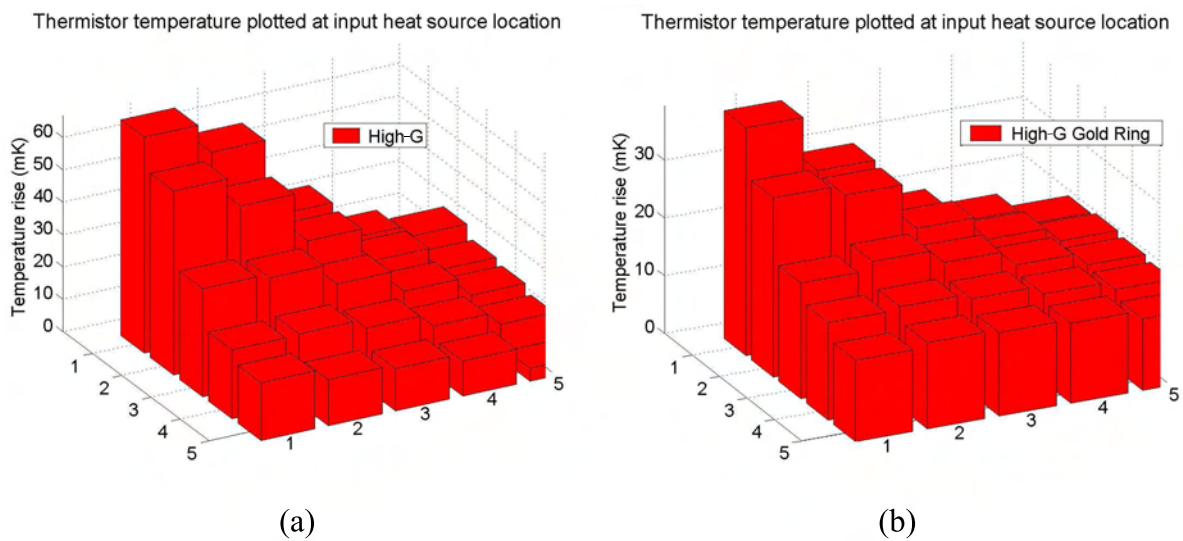


Figure 6.70: Thermistor temperature plotted at the input heat radiation location for High-G layout. The incident beam has uniform input pattern. Thermistor at position [1,1].

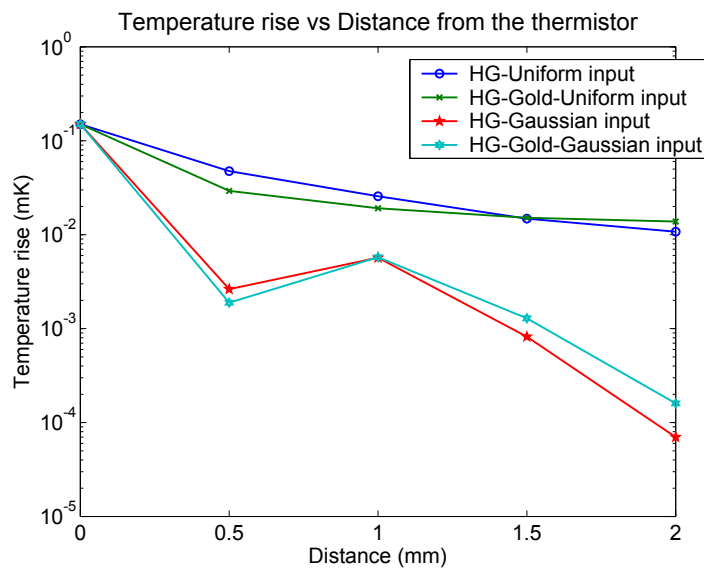


Figure 6.71: Change in temperature detected by the thermistor as a function of distance.

Two types of distribution for the input radiation are simulated; a gaussian and an uniform radiation pattern. Fig. 6.69 (a) shows the normalized gaussian input function. In both cases, the Au-Pd/Mo thermistor is placed on part 1. Subplot (b) shows the normalized amplitude. The incident beam has an input power of 1 pW. Using the FEA model, a change in the temperature of the silicon nitride membrane due to the input radiation is calculated. The silicon wafer is maintained at the bath temperature of 300 mK.

Table 6.9: *Quality factor* calculations and the thermal properties of the High-G layout.

	σ (mK)	Total (mK)	Mean (mK)	<i>Quality factor</i> Q
Uniform input radiation				
High-G	14.01	398.82	15.95	0.12
High-G with Au ring	5.27	533.16	21.32	0.75

6.12.2 High-G layout

The addition of the gold ring makes the absorbing center patch a more uniformly thermalized area. This leads to an increase in the total temperature due to the incident radiation. In order to compare the amount of thermalization between different bolometers, a *Quality factor* (Q) is defined.

$$Q = 1 - \frac{\sigma}{\bar{x}}, \quad (6.2)$$

where, σ is the standard deviation and \bar{x} is a mean of the temperature distribution. The ratio of σ/\bar{x} determines the amount of thermalization for a particular bolometer geometry. Q is 1 for a perfectly thermalized area and 0 for an unthermalized area. The incident radiation changes the temperature of the silicon nitride membrane, which is detected by the thermistor. The addition of a gold ring increases the thermalization of the center patch, hence the change in temperature is higher than without the gold ring structure. Since the incident signal is similar for all the bolometer geometries, Q can be compared between the different bolometer layouts. An increase in Q means an improvement in the thermalization of the center patch, i.e, when the radiation falls on the absorbing center patch, a larger fraction will be detected by the thermistor. Due to the gold ring, the change in temperature is uniformly distributed, hence the peak value of the change in temperature is reduced. The simulations with uniform heat input shows that the addition of the gold ring increases the thermalization of the absorbing center patch at the expense of reduction in the peak signal (Fig. 6.71). Table 6.9 show statistical calculations of the temperature distribution along the absorbing center patch of the High-G layout. The advantages of the gold ring are:

1. The thermalization of the the silicon nitride membrane increases.
2. The large increase in the total temperature which is coupled to the thermistor. Hence, the sensitivity of the bolometer increases.

The disadvantage of the gold ring is that it increases the heat capacity so the time constant of bolometer also increases.

6.12.3 Medium-G layout

A similar analysis is performed for the Medium-G layout. Fig. 6.72 shows the thermistor temperature plotted at the heat input location for an uniform radiation input source. Since the Medium-G layout has a structured silicon nitride membrane, the heat flow is defined by the legs hence the absorbing center patch has higher degree of thermalization than the High-G layout. Similar to High-G layout, the behavior of the silicon nitride membrane is simulated considering the normalized uniform beam.

The change in the Q , in comparison with High-G layout, is smaller because in the Medium-G layout the silicon nitride membrane is already structured so the effects due to the Au ring reduces. Table 6.10 shows the statistical calculations for Medium-G layout. The change in the total temperature of the Medium-G layout is smaller than that of High-G layout. Due to the structuring of the silicon nitride

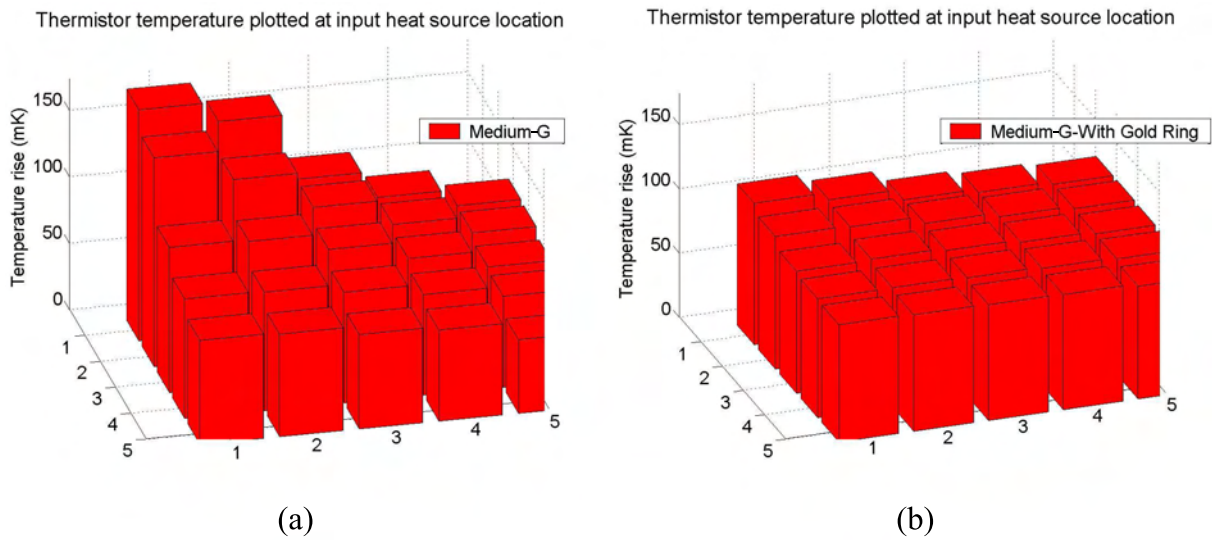


Figure 6.72: Thermistor temperature plotted at the input heat radiation location for Medium-G layout. The incident beam has uniform input pattern. Thermistor at position [1,1].

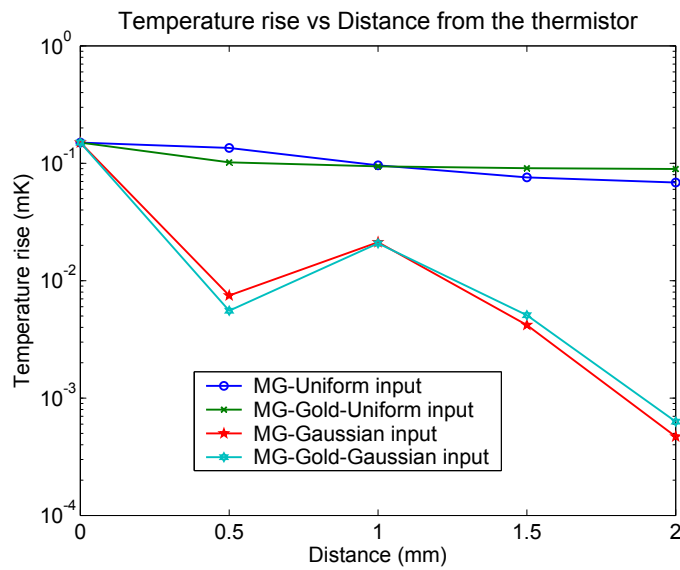


Figure 6.73: Change in temperature detected by the thermistor as a function of distance.

Table 6.10: Quality factor calculations and the thermal properties of the Medium-G layout

	σ (mK)	Total (mK)	Mean (mK)	Quality factor Q
Uniform input radiation				
Medium-G	6.67	972.61	38.91	0.83
Medium-G with Au ring	4.21	1018.39	40.73	0.89

Table 6.11: *Quality factor* calculations for different geometries layouts.

	σ (mK)	Total (mK)	Mean (mK)	<i>Quality factor</i> Q
Uniform input radiation				
High-G with Double Au ring thickness	4.27	545.67	21.82	0.81
High-G with 20 times Au ring thickness	3.83	579.71	23.18	0.83
Uniform input radiation				
Low-G	3.26	2894.33	115.77	0.97
Low-G with Au ring	2.67	3090.57	123.62	0.98

membrane in Medium-G layout, the effects due to the gold ring are not significant. The change in the temperature is big because of the same high incident power assumed during the simulations.

The increase in Q improves the current responsivity of the TES so the SNR in the Medium-G layout with the gold ring should be higher than that of Medium-G layout without the gold ring. The experiments were performed for Medium-G layout with the Au ring (§ 6.11). By comparison with Fig. 6.45 and 6.61, an increase in the overall SNR is observed. The NEP of Medium-G layout without Au ring is 1.7×10^{-16} W/ $\sqrt{\text{Hz}}$ while that of the Medium-G layout with Au ring is 1.9×10^{-16} W/ $\sqrt{\text{Hz}}$, thus the sensitivity of TES increases somewhat due to the addition of the gold ring. The Medium-G layout (4SN 1762) is fabricated with and without the Au ring on one wafer (§ 6.11) hence all the wafers and the silicon nitride membrane characteristics are similar. The Au ring is the only difference in the two geometries hence it is possible to measure the changes in bolometer behavior due to the Au ring accurately. As mentioned, the addition of Au increases the total C hence the time constant of the bolometer increases. Comparison of Fig. 6.46 (a) and 6.62 (a) shows the increase in the time constant due to the gold ring.

The increase in time constant can be useful in case of multiplexing of the electronics. During multiplexing, each bolometer is sampled with one readout SQUID at a predefined sampling frequency which is higher than the time constant of the bolometer. The increase of the time constant allows sampling of the bolometers at a lower frequency or presents the possibility of sampling a larger number of bolometers with one SQUID amplifier. The scheme of sampling electronics is explained in § 3.6. Thus by varying the Au ring thickness, it is possible to tune the time constant of the bolometers according to the requirements of the electronics circuit.

6.12.4 Different geometries

Table 6.11 shows the calculation of Q for different geometries e.g. Low-G, Low-G with Au ring, and with an increased Au ring thickness. The simulations are performed by increasing the Au ring thickness by the factor of 2 and 20. The Q increases due to increase in the Au thickness.

The effects of the Au ring in the Low-G layout are shown in Table 6.11. The increase in Q reduces from High G , Medium-G to the Low-G layout. The Low-G layout has thinner silicon nitride membrane legs so the thermalization is better in comparison with the Medium-G and High-G layouts. Therefore, in Low-G layout, the addition of the Au ring does not significantly change the value of Q .

Chapter 7

Summary and Conclusions

In (sub)millimeter astronomy there is a growing demand for new generation large format detectors of continuum radiation. Realizing the advantages of the superconducting transition edge sensor (TES) technology in terms of speed, sensitivity, fabrication process and linearity, a development of voltage biased superconducting bolometers (VSBs) was started by the bolometer research group at the Max Planck Institute for Radio Astronomy (MPIfR) in collaboration with the Institute for Photonic Technology (IPHT) in Jena.

The aim of this dissertation was to design, develop and test a seven-element array in different configurations. The bolometers and the SQUID amplifiers were developed and built at the IPHT, while the testing, modeling and the simulations of the bolometers was performed by me at the MPIfR. For each array the load curves, temperature transition from a superconducting to a normal state, the time constant, noise, spectral response, and the NEP of the individual bolometers were measured.

Software for the data acquisition (in *LabVIEW*), the data analysis and the bolometer modeling (in *MATLAB*) was written by me. I also performed the finite element analysis simulations for the different bolometer geometries.

The results obtained from the experiments were conveyed to IPHT for further modifications to a bolometer design. The design and material selection for the bolometer fabrication was influenced by the bolometer modeling and the finite element analysis in an iterative manner.

The development efforts started with the fabrication and testing of 7-element arrays. The base temperature of 300 mK is established in a liquid ^4He cryostat with an integrated ^3He stage. The sensitivity of the bolometer is highest when the transition temperature is ~ 1.5 times the base temperature. Consequently, a transition temperature of 450 mK was chosen.

The superconducting thermistor consists of 8.6 nm of gold-palladium deposited on a 86 nm thick molybdenum layer and has transition temperature of 450 mK determined by the proximity effect.

Crossed dipoles made of a Au-Pd alloy with a surface resistance of $10 \Omega/\square$ are deposited on the silicon nitride membrane, acting as radiation absorbers.

The bolometer is maintained in the transition range with a constant bias voltage between 1 and 6 V. A constant bias current I_{bias} is provided by a series bias resistor with a resistance of 1045Ω . A shunt resistor of $33 \text{ m}\Omega$, which is much smaller than the bolometer resistance of $\sim 3 \Omega$, provides a constant bias voltage at the bolometer. The bolometer current is detected by SQUID amplifiers. In the future, for larger arrays, the readout of the SQUID electronics will be time division multiplexed. The multiplexing of the electronics will allow a reduction in the number of wires and of warm electronics channels, which is essential for large format arrays.

The pass band characteristics are defined by filters mounted at the 300 K, 77 K and 1.5 K cooling

stages. The bolometers were designed for the 1.2 mm atmospheric window. The surfaces of the 77 K and 1.5 K filters are anti-reflection structured. The incoming signal is coupled to Au-Pd absorbers via an aluminum horn antenna. The temperature of the ^3He stage is monitored by a Germanium sensor. The time constant of the bolometer is derived by measuring the modulated signal from a blackbody with a lock-in amplifier. The noise is measured in a *timeseries* and analyzed using National Instruments' *LabVIEW* package. The resistance-temperature and voltage-current characteristics are measured using *LabVIEW*. The spectral response of the whole system is measured with a Martin-Puplett interferometer. The metallic parts inside the optical path, e.g., inside of ^3He shield and the outer area of horn antenna are coated with a special sub-millimeter black coating to avoid interference from reflections.

The experiments were started with an *Initial layout*. In order to understand the behavior of the silicon nitride membrane and the Au-Pd/Mo thermistor, the *Basic layout* array was fabricated, with seven thermistors of different geometry and material properties. The sensitivity of the bolometer is inversely proportional to the thermal conductance, hence to improve its sensitivity the thermal conductance was reduced by structuring the silicon nitride membrane. A first array (4SN 1601) was manufactured with bolometers in three different layouts, High-G, Medium-G and Low-G, depending on their thermal conductance. The silicon nitride membrane is continuous for the High-G layout and it is structured into 8-leg spider geometry for the Medium-G and Low-G layouts. The thermal conductance for the Low-G layout is insufficient to work at 300 K background, i.e, the power from the 300 K background drives the bolometers from the superconducting to the normal state. The Medium-G design is ideal to work at 300 K background. During the experiments on the *Basic layout*, it was found that a thermistor of $100\ \mu\text{m}$ square geometry shows the best performance in terms of linearity, transition range width and the steepness of the transition curve.

In the next array, 4SN 1610, all the seven thermistors were fabricated with a $100\ \mu\text{m}$ square geometry and the silicon nitride membrane was structured to tune the thermal conductance of the bolometer. To determine the time constant of the bolometer, the signal from a blackbody or a Gunn diode was modulated at different frequencies.

For the High-G layout, the signal-to-noise ratios (SNRs) are dependent on the bolometer voltage and are in the range 1000 and 1500. The time constant is ~ 3 ms. The transition temperatures for the different channels were within 20 mK of 450 mK. The designed normal state resistance of the TES was $1\ \Omega$ and the resistance measured during the experiment was $0.8\ \Omega$. For the High-G layout bolometer, the measured optical NEP is $4.5 \times 10^{-16}\ \text{W}/\sqrt{\text{Hz}}$.

In another layout (4SN 1762), all the seven bolometers were fabricated in the Medium-G layout. For technological reasons, the silicon nitride membrane was structured with 16 or 32 legs, instead of 8 legs. In this design, the normal state resistance was changed to $3\ \Omega$. The increase in the normal resistance allows better impedance matching with the SQUIDs. The transition temperature is 450 ± 15 mK. The transition widths are around 2.5 mK. With a 300 K background, the measured time constant is in the range of 0.2 to 0.38 ms. The SNRs range from 1700 to 1900, depending on the applied bias voltage. The calculated optical NEP is $1.9 \times 10^{-16}\ \text{W}/\sqrt{\text{Hz}}$. The thermal conductance of the Medium-G layout is smaller than that of the High-G layout, hence the NEP of the Medium-G layout is reduced. Finite element analysis showed a small increase in the sensitivity of the bolometer expected from the addition of a gold ring, hence in this array, a 150 nm thick gold ring is deposited around the center patch on the silicon nitride membrane. The addition of the gold ring increases the thermalization of the center absorbing patch, hence the sensitivity of the bolometer increases. Gold has high heat capacity, hence the gold ring significantly increases the heat capacity of the bolometer. The experiments with the Medium-G layout with gold ring show a transition temperature of 450 ± 20 mK and a the normal state resistance of $\sim 3\Omega$. The measured time constant is between 1.4 and 2 ms. The increase in time constant is due to the extra heat capacity of the gold. The SNR is between 1750 and 2000 which corresponds to an optical NEP of $1.7 \times 10^{-16}\ \text{W}/\sqrt{\text{Hz}}$. The addition of gold ring decreases the NEP by $\sim 10\%$ and increases the time constant by a factor of ~ 6 .

A bolometer model was developed to study the physical properties of the bolometer. The thermal conductance of the bolometers for different geometries is estimated using finite element analysis. Using VSB theory, simulations are performed to optimize the design. Modeling of High-G, Medium-G and Low-G bolometers were done and the results from the models are compared with experimental measurements. The total noise current, calculated by considering the contributions from the different sources of noise, is compared with the noise measurements. From the model, the electrical NEP is calculated with and without consideration of photon noise from the 300 K background and is compared with the experimentally measured optical NEP. Heat capacity budget calculations are performed for the bolometers of different geometries. The total heat capacities are 8.9×10^{-12} , 6.9×10^{-13} , 7.1×10^{-13} and 7.0×10^{-12} J/K, respectively for the High-G, Low-G, and Medium-G without the gold ring and Medium-G with the gold ring. The continuous titanium film absorbers have higher heat capacity than the Au-Pd cross absorbers. In the case of the Low-G and Medium-G without gold ring layouts, the heat capacities of the radiation absorber and the thermistor dominate the total heat capacity of the bolometer. The niobium wires are very thin hence they have very small heat capacity.

The 7-element superconducting array has been steadily optimized for astronomical observations. Efforts were made to understand the properties of the silicon nitride membrane, the Au-Pd/Mo thermistor and the SQUIDs. The structuring of the membrane in spider geometry increases the sensitivity of TES. The experiments show that Medium-G bolometer has very good sensitivity for 300 K background operation. The measured optical NEP is $\sim 2 \times 10^{-16}$ W/ $\sqrt{\text{Hz}}$. The measured $\text{NEP}_{\text{optical}}/\text{NEP}_{\text{photon}}$ is ~ 1.3 which means that the optical performance of our VSB designs is very close to 300 K background limit in the 1.2 mm atmospheric window. The thickness of the gold ring can be adjusted to tune the time constant of the bolometer. The Medium-G layout is a good choice for future superconducting bolometer arrays intended to operate under a relatively high background environment, like that of ground based telescope.

The sensitivity of the bolometer on the telescope is represented by the Noise Equivalent Flux Density (NEFD). This is the flux density that produces a signal-to-noise of unity in a second of integration, and is given by:

$$\text{NEFD} = \frac{2 \text{NEP}}{\eta_c \eta_t A_e e^{-\tau A} \Delta\nu} \quad [W/\sqrt{\text{Hz}}], \quad (7.1)$$

where, η_c is chopping efficiency, η_t is overall optical efficiency, A_e is the effective area of the telescope primary, $e^{-\tau A}$ is the sky transmission in which τ is the zenith optical depth and A is the airmass, and $\Delta\nu$ is the filter passband. The factor of 2 has been introduced to account for optical chopping: $\sqrt{2}$ because the on-source time is half the total time, and $\sqrt{2}$ because the result is a differenced measurement.

The seven element TES array presented here was designed for the 1.2 mm transmission band in which the Max-Planck Millimeter Bolometer (MAMBO) semiconductor arrays installed at the IRAM 30-m Millimeter Radio Telescope (MRT) work. The measured NEP of MAMBO-2, $\text{NEP}_{\text{MAMBO-2}}$, is 3×10^{-16} W/ $\sqrt{\text{Hz}}$. The $\text{NEP}_{\text{MAMBO-2}}$ at the IRAM 30-m MRT corresponds to the NEFD of 30 mJy/ $\sqrt{\text{Hz}}$, without any opacity corrections. The calculations are performed by assuming the η_c and η_t of 40%, an effective telescope area (corrected for efficiencies) of 250 m², and a bandwidth, $\Delta\nu$, of 50 GHz. The NEP of the Medium-G layout with gold ring, NEP_{TES} , is 1.7×10^{-16} W/ $\sqrt{\text{Hz}}$. Considering the same telescope parameters and the NEP_{TES} , the NEFD of the Medium-G TES with gold ring is expected to be 17 mJy/ $\sqrt{\text{Hz}}$, without any opacity corrections.

As shown in Eq. 7.1, the NEFD is dependent on the weather and varies with sky transmission, even in the 1.2 mm band (and *much* more so in the submm wavebands). In the Rayleigh-Jeans limit of the

black body spectrum, the sky emission fluctuations in the 350 GHz (870 μm) window are higher by a factor $(350 \text{ GHz}/250 \text{ GHz})^2 = 2$, than in the 250 GHz (1.2 mm) atmospheric window. The NEP of the bolometer is dependent on the throughput of the system, which is proportional to λ^2 , where λ is a wavelength of the incoming radiation. The ratio of the throughput in the 1.2 mm and in the 870 μm band is $(1.2^2/0.87^2) = 2$. Thus, the fluctuations in the sky emission in the different atmospheric windows is canceled by the difference in the throughput of the system.

For the 870 μm window, the $\text{NEFD}_{\text{TES},870\mu\text{m}}$ at the APEX telescope would be $30 \text{ mJy}/\sqrt{\text{Hz}}$, assuming η_c and η_t of 60%, an effective telescope area of 100 m^2 , and a $\Delta\nu$ of 30 GHz.

Similarly, for 350 μm window, the $\text{NEFD}_{\text{TES},350\mu\text{m}}$ at APEX telescope would be $65 \text{ mJy}/\sqrt{\text{Hz}}$, assuming η_c and η_t of 40%, the telescope's effective area as 66 m^2 , and $\Delta\nu$ as 50 GHz.

Table 7.1 compares the calculated values for the Seven Element TES Array (SETA) in different atmospheric windows with existing bolometer cameras at various ground-based astronomical telescopes. Since their performance is limited mainly due to the background, these instruments are designed for high background operation. The main advantage of superconducting bolometers over semiconducting bolometer is that they can be designed for very low background operation, up to an NEP of $\sim 10^{-19} \text{ W}/\sqrt{\text{Hz}}$ and are, thus detectors of choice for future space borne telescopes. The integration time on the sky to map a given area, A , on the sky to an rms noise level, σ is

$$t_{\text{int}} = \left(\frac{\text{NEFD}}{\sigma} \right)^2 \frac{1}{N_{\text{channels}}} \frac{A}{\Omega} \quad [\text{seconds}], \quad (7.2)$$

where, N_{channels} is the number of channels and Ω is the beam size of an instrument. A large pixel number superconducting bolometer camera at 870 μm on APEX, e.g., LABOCA-2 (~ 300 channels) will be very useful for deep large surveys.

The atmosphere opacity at APEX in 350 μm window is ~ 0.5 , thus, a superconducting bolometer camera with Medium-G layout bolometers will allow very sensitive galactic observations. A 37 channel, Small Apex Bolometer Camera (SABOCA), designed for the 350 μm transmission band, with the Medium-G with gold ring layouts of the superconducting bolometers, will be installed on the APEX telescope in the near future.

Table 7.1: Noise Equivalent Flux Density comparison for different bolometer arrays.

Instrument Name	Wavelength μm	NEFD $\text{mJy}/\sqrt{\text{Hz}}$
SHARC-II * (CSO)	350	500
† SETA * (APEX)	350	65 ‡
SCUBA * (JCMT)	450 850	500 80
SCUBA-2 * (JCMT)	450 850	100 30
LABOCA * (APEX)	870	125
† SETA * (APEX)	870	30 ‡
MAMBO-2 * (IRAM 30-m)	1200	30
† SETA * (IRAM 30-m)	1200	17 ‡
BoloCAM * (CSO)	1400	35
† Seven Element TES Array (SETA). ‡ Calculated values. * Semiconducting bolometers. * Superconducting bolometers.		

Appendix A

Photographs of experimental setup

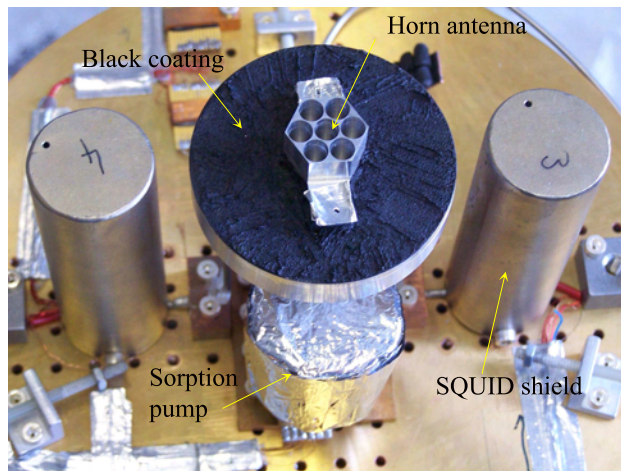


Figure A.1: The incoming radiation is coupled to the bolometer via multiple feed horn antennas. In order to avoid reflections from the metal surface, a black coating is applied inside the ^3He shield. The SQUIDs are placed next to the array in Cryoperm magnetic shielded containers.

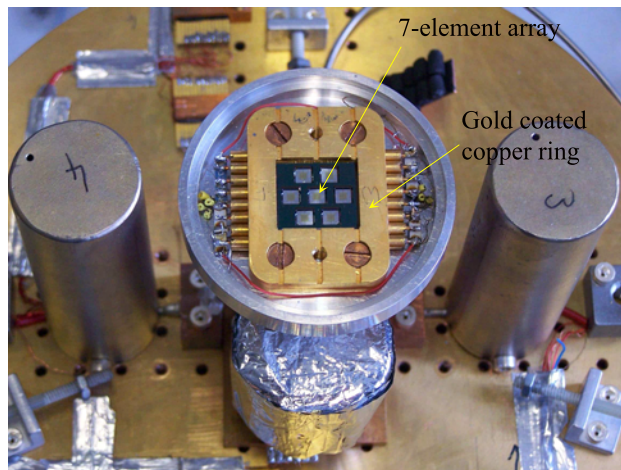


Figure A.2: The figure shows the 7-element array bounded in a gold coated copper ring. The assembly is placed in an aluminum mount. Aluminum is superconducting at the operating temperature of 0.3 K, hence it provides perfect magnetic shielding.

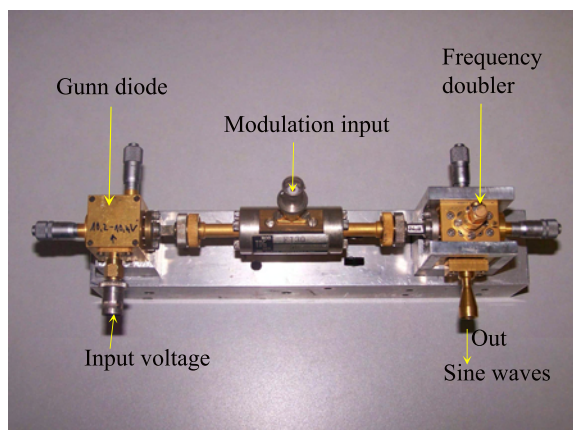


Figure A.3: This photograph shows the Gunn diode used in the experiments to determine the time constants of the bolometers.

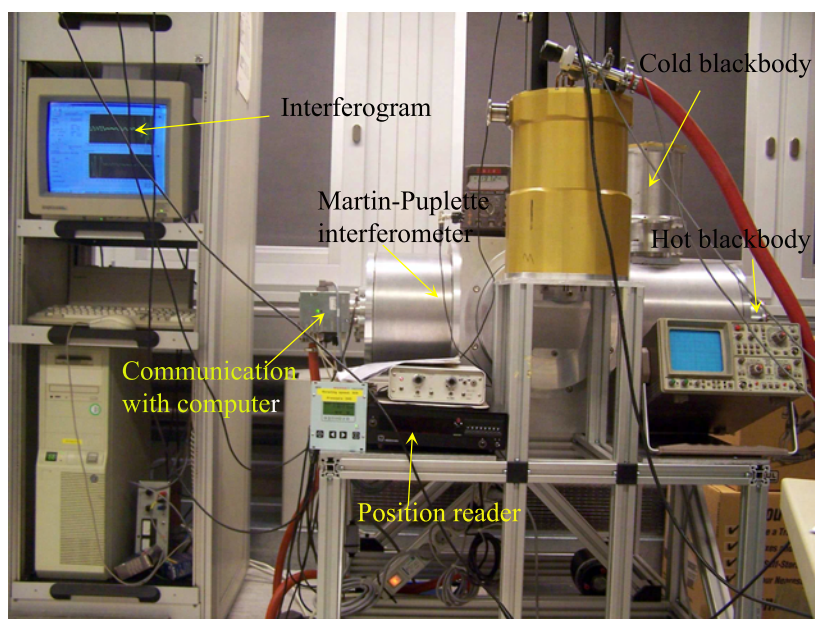


Figure A.4: This photograph shows the experimental setup of the Martin-Puplett interferometer. The mirror position is read on the optical scale placed next to mirror path. The mirror position reader has accuracy of $0.1 \mu\text{m}$. The rotating mirror placed inside the assembly of interferometer generates the signal from a cold or hot blackbody. The cold blackbody is at 77 K , while the hot blackbody is at the room temperature. The interferogram is recorded with *LabVIEW* software and the spectral response of the system is calculated.

Bibliography

- Aspin, C., Sandell, G., & Weintraub, D. A. 1994, *A&A*, 282, L25
- Baker, C. G. B. & Wyatt, A. F. G. 1987, *J. Phys E: Sci. Instrum*, 20, 1461
- Bartelmann, M., Huss, A., Colberg, J. M., Jenkins, A., & Pearce, F. R. 1998, *A&A*, 330, 1
- Beckwith, S. V. W., Sargent, A. I., Chini, R. S., & Guesten, R. 1990, *AJ*, 99, 924
- Birkinshaw, M. 1999, *Phys. Rep.*, 310, 97
- Bond, J. R., Contaldi, C. R., Pen, U.-L., et al. 2005, *ApJ*, 626, 12
- Born, M. & Wolf, W. 1975, *Principles of Optics* 4th ed. (Pergamon, Oxford)
- Boucher, R., May, T., Wagner, T., et al. 2006, *Superconducting science Tech.*, 19, 138
- Boyle, W. S. & Rogers, K. F. J. 1959, *J. Opt. Soc. Am.*, 33, 92
- Carilli, C. L. & Yun, M. S. 1999, *ApJ*, 513, L13
- Carlstrom, J. E., Joy, M., & Grego, L. 1996, *ApJ*, 461, L59+
- Clarke, J. 1971, *Physics Today*, 1, 30
- . 1974, *Science*, 1, 34
- Clarke, J., Hoffer, G. I., Richards, P. L., & Yeh, Y. H. . 1977, *J. Appl. Phys.*, 48, 4865
- Colin, A. E. S. 2006, Ph.D. Thesis, Characterization of LABOCA, University of Granada, Spain.
- de Korte, P. A. J., de Nivelles, M. J. M. E., & Wijnbergen, J. J. 1995, *Proc. SPIE*, 2578, 294
- de Nivelles, M. J. M. E., Bruijijn, M. P., de Vries, R., et al. 1997, *J. Appl. Phys.*, 82, 4719
- Downey, P. M., Jeffries, A. D., Meyer, S. S., et al. 1984, *Appl. Opt*, 23, 910
- Drew, H. D. & Sievers, A. J. 1969, *Appl. Phys.*, 8, 2067
- Drung, D., Cantor, R., Peters, M., Scheer, H. J., & Koch, H. 1990, *Appl. Phys. Lett*, 57, 406
- Du Chatenier, F. J. & De Nobel, J. 1961, *Physica*, 28, 181
- Electro Optical Inc. 1995, <http://www.electro-optical.com/>
- Evrard, A. E., MacFarland, T. J., Couchman, H. M. P., et al. 2002, *ApJ*, 573, 7
- Gemünd, H.-P., Kreysa, E., Schubert, J., & Krätschmer, W. 1994, *Proc. SPIE*, 272, 2268

- Goldsmid, H. J. 1966, School of Physics, Bristol college of science and technology, 1, 24
- Greaves, J. S., Holland, W. S., Moriarty-Schieven, G., et al. 1998, ApJ, 506, L133
- Gromke, J. 1996, Diploma Thesis at Max-Planck-Institut für Radioastronomie
- Guiderdoni, B., Hivon, E., Bouchet, F. R., & Maffei, B. 1998, MNRAS, 295, 877
- Hansen & Wu, G. 2006, Theoretische Elektrotechnik group, University of Wuppertal (<http://www.tet.uni-wuppertal.de/>)
- Henning, T., Klein, R., Chan, S. J., et al. 1998, A&A, 338, L51
- Hoevers, H. F. C., Mels, W. A., Frericks, M., & Korte, P. A. J. 2000, Appl. Superconductivity Conf., VA, USA, 1, 50
- Hogerheijde, M. R., Jayawardhana, R., Johnstone, D., Blake, G. A., & Kessler, J. E. 2002, AJ, 124, 3387
- Holland, W. S., Greaves, J. S., Zuckerman, B., et al. 1998, Nature, 392, 788
- Holmes, W., Gildemeister, J. M., & Richards, P. 1999, Appl. Physics Letters, 72, 18
- Hughes, D. H., Aretxaga, I., Chapin, E. L., et al. 2002, MNRAS, 335, 871
- Hughes, D. H., Serjeant, S., Dunlop, J., et al. 1998, Nature, 394, 241
- Irwin, K. D. 1995, Appl. Phys. Lett., 66, 1998
- . 2002, Physica C, 368, 203
- Jewitt, D., Aussel, H., & Evans, A. 2001, Nature, 411, 446
- Jewitt, D. & Luu, J. 1992, AJ, 104, 398
- Johnstone, D. & Bally, J. 1999, ApJ, 510, L49
- Josephson, B. D. 1962, Phys. Lett., 1, 251
- Kempner, J. C., Sarazin, C. L., & Ricker, P. M. 2002, ApJ, 579, 236
- Kittel, C. & Kroemer, H. 1980, Thermal physics 2nd ed. (Freeman, New York)
- Koerner, D. W., Sargent, A. I., & Beckwith, S. V. W. 1993, ApJ, 408, L93
- Kreysa, E., Beeman, J. W., & Haller, E. E. 1996, in ESA SP-388: Submillimetre and Far-Infrared Space Instrumentation, ed. E. J. Rolfe & G. Pilbratt, 111–+
- Kreysa, E., Gemuend, H.-P., Gromke, J., et al. 1998, in Proc. SPIE Vol. 3357, p. 319-325, Advanced Technology MMW, Radio, and Terahertz Telescopes, Thomas G. Phillips; Ed., ed. T. G. Phillips, 319–325
- Kreysa, E., Gemünd, H.-P., Raccanelli, A., Reichertz, L. A., & Siringo, G. 2002, in AIP Conf. Proc. 616: Experimental Cosmology at Millimetre Wavelengths, ed. M. de Petris & M. Gervasi, 262–269
- Kuo, C. L., Ade, P. A. R., Bock, J. J., et al. 2004, ApJ, 600, 32
- Lamarre, J. M. 1986, Appl. Opt., 25, 870
- Langley, S. P. 1900, ApJ, 12, 370

- Lee, A. T., Richards, P. L., Nam, S. W., Cabrera, B., & Irwin, K. D. 1996, *Appl. Phys. Lett.*, 69, 1801
- Lee, S., Gildemeister, J. M., Holmes, W., Lee, A. T., & Richards, P. L. 1998, *Appl. Opt.*, 37, 3391
- Low, F. J. 1964, *AJ*, 69, 143
- Mannings, V. 1994, *MNRAS*, 271, 587
- Martin, D. H. & Puplett, E. 1969, *Infrared Physics*, 10, 105
- Martinis, J. M. & Clarke, J. 1986, *J. of Low Temp. Phys.*, 86, 459
- Mason, B. S., Pearson, T. J., Readhead, A. C. S., et al. 2003, *ApJ*, 591, 540
- Mather, J. C. 1982, *Appl. Opt.*, 21, 1125
- Matsuo, S., Sugiura, H., & Noguchi, S. 1973, *J. of Low Temp. Phys.*, 15, 481
- Maul, M. K., Strandberg, M. W. P., & Kyhl, R. L. 1969, *Physical Review*, 182, 522
- Mauskopf, P. D., Bock, J. J., Castillo, H. D., Holtzapfel, W. L., & Lange, A. E. 1997, *Appl. Opt.*, 36, 765
- Mezger, P. G., Mathis, J. S., & Panagia, N. 1982, *A&A*, 105, 372
- Motte, F., Andre, P., & Neri, R. 1998, *A&A*, 336, 150
- Nishioka, N. S., Richards, P. L., & Woody, D. P. 1978, *Appl. Opt.*, 17, 1562
- Osterman, D., Patt, R., Hunt, R., & Peterson, J. 1997, *Appl. Phys. Lett.*, 71, 2361
- Oukhanski, M., Stolz, R., Zakosarenko, V., & Meyer, H.-G. 2003, *6th Workshop From Andreev Reflection to the International Space Station*, Björkliden, Kiruna, Sweden.
- Oukhanski, N., Stolz, R., & Meyer, H.-G. 2006, *Institute of Physics Publishing*, 43, 1270
- Pobell, F. 1992, *Matter and Methods at low temperatures*, Springer
- Reese, E. D., Carlstrom, J. E., Joy, M., et al. 2002, *ApJ*, 581, 53
- Richards, P. L. 1994, *J. Appl. Phys.*, 76, 1
- Sandell, G. & Weintraub, D. A. 1994, *A&A*, 292, L1
- Schulz, R. 2002, *A&A Rev.*, 11, 1
- Simon, M. & Guilloteau, D. 1992, in *Astronomical Society of the Pacific Conference Series*, Vol. 32, IAU Colloq. 135: Complementary Approaches to Double and Multiple Star Research, ed. H. A. McAlister & W. I. Hartkopf, 66–+
- Sunyaev, R. A. & Zel'dovich, Y. B. 1970, *Ap&SS*, 7, 3
- Supracon. 2003, Dr. V. Zakosarenko – IPHT (<http://www.supracon.com/>)
- Swartz, E. T. & Pohl, R. O. 1989, *Reviews of Modern Phys.*, 61, 3
- Trujillo, C. A., Luu, J. X., Bosh, A. S., & Elliot, J. L. 2001, *AJ*, 122, 2740
- van Vliet, K. M. 1967, *Appl. Opt.*, 6, 1145
- Weintraub, D. A., Sandell, G., & Duncan, W. D. 1989, *ApJ*, 340, L69

Weintraub, D. A., Sandell, G., Huard, T. L., et al. 1999, *ApJ*, 517, 819

White, G. 1979, *Experimental techniques in low-temperature physics*

Zaroubi, S., Squires, G., de Gasperis, G., et al. 2001, *ApJ*, 561, 600

Curriculum Vitae

Name: Nikhil S. Jethava
Date of Birth: 21.05.1981
Nationality: Indian
Sex: Male
Present Address: Max-Planck-Institut für Radioastronomie
Auf dem Huegel 69, 53121, Bonn

Education:

07/2004 – 07/2007: Graduate student,
Max-Planck-Institut für Radioastronomie (MPIfR)
08/2002 – 06/2004: M.S. (Radio Astronomy and Space Science),
Chalmers University of Technology, Göteborg, Sweden
08/1998 – 07/2002: B.E. (Instrumentation and Control Engineering),
Government College of Engineering Pune (COEP),
University of Pune, Maharashtra, India
06/1996 – 06/1998: Higher Secondary School,
K. T. H. M. College, Nashik, Maharashtra, India

Research Experience:

PhD Thesis, 2004 – 2007 : Superconducting bolometers for millimeter and
submillimeter wave astronomy.
Millimeter and Submillimeter Astronomy Group , MPIfR, Bonn
Master Thesis, 2003 – 2004 : Optics alignment tool, Group of Advanced Receiver Development,
Onsala Space Observatory, Sweden.
Summer Project, 2003: COBRA system programming and VLA data reduction.
Jodrell bank Observatory
University of Manchester, UK
Bachelor Project, 2001 – 2002 : Fire Optics LAN development
Giant, Meter-wave Radio Telescope
National Center for Radio Astrophysics, Pune, India
Summer Project, 2000 : Dual channel LASER communication
Bhabha Atomic Research Center, Mumbai, India
Mini Project, 2000 : Fluid color detection
COEP, India

Acknowledgments

A lot that cannot be said is at times best expressed in the words: “Thank you”. Here, I mention some of the countless number of persons who are instrumental, in more ways imaginable, for the fruits of my studies and making my stay in PhD thesis a delight.

I sincerely thank my supervisor, Dr. Ernst Kreysa, for his uncompromised support, which I consider a priceless gift in my journey as a PhD researcher. He has provided challenges to strive, which has been proved the most useful for reaching the finish line. I could not have imagined having a better advisor and mentor for my PhD. Without his knowledge, perceptiveness, experience, invaluable lessons and discussions, I would never have finished. Ernst, thanks a lot for always being there and patiently answering all my stupid questions. I have learned a lot from you and learned the effectiveness of ‘being nice & simple’.

With my deepest gratitude, I thank Prof. Karl Menten for giving me an opportunity to work in mm/submm group and careful mentoring at every crucial moment. His guidance has helped in numerous ways which I find difficult to put into words. He believed in me and offered various interesting and challenging projects which improved my astronomical knowledge exponentially. I thank you, for bearing with my impatient behavior and supporting me in all the situations.

Prof. Frank Bertoldi has always kept a check on the progress of the thesis and provided very useful suggestions. He has been a very friendly face during my thesis, and never said ‘no’ to any of my requests. Frank, I wish to thank you for all your help and support.

I thank Prof. Hans-Georg Meyer from Institute for Photonic Technology, Jena and Prof. Rainer Streubel from University of Bonn for agreeing to referee my thesis.

My astronomical work is greatly boosted by the support from Dr. Christian Henkel. He has not only provided me some data but also helped me to learn the data reduction and analysis. We had wonderful time at Effelsberg telescope; he has shown different ways to reach there! Christian, I wish to thank you, with all my respect. You have been very kind and very understanding.

I am grateful to our collaborators at Jena who have offered help and insights to all the requests. It has been wonderful to know Dr. Torsten May. Torsten has given me a wonderful company during the SPIE meeting and I look forward to see him. Dr. Zakosarenko had immediately provided the SQUID calculations, upon my request.

I thank Prof. Anton Zensus and Dr. Eduardo Ros for supporting my travels and very friendly useful comments.

During my visit to Grenoble, Dr. Jan Martin (IRAM) and Dr. R. Nari (IRAM) have greatly helped me to reduce and understand the PdBI data. Prof. Mark Reid (CfA) has been very helpful for VLBI data reduction. Under the supervision of Mark, I have learned to use AIPS, methodologically. Dr. Chris Carilli (NRAO) has offered his help on VLA data reduction. He has shown some of the tricks to reduce the *noisy* data.

Since the day I arrived, Dr. Giorgio Siringo has been a great support. He has helped me through various computer problems and also taught me many bolometer basics. He has been very helpful during the Martin-Puplette interferometric measurements. Giorgio, very many thanks for helping me in countless number of occasions.

I thank Mr. Walter Esch for helping me out during all the experiments. Walter has been very accommodating in all the situations. He has shown that, tapping an instrument can also solve the problem! Walter has sorted out various electronics, wiring and soldering problems. My sincere thanks to him. Ms. Gundula Lundershausen has helped me to bond all the arrays inside the copper ring. Her Zwiebelkuchen has been amazingly tasty and every time, I have almost licked the plates. Many thanks to Mr. Hans-Peter Gemünd for providing the filters and having various discussions. Peter has been a great help to translate the letters from German to English and offered all the support unconditionally. Mr. Bernd Ufer has been very helpful to get the liquid Helium and Nitrogen.

I am grateful to Ms. Lahr-Nilles, Ms. Breuer, Ms. Lewinsky, Ms. Fingas and Ms. Salas, for helping me through all administration hurdles.

Dr. Hans-Joachim Wunsch has introduced me to COSMOS programs and helped to understand them. I would not have been able to perform the finite element analysis without his support. He was accessible to me at all the required times and it really boosted my work. Thank you very much Joachim.

Millimeter and Submillimeter group has always provided a very wonderful atmosphere. There have always been many helping hands for various issues. I thank to many staff members of the Max Planck Institute for the administrative support. Very many thanks to Jagadheep, Gayoung and Dharam for reading my thesis and providing very essential comments.

The work and life would be very dull without my fellow colleagues and friends. Thushara, Jens, Jan, Hauke have been great friends from the beginning years. My friend, Manolis has always given me an enjoyable company with a broad smile on his face. Thanks to Rupal, Anupreeta, Hyunjoo, Carolin, Lies, Kazi, Peng, Fatemeh, Axel, Frederic, Attila, Simone, Violetta, Nadia, Kosmas, Sang-Sung, Nicola, Subramanian for wonderful discussions in every day-to-day life. Manuel has been a great roomy; he has been very understanding during this last phase of PhD.

I have immensely enjoyed the *BonnIndians* group. I have made some very good friends in Bonn. There are many who have supported me in one way or another. Hari, Giri, Gupta-s, Jain-s, Sadanand, Kusum, Amit, Poornnima, Sara, Deepak-s, Preethi, Bhadresh, Schubani, Satish, Shreedhar have made my everyday enjoyable. Many thanks to Nital for wonderful conversations. Talking to her was very delightful, especially during the last phase.

I must not forget my friends from school and college. They are the ones who have shared with me for really long time. Many of them are geographically located around the world and I hope to see them sometime in the future. My sincere apologies if I have forgotten any important names.

Last but definitely not the least, my sincere thanks to my family. My parents, brother, sister and her family have been a great source of support. They have provided the fuel for all my work and life. I am really looking forward to see them all soon.